UNIVERSITAT DE BARCELONA

Monte Carlo based methods applied to heterogeneous catalysis and gas separation

Hèctor Prats Garcia

Memòria presentada per

Hèctor Prats Garcia

per a optar al grau de Doctor per la Universitat de Barcelona

Programa de doctorat en Química Teòrica i Computacional

Monte Carlo based methods applied to heterogeneous catalysis and gas separation

Dirigida per:

Dr. Ramón Sayós Ortega
(Universitat de Barcelona)

Dr. Francesc Illas Riera
(Universitat de Barcelona)

Tutor:

Dr. Francesc Illas Riera
(Universitat de Barcelona)

UNIVERSITAT DE BARCELONA

Barcelona, 2019

UNIVERSITAT DE BARCELONA

FACULTAT DE QUÍMICA

DEPARTAMENT DE CIÈNCIA DE MATERIALS I QUÍMICA FÍSICA

INSTITUT DE QUÍMICA TEÒRICA I COMPUTACIONAL

MONTE CARLO BASED METHODS APPLIED TO HETEROGENEOUS CATALYSIS AND GAS SEPARATION

Hèctor Prats Garcia

2019

“If the elements are the alphabets of chemistry,
then the compounds are its plays, its poems, and its novels”

Peter Atkins

The work presented in this doctoral thesis has been carried out at the Department of Material Science and Physical Chemistry and the Institute of Theoretical and Computational Chemistry (IQTC) of the University of Barcelona (UB).

This project has been possible thanks to financial support provided by the Spanish *Ministerio de Economia y Competitividad* (Grants CTQ2012-30751 and CTQ2014-53987-R) and by the *Generalitat de Catalunya* (Grants 2014SGR97, 2014SGR1582). Computer resources were provided by the IQTC and by the *Consorci de Serveis Universitaris de Catalunya* (CSUC).

Hector Prats Garcia is grateful for the pre-doctoral grant from the *Generalitat de Catalunya* (FI-DGR-2015).

Acknowledgements

Han sigut moltes les persones que s'han esforçat per a fer aquesta tesi possible. En primer lloc, vull agrair als meus directors de tesis, el Prof. Ramón Sayós i el Prof. Francesc Illas, per la seva dedicació durant aquests quatre anys de tesis i l'aprenentatge rebut. De fet, ja fa més de sis anys que li dec un agraïment immens al Ramón. Des de que em va acollir com a alumne intern durant l'estiu de l'any 2012, i em va endinsar en l'apassionant món de la química computacional, s'ha mostrat sempre amb la voluntat d'ensenyar-me i ajudar-me en el meu camí cap a científic. En aquest temps hem compartit una infinitat de discussions científiques, viatges a congressos i fins i tot aficions com ara el *running*. Va ser l'any 2015 quan vaig començar a treballar també amb el *Xino*, i ens vam iniciar els tres junts en les simulacions de reaccions en superfície. Particularment, vull agrair al Francesc, amb qui comparteixo també l'afició pel submarinisme, que em proposés la idea de treballar amb el mètode kMC. Tot i representar dos estils de treballar diferents i liderar grups d'investigació fins aleshores independents, s'han complementat de manera excel·lent i m'he pogut beneficiar de les millors qualitats de cadascú. Em sento realment molt afortunat d'haver pogut comptar amb aquests dos mentors, que han dipositat en mi la seva més absoluta confiança des d'un inici, i també molt agraït per la sincera amistat que ha sorgit durant tot aquest temps treballant junts.

A banda dels meus directors, també vull agrair especialment al Dr. Pablo Gamallo, el meu tercer mentor i tota una referència per a mi a nivell científic i personal, i amb qui també he tingut el plaer de treballar durant aquests anys. Agrair també sincerament a la resta de membres (alguns ja ex-membres) dels dos grups, en especial al Dr. Daniel Bahamón, al Dr. Xavi Giménez i al Dr. Francesc Viñes, amb els que he tingut el gust del col·laborar directament.

I must also acknowledge Dr. Mie Andersen and Prof. Karsten Reuter, who hosted me during my research stay in the Technical University of Munich. Through our discussions I have learnt the very basics of kMC, computer science, and many tools for computational chemistry that have made my research easier. I also want to thank all the members of the *Theoretische Chemie* group, especially Dr. Albert Bruix, Joana Avelar, David Egger and Christian Kunkel, who made the visit more pleasant.

I want to thank all the open source contributors. I cannot imagine my scientific work without tools like *python*, *ASE*, *matplotlib*, *Fortran*, *Zotero*, *virtualenv* and many

others! Moreover, many thanks to all VASP, LAMMPS, ZACROS, KMOS, ProFIT, SLURM and VMD contributors and all the Stack Overflow community.

Un agraïment immens també per als meus companys de departament a la UB, en especial al Gerard i al Manel. M'heu aguantat durant les meves frustracions i m'heu acompanyat en els èxits d'aquesta tesi. Em sento molt afortunat d'haver pogut treballar durant aquests anys rodejat d'amics com vosaltres. Menció especial també per la Estefania, amb qui vam forjar una molt bona amistat des de el meu primer viatge a un ESPA; al Carles, ex-company de despatx i de moltes cerveses, i al Pablo Lozano, a qui vaig tenir d'alumne fa uns anys i ara tinc el gust de poder guiar durant la seva recerca del màster. Vull agrair també als membres joves del departament per la seva amistat companyia: el Biel, el Marc, l'Angel, el Juanjo, el Toni, l'Efrem, l'Oriol P., la Lorena, el Joan, el Raúl, el Pablo B., la Cristina... i molts més; i també als ex-membres que ja no hi són: l'Anna P., el Víctor, l'Oriol L., el Sergi... etc. Tots plegats heu contribuït a crear un ambient de departament on un se sent com a casa seva. I si en alguna cosa destaca aquest departament, apart de la recerca científica, és en la gran qualitat humana dels diferents professors que hi formen part. Menció especial per al *Pani*, un exemple a seguir per a mi, i que m'ha endinsat en el món de la mecànica quàntica i de l'escalada; al Fermín, el *Messi* de la docència i a qui és impossible no veure somrient; a l'Antonio, un gran exemple d'integritat, que haurien de seguir molts polítics; a l'Albert, amb qui hem compartit des de acudits fins a discussions sobre termodinàmica; i al Jaime de Andrés, que malauradament ens va deixar l'any passat. Trobem molt a faltar els teus tes! També he de donar les gràcies a dues persones sense les quals aquesta tesi no hagués estat possible: el Jordi i la Teresa, tècnics del IQTC, sempre molt eficients en resoldre qualsevol problema informàtic que he tingut.

No em puc oblidar dels meus amics de la carrera amb qui encara conservo una forta amistat: Ferran, Ernest, Anna S. i Miquel P.; i també els companys de màster: Roser, Tonino, Miquel B. i Arturo. Però per suposat, hi ha molts amics de fóra de la Facultat a qui dec moltíssim, en especial al Ivan, l'Efrén, el Kirian, l'Adrià, el Tomas i el Rachid. Tots vosaltres heu ajudat a que hagi superat aquesta etapa mantenint la meva salut mental.

Aquesta tesi va dedicada als meus pares i a la meva germana, als qui dec tot el que sóc, i que sempre m'han animat a aconseguir els meus objectius. I, per acabar, també vull dedicar aquesta tesi a la Laura, la persona que més de prop ha viscut aquest cicle, i a qui no puc dir-li res que no sàpiga ja. T'estimo.

Table of contents

Glossary

AI-MD	Ab-initio molecular dynamics
AS-kMC	Accelerated superbasin kinetic Monte Carlo
CCS	Carbon capture and storage
DFT	Density functional theory
ESA	Electric swing adsorption
FF	Force field
FRM	First reaction method
GCMC	Grand canonical Monte Carlo
GGA	Generalized gradient approximation
GTO	Gaussian-type orbitals
HF	Hartree-Fock
HK	Hohenberg-Kohn
IAST	Ideal adsorbed solution theory
IZA-SC	Structure commission of the International Zeolite Association
kMC	Kinetic Monte Carlo
KS	Kohn-Sham
LCAO	Linear combination of atomic orbitals
LDA	Local-density approximation
LTA	Linde type A
MC	Monte Carlo
MCSCF	Multi-configurationally self-consistent field theory
MD	Molecular dynamics
MEA	Monoethanolamine
MM	Microkinetic modelling
MOF	Metal-organic framework
MP2	Møller-Plesset perturbation theory to second order
PBE	Perdew, Burke and Ernzerhof
PES	Potential energy surface
PSA	Pressure swing adsorption
PP	Pseudopotential
PPN	Porous polymer network

PW	Plane wave
PW91	Perdew and Wang 91
RSM	Random selection method
STO	Slater-type orbitals
TM	Transition metal
TOF	Turnover frequency
TSA	Temperature swing adsorption
TST	Transition state theory
vdW	Van der Waals
VOC	Volatile organic compound
VSA	Vacuum swing adsorption
VSSM	Variable step size method
VPSA	Vacuum-pressure swing adsorption
WGSR	Water-gas shift reaction
ZIF	Zeolitic imidazolate framework

CHAPTER ONE

Introduction

1.1. Motivation and outline of the thesis

The research work presented in this thesis is divided in two main topics: gas separation and heterogeneous catalysis. Although the systems studied in one part and another are quite different, they share two fundamental features: both topics have a special industrial interest and they have been studied through stochastic Monte Carlo based methods.

The present work on gas separation aims to assess the performance of several faujasite structures, a well-known family of zeolites, in CO_2 capture processes. Concretely, ten faujasite structures with different Al content have been evaluated in the separation of post-combustion CO_2 mixtures via simulation of swing adsorption processes.

On the other hand, the research work on chemical reactivity focus on the study of the water-gas shift reaction (WGSR) on copper surfaces both from a thermodynamic and from a kinetic point of view.

A descriptive introduction on post-combustion CO_2 capture and the water-gas shift reaction is presented in Chapter 1. In Chapter 2 a brief overview of the theory behind the present work and the different computational methods used are given. From lower to higher complexity, Section 2.1 starts by introducing the main computer simulation method for studying the adsorption of gases in adsorbents: Grand Canonic Monte Carlo (GCMC). The energetic interactions at a quantum mechanical level are introduced in Section 2.2 with the Density Functional Theory (DFT). Then, the application of Transition State Theory (TST) to compute the rates of surface processes from DFT data is presented in Section 2.3. Finally, two possible ways to study the kinetics of macroscopic systems from microscopic data are presented: microkinetic modelling (MM) (Section 2.4) and the kinetic Monte Carlo method (kMC) (Section 2.5). Results start in Chapter 3 with the discussion of the three different swing adsorption processes studied to separate CO_2 from a post-combustion mixture using faujasites. Several adsorbent evaluation criteria such as selectivity, working capacity, purity or thermal regeneration energy, among others, are considered to analyze the separation performance for each faujasite under realistic conditions. Chapter 4 deals with the DFT-based first-principles kMC simulations of the water-gas shift reaction on Cu(111). The main objectives of this chapter are to investigate how the temperature and the reactants partial pressures affect the coverages of the different species and the turnover frequency of the reaction, as well

as to understand the microscopic molecular mechanism of the WGSR. A comparison to previous microkinetic study and experimental results is also presented. The impact of van der Waals (vdW) interactions on the description of heterogeneously catalyzed reactions is discussed in Chapter 5, using the WGSR on Cu(321) as a practical example. In Chapter 6, the effect of step sites on the WGSR is studied by comparing kMC simulation results from both the flat Cu(111) and the stepped Cu(321) surfaces. Chapter 7 discusses typical assumptions, advantages, drawbacks, and differences between MM and kMC simulations. Thus, several issues, as for instance minimum energy diagrams, diffusion processes, lateral interactions, or the accuracy of the reaction rates are discussed. Finally, Chapter 8 contains the main conclusions of this thesis. The list of publications that have come out from the following results, and the contribution to each of the papers are listed in Chapter 9. A preceptive summary of the thesis in Catalan is given in Chapter 10.

1.2. Post-combustion gas separation

Economic growth and industrial development have resulted in an increased burning of fossil fuels (e.g., oil, coal and natural gas)[1]. Currently, fossil fuel fired power plants account for 80% of total energy production worldwide[2] and will continue to be a major source of energy for the foreseeable future. However, electricity production from fossil fuel power plants will be challenged by growing concerns that anthropogenic emissions of greenhouse gases, such as carbon dioxide (CO_2) are contributing to global climate change. In fact, the combustion of fossil fuels accounts for 86% of anthropogenic greenhouse emissions, the remainder arising from land use change (primarily deforestation) and chemical processing[3].

These emissions may be reduced by a variety of measures, such as improving energy efficiency, and/or developing alternative energy sources (e.g., wind and solar power). However, the necessary transition into a sustainable energy mix, and the phasing out of fossil fuel combustion, is unlikely to occur at a sufficiently fast pace, unless additional negative emission methods are considered. Therefore, many efforts have been addressed to the development of cost-efficient technologies for separation and capture of carbon dioxide[4,5].

1.2.1. Technologies for CO_2 capture

Reduction of energy-related CO_2 emissions might be undertaken by means of Carbon Capture and Storage (CCS) techniques. In CCS, CO_2 is separated from the flue gas of a power plant, compressed to supercritical conditions to transport it, and either stored in any of a variety of suitable geologic formations or reused as a raw material in industry[5–9] (see Figure 1.1). However, if the promise of this method is to come to fruition, capture costs will have to be reduced.

In the post-combustion capture, the CO_2 is separated from the flue gas emitted after the combustion of fossil fuels (e.g., from a standard gas turbine combined cycle, or a coal-fired steam power plant). The largest flue gas components in dry weight by volume are N_2 (~80%), CO_2 (~15%) and O_2 (~5%), with total pressures near 1 bar and at relatively low temperature (i.e., between 40 and 60 ºC)[10].

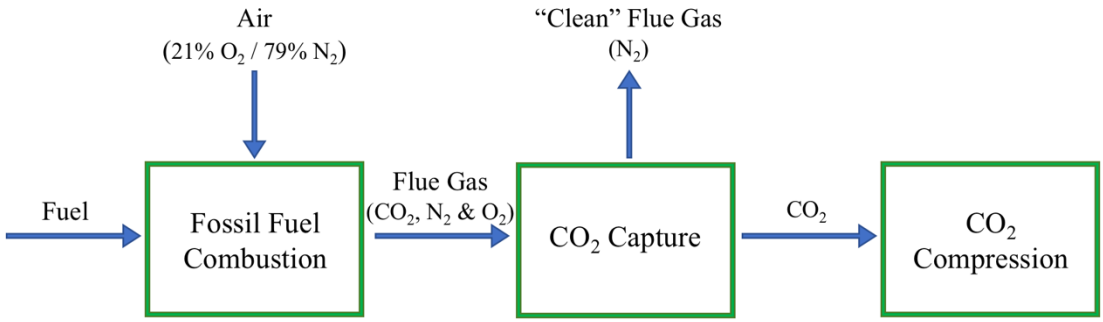

Fig. 1.1 Simplified post-combustion CO_2 capture block diagram

Separation technologies with proven adequacy for post-combustion processes under the aforementioned conditions are absorption, membrane use, cryogenic separation and adsorption[6]. Absorption with aqueous amine solutions is currently the dominant capture technology, being monoethanolamine (MEA) in water the benchmark solvent against which competing technologies are generally compared. In fact, this technology has been used in the natural gas industry for more than 60 years[11]. The aqueous basic solvents selectively absorb the mildly acidic CO_2 under ambient conditions. Then the solvent is regenerated by heating the solution at temperatures well above 100ºC. The low solvent cost and proven effectiveness make MEA an attractive absorbent for many applications. However, it suffers from high parasitic energy consumption (i.e., about 30%

of the output of the power plant[12]) as well as adverse environmental impact in the form of solvent losses and corrosion issues[13–15].

Membranes have been extensively studied for CO_2 separation because of their high selectivity, their low energy consumption, and their simplicity[3]. Separation is achieved by selectively passing one or more components of a stream through the membrane while retarding the passage of one or more other components. The driving force comes from the differences in the components partial pressures on the two sides of the membrane. However, there are a number of issues associated with the capture of CO_2 from flue gases which limit the use of membranes[16,17]. First of all, when treating mixtures with low CO_2 partial pressure, additional energy is needed to compress the feed gas, lowering the thermal efficiency of the power plant[3]. Additionally, the gases need to be cooled below 100ºC, because the high temperatures of flue gases can rapidly destroy a membrane. Likewise, the harsh chemicals contained within flue gases must be removed prior to membrane separation, unless the membrane is chemically resistant to these chemicals.

Cryogenic CO_2 removal methods can capture CO_2 in a liquid form thus making it relatively easy to pump underground for storage or send for enhanced gas or oil recovery[18]. Another advantage with respect to absorption is that no chemical absorbents are required and that the process can be operated at atmospheric pressure. However, the water content in the feed stream to the cooling units should be minimal in order to prevent plugging by ice or an unacceptably high rise in pressure drop during operation[16,19]. Moreover, great amount of energy is required for refrigerating.

Alternatively, CO_2 can be captured through adsorption in the surfaces or pores of solid materials[13,15]. This technology takes advantage of the preferential adsorption of CO_2 in specific sites of adsorbents compared to other flue gas components, and will be discussed in more detail in the next section.

1.2.2. Swing adsorption processes

CO_2 adsorption in porous solid materials is typically accomplished by Swing Adsorption processes (Figure 1.2). After the adsorption step, molecules are desorbed from the solid by lowering the pressure (Pressure Swing Adsorption, PSA), increasing the temperature (Temperature Swing Adsorption) or by application of electrical current (Electric Swing Adsorption, ESA). Particularly, a PSA process in which the desorption

is performed below atmospheric pressure is referred to as Vacuum Swing Adsorption (VSA). After this operation, the adsorbent is ready for a further cycle. All these processes are considered viable economic and ecological possibilities, and indeed numerous examples of commercial gas separation/purification processes, such as air fractionation, hydrogen production, CO_2 capture and volatile organic compounds (VOC) removal are already available, just to name a few[20–24].

The classical method for regeneration of an impurity-loaded adsorbent is to heat it to high temperature at constant pressure, as done in TSA process. This method is particularly promising, owing to difficulties with compressing or applying a vacuum to such large volumes of gas stream (as it is done in P(V)SA), as well as to the potential availability of cheap, low-grade heat in a power plant as a source of energy for regeneration[25,26]. Although the cleaning effect of a temperature-swing regeneration is very effective, it has the disadvantage that the number of cycles obtainable in any given time is limited by the relatively slow heating and cooling steps.

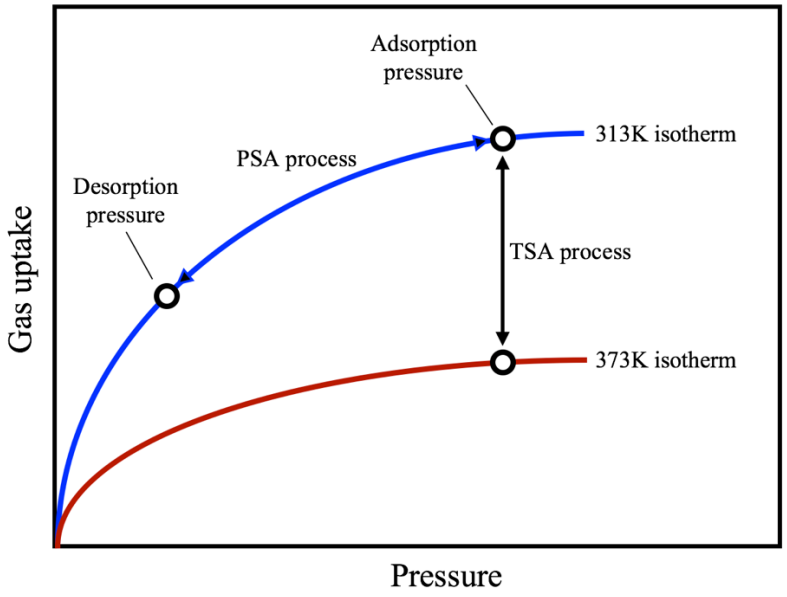

Fig. 1.2 Scheme of PSA and TSA processes

On the other hand, the removal of the CO_2 in a P(V)SA process depends on reducing the CO_2 uptake by lowering the pressure at essentially constant temperature. Because a P(V)SA system allows a much more rapid cycling, it can remove large quantities of CO_2. Also, due to the low energy requirement and fast regeneration, PSA and VSA are now used as a commercial technology for several applications[27].

Finally, ESA is a type of TSA process where the regeneration heat is provided by running an electric current through a conducting monolithic adsorbent, and it is also being tested for CO_2 capture[20,28]. The main advantage of ESA over TSA is that electric heating is much faster. However, for removing large contents of gas P(V)SA seems more appropriate than ESA or TSA. Chapter 3 of the present thesis focuses only in P(V)SA and TSA processes.

1.2.3. Adsorbent evaluation criteria

In separation processes, a good indication of the separation ability is the selectivity ($s_{A/B}$) of the porous adsorbent. Selectivity for species A relative to B is calculated by

$$s_{A/B} = \left(\frac{x_A}{x_B}\right) / \left(\frac{y_A}{y_B}\right) \quad (1.1)$$

where x_i is the molar fraction of i-component in the adsorbed phase and y is the molar fraction of i-component in the bulk/gas phase (i.e., feeding conditions).

Apart from the adsorption selectivity, there are other quantities frequently used as evaluation criteria[29]: the uptake (N_A^{ads}), working capacity (WC_A), regenerability (R_A), and purity at outlet (X_A), among others.[30] The uptake is the amount of gas molecules adsorbed at a certain pressure and temperature, and it is usually expressed as mass uptake (moles of species A adsorbed per kilogram of adsorbent) or volumetric uptake (moles of species A adsorbed per dm^3 of adsorbent). The working capacity is defined as

$$WC_A = N_A^{ads} - N_A^{des} \quad (1.2)$$

where N_A^{ads} and N_A^{des} are the uptake under adsorption or feeding and desorption or regeneration conditions, respectively. Just as with the uptake, the working capacity can be expressed in terms of mass or volume of adsorbent. This criterion is generally more relevant than the total uptake at the adsorption pressure, since it really determines the amount of A that can be recovered at each adsorption cycle. The latter two quantities are defined as

$$R_A = \left(WC_A / N_A^{ads}\right) \times 100\% \quad (1.3)$$

$$X_A = N_A^{out} / N_{TOT}^{out} \quad (1.4)$$

where N_A^{out} and N_{TOT}^{out} are the amount of A species and the total number of gas species at the outlet of the adsorber, respectively.

Another important thermodynamic quantity for understanding the possible thermal effects related to adsorption is the isosteric heat of adsorption q_{st}^{A} (or adsorption enthalpy ΔH_{ads}, $q_{st}^{A} = -\Delta H_{ads}$). This quantity provides information about the energy released during the adsorption process, and depends on the temperature and surface coverage. Additionally, it can be used to compare the interaction strength of the adsorbates with various adsorbents, or to assess whether or not the pore surface of an adsorbent is homogeneous for adsorption. The isosteric heat of adsorption can be obtained experimentally using the Clausius-Clapeyron equation, or directly from microcalorimetry measurements[31]. However, on the basis of MC simulations, the isosteric heat can be calculated from the energy/particle fluctuations in the grand canonical (GC) ensemble as[32]

$$q_{st}^{A} = -\frac{\langle U \times N \rangle - \langle U \rangle \langle N \rangle}{\langle N^2 \rangle - \langle N \rangle^2} + \langle U_g \rangle + k_B T \qquad (1.5)$$

where U is the total potential energy of the N adsorbed molecules, U_g is energy of an isolated adsorbate molecule in the ideal-gas state, and the brackets denote an average in the GC ensemble.

Finally, in order to determine the energy requirements to capture and separate a given amount of CO_2, there are two other criteria: the adiabatic work for pressurizing W_{feed} (in PSA) or vacuuming W_{vacuum} (in VSA), and the thermal regeneration energy $Q_{thermal}$ (in TSA). These quantities will be discussed in more detail in Chapter 3.

1.2.4. Zeolites and other new adsorbent materials for CO_2 capture

Many research efforts have been addressed, in particular, towards overcoming the energy intensive solvent regeneration step and chemical degradation issues, which are characteristic of conventional amine-based absorbents. New candidate materials must present high CO_2 working capacity, high selectivity for CO_2 over N_2, good stability for a wide range of pressures and temperatures, no degradable in presence of impurities and, most importantly, its full life cycle must give the smallest increase in the price of electricity.

Microporous and mesoporous solid materials have been considered for CCS, including activated carbon[33], carbon molecular sieves[34], zeolitic imidazolate frameworks[35] (ZIFs), porous polymer networks[36] (PPNs), metal-organic frameworks[37] (MOFs) and zeolites,[23,38] among others. Among these materials, zeolites look especially

adequate (see below), and thus the present study on gas separation has focused entirely on them.

Classically, zeolites are defined as hydrated aluminosilicate minerals made from interlinked tetrahedra of alumina (AlO_4) and silica (SiO_4). This definition has been expanded to include T-atoms other than Si and Al in the framework, and organic species (cationic or neutral) in the pores. Zeolites possess multiple channels, windows and cages of molecular dimensions, and the different ways in which they can be connected lead to a rich variety of zeolite structures[38–40]. The chemical composition formula of a zeolite is

$$M_{x/n}\left[(AlO_2)_x(SiO_2)_y\right] \cdot wH_2O \tag{1.6}$$

where M represents the non-framework cation of valence n (usually Na or Ca in artificial synthesis), x and y are the number of Al and Si atoms per unit cell (i.e., usually $1 \leq y/x \leq 5$) and w is the number of water molecules per unit cell.

Back in 1756, the Swedish geologist Axel F. Cronstedt (1722-1765) observed that rapidly heating the material produced large amounts of steam from water that had been adsorbed by the material, and then coined the term *zeolite*, that means "boiling stone". At that time, it was impossible to imagine all the ways in which zeolites could be exploited.

Nowadays, about 40 naturally occurring zeolites have been found[41], forming in both sedimentary and volcanic rocks. The most commonly mined structures include chabazite, clinoptilolite, stibilite and mordenite (Figure 1.3). Moreover, many synthetic zeolites that have been designed for specific purposes, being Linde type A (LTA) one of the most commercially successfully zeolites that has no natural counterpart, for its use in spacio-specific catalysis due to its special supercage structure.

Each time a new zeolite framework is reported, the members of The Structure Commission of the International Zeolite Association (IZA-SC) check to see if it has a unique framework type. If it does, a unique three letter code is assigned. These codes do not include numbers, and are generally derived from the names of the type materials (e.g., FAU to designate "faujasite"). The IZA-SC has classified 228 different zeolite framework types until now[41].

Zeolites can resist rather harsh of environmental conditions that challenge many other materials. They present high thermal stability (i.e., melting point over 1000ºC) and also resist high pressures. Moreover, they don't dissolve in water or in other inorganic solvents, and don't oxidize in air. They're not believed to cause health problems through skin contact or inhalations and, since they are based on naturally occurring minerals,

they're not believed to have any harmful environmental impacts. However, one of the most interesting properties of zeolites is trapping molecules inside them.

Fig. 1.3. Images of four natural zeolites. Chabazite[42] (up left), Stilbite[43] (up right), Mordenite[44] (down left) and Faujasite[45] (down right).

The properties of zeolites depend strongly on the Si/Al ratio (i.e., y/x in Eqn. 1.6). As the Si/Al ratio increases, the cation content decreases, the thermal stability increases, the surface becomes more hydrophobic and the zeolite loses its catalytic properties. Alumina-rich zeolites can capture polar molecules such as water, while silica-rich zeolites work better with nonpolar molecules. Synthetic zeolites are manufactured in very precise and uniform sizes (i.e., typically from 1 μm to 1 mm) with a certain Si/Al ratio to suit a particular application.

Zeolites are frequently used in PSA and VSA processes to remove CO_2 from air as an impurity because of their high CO_2 selectivity[46]. Moreover, they offer a much better thermal and mechanical stability than other adsorbent materials recently described in the literature, such as MOFs, even though the latter possess higher pore volumes and surface areas[29]. Apart from its use on post-combustion gas separation, the cage-like structure of zeolites makes them useful in other applications, such as ion-exchange water softeners, odor control and pet litter.

1.3. A briefing on heterogeneous catalysis

Catalysis is a phenomenon known from very ancient times, although not so its theory or characteristics. It became a scientific discipline in the early part of the last century, and nowadays it plays a fundamental role in the transformation of natural resources into energy and valuable chemical compounds. The term *catalysis* was first introduced by the Swedish chemist J. J. Berzelius (1779-1848), and comes from the Greek words *kata* meaning down and *lyein* meaning loosen. Berzelius wrote that by the term "*catalytic power*" he meant "*the property of exerting on other bodies an action which is very different from chemical affinity, an influence which consists in the production of a displacement, and a new arrangement of their elements, without their directly and necessarily participating in it. By means of this action, they produce decomposition in bodies, and from new compounds into the composition of which they do not enter*".[47] Some decades later, the German chemist W. Ostwald, introduced thermodynamics into the physical chemical definition of a catalyst, specifying that "*Catalysts are substances which change the velocity of a reaction without modification of the energy factors of the reaction*". This definition excludes substances that accelerate the reaction rate by entering into reaction with a resultant disruption of the reaction equilibrium. The Ostwald definition is very similar to the present IUPAC definition of catalysts: "*a substance that increases the rate of reaction without modifying the overall standard Gibbs free energy change in the reaction*"[48]. In fact, the catalyst is both a reactant and product of the reaction, which provides an alternative reaction mechanism with different transition state energies (Figure 1.4).

Catalysis can be classified as homogeneous catalysis, in which only on phase is involved, and heterogeneous catalysis, in which the reaction occurs at or near an interface between phases. Most heterogeneous catalysts are solids that act on substrates in a liquid

or gaseous reaction mixture. In these circumstances, reactants diffuse to the catalyst surface and adsorb onto it, via the formation of chemical bonds. Then, a series of elementary steps take place on the surface until the final products desorb from the surface and diffuse away.

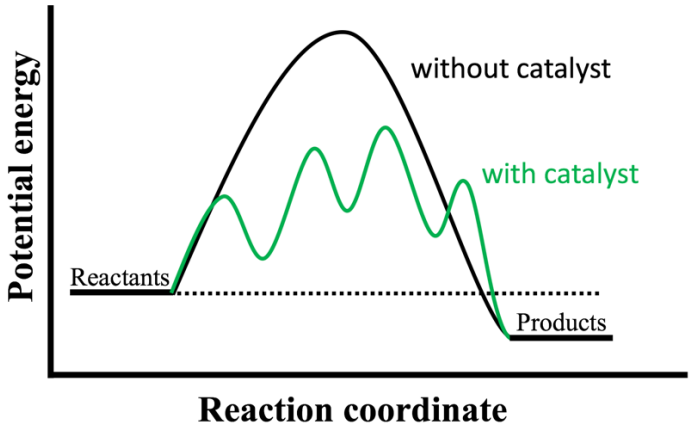

Fig. 1.4 Generic potential energy diagram showing the effect of a catalyst in an exothermic chemical reaction.

A heterogeneous catalyst has active sites, which are the group of atoms or crystal faces where the adsorbates bind and undergo a chemical reaction. Depending on the system, the catalytic activity can occur either on a flat surface, on a step site with low coordination number or on a combination of the two. Finding out the nature of the active site is challenging, but it is crucial for the development of new catalysts.

Transition metals (TM), such as chromium, iron, nickel and copper are known to be good metal catalysts and are present in many industrial processes. A common feature among the TM is that they have an incomplete *d* sub-shell, or can give rise to cations with an incomplete *d* sub-shell[48]. Their ability to lend or withdraw electrons from the reactant species, to be in a variety of oxidation states, and to form complexes with the reagents make TM good catalysts.

One of the most influential catalytic reactions of the 20th century is the Haber-Bosch process[49] (Nobel prizes in chemistry of 1918 and 1931). On 13 October 1908, Fritz Haber filed this patent on the "synthesis of ammonia from its elements". This process opened the way for inexpensive production of fertilizers for agricultural crops, which solved the food shortage problem on Earth in the beginning of the 20th century and may be linked to the fourfold population increase in the last hundred years. The process converts atmospheric nitrogen to ammonia by a reaction with hydrogen using a metal

catalyst (usually iron-based promoted with K_2O, CaO, SiO_2 and Al_2O_3) under high temperatures and pressures

$$N_2 + 3H_2 \rightarrow 2NH_3 \quad (1.7)$$

This ammonia is used as a feedstock for all other nitrogen fertilizers, such as anhydrous ammonium nitrate (NH_4NO_3) and urea ($CO(NH_2)_2$).

1.4. Hydrogen production: the water-gas shift reaction

Hydrogen, which is required to operate the Haber-Bosch process, plays also a central role in many other industries, from chemical and oil refining to metallurgical, glass and electronics[50]. The use of hydrogen is mostly based on its reactivity rather than its physical properties, and can be broadly divided into the following categories: 1) as a reactant in hydrogenation processes – to saturate compounds or to cleave the molecule to remove heterogeneous atoms such as S and N, 2) as a O_2 scavenger – to remove trace amounts of O_2 to prevent oxidation and corrosion, 3) as a fuel in rocket engines and fuel cells and 4) as a coolant in electrical generators.

Currently the dominant technology for direct production of hydrogen is steam reforming from hydrocarbons fuels such as methane or natural gas. This process consists of heating the gas in the presence of steam (around 700ºC) and a nickel catalyst[51]. The resulting endothermic reaction breaks up the methane molecules and forms carbon monoxide and hydrogen

$$CH_4 + H_2O \rightleftarrows CO + 3H_2 \quad (\Delta_r G^o_{298.15K} = 1.47 \text{ eV}) \quad (1.8)$$

Additional hydrogen can be recovered in a second stage through the exergonic WGSR[52]

$$CO + H_2O \rightleftarrows CO_2 + H_2 \quad (\Delta_r G^o_{298.15K} = -0.30 \text{ eV}) \quad (1.9)$$

The produced CO_2 can be separated from H_2 through a PSA unit[53] (as explained in Section 1.2.2) or using membranes[54].

Originally, the WGSR was discovered by the Italian physicist Felice Fontana in 1780. However, it was not until the development of new industrial processes that required hydrogen, such as the Haber-Bosch ammonia synthesis, that the industrial value of this reaction was realized. Moreover, the WGSR is one of the most important reactions used to balance the H_2/CO ratio in the Fischer-Tropsch process[55]. Nowadays, the interest of

the WGSR has been renewed due to the stringent requirements of high purity hydrogen needed in fuel cells,[56] where CO concentration below 0.5% is needed to prevent poisoning of the Pt anode, a key component of these devices. Note that it is an equilibrium-limited reaction, where CO conversion if favored at low temperatures due to its exergonicity. As the temperature increases, the equilibrium constant and the final conversion inherently decrease. Hence, this process is typically carried out in two stages: a first one at quite high temperature (300-450 ºC) favoring fast CO consumption, and a second one at a lower temperature (200-300 ºC) to reach higher conversions[57]. The high temperature stage uses iron oxide-chromium oxide based catalysts[58] ($Fe_2O_3/Cr_2O_3/MgO$), while copper based catalysts with inclusion of Zn, Cr and Al oxides are used in low temperature reactors[59,60], although other metals and supports have also been proposed[61,62].

1.5. References

1 M. M. F. Hasan, E. L. First and C. A. Floudas, Cost-effective CO_2 capture based on in silico screening of zeolites and process optimization, *Phys. Chem. Chem. Phys*., **2013**, 15, 17601.

2 B. P. Spigarelli and S. K. Kawatra, Opportunities and challenges in carbon dioxide capture, *J. CO_2 Util*., **2013**, 1, 69–87.

3 D. M. D'Alessandro, B. Smit and J. R. Long, Carbon dioxide capture: prospects for new materials, *Angew. Chem. Int. Ed*., **2010**, 49, 6058–6082.

4 R. M. Cuéllar-Franca and A. Azapagic, Carbon capture, storage and utilisation technologies: a critical analysis and comparison of their life cycle environmental impacts, *J. CO2 Util*., **2015**, 9, 82–102.

5 N. Hedin, L. Andersson, L. Bergström and J. Yan, Adsorbents for the post-combustion capture of CO_2 using rapid temperature swing or vacuum swing adsorption, *Appl. Energy*, **2013**, 104, 418–433.

6 N. MacDowell, N. Florin, A. Buchard, J. Hallett, A. Galindo, G. Jackson, C. S. Adjiman, C. K. Williams, N. Shah and P. Fennell, An overview of CO_2 capture technologies, *Energy Environ. Sci*., **2010**, 3, 1645–1669.

7 S. Chaemchuen, N. A. Kabir, K. Zhou and F. Verpoort, Metal–organic frameworks for upgrading biogas via CO_2 adsorption to biogas green energy, *Chem. Soc. Rev.*, **2013**, 42, 9304–9332.

8 J. Wang, L. Huang, R. Yang, Z. Zhang, J. Wu, Y. Gao, Q. Wang, D. O'Hare and Z. Zhong, Recent advances in solid sorbents for CO_2 capture and new development trends, *Energy Environ. Sci*., **2014**, 7, 3478–3518.

9 S. Chu, Carbon capture and sequestration, *Science*, **2009**, 325, 1599–1599.

10 E. J. Granite and H. W. Pennline, Photochemical removal of mercury from flue gas*, Ind. Eng. Chem. Res*., **2002**, 41, 5470–5476.

11 H. Yang, Z. Xu, M. Fan, R. Gupta, R. B. Slimane, A. E. Bland and I. Wright, Progress in carbon dioxide separation and capture: a review, *J. Environ. Sci*., **2008**, 20, 14–27.

12 J. D. Figueroa, T. Fout, S. Plasynski, H. McIlvried and R. D. Srivastava, Advances in CO_2 capture technology—The U.S. Department of Energy's Carbon Sequestration Program, *Int. J. Greenh. Gas Control*, **2008**, 2, 9–20.

13 K. Sumida, D. L. Rogow, J. A. Mason, T. M. McDonald, E. D. Bloch, Z. R. Herm, T.-H. Bae and J. R. Long, Carbon dioxide capture in metal–organic frameworks, *Chem. Rev*., **2012**, 112, 724–781.

14 L.-C. Lin, A. H. Berger, R. L. Martin, J. Kim, J. A. Swisher, K. Jariwala, C. H. Rycroft, A. S. Bhown, M. W. Deem, M. Haranczyk and B. Smit, In silico screening of carbon-capture materials, *Nat. Mater*., **2012**, 11, 633.

15 J. M. Huck, L.-C. Lin, A. H. Berger, M. N. Shahrak, R. L. Martin, A. S. Bhown, M. Haranczyk, K. Reuter and B. Smit, Evaluating different classes of porous materials for carbon capture, *Energy Env. Sci*, **2014**, 7, 4132–4146.

16 A. Brunetti, F. Scura, G. Barbieri and E. Drioli, Membrane technologies for CO_2 separation, *J. Membr. Sci*., **2010**, 359, 115–125.

17 C. E. Powell and G. G. Qiao, Polymeric CO_2/N_2 gas separation membranes for the capture of carbon dioxide from power plant flue gases, *J. Membr. Sci*., **2006**, 279, 1–49.

18 A. Hart and N. Gnanendran, Cryogenic CO_2 capture in natural gas, *Energy Procedia*, **2009**, 1, 697–706.

19 M. J. Tuinier, M. van Sint Annaland, G. J. Kramer and J. A. M. Kuipers, Cryogenic CO_2 capture using dynamically operated packed beds, *Chem. Eng. Sci*., **2010**, 65, 114–119.

20 C. A. Grande, R. P. L. Ribeiro, E. L. G. Oliveira and A. E. Rodrigues, Electric swing adsorption as emerging CO_2 capture technique, *Energy Procedia*, **2009**, 1, 1219–1225.

21 R. P. P. L. Ribeiro, C. A. Grande and A. E. Rodrigues, Electric swing adsorption for gas separation and purification: a review, *Sep. Sci. Technol*., **2014**, 49, 1985–2002.

22 S. Sircar, Basic research needs for design of adsorptive gas separation processes, *Ind. Eng. Chem. Res*., **2006**, 45, 5435–5448.

23 T.-H. Bae, M. R. Hudson, J. A. Mason, W. L. Queen, J. J. Dutton, K. Sumida, K. J. Micklash, S. S. Kaye, C. M. Brown and J. R. Long, Evaluation of cation-exchanged zeolite adsorbents for post-combustion carbon dioxide capture, *Energy Env. Sci*, **2013**, 6, 128–138.

24 M. A. Granato, T. J. H. Vlugt and A. E. Rodrigues, Molecular simulation of propane−propylene binary adsorption equilibrium in zeolite 13X, *Ind. Eng. Chem. Res*., **2007**, 46, 7239–7245.

25 K. Z. House, C. F. Harvey, M. J. Aziz and D. P. Schrag, The energy penalty of post-combustion CO_2 capture & storage and its implications for retrofitting the U.S. installed base, *Energy Environ. Sci*., **2009**, 2, 193–205.

26 A. Ntiamoah, J. Ling, P. Xiao, P. A. Webley and Y. Zhai, CO 2 Capture by temperature swing adsorption: use of hot CO_2-rich gas for regeneration, *Ind. Eng. Chem. Res*., **2016**, 55, 703–713.

27 D. Aaron and C. Tsouris, Separation of CO_2 from flue gas: a review, *Sep. Sci. Technol*., **2005**, 40, 321–348.

28 P. D. Sullivan, M. J. Rood, G. Grevillot, J. D. Wander and K. J. Hay, Activated carbon fiber cloth electrothermal swing adsorption system, *Environ. Sci. Technol*., **2004**, 38, 4865–4877.

29 Y.-S. Bae and R. Q. Snurr, Development and evaluation of porous materials for carbon dioxide separation and capture, *Angew. Chem. Int. Ed*., **2011**, 50, 11586–11596.

30 S. U. Rege and R. T. Yang, A simple parameter for selecting an adsorbent for gas separation by pressure swing adsorption, *Sep. Sci. Technol*., **2001**, 36, 3355–3365.

31 C. T. Campbell and J. R. V. Sellers, Enthalpies and entropies of adsorption on well-defined oxide surfaces: experimental measurements, *Chem. Rev*., **2013**, 113, 4106–4135.

32 T. J. H. Vlugt, E. García-Pérez, D. Dubbeldam, S. Ban and S. Calero, Computing the heat of adsorption using molecular simulations: the effect of strong coulombic interactions, *J. Chem. Theory Comput*., **2008**, 4, 1107–1118.

33 M. G. Plaza, S. García, F. Rubiera, J. J. Pis and C. Pevida, Post-combustion CO_2 capture with a commercial activated carbon: comparison of different regeneration strategies, *Chem. Eng. J.*, **2010**, 163, 41–47.

34 A. Wahby, J. Silvestre-Albero, A. Sepúlveda-Escribano and F. Rodríguez-Reinoso, CO_2 adsorption on carbon molecular sieves, *Microporous Mesoporous Mater.*, **2012**, 164, 280–287.

35 R. Banerjee, A. Phan, B. Wang, C. Knobler, H. Furukawa, M. O'Keeffe and O. M. Yaghi, High-throughput synthesis of zeolitic imidazolate frameworks and application to CO_2 capture, *Science*, **2008**, 319, 939–943.

36 W. Lu, D. Yuan, D. Zhao, C. I. Schilling, O. Plietzsch, T. Muller, S. Bräse, J. Guenther, J. Blümel, R. Krishna, Z. Li and H.-C. Zhou, Porous polymer networks: synthesis, porosity, and applications in gas storage/separation, *Chem. Mater.*, **2010**, 22, 5964–5972.

37 J.-R. Li, J. Sculley and H.-C. Zhou, Metal–organic frameworks for separations, *Chem. Rev.*, **2012**, 112, 869–932.

38 Y. Li and J. Yu, New stories of zeolite structures: their descriptions, determinations, predictions, and evaluations, *Chem. Rev.*, **2014**, 114, 7268–7316.

39 M. E. Davis, Ordered porous materials for emerging applications, *Nature*, **2002**, 417, 813.

40 C. Martínez and A. Corma, Inorganic molecular sieves: preparation, modification and industrial application in catalytic processes, *Coord. Chem. Rev.*, **2011**, 255, 1558–1580.

41 Database of Zeolite Structures, http://www.iza-structure.org/databases/, (accessed January 31, 2018).

42 Salmon-pink chabazite upon pearlescent heulandite crystals. Attribution: Rob Lavinsky, iRocks.com - CC-BY-SA-3.0.

43 A large, cauliflowerlike cluster of ivory colored stilbite. Attribution: Rob Lavinsky, iRocks.com - CC-BY-SA-3.0.

44 Spherical mordenite on a field of stilbite crystals. Attribution: Rob Lavinsky, iRocks.com - CC-BY-SA-3.0.

45 Faujasite with a beautiful "crackled glaze" surface. Attribution: Modris Baum - Public domain.

46 M. Palomino, A. Corma, F. Rey and S. Valencia, New insights on CO_2 −methane separation using LTA zeolites with different Si/Al ratios and a first comparison with MOFs, *Langmuir*, **2010**, 26, 1910–1917.

47 J. Wisniak, The history of catalysis. From the beginning to Nobel Prizes, *Educ. Quim*., **2010**, 21, 60–69.

48 IUPAC. Compendium of Chemical Terminology, 2nd ed. (the "Gold Book"). Compiled by A. D. McNaught and A. Wilkinson. Blackwell Scientific Publications, Oxford, **1997**.

49 J. W. Erisman, M. A. Sutton, J. Galloway, Z. Klimont and W. Winiwarter, How a century of ammonia synthesis changed the world, *Nat. Geosci*., **2008**, 1, 636-639.

50 R. Ramachandran and R. K. Menon, An overview of industrial uses of hydrogen, *Int. J. Hydrog. Energy*, **1998**, 23, 593–598.

51 S. Rakass, H. Oudghiri-Hassani, P. Rowntree and N. Abatzoglou, Steam reforming of methane over unsupported nickel catalysts, *J. Power Sources*, **2006**, 158, 485–496.

52 H. Prats, L. Álvarez, F. Illas and R. Sayós, Kinetic Monte Carlo simulations of the water gas shift reaction on Cu(111) from density functional theory based calculations, *J. Catal*., **2016**, 333, 217–226.

53 L. Riboldi and O. Bolland, Overview on pressure swing adsorption (PSA) as CO_2 capture technology: state-of-the-art, limits and potentials, *Energy Procedia*, **2017**, 114, 2390–2400.

54 S. H. Lee, J. N. Kim, W. H. Eom, Y. D. Ko, S. U. Hong and I. H. Back, Development of water gas shift/membrane hybrid system for precombustion CO_2 capture in a coal gasification process, *Energy Procedia*, **2011**, 4, 1139–1146.

55 D. B. Bukur, B. Todic and N. Elbashir, Role of water-gas-shift reaction in Fischer–Tropsch synthesis on iron catalysts: a review, *Catal. Today*, **2016**, 275, 66–75.

56 J.R. Ladebeck, J.P. Wagner, in: W. Vielstich, A. Lamm, A.H. Gasteiger (Eds.), Handbook of fuel cells: fundamentals, technology and applications, vol. 3, John Wiley and Sons, Chichester, UK, **2003**.

57 D. Mendes, A. Mendes, L. M. Madeira, A. Iulianelli, J. M. Sousa and A. Basile, The water-gas shift reaction: from conventional catalytic systems to Pd-based membrane reactors - a review, *Asia-Pac. J. Chem. Eng*., **2010**, 5, 111–137.

58 D. S. Newsome, The water-gas shift reaction, *Catal. Rev*., **1980**, 21, 275–318.

59 D.-W. Jeong, W.-J. Jang, J.-O. Shim, W.-B. Han, H.-S. Roh, U. H. Jung and W. L. Yoon, Low-temperature water–gas shift reaction over supported Cu catalysts, *Renew. Energy*, **2014**, 65, 102–107.

60 N. A. Koryabkina, A. A. Phatak, W. F. Ruettinger, R. J. Farrauto and F. H. Ribeiro, Determination of kinetic parameters for the water–gas shift reaction on copper catalysts under realistic conditions for fuel cell applications, *J. Catal*., **2003**, 217, 233–239.

61 A. Bruix, J. A. Rodriguez, P. J. Ramírez, S. D. Senanayake, J. Evans, J. B. Park, D. Stacchiola, P. Liu, J. Hrbek and F. Illas, A new type of strong metal–support interaction and the production of H_2 through the transformation of water on Pt/CeO_2(111) and Pt/CeO_x/TiO_2(110) catalysts, *J. Am. Chem. Soc*., **2012**, 134, 8968–8974.

62 J. A. Rodriguez, P. J. Ramírez, G. G. Asara, F. Viñes, J. Evans, P. Liu, J. M. Ricart and F. Illas, Charge polarization at a Au-TiC interface and the generation of highly active and selective catalysts for the low-temperature water-gas shift reaction, *Angew. Chem. Int. Ed*., **2014**, 53, 11270–11274.

CHAPTER TWO

Theoretical background

The aim of this chapter is to provide overview of the theoretical background behind the present work and of the different computational methods used. From lower to higher complexity, this chapter starts by introducing the force fields (FF) and the computer simulation method used for studying the adsorption of gases over the zeolites: GCMC. The DFT is then introduced, a computational method used here to describe the interactions between adsorbate species and the metallic catalyst surface from a quantum mechanical level in the context of heterogeneous catalysis. Then, the TST is presented, which will be used to compute the reaction rates from *ab-initio* data. Finally, two possible ways to study the kinetics of macroscopic systems from microscopic data obtained from DFT and TST are presented: the MM and the kMC method. The second one will be used to simulate the time evolution of the water-gas shift reaction.

2.1. Molecular simulations

If we wish to study the motion of more than two interacting bodies, even the relatively simple laws of Newtonian mechanics become essentially analytically unsolvable. However, using a computer, we can get the answer to any desired accuracy. One of the most common applications of computer simulations is to predict the properties of materials. The need for such simulations may not be immediately obvious. After all, it is much easier to measure the heat capacity for a given zeolite than to extract it from a computer simulation. The point is, of course, that it is easy to measure the heat capacity of a zeolite at 1 atmosphere, but often very difficult and therefore expensive to measure the properties of real materials at very high pressures or temperatures. The computer does not care: the power consumption is the same when you ask it to simulate a system at 50 bar or at cryogenic temperatures. Moreover, computer simulations can be used to screen among many different materials, many of which may have not yet been synthesized experimentally.

2.1.1. Statistical mechanics

In a molecular dynamics simulation of CO_2 diffusing through a zeolite, we can determine the instantaneous positions and velocities of all CO_2 molecules at any time. However, this kind of information cannot be compared to experimental data, because no real experiments provide us with such detailed information. Experiments measure an

average property, averaged over a large number of particles and, usually, also averaged over the time of the measurement. In order to use molecular simulation as the numerical counterpart of real experiments, we must know what kind of averages we should compute. Thus, we need to use the language of statistical mechanics.

The macrostate or thermodynamic state of a system becomes completely defined once a sufficient (in general small) set of thermodynamic variables (e.g., pressure, temperature, density, composition,…) has been specified. From a microscopic point of view, on the other hand, there will be an enormous number of quantum states (microstates) consistent with the fixed macroscopic properties. Thus, it is generally impossible to ever determine in which one of the quantum states the system is. The state of the system must be known, however, in order to calculate a mechanical thermodynamic property, such as the pressure, since the values of that property in each of the possible quantum states would, in general, be different[1].

Because of the fast motion of atoms and molecules, in the time required to perform a measurement the system will visit a huge number of microstates. The value of any property can be obtained as a time averaged value. This average is taken over all microstates that the system visits during the time necessary to perform the measurement. Boltzmann and Gibbs suggested replacing the time-average by an ensemble-average. An ensemble is a (mental or virtual) collection of replicas of the system with different microscopic characteristics but sharing all macroscopic properties defining the ensemble. The complete ensemble is specified by giving all microstates consistent with the common macroscopic characteristics of the ensemble. Now, we can formulate the two fundamental postulates of statistical mechanics:

- Principle of equal a priori probabilities: "*for an isolated macroscopic system in equilibrium, all microscopic states corresponding to the same set of macroscopic observables are equally probable"*
- Ergodic hypothesis: "*the value of any mechanical property of a thermodynamic system in equilibrium is equal to the average of that property in each and every one of the microstates that are consistent with the few parameters necessaries to specify the macrostate"*

Depending on the conditions under which our thermodynamic system is, several ensembles can be defined. The most important ones in statistical mechanics are the microcanonical ensemble (fixed number of molecules N, volume V and energy E), the canonical ensemble (fixed N, V and temperature T), the grand canonical ensemble (fixed

V, T and chemical potential μ) and finally the isothermal-isobaric ensemble (fixed N, P and T).

The partition function is the workhorse of statistical mechanics. It can be derived using the language of quantum mechanics as follows. We start denoting by $\Omega(N, V, E)$ the number of eigenstates with energy E of a system of N particles in a volume V. Then, the first postulate of statistical mechanics can be expressed as follows: a system with fixed N, V and E is equally likely to be found in any of its $\Omega(E)$ eigenstates. Now, consider a system with total energy E that consists of two weakly interacting subsystems (i.e., we can write the total energy of the system as $E = E_1 + E_2$). The total energy can be distributed in many different ways over the two subsystems. For a given value of E_1, the total number of degenerate microstates of the system is $\Omega_1(E_1) \times \Omega_2(E_2)$. It is convenient to have a measure of the degeneracy of the subsystems that is additive. Hence, we can take the natural logarithm of the degeneracy

$$\ln \Omega(E_1, E - E_1) = \ln\Omega_1(E_1) + \ln\Omega_2(E - E_1) \tag{2.1}$$

We know from the principle of equal a priori probabilities that every energy state of the total system is equally likely. However, the number of eigenstates that correspond to a given distribution of the energy over both subsystems depends very strongly on the value of E_1. The most likely value of E_1 will be the one that maximizes $\ln \Omega(E_1, E - E_1)$

$$\left(\frac{\partial \ln \Omega(E_1, E - E_1)}{\partial E_1}\right)_{N,V,E} = 0 \tag{2.2}$$

or:

$$\left(\frac{\partial \ln\Omega_1(E_1)}{\partial E_1}\right)_{N_1,V_1} = \left(\frac{\partial \ln\Omega_2(E_2)}{\partial E_2}\right)_{N_2,V_2} \tag{2.3}$$

It is convenient to introduce the following shorthand notation

$$\beta(E, V, N) = \left(\frac{\partial \ln\Omega(E, V, N)}{\partial E}\right)_{N,V} \tag{2.4}$$

Eq. (2.3) can be written as $\beta(E_1, V_1, N_1) = \beta(E_2, V_2, N_2)$. This equation will be satisfied only when both subsystems are in thermal equilibrium. At that point, $\ln \Omega$ of the total system is at maximum. This suggests that $\ln \Omega$ is related to the thermodynamic entropy S. For historical reasons, the entropy is related to the number of degenerate states as $S(E, V, N) = k_B \ln\Omega(E, V, N)$ where k_B is the Boltzmann constant.

In thermal equilibrium $\beta_1 = \beta_2$. Then, β should be related to the absolute temperature. Knowing that the thermodynamic definition of temperature is $1/T = (\partial S/\partial E)_{V,N}$ we find that $\beta = 1/(k_B T)$.

Consider now that we have a system A, that is prepared in one specific quantum state i with energy E_i, and is in thermal equilibrium with a large heat bath (denoted by B). In the same way as before, the total energy can be written as $E = E_i + E_B$, and the degeneracy of the bath is given by $\Omega_B(E - E_i)$. The probability P_i to find system A in state i is

$$P_i = \frac{\Omega_A(E_i)}{\sum_j \Omega_A(E_j)} = \frac{\Omega_B(E - E_i)}{\sum_j \Omega_B(E - E_j)} \tag{2.5}$$

Expanding $\ln\Omega_B(E - E_i)$ around $E_i = 0$ and using Eq. (2.5)

$$\ln\Omega_B(E - E_i) \approx \ln\Omega_B(E) - E_i \frac{\partial \ln\Omega_B(E)}{\partial E} = \ln\Omega_B(E) - E_i/(k_B T) \tag{2.6}$$

If we insert this result in Eq. (2.5) we get the well-known Boltzmann distribution for a system at temperature T

$$P_i = \frac{e^{-E_i/k_B T}}{\sum_j e^{-E_j/k_B T}} \tag{2.7}$$

The average energy $\langle E \rangle$ of the system at a given temperature can be calculated from the Boltzmann distribution as follows[1]

$$\begin{aligned} \langle E \rangle = \sum_i E_i P_i = \frac{\sum_i E_i e^{-\frac{E_i}{k_B T}}}{\sum_j e^{-\frac{E_j}{k_B T}}} = \\ = -\frac{\partial \ln \sum_j e^{-\frac{E_j}{k_B T}}}{\partial\left(\frac{1}{k_B T}\right)} = -\frac{\partial \ln Q}{\partial\left(\frac{1}{k_B T}\right)} \end{aligned} \tag{2.8}$$

We have defined here the partition function Q

$$Q = \sum_i \exp\left(-E_i/k_B T\right) \tag{2.9}$$

as a sum over all quantum states. Specifically, this is the canonical partition function for a classical discrete system. The partition function describes the statistical properties of a system in thermodynamic equilibrium. Basically, it tells you how many microstates are accessible to the system in a given ensemble. The appropriate mathematical expression for the partition function depends on the degrees of freedom of the system, whether the context is classical mechanics or quantum mechanics, and whether the spectrum of states

is discrete or continuous. Finally, consider the average of some observable A. We know how to calculate probability that a system at temperature T will be found in an energy eigenstate with energy $\mathrm{E_i}$. Therefore, we can compute the thermal average of A as

$$\langle A\rangle = \frac{\sum_{\mathrm{i}} \exp\left(-\mathrm{E_i}/\mathrm{k_B T}\right)\langle i|A|i\rangle}{\sum_{\mathrm{j}} \exp\left(-\mathrm{E_j}/\mathrm{k_B T}\right)} \tag{2.10}$$

where $\langle i|A|i\rangle$ denotes the expectation value of the operator A in quantum state i.

2.1.2. Monte Carlo simulations

To address the calculation of macroscopic thermodynamic properties, two molecular simulation techniques can be used: MC method and MD. This section presents a short overview of the first method.

We start from the classical expression for the partition function[2] $\mathrm{Q_{classical}}$

$$\mathrm{Q_{classical}} = \mathrm{c}\int \mathrm{dp^{3N} dr^{3N} e^{-\mathcal{H}/k_B T}} \tag{2.11}$$

where $\mathrm{r^N}$ and $\mathrm{p^N}$ stand for the coordinates and momenta of all N particles, $\mathcal{H}$ is the Hamiltonian of the system (i.e., $\mathcal{H} = \mathrm{K} + \mathrm{U}$, where K is the kinetic energy of the system and U is the potential energy) and c is a constant of proportionality (i.e., for a system of N identical atoms, $\mathrm{c} = 1/(\mathrm{h^{3N}N!})$). The classical equation corresponding to Eq. (2.10) is[1]

$$\langle \mathrm{A}\rangle = \frac{\int \mathrm{dp^{3N} dr^{3N} A(p^{3N}, r^{3N})\cdot e^{-\mathcal{H}/k_B T}}}{\int \mathrm{dp^{3N} dr^{3N} e^{-\mathcal{H}/k_B T}}} \tag{2.12}$$

In Eq. (2.10), the observable A is expressed as a function of coordinates and momenta. The integration over momenta can be carried out analytically (K is a quadratic function of the momenta), and therefore averages of functions that depend on momenta only are usually easy to evaluate. The difficult problem, however, is the computation of averages of functions $\mathrm{A(r^N)}$. Except for a few cases, numerical techniques must be used to solve the multidimensional integral over particle coordinates.

In 1953, Metropolis et al[3] developed the Monte Carlo importance sampling algorithm to solve numerically the thermal averages from Eq. (2.12) Instead of performing a random sampling, the idea behind the importance sampling is to sample many points where the Boltzmann factor ($\exp[-\mathrm{E}/\mathrm{k_B T}]$) is large and few elsewhere. In the Metropolis scheme, a random walk is constructed through that region of space where the integrand is nonnegligible. The general approach is first to prepare the system in a

configuration r^{3N}, which we denote by α, that has a Boltzmann factor different from zero. Next, a new trial configuration r'^{3N}, denoted by β, is generated by performing a small random displacement. We must now decide whether we will accept or reject this trial configuration. The usual procedure is to always accept the trial move if $U(\beta) < U(\alpha)$, where U is the potential energy of the system. On the other hand, if $U(\beta) > U(\alpha)$ a random number from a uniform distribution in the interval [0,1] is generated. Only if the random number is lower than $\exp\left[-\left(U(\beta) - U(\alpha)\right)/k_B T\right]$ the trial move is accepted.

Conventional MC simulations measure (time) averages in the canonical ensemble (i.e., constant NVT). For some systems, however, one would like to obtain information on the average number of particles as a function of the external conditions (e.g., adsorption studies). In those cases, the natural ensemble to use is the grand-canonical ensemble (i.e., constant μVT), where the number of particles is allowed to change during the simulation.

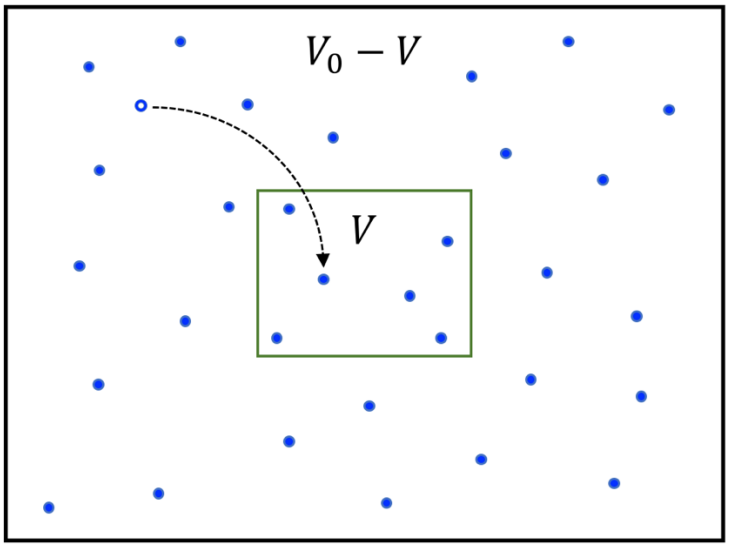

Fig. 2.1 N-particle system of volume V surrounded by a reservoir

In the GCMC scheme, one first chooses randomly whether a trial MC displacement step (i.e., translation or rotation) or GCMC exchange step (i.e., insertion or deletion) is attempted (see Figure 2.1). If translation is chosen, a particle is selected with uniform probability and is displaced a random distance d in a random direction, where $d \in [0, d_{max}]$ (usually d_{max} is set to 0.5Å). If rotation is chosen, a particle also selected and then rotated a random angle around a random axis. If insertion is chosen, a particle is placed with uniform probability density inside the system. Finally, if deletion is chosen,

then one out of *N* particles is deleted randomly. The trial move is then accepted or rejected according to the usual Monte Carlo lottery[1]

- *Displacement of particles*. If a translation or rotation from state s to state s′ is selected, the move is accepted with probability

$$p(s \to s') = \min\left[1, e^{\left[-\left(U\left(s'^{N}\right)-U\left(s^{N}\right)\right)/k_B T\right]}\right] \tag{2.13}$$

- *Exchange of particles*. If a particle insertion is chosen, the move is accepted with probability

$$p(N \to N+1) = \min\left[1, \frac{V}{\Lambda^3 (N+1)} e^{\left[(\mu - U(N+1) + U(N))/k_B T\right]}\right] \tag{2.14}$$

Conversely, if a deletion is selected, the removal of a particle is accepted with a probability

$$p(N \to N-1) = min\left[1, \frac{\Lambda^3 N}{V} e^{\left[-(\mu + U(N-1) - U(N))/k_B T\right]}\right] \tag{2.15}$$

where N is the total number of particles, μ the chemical potential and $\Lambda = \sqrt{h^2/(2\pi m k_B T)}$ is the thermal de Broglie wavelength. These equations are based on the idea that particles are exchanged with a reservoir containing the same molecules at the same chemical potential, the only difference being that, in the reservoir, the molecules do not interact. Experimentally, however, usually the pressure rather than the chemical potential of the reservoir is fixed. To compare the experimental data with the simulation results it is necessary therefore to determine the pressure that corresponds to a given value of the chemical potential and temperature of our reservoir.

2.1.3. Force fields

The molecular models used to describe the interactions in a system can be divided in two groups: quantum mechanical models and classical mechanical models. The former are based on solving the electronic Schrödinger equation and allow the study of properties associated with the electron density of the system. The different methods for solving the Schrödinger equation are also called ab-initio methods. The simplest, but less accurate, is the Hartree-Fock method. More accurate methods have been developed, like DFT (see Section 2.4), multi-configurationally self-consistent field theory (MCSCF) or Møller-Plesset perturbation theory (MP). These methods do not rely on any empirical input, but

instead they are built using the quantum mechanical postulates. Their high computational cost, however, limits their application to small systems (i.e., about 100 atoms on a supercomputer). In order to describe the interactions between a large number of atoms or molecules, less accurate but much cheaper classical mechanical methods are needed.

Classical methods consider molecules composed by a set of spheres (i.e., atoms) of different sizes and masses, connected by rigid or flexible bonds and governed by classical potential energy functions. As a direct consequence of this model, the total energy of a molecule is obtained as the sum of several contributions or perfectly defined terms that depend on the spatial coordinates of the nuclei. The functional form and parameter sets used to calculate the potential energy of a system of atoms is referred as a force field (FF), since the derivatives of the potential energy function determine the forces on the atoms. Traditional force fields are unable to model chemical reactions because of the requirement of breaking and forming bonds (i.e., all bonds must be defined explicitly on the functional form). New reactive force fields like ReaxFF[4] have been developed to study chemical reactions, where explicit bonds are replaced by bond orders, allowing for continuous bond formation/breaking. The general form for the total energy calculated by a traditional (non-reactive) force field can be written as

$$\mathrm{E_{total}} = \mathrm{E_{bonded}} + \mathrm{E_{nonbonded}} \tag{2.16}$$

where $\mathrm{E_{bonded}}$ and $\mathrm{E_{nonbonded}}$ terms stand for the bonded and nonbonded contributions. In rigid force fields (i.e., force fields where the molecules are considered as rigid bodies) the first term in Eq. (2.16) is zero, and only long-range interactions between different molecules are considered. Otherwise, when bonds can stretch or bend the force field is called flexible. The $\mathrm{E_{bonded}}$ term can be calculated as the following summation

$$\mathrm{E_{bonded}} = \sum_{\mathrm{bonds}} \mathrm{E_{bond}} + \sum_{\mathrm{angles}} \mathrm{E_{angle}} + \sum_{\mathrm{dihedrals}} \mathrm{E_{dihedral}} \tag{2.17}$$

For practical systems, using harmonic functional forms for bonds, bends and torsions can be sufficient to reproduce the molecular structure by tuning the equilibrium bond length, bond angles, and dihedral angles. The force field parameters for the bonded interactions can be obtained from more accurate calculations such as those based on DFT, or by fitting them to the experimental vibrational frequencies. Note, however, that the real vibrational spectrum depends also to all of their cross-terms such as bond-angle, bond-dihedral, angle-angle, angle-dihedral, and so forth. Adding these couplings as extra terms in Eq. (2.17) make the force field more accurate but also computationally more expensive.

The non-bonded interaction term describes how the atoms or molecules interact with each other through forces that are not due to chemical bonds. Since the nonbonded terms are most computationally intensive, a popular choice is to limit interactions to pairwise energies. The $E_{nonbonded}$ term can be calculated as the following summation

$$E_{nonbonded} = \sum_{pairs} E_{electrostatic} + \sum_{pairs} E_{vdW} \tag{2.18}$$

where $E_{electrostatic}$ and E_{vdW} stand for the long-range electrostatic forces and van der Waals contributions. The van der Waals pairwise interaction between atoms i and j is usually computed with a Lennard-Jones potential

$$E_{vdW,ij} = 4\varepsilon_{ij}\left[\left(\frac{\sigma_{ij}}{r_{ij}}\right)^{12} - \left(\frac{\sigma_{ij}}{r_{ij}}\right)^{6}\right] \tag{2.19}$$

where ε_{ij} is the depth of the potential well, σ_{ij} is the finite distance at which the inter-particle potential is zero and r_{ij} is the distance between the particles. On the other hand, the pairwise electrostatic interaction is usually computed with Coulomb's law

$$E_{electrostatic,ij} = \frac{1}{4\pi\varepsilon_0}\frac{q_i q_j}{r_{ij}} \tag{2.20}$$

Both van der Waals and Coulomb terms can be buffered or scaled by a constant factor to account for electronic polarizability and produce better agreement with experimental observations. Finally, some FF also include an extra term in Eq. (2.18) accounting for the H bond interactions.

2.2. Density Functional Theory

The density functional theory is presently the most successful (and also the most promising) approach to compute the electronic structure of solid materials. This theory provides an alternative to the conventional ab-initio methods used in physics and chemistry to investigate the electronic structure (principally the ground state) of many-body systems, in particular atoms, molecules and condensed phases. Within this theory, the properties of a many-electron system can be determined by using functionals (i.e., functions of another function), which in this case is the spatially dependent electron density $\rho(r)$. Note, however, that the exact for of the so-called universal (exact) functional is unknown.

2.2.1. The Hohenberg-Kohn theorems

The origin of DFT dates back to the 1920's, when Thomas and Fermi developed the statistical electron gas model[5], which expressed the properties of the ground state of a system constituted by uniformly distributed electrons under the influence of a nuclear field as a function of $\rho(r)$. This model was later improved by Dirac[6,7] and Bloch[8] by including an exchange term giving rise to the Thomas-Fermi-Dirac model. However, both approaches were less accurate than conventional wavefunction methods and inapplicable to chemical systems until the appearance of the theory developed by Hohenberg and Kohn[9] in 1964. They introduced two theorems that established the basis for the modern DFT:

- First theorem: "*The external potential $V_{ext}(r)$ of a non-degenerate electronic state, and hence the total energy, is a unique functional of $\rho(r)$*"
- Second theorem: "*The ground state energy can be obtained variationally: the density that minimizes the total energy is the exact ground state density*"

The first theorem establishes a direct relation between the electronic density and the wave function through the external potential. For a given $V_{ext}(r)$ the total energy functional is

$$E[\rho] = \int \rho(r)\, V_{ext}(r) dr + F_{HK}[\rho] \tag{2.21}$$

where $F_{HK}[\rho]$ is a universal functional of $\rho(r)$ (also known as the Hohenberg-Kohn functional) consisting of a kinetic energy term $T[\rho]$ and an interaction term $V_{ee}[\rho]$ accounting for the electronic repulsion. If this functional is known, we can use the second theorem to obtain the exact ground density and the total energy. Simple yet powerful as the HK theorems are, they do not provide a route to construct functionals or a method to calculate the ground state density. This is why the resulting approximations cannot be classified as truly ab initio.

2.2.2. The Kohn-Sham equations

Almost a year after the HK theorems were published, Kohn and Sham presented an approach that enables to replace the intractable many-body problem of N interacting electrons in a static external potential to a tractable problem of N non-interacting electrons moving in an effective potential[10]. The resulting set of independent particle equations can

be solved numerically. In the Kohn-Sham formulation, the dynamics of the system are governed by

$$E_{KS}[\rho] = T_{KS} + \int \rho(r)\, V_{KS}(r) dr \qquad (2.22)$$

where T_{KS} is the Kohn-Sham kinetic energy and $V_{KS}(r)$ is the effective KS potential, which includes the external potential $V_{ext}(r)$, the classical Coulomb interaction between electrons $V_C(r)$ and a third term accounting for the exchange-correlation potential $V_{XC}(r)$

$$V_{KS}(r) = V_{ext}(r) + V_C(r) + V_{XC}(r) \qquad (2.23)$$

The exchange-correlation potential is the 'functional derivative' of the exchange-correlation functional $E_{XC}[\rho]$, and accounts for the difference of kinetic and internal interaction energies of the true interacting many-body system from those of fictitious auxiliary independent-particle systems. The exact expression for the exchange-correlation functional $E_{XC}[\rho]$ is not known, and therefore has to be approximated.

2.2.3. Exchange-correlation functionals

The predictive ability of KS formulation depends on the accuracy of the chosen $E_{XC}[\rho]$. In the simplest approximation, called the local-density approximation[10] or LDA, $E_{XC}[\rho]$ is fitted to reproduce the properties of the homogeneous electron gas, which is based upon exact exchange and correlation energy for a uniform electron gas. Experience has shown that the LDA gives ionization energies of atoms, dissociation energies of molecules and cohesive energies with a fair accuracy of typically 10-20%. However, the LDA gives bond lengths of molecules and solids typically with an astonishing accuracy of ~ 2%. This moderate accuracy that LDA delivers is certainly insufficient for most applications in chemistry. The first logical step to go beyond LDA is to use not only the information about the density at a particular point, but to supplement also the density with information about the gradient of the charge density in order to account for the non-homogeneity of the true electron density. This level of approximation is known as the generalized gradient approximation or GGA[11]. GGA has reduced the LDA errors of atomization energies of standard set of small molecules by a factor 3-5. This improved accuracy has made DFT a significant component of quantum chemistry.

Nowadays, more complex and accurate meta-GGA and hybrid functionals have been developed. The former is a straightforward extension of the concept underlying GGA where, in addition to the dependence on the density and its gradient, it also

introduces a dependence on the Laplacian of the density. The latter consists on functionals that are characterized by mixing non-local Fock exchange and a local or semi-local DFT exchange in certain proportions.

In the present thesis, two of the most popular GGA functionals, PW91[12] and PBE[13], have been used. PW91 is the first reasonable GGA that can be reliably used over a very wide range of materials, and contains much of the known correct physics of the exchange and correlation interactions. On the other hand, PBE is based on PW91, but has a different analytical form and is derived in a different way. In words of Burke: "*PBE is a simplification of PW91, which yields almost identical numerical results with simpler formulas from a simpler derivation*"[14]. Both of them achieve the inclusion of gradient correction without introducing experimentally fitted parameters.

2.2.4. Plane waves and pseudopotentials

In non-periodic quantum chemistry calculations of molecules, molecular orbitals are usually described as a linear combination of atomic orbitals (LCAO approximation). The expression (linear expansion) for the *i*th molecular orbital ϕ_i would be

$$\phi_i = \sum_r c_{ri}\chi_r \tag{2.24}$$

where χ_r is the rth atomic orbital and c_{ri} the corresponding coefficient (i.e., weight of the contribution of the rth atomic orbital to the molecular orbital). Each atomic orbital χ_r is, in turn, described by a combination of nuclei-centered functions such as Gaussian-type orbitals (GTO) or Slater-type orbitals (STO). However, when dealing with periodic systems, the most common choice is to use a basis set of plane wave (PW) functions, which are expressed as

$$\eta^{PW} = e^{i\vec{k}\vec{T}} \tag{2.25}$$

where the vector $\vec{k}$ is related to the momentum $\vec{p}$ of the plane wave through $\vec{p} = \hbar\vec{k}$ and $\vec{T}$ is any translational vector leaving the Hamiltonian invariant. Plane waves are a simple way of representing electron wavefunctions. They offer a complete basis set that is independent of the type of crystal and treats all areas of space equally, in contrast to other basis sets which use localised functions such as GTO's or STO's. Thus, PW basis sets do not exhibit basis set superposition error. Moreover, they implicitly involve the concept of

periodicity and are therefore appropriate for calculations with periodic boundary conditions.

Unfortunately, valence wavefunctions tend to have rapid oscillations near ion cores due to the requirement that they must be orthogonal to the core states; this situation is problematic because it requires a huge number of plane waves to describe the wavefunction accurately. However, many of the chemical and physical properties of atoms are determined by only a few electrons, the outermost or valence electrons. Thus, pseudopotentials (PP) are constructed to replace the atomic all-electron potential such that core states are eliminated (core electrons are 'frozen') and the valence electrons are described by pseudo (PS) wavefunctions with significantly fewer nodes, making PW basis sets practical to use. In addition, the pseudopotential approximation can simulate very well the electronic structure of heavy atoms, where relativistic effects need to be considered[15].

2.2.5. Dispersion forces

Popular and semi-local density functionals are unable to describe correctly van der Waals (vdW) interactions resulting from dynamical correlations between fluctuating charge distributions. The effect of vdW interactions on adsorption properties has been the focus of an intense research in the past few years, especially after the landmark contributions of Grimme and coworkers[16–18], which has triggered many new theoretical developments and the appearance of a plethora of new functionals aiming to account for these terms in an accurate and non-empirical way as recently critically reviewed by Klimes and Michaelides[19]. A pragmatic method to work around this problem is to add a correction to the conventional Kohn-Sham DFT energy

$$E_{DFT-disp} = E_{KS-DFT} + E_{disp} \tag{2.26}$$

This additional term is computed using some of the available approximate methods. All of them add vdW correction for potential energy and interatomic forces, as well as stress tensor and hence simulations such as atomic and lattice relaxations, molecular dynamics and vibrational analysis can be performed. In the popular D2 method of Grimme[16], E_{disp} is an empirical dispersion given by

$$E_{disp} = -\frac{1}{2}\sum_{i=1}^{N}\sum_{j=1}^{N}\sum_{L}{}' \frac{C_{6,ij}}{r_{L,ij}^{6}} f_{dmp}(r_{ij}) \tag{2.27}$$

where the summations are over all atoms N and all translations of the unit cell $L = (l_1, l_2, l_3)$. The prime indicates that $i \neq j$ for the reference cell $L = 0$; $C_{6,ij}$ denotes the dispersion coefficient for atom pair ij; and $r_{L,ij}$ is the distance between atom i located in the reference cell $L = 0$ and atom j in the cell L. In order to avoid near-singularities for small $r_{L,ij}$, a damping function f_{dmp} must be used. The dispersion coefficients are computed using the following combination rule

$$C_{6,ij} = \sqrt{C_{6,ii} \cdot C_{6,jj}} \tag{2.28}$$

The values of $C_{6,ij}$ are tabulated for each element and are insensitive to the particular chemical situation.

2.3. Transition State Theory

Catalysis is in the end really all about speeding up a reaction, where the reactants and products are not in equilibrium, so we must be able to address reaction rates to obtain a detailed picture of what goes on at catalytic surfaces under relevant conditions. This reaction rates will be used to perform kMC simulations (Section 2.5). At present, the most commonly employed approach to obtain the absolute values of the thermal rates in the area of surface chemistry and catalysis is conventional TST, published almost simultaneously by H. Eyring, M. G. Evans and M. Polanyi in 1935.

Suppose a bimolecular reaction between reactants A and B in gas phase

$$A_{(g)} + B_{(g)} \rightleftarrows X^{\neq}{}_{(g)} \longrightarrow Y_{(g)} + Z_{(g)} \tag{2.29}$$

where $X^{\neq}{}_{(g)}$ is the so-called activated complex or transition state (TS), which lies at the saddle point over the reaction path. The rate constant for the above reaction can be obtained from the statistical formulation of TST based on the following assumptions[20–22]:

- Molecular systems that have surmounted the TS in the direction of products cannot turn back and form reactants again.
- Reactants are in chemical equilibrium with activated complexes even the whole system does not.
- It is possible to separate the motion of the system over the energy barrier (translation mode from reactants to products) from the other motions associated with the TS.

- Classical motions over the barrier are reliable (quantum effects ignored).

Consider now the concentration of molecules in a dividing surface of a very small width orthogonal to the MEP, where the saddle point is located. In thermal equilibrium conditions of reactants, the concentration of molecules in the TS $[X^{\neq}]$ can be calculated from statistical mechanics (the sign $\neq$ is used to label any variable associated with the conventional transition state)

$$K_c^{\neq} = \frac{[X^{\neq}]}{[A][B]} = V\frac{q^{\neq}}{q_{A_{(g)}}q_{B_{(g)}}}e^{-\Delta E^{o\neq}/k_B T} \tag{2.30}$$

where $K_c^{\neq}$ is the equilibrium constant between reactants and the molecules in the TS, $q^{\neq}$ is the partition function of the TS, $q_{A_{(g)}}$ and $q_{B_{(g)}}$ are the partition of reactants A and B, respectively, V is the volume, $\Delta E^{o\neq}$ is the energy difference between the lowest energy level of the TS and the lowest energy level of reactants and k_B the Boltzmann constant. The derivation by Eyring, Evans and Polanyi leads to the following expression for a bimolecular reaction[22]

$$k = \frac{k_B T}{h}V\frac{q^{\neq}}{q_{A_{(g)}}q_{B_{(g)}}}e^{-\Delta E^{o\neq}/k_B T} \quad (m^3 \cdot molec^{-1} \cdot s^{-1}) \tag{2.31}$$

For unimolecular reactions in gas phase, Eq. (2.31) becomes

$$k = \frac{k_B T}{h}\frac{q^{\neq}}{q_{A_{(g)}}}e^{-\Delta E^{o\neq}/k_B T} \quad (molec^{-1} \cdot s^{-1}) \tag{2.32}$$

Let us now apply TST to gas-surface elementary processes. It can be shown that for an activated adsorption (i.e., $A_{(g)} + * \rightarrow A$) the rate constant is given by

$$k = \frac{k_B T}{h}V\frac{q^{\neq}}{q_{A_{(g)}}q_*}e^{-\Delta E^{o\neq}/k_B T} \quad (m^3 \cdot molec^{-1} \cdot s^{-1}) \tag{2.33}$$

where $(*)$ represents an adsorption free surface site ($q_* = 1$) and β its area (m^2). For an Eley-Rideal (ER) reaction (i.e., $A_{(g)} + B \rightarrow AB_{(g)} + *$)

$$k = \frac{k_B T}{h}V\frac{q^{\neq}}{q_{A_{(g)}}q_B}e^{-\Delta E^{o\neq}/k_B T} \quad (m^3 \cdot molec^{-1} \cdot s^{-1}) \tag{2.34}$$

Finally, for Langmuir-Hinshelwood (LH) reaction (i.e., $A + B \rightarrow AB_{(g)} + 2*$)

$$k = \frac{k_B T}{h}\beta\frac{q^{\neq}}{q_A q_B}e^{-\Delta E^{o\neq}/k_B T} \quad (m^2 \cdot molec^{-1} \cdot s^{-1}) \tag{2.35}$$

Equations (2.33)–(2.35) allow the analytic evaluation of the rate constants used in microkinetic modelling of gas-surface reactions (see Section 2.4). Note that, for adsorbed species, the partition functions for reactants and activated complex have only vibrational

components, since an adsorbed atom or molecule loses its ability to rotate or move freely over the surface, and its corresponding frustrated rotations and translations are treated as vibrations. For the activated complex, the vibrational contribution corresponding to the imaginary frequency is not included for the calculation of $q^{\neq}$. See Section 2.5.4 for the expressions of the partition functions.

One should be aware that the rate constants derived in this section are not necessarily the same rates that one has in kMC simulations. This will be discussed in more detail in Section 2.5.4.

2.4. Microkinetic modelling

Kinetic models can be used for the study of many complex reactions (e.g., gas-phase, solution-phase or gas-surface processes), including also the transport phenomena when they are relevant (i.e., diffusivity, viscosity and heat conduction). When dealing with the kinetics of surface reactions, MM or kMC techniques can be used. These techniques are used to extend both experimental and theoretical observations to predict the results of complex chemical reactions under various critical conditions.

In MM, a set of elementary reactions that are thought to be relevant for an overall chemical transformation are specified. For each process, a rate constant is required for both the forward and reverse direction. These rate constants at a given temperature can be obtained from experiments or calculated using DFT along with TST, as shown in the previous section. Once all rate constants are known, a master equation for the entire reaction network can be written. This master equation expresses the rate of change of each adsorbate coverage as a function of the instantaneous coverage of all species in the model, represented as a system of ordinary non-linear differential equations. These equations, commonly called macroscopic rate equations, Mean Field equations, or phenomenological equations, can be solved numerically using algorithms such as the backward differentiation formula (BDF), and can be written as

$$\frac{d\theta_X}{dt} = \sum_n I_X^{(n)} k^{(n)} f^{(n)}(\theta_A, \theta_B \dots) \tag{2.36}$$

where θ_X is the surface coverage of species X at time t, $I_X^{(n)}$ is the stoichiometric number for species X in reaction n (positive or negative for species formation or removal, respectively), $k^{(n)}$ is the thermal rate constant of reaction n, and $f^{(n)}$ is a function of

several coverages indicating how the rate of reaction n depends on the coverage. The summation covers all possible surface processes where species X is involved.

In general, MM returns a set of coverages and rates as a function of time. The inspection of the results at the steady-state provide us with information about which are the most predominant species on the surface, what is the overall TOF (i.e., turnover frequency, a measure of catalytic activity) and what is the selectivity of the catalysts towards the desired product.

2.5. The kinetic Monte Carlo method

The problem with MM is that the assumption that the adsorbates are randomly distributed over the sites is rarely correct. The main reason is that there are lateral interactions between the adsorbates, both attractive and repulsive, and they lead to correlation in the occupation of neighboring sites. At very low temperature these interactions may even result in island formation or ordered adlayers. Another reason is that the sites might differ because of defects in the substrate (e.g., edges). Moreover, reaction themselves may also lead to correlation. The reaction $CO + O \rightarrow CO_2$ in the previous example removes CO's and O's when they are neighbors. This will make less likely that a neighboring $CO - O$ pair is found. This effect can be very strong when the rate constant of the reaction is high and the adsorbates diffuse slowly.

One may think that, if the adsorbates are not randomly distributed, we might try to derive a new form for f in Eq. (2.36) that reflects the way the adsorbates are actually found on the surface. For example, if CO molecules form islands then the θ_{CO} dependence in f should reflect that only the CO species on the edge of the island can react with O atoms. There are two problems with this idea. The first one is that in general it is not clear in which way the adsorbates are distributed over the sites: this is one of the results of the kinetic problem. The other problem is that many systems form ordered adlayers at low temperatures and disordered distributions at high temperatures. This means that the coverage dependence in f is different at low and high temperatures.

The discussion above shows the shortcomings of the microkinetic models and the need for a more sophisticated approach. Such an approach is the kinetic Monte Carlo method, which can include, among other things, interactions between adsorbates and incorporates the dependence on the lattice structure properly.

2.5.1. Length and time gaps

In order to understand the kinetics of a certain reaction we need to know the structure of the adlayer on an atomic scale. However, kinetics is generally studied on meso- or macroscopic scale. Atomic scales are of the order of Ångstrøm, but length scales in laboratory are typically between micrometers to centimeters. The difference in time scales is even larger: vibrations of molecules have periods in the order of femtoseconds, some reactions take a few nanoseconds, but others may take from seconds to many hours. This means that there are many orders of magnitude of difference in length and time scales between the individual reactions and the resulting kinetics.

The length gap is not always a problem. For reactions in the gas phase and in solutions we can assume that the system is homogeneous. Then, the kinetics of a macroscopic system can be reduced to the kinetics of a few reacting molecules on a microscopic portion of space.

The real problem is however the time gap. The fastest vibrations have a reciprocal wavelength of ~4000 cm^{-1} and a period of ~8 fs, while reactions in catalysis can take place in the order of seconds or more. The origin in these fifteen orders of magnitude difference is due to the very small probability that the system overcomes energy barriers. A reaction can be regarded as a movement of the system from one local minimum to another on a potential energy surface (PES). Most of the time the system moves around one local minimum, with fast oscillations corresponding to a superposition of all possible vibrations. Every time that the system moves in the direction of the energy barrier can be regarded as an attempt to react. The probability that the reaction actually succeeds can be estimate by calculating a Boltzmann factor that gives the relative probability of finding the system at a local minimum or on top of the energy barrier $\exp[\Delta E^{o\neq}/k_B T]$, where $\Delta E^{o\neq}$ is the height of the barrier. A barrier of 1 eV (~100 kJ/mol) at room temperature gives a Boltzmann factor of about 10^{-18}.

The standard method for studying the physical motion of atoms and molecules on an atomic scale is MD, as explained in Section 2.1.3. In MD, a reaction with a high energy barrier is called a rare event. Simulating rare events if often prohibitive, especially if the equations of motion are high-dimensional, as is the case in MD, and various techniques[23] have been developed to get a reaction even when a standard simulation would require exceedingly long simulation time to show it. However, these techniques work for a small

number of reacting molecules, but not when one is interested in the combination of thousands or more reacting molecules that one has when studying kinetics. In those cases, some of the detailed information present in MD simulations must be sacrificed. Instead of working with the exact position of all atoms in a system, in kMC method one only specifies near which minimum of the PES the system is. The reactions are considered as elementary events (i.e., executing a reaction implies that the system moves from a minimum of the PES to another instantaneously). Moreover, because one doesn't know where the atoms are exactly and how they are moving, one cannot determine the times for the reactions exactly either. Instead one can only give probabilities for the reactions to occur. However, this information is more than sufficient for studying kinetics, and is the basis of the kMC method.

In return, kMC provides comprehensive information about the time-resolved arrangement of adsorbates at all the active sites during catalyst operation. Apart from a wealth of mechanistic information (e.g., about correlations in the occupation of neighboring sites) this allows to obtain proper (not erroneous mean-field) mesoscopic averages of quantities like TOFs that ultimately are required for reactor level modeling.

2.5.2. Lattice model

The forces acting adsorbed atoms or molecules displace theme to well defined positions on the surface called sites. Adsorption at these sites corresponds to minima in the PES for the adsorbate. In general, each surface site correspond to a point in the kMC lattice model. For periodic surfaces, sites form a regular lattice. However, this does not mean that all sites are in the same plane. Different lattice points may correspond to positions for adsorbates in different layers that are stacked on top of each other, or to different terraces in a stepped surface. Lattices can also be used to model surfaces that are much more complicated than simple Miller low index crystal surfaces, like metal nanoparticles[24].

In order to indicate if a certain lattice point is occupied or not, and if it is occupied with which adsorbate, labels are used. The short hand notation $(n_1 : l_1, n_2 : l_2, ...)$ indicates that the lattice point number n_1 is labeled as l_1, the lattice point number n_2 is labeled as l_2, etcetera. A particular labeling of all lattice points defines a *configuration* (denoted by small Latin letters u, v, …). A transition from one configuration to another proceeds through the occurrence of an event (denoted by small Greek letters α, β, …) that can be

regarded as nothing but a change in the labels. For example, a CO adsorption on site nº 1 might be specified by $\{(1{:}*) \rightarrow (1{:}\,\mathrm{CO})\}$. Here, $*$ stands for an empty site. A reaction implying two adsorption sites can be specified by $\{(1{:}\,\mathrm{CO}, 2{:}\,\mathrm{O}) \rightarrow (1{:}\,\mathrm{CO_2}, 2{:}*)\}$, and a diffusion from one site to a neighboring one by $\{(1{:}\,\mathrm{CO}, 2{:}*) \rightarrow (1{:}* , 2{:}\,\mathrm{CO})\}$. In fact, in kMC algorithms these labels correspond to integer occupation values (e.g., 0 for empty site, 1 for adsorbed CO, 2 for adsorbed O, etcetera).

All lattice points should not always correspond to the same site type. For example, the (111) surface of an fcc metal such as Cu(111), has four different high symmetry site types: top, bridge, fcc and hcp. However, including explicitly all these sites in the lattice model can be very complex, and implies the use of multidentate species (i.e., adsorbate species that occupy more than one adsorption site) even for the small adsorbates, because the different sites are too close to each other. Thus, it is common to use the concept of a generalized site. For instance, the lattice model for a (111) surface of an fcc metal is typically represented as a hexagonal periodic grid of terrace sites. In the same way, a stepped surface (e.g., Cu(211)) can be represented as a collection of terrace and step sites, or 2D nanoparticle islands on an inert support can be regarded as a grid of terrace and edge sites.

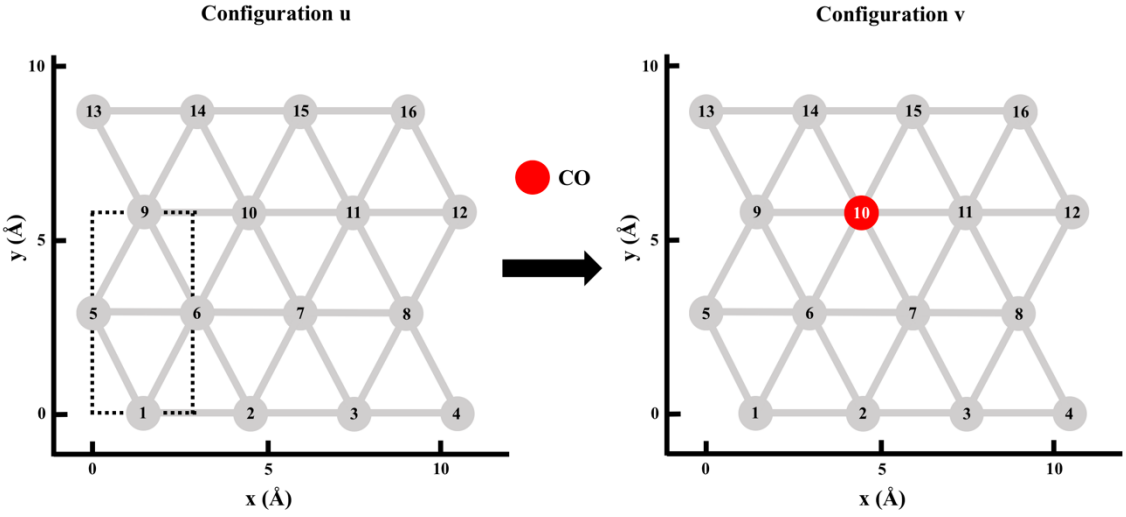

Fig. 2.2. Graph pattern representing the $\{(10{:}*) \rightarrow (10{:}\,CO)\}$ event on a hexagonal periodic grid. The dashed black lines denote the unit cell.

Finally, the surface of a real catalyst contains many more sites than we can include in a kMC simulation. In fact, a real surface is generally regarded as infinite in two directions. In a kMC simulation we need to restrict ourselves to a limited number of sites and use periodic boundary conditions (vide infra). For instance, the unit cell of an

hexagonal periodic lattice contains two terrace sites (see Figure 2.2). We can construct a 10×10 supercell containing 200 adsorption sites. In that case, all sites inside the supercell are explicitly included in the simulation. Sites outside the supercell are then though to have the same label as those inside.

As a simple example, consider the event $\{(10{:}*) \rightarrow (10{:}\,\mathrm{CO})\}$ (Figure 2.2). This event belongs to the CO adsorption reaction. The lattice model in Figure 2.2 consists on a hexagonal periodic grid of terrace sites, where an adsorbed species in a given site is allowed to interact with its six nearest neighbors. Concretely, a 4×2 supercell containing 16 adsorption sites is simulated. Periodic boundary conditions implies that when an adsorbate passes through one side of the supercell, it re-appears on the opposite side. In topological terms, the space made by a 2D lattice can be thought of as being mapped onto a torus (compactification). Thus, a given adsorbate on site nº 8 can diffuse in the positive x direction to site nº 5, or a CO molecule on site nº 1 can react with an O atom on site nº 13 to produce CO_2.

2.5.3. kMC algorithm

The time evolution in kMC is characterized by a so-called rare-event dynamics[25]. Due to the time scale between vibrations and elementary events (e.g., adsorption, diffusion, reaction, desorption), prevalent microkinetic theory[26] generally assumes that any such event occurs independent of all preceding ones (i.e., it applies a Markov approximation). In this case, it is possible to coarse gran the full trajectory in discrete jump processes. The transitions from configuration u to configuration v through the consecutive occurrence of elementary events (jumps) are described by a Markovian master equation

$$\frac{d\rho_u(t)}{dt} = \sum_v [\omega_{v\rightarrow u}\rho_v - \omega_{u\rightarrow v}\rho_u] \qquad (2.37)$$

where $\rho_u(t)$ is the probability for the system to be in configuration u at time t, and $\omega_{u\rightarrow v}$ is the transition rate (also called rate, units of time^{-1}) at which configuration u changes to configuration v.

The idea behind kMC simulations is to achieve a numerical solution of the master equation by generating an ensemble of trajectories of the underlying Markov processes, where each trajectory propagates the system correctly in the sense that the average over the entire ensemble of trajectories yields the probability densities $\rho_u(t)$. Analysis of any

single (stochastic) kMC trajectory is meaningless, unless a steady-state is achieved, allowing to replace the ensemble average by a time average over one trajectory. For this, the kMC code generally only needs to store the evolving occupation values on the lattice, and generates on-the-fly the transition rates $\omega_{u\to v}$, that are actually required to propagate the trajectory.

Changes in configuration due to an event are typically narrowly confined to as few as ~1-4 sites. Due to this locality, it is convenient to define any elementary process 'a' in terms of the initial local reactant R_a lattice configuration and the final local product P_a lattice configuration reached after the event, as well as the concomitant transition rate r_a,

$$a: R_a \overset{r_a}{\to} P_a \tag{2.38}$$

The local lattice configurations extend at least over all sites that actually change occupation due to the occurring event. For a simple CO adsorption step the local lattice configuration must contain at least the only site involved that changes its occupation from 0 (empty) to 1 (CO). For a $CO + O \to CO_2$ reaction the minimum local lattice configuration must extend over the two neighboring sites containing CO and O species, and for more complex reactions involving species covering multiple sites the minimum lattice configuration span even larger lattice areas. When lateral interactions are included further nearby lattice sites, which do not change their actual occupation from reactant to product configuration, but occupation value of which is a necessary information to determine the transition rate ω_a, must also be included to the local lattice configuration.

There can be a large number of events $\alpha, \beta, \gamma, \ldots$ that in fact all represent the same elementary process a, just occurring at different lattice sites. Consider, for instance, a CO adsorption on an empty periodic surface featuring a given terrace site. Since adsorption into any terrace site is equivalent, adsorption events on sites i and j are different events in terms of the overall lattice configuration, yet they would both be grouped to the same elementary process 'a' by their identical local reactant and product configurations.

It is useful to define the set of available events σ_u for any configuration u as the set of all events $\alpha_{u\to v}$ that lead from configuration u to any other configuration v

$$\sigma_u = \{\alpha_{u\to v} | \omega_{u\to v} \neq 0\} \tag{2.39}$$

Due to the locality of the elementary process, there are no events connecting largely different lattice configurations. Thus, σ_u is much smaller than the total size of the transition matrix $\boldsymbol{\omega}$.

Most of the kMC algorithms assume that waiting times for uncorrelated events are Poisson distributed[27,28]. This means that given a rate $\omega^a_{u\to v}$ for an event belonging to the elementary process 'a', the probability that this event occurs n times in an interval Δt is

$$p_n(\omega^a_{u\to v}, \Delta t) = (\omega^a_{u\to v}\Delta t)^n e^{-\omega^a_{u\to v}\Delta t}/n! \tag{2.40}$$

Now suppose we have N possible events with rates ω_1, ω_2, … ω. The waiting time between two consecutive events is then simply given by the case that no events occur

$$p_0(\omega_{tot}, \Delta t) = e^{-\omega_{tot}\Delta t} \tag{2.41}$$

for which a suitably distributed random number can be directly computed from a uniformly distributed random number $r \in [0,1]$ as

$$\Delta t = -\frac{\ln(r)}{\omega_{tot}} \tag{2.42}$$

where $\omega_{tot} = \sum_{n=1}^{N} \omega_n$.

All kMC algorithms must be able to determine repeatedly the time that next process will occur, the type of process that will occur and the site at the surface where the process will occur. Each of these steps can be performed in a number of ways, resulting in many different algorithms. Few of them are, however, efficient. The three most popular algorithms are the First Reaction Method (FRM), the Random Selection Method (RSM), and the Variable Step Size Method (VSSM). The latter will be discussed in detail below, since it is probably the most widely used algorithm for kMC simulations. In fact, sometimes the name kMC is specifically used to denote this method. The equivalence between them has been shown by Lukkien *et al.*[29], such that a preference for one or the other emerges only out of computational efficiency considerations depending on the system. The VSSM algorithm is as follows

1. Initialize

Start from an initial configuration u

Set $t = 0$

Make a list of all available events and calculate the corresponding rates

Calculate $\omega_{tot,u} = \sum_{v \in \sigma_u} \omega_{u \to v}$ with the sum being done only over the processes in the list

Choose conditions when to stop the simulation

2. Time

Draw two random numbers $r_1, r_2 \in [0,1]$

Generate a time interval Δt when no process occurs $\Delta t = -\ln(r_1)/\omega_{tot,u}$

Change time to $t \to t + \Delta t$

3. Process

Select the event j from the list for which $\sum_v^{j-1} \omega_{u \to v} < r_2 \omega_{tot,u} \leq \sum_v^j \omega_{u \to v}$

(i.e., choose the process $u \to v$ with probability $\omega_{u \to v}/\omega_{tot,u}$)

4. Update

Update the list adding new enabled processes and removing disabled processes

5. Continuation

If the stop conditions are fulfilled then stop. If not repeat at step 2

The main bottleneck of VSSM algorithm is the necessity to update the list of available events and compute $\omega_{tot,u}$ at every kMC step[30]. A naïve approach that is very easy to implement is to determine σ_u through iteration over all lattice sites. However, the number of lattice sites typically go up to thousands, and the evaluation of the full lattice will drastically impede the overall performance. The scaling of both calculation steps can be largely reduced by exploiting the locality of the elementary reactions. Given an event $\alpha_{u \to v}$, all events in $\sigma_v \setminus \sigma_u$ (i.e., the set that contains all those elements of σ_v that are not in σ_u) are said to be enabled by $\alpha_{u \to v}$, while all events in $\sigma_u \setminus \sigma_v$ are said to be disabled by $\alpha_{u \to v}$. Then, at every kMC step the new σ_v can be obtained from the previous set of available events σ_u just by removing all disabled events and adding all enabled events, or formally

$$\sigma_v = \left(\sigma_u \setminus (\sigma_u \setminus \sigma_v)\right) \cup (\sigma_v \setminus \sigma_u) \tag{2.43}$$

Further, the computation of the new $\omega_{tot,v}$ value can be calculated in a similar way by counting and storing the number of events $N_{a,v}^{avail}$ that belong to the same elementary reaction a. Then, if an event $\alpha_{v \to w}$ belonging to an elementary reaction a is added to σ_v, the corresponding counter $N_{a,v}^{avail}$ is simply increased by 1, whereas if $\alpha_{v \to w}$ is removed, the counter is decreased by 1. As a result, $\omega_{tot,v}$ can be calculated simply by

$$\omega_{\mathrm{tot,v}} = \sum_{\mathrm{a}} \omega_{\mathrm{a}} \mathrm{N}_{\mathrm{a,v}}^{\mathrm{avail}} \tag{2.44}$$

where the sum does not iterate over all elements in σ_{v}, but only over the much smaller set of elementary reactions.

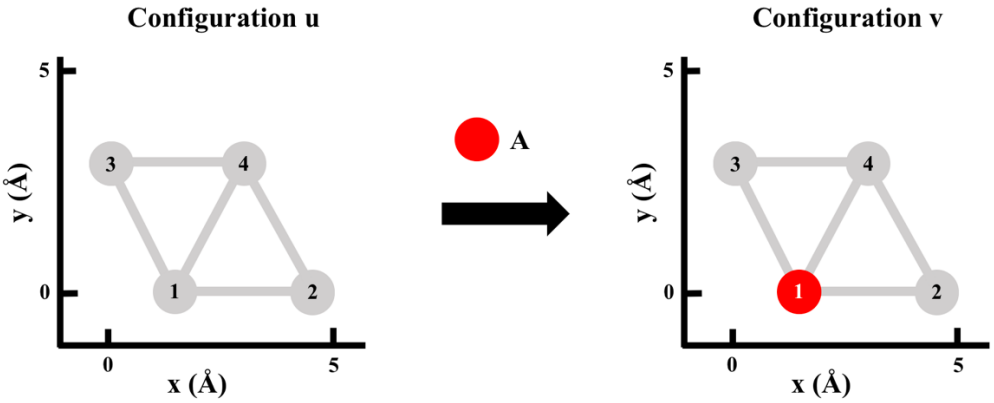

Fig. 2.3 Graph pattern representing the $\{(1{:}*) \rightarrow (1{:}\,A)\}$ event on a hexagonal periodic grid.

As a simple example, consider the reactant configuration represented on Figure 2.3 (left). The unit cell contains four empty sites. Now suppose that the reaction mechanism includes the following steps

$$\begin{aligned} A_{(g)} + * &\xrightarrow{\omega_{ads}} A \\ A &\xrightarrow{\omega_{des}} A_{(g)} + * \\ A + * &\xleftrightarrow{\omega_{dif}} * + A \end{aligned} \tag{2.45}$$

where $*$ represents a free adsorption site. The list of available events σ_{u} at reactant configuration contains the following elements

$$\begin{aligned} \sigma_{\mathrm{u}} = [&\{(1{:}*) \rightarrow (1{:}\,A)\},\ \{(2{:}*) \rightarrow (2{:}\,A)\},\ \{(3{:}*) \rightarrow (3{:}\,A)\}, \\ &\{(4{:}*) \rightarrow (4{:}\,A)\}] \end{aligned} \tag{2.46}$$

which correspond to the four possible adsorptions, and the total rate will be $\omega_{\mathrm{tot,u}} = 4\omega_{\mathrm{ads}}$. Now assume that at step 3 of the algorithm, event $\{(1{:}*) \rightarrow (1{:}\,A)\}$ is selected with a probability equal to ¼. We are now in a new configuration v and the list of available events σ_{v} must be updated. The old available event $\{(1{:}*) \rightarrow (1{:}\,A)\}$ is now disabled, and four new available events have been enabled

$$\begin{aligned} \sigma_{\mathrm{v}} \setminus \sigma_{\mathrm{u}} = [&\{(1{:}\,A, 2{:}*) \rightarrow (1{:}*\,, 2{:}\,A)\},\ \{(1{:}\,A, 3{:}*) \rightarrow (1{:}*\,, 3{:}\,A)\}, \\ &\{(1{:}\,A, 4{:}*) \rightarrow (1{:}*\,, 4{:}\,A)\},\ \{(1{:}\,A) \rightarrow (1{:}*)\}] \end{aligned} \tag{2.47}$$

where the first three new elements correspond to diffusions of adsorbate A from site 1 to the other sites, and the last term correspond to desorption of A. The updated list of

available events σ_v contains now 7 elements. The total reaction rate for the new configuration v will be $\omega_{tot,v} = 3\omega_{ads} + 3\omega_{dif} + \omega_{des}$.

2.5.4. Reaction rates

The transition probabilities (rates) in kMC simulations are those we find in the master equation (2.36). They specify the rate with which the adlayer changes due to events that can take place. These rates are commonly called rate constants or rate coefficients, but one should be aware that they are not necessarily the same thermal rate constants that appear in macroscopic rate equations. The original TST by Eyring, Evans and Polanyi[20,21] was derived for bimolecular chemical reactions in solution. As shown in most physical chemistry books, this method can also be applied to unimolecular reactions as well as to gas phase or gas-surface chemical processes, leading to the expressions for the rate constants presented in Section 2.3. The units of these rate constants must be consistent with the corresponding rate law. Consider, for instance, a bimolecular elementary reaction in gas phase $A + B \rightarrow P$. The reaction rate, measured as the number of product molecules that are formed per unit of volume and time is proportional to the concentration (and therefore the partial pressure) of both reactants

$$\frac{dN_P}{dt} = k[A][B] \tag{2.48}$$

where [A] and [B] are the concentrations of reactants A and B. The TST expression for the rate constant is Eq. (2.31) and, if the volume is in m^3, its units are $m^3 \cdot molec^{-1} \cdot s^{-1}$, as for all second order reactions. Obviously, if the order of the reaction is different, the units for the rate constant change.

In kMC framework, however, we must approach the problem in a more abstract way, momentarily forgetting that we are going to apply this method to a chemical system. Our goal is to solve numerically the master equation for Markovian jump processes (Eq. (2.37)). The transition rates $\omega_{u \rightarrow v}$ describe how the modelled system propagates in time from one coarse grained configuration to another. These transition rates are then used by the kMC algorithm to simulate a trajectory, and must have units of inverse time regardless of the type of process they represent. In fact, processes (events) in kMC go beyond chemical reactions. Any physical process that causes a change in the current configuration of the system is a valid event, such adsorbate diffusion, surface reconstruction or *cis-trans* isomerism.

The final expressions for the transition rates can also be derived directly from the master equation in a way that resembles the original TST[31]. For a surface reaction of the type $A + B \rightarrow C$, the partition functions of all species have only vibrational components, and the rate can be calculated as

$$\omega_{surface} = \frac{k_b T}{h} \frac{q^{\neq}_{vib}}{q_{vib,A} \cdot q_{vib,B}} e^{-\Delta E^{o\neq}/k_B T} \tag{2.49}$$

where $q_{vib,i}$ and $q^{\neq}_{vib}$ are the molecular partition functions of species i and transition state, respectively. In order to calculate the vibrational partition functions, one can often use the harmonic approximation. Then, the vibrations can be decoupled again into so-called normal modes, and we can write

$$q_{vib,i} = \prod_k \frac{1}{1 - e^{-h\nu_k/k_B T}} \tag{2.50}$$

where ν_k is the vibrational frequency of the kth normal mode. In the equation above we choose the first vibrational level to be the zero of energy, since the ZPE is already included in $\Delta E^{o\neq}$. Otherwise, the numerator in Eq. (2.50) must be $e^{-h\nu_k/2k_B T}$).

Diffusion processes of adsorbed species can also be treated similarly. The rate for a diffusion process of the type $A + * \rightarrow * + A$

$$\omega_{diffusion} = \frac{k_B T}{h} \frac{q^{\neq}_{vib}}{q_{vib,A}} e^{-\Delta E^{0\neq}_{diff}/k_B T} \tag{2.51}$$

where $\Delta E^{0\neq}_{diff}$ is the energy barrier along the MEP between the two sites, $Q^{\neq}_{vib}$ the corresponding (vibrational) partition function at this barrier, and $Q_{vib,A}$ the partition function at the bound state in the initial site. However, in most cases diffusion rates must be lowered by a scaling factor α, as it will be clearly shown in the next section.

Because the initial state of adsorption is a gas molecule, we need to include the gas phase if we want to calculate the rate for adsorption. For non-activated adsorption of the type $A_{(g)} + * \rightarrow A$ one assumes an early 2D gas-like transition state and thus the rate for adsorption simplify to

$$\omega^{non-act.}_{ads} = S_{st} \frac{PA_{site}}{\sqrt{2\pi m k_B T}} \tag{2.52}$$

where P is the partial pressure of $A_{(g)}$ and A_{site} is the area of a single site. An additional factor S_{st} is typically added. This extra factor is the so-called sticking coefficient, and it is introduced to take into account the fact that only a fraction of the incoming molecules

will be adsorbed due to the influence of trajectories in phase space that cross and then recross the dividing surface. An activated adsorption step can be treated similarly[32]

$$\omega_{ads}^{act.} = N_A S_{st} \frac{k_B T}{h} \frac{q_{vib}^{\neq}}{q_{trans,3D} q_{int}} e^{-\Delta E_{ads}^{0\neq}/k_B T} \tag{2.53}$$

where N_A is the number of *A* molecules in the gas phase, $\Delta E_{ads}^{0\neq}$ is the energy barrier for adsorption, $q_{trans,3D}$ is the 3D translational partition function for the molecule in the gas phase, q_{int} is the partition function for the internal motions and $q_{vib}^{\neq}$ is the (vibrational) partition function for the TS. In the above equation, q_{int} can be subdivided into partition functions with obvious nomenclature

$$q_{int} \approx q_{rot} \cdot q_{vib} \cdot q_{electr} \tag{2.54}$$

At temperatures of interest to us, the rotational partition function q_{rot} for a linear molecule can be calculated as

$$q_{rot\,(2D)} = \frac{T}{\sigma \theta_{rot}} \tag{2.55}$$

where σ is the symmetry number and θ_{rot} is the rotational temperature, which includes the moment of inertia *I* and other constants

$$\theta_{rot} = \frac{h^2}{8\pi^2 I k_B} \tag{2.56}$$

For a freely rotating non-linear molecule we have

$$q_{rot\,(3D)} = \frac{\sqrt{\pi}}{\sigma} \left(\frac{T^3}{\theta_{rot,A} \theta_{rot,B} \theta_{rot,C}} \right)^{1/2} \tag{2.57}$$

The vibrational partition function q_{vib} for the molecule in gas phase can be calculated using Eq. (2.50), where the product runs over all the $3N_{atoms} - 6$ normal modes ($3N_{atoms} - 5$ if the molecule is linear). The electronic separations from the ground state are usually very large, so for most cases $q_{electr} = 1$. An important exception arises in the case of atoms and molecules having electronically degenerate ground states, in which case

$$q_{electr} = g^E \tag{2.58}$$

where g^E is the degeneracy of the electronic ground state. Finally, for $q_{trans,3D}$ in the classical limit we have

$$q_{trans,3D} = V \left[\frac{2\pi m k_B T}{h^2} \right]^{3/2} \tag{2.59}$$

The direction perpendicular to the surface can be used as a reaction coordinate, thereby motivating the decoupling of the z component of the translational partition function as follows

$$q_{trans,3D} = q_{trans,2D}\frac{L_z\sqrt{2\pi m k_B T}}{h} \tag{2.60}$$

where L_z is the length of the gas-phase in the z-direction and $q_{trans,2D}$ is the 2D translational partition function

$$q_{trans2D} = A_{site}\frac{2\pi m k_B T}{h^2} \tag{2.61}$$

If we substitute expressions (2.60) in Eq. (2.53) and use $PV = N_A k_B T$ we have

$$\omega_{ads}^{act.} = S_{st}\frac{q_{vib}^{\neq}}{q_{trans,2D}q_{int}}\frac{PA_{site}}{\sqrt{2\pi m k_B T}}e^{-\Delta E^{0\neq}/k_B T} \tag{2.62}$$

The desorption rates for non-activated or activated adsorptions can be obtained from the equilibrium constant K_{eq}

$$K_{eq} = \frac{\omega_{ads}}{\omega_{des}} = \frac{q_{vib,A}}{q_{A_{(g)}}}e^{-\Delta_r E_{ads}^0/k_B T} \tag{2.63}$$

where $\Delta_r E_{ads}^0$ is the adsorption energy of adsorbate A. This expression is completely independent of the TS, because the equilibrium depends only on the thermodynamic properties of the initial and final states. The possible recrossings on the dividing surface do not affect the equilibrium. This means that including a sticking coefficient in the adsorption rate forces us to include it also in the desorption rates, as otherwise we get an incorrect equilibrium

$$\omega_{des}^{non-act.} = S_{st}\frac{k_B T}{h}\frac{q_{trans,2D}q_{int}}{q_{vib,A}}e^{-\Delta E_{ads}^0/k_B T} \tag{2.64}$$

$$\omega_{des}^{act.} = S_{st}\frac{k_B T}{h}\frac{q_{vib}^{\neq}}{q_{vib,A}}e^{-(\Delta E_{ads}^{0\neq} - \Delta_r E_{ads}^0)/k_B T} \tag{2.65}$$

Finally, for elementary reactions involving hydrogen atom transfer, one can introduce a one-dimensional tunneling correction factor ($\kappa > 1$) in the calculation of reaction rates. The tunneling correction factor can be computed from the expression derived from a symmetrical Eckart barrier[33] as

$$\kappa(T) = 1 + \frac{1}{24}\left|\frac{h\nu_{img}}{k_B T}\right|^2\left(1 + \frac{k_B T}{\Delta E^{0\neq}}\right) \tag{2.66}$$

where ν_{img} is the imaginary frequency of the TS.

2.5.5. Modelling fast processes

The vast majority of complex heterogeneous reactions contain processes with very dissimilar reaction rates. The slowest surface elementary steps are commonly chemical reaction processes with high energy barriers of up to 2 eV. On the other hand, the fastest ones are usually diffusion processes with energy barriers of only a few hundredths of eV and quite often adsorption/desorption processes can be also very fast. At a temperature of 625 K a slow surface process with an energy barrier of 1.6 eV will have a reaction rate of around 1 s^{-1}, while the reaction rate for a fast diffusion process with an energy barrier of only 0.05 eV will be around 10^{12} s^{-1}. This implies that diffusion processes will dominate and extremely long kMC simulations are required to observe some evolution of the overall chemical process.

In order to improve the performance of kMC simulations, some solutions have been proposed. The first, and most straightforward solution consists on multiply the reaction rates of fast processes by some scaling factor $\alpha < 1$. This solution has been successfully applied in many kMC studies[24,34–36]. Another equivalent solution is to increase all the energy barriers of these processes by the same amount[37]. The other, more sophisticated solution, is to use accelerated algorithms. Chaterjee and Voter[38] developed a temporal acceleration scheme by automatically modifying the reaction rates of fast processes without the need for the user to specify these processes in advance. In this method, called Accelerated Superbasin Kinetic Monte Carlo (AS-kMC), the algorithm keeps track of how often configurations are revisited. When this occurs too often one has an indication of the system being stuck in a set of configurations connected by fast processes (i.e., the superbasin). The reaction rates of these processes are then decreased. This procedure may be repeated until the fast processes are slowed down enough so as escape from the superbasin finally occurs. However, the fact that AS-kMC identifies processes based on the configuration of the entire system is likely to make it not efficient enough for complex reaction models such as the WGSR of Fischer-Tropsch synthesis where an enormous number of possible configurations needs to be considered. This latter problem was addressed in the recently developed algorithm by Dybeck *et al*.[39], where the acceleration is accomplished by reducing the reaction rates of the fast quasi-equilibrated processes to enable more frequent execution of the slower reactive surface processes. The main improvement is that the partitioning and the scaling is applied to all of the processes

in a given reaction channel rather than to the individual processes as done in the Voter scheme.

2.5.6. Lateral interactions

A physically meaningful representation of the description of the kinetics of complex surface reactions requires a quantitative account of the attractive or repulsive lateral interactions between coadsorbed species. In DFT calculations of energy barriers, one usually computes the *zero-coverage limit* energy barrier, which is a situation where only reactants or products and no additional spectator species are present at the surface.

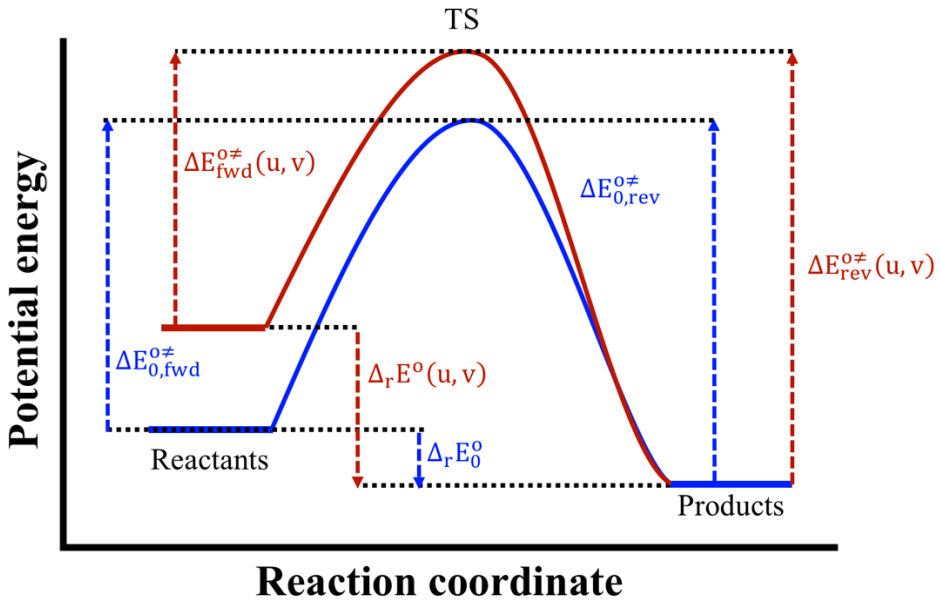

Fig. 2.4 Potential energy diagram showing the effect of lateral interactions on the energy barrier of an elementary step. The blue solid line pertains to the energy profile in the zero-coverage limit, whereas the red solid line correspond to a situation where repulsive interactions between the reactants and neighboring adsorbates raise the energy of the initial state. In the red plot we assume that there are no lateral interactions between products and the neighboring adsorbates.

In real systems, however, the coadsorbed reactant or product pairs are not alone on the surface. They may be surrounded by neighboring adsorbates that can raise or decrease the energy of the initial state, the final state and the TS (see Figure 2.4). Since reaction rates are proportional to the exponential of the energy barrier, even minor changes to the energy barrier can have a significant impact on the associated rate. To calculate these barriers, theoretically, one has to do a TS calculation for every possible local configuration of adsorbates. In practice, this works only for the simplest systems.

To circumvent this problem, the modified energy barrier is linearly approximated by the so-called Brønsted-Evans-Polanyi (BEP) relation[40,41], which assumes that the shape of the PES do not change. Instead, the initial and final states are merely shifted in energy; upwards for repulsive interactions and downwards for attractive interactions. The configuration-dependent BEP energy barrier $\Delta E_{BEP}^{o\neq}(u,v)$ is then

$$\Delta E_{BEP}^{o\neq}(u,v) = \Delta E_{0}^{o\neq} + \beta(\Delta_r E^{o}(u,v) - \Delta_r E_{0}^{o}) \tag{2.67}$$

where $\Delta E_{0}^{o\neq}$ and $\Delta_r E_{0}^{o}$ are the zero-coverage limit energy barrier and reaction energy, respectively, $\Delta_r E^{o}(u,v)$ is the configuration-dependent reaction energy (i.e., including the effect of lateral interactions), and β is the so-caled proximity factor[42] ranging from 0 for a reactants-like TS, to 1 for a products-like TS. In that way, selecting β = 0 keeps the forward energy barrier fixed at the zero-coverage limit DFT value and the reverse energy barrier is chosen to be thermodynamically consistent, whereas in the limit β = 1 the reverse barrier is fixed to the DFT value and the forward one is adjusted.

In the equation above, $\Delta_r E^{o}(u,v)$ remains to be determined. A well-defined method to capture lattice energetics is the cluster expansion (CE) of a lattice-gas Hamiltonian[43–45]. The formulation of such expansions amounts to expressing the energy of the system as a sum of single-, two-, and multibody terms called *clusters* (or *figures*). A cluster can be a single adsorbed species or a group of two or more neighboring species having a certain local lattice configuration. The simplest cluster expansion, widely used in most kMC studies, is the Ising model with nearest-neighbour pairwise additive interactions. The formulation of CE expands the energy of a configuration of adsorbates u as a sum of cluster energies

$$E(u) = \sum_{k=1}^{N_C} n_k(u) \cdot CE_k \tag{2.68}$$

where $E(u)$ is the total energy of the system (i.e., energy of a lattice configuration), N_C is the total number of clusters included in the model, CE_k is the cluster energy of figure k and $n_k(u)$ is the number of times that pattern of cluster k appears in the lattice. Then, $\Delta_r E^{o}(u,v)$ is calculated as

$$\Delta_r E^{o}(u,v) = E(v) - E(u) \tag{2.69}$$

If the process involves gas species, an additional term accounting for the change in the energy of gas species must be added in the previous equation. Finally, the corrected energy barrier $\Delta E^{o\neq}(u,v)$ used in the kMC simulations is calculated as

$$\Delta E^{o\neq}(u,v) = \max[0,\ \Delta_r E^o(u,v),\ \Delta E^{o\neq}_{BEP}(u,v)] \tag{2.70}$$

where the max operator filters negative values, as well as values lesser than the $\Delta_r E^o(u,v)$ if the latter is positive.

In order to model the lattice energetics with a CE, we need to map all the DFT-computed energies into the cluster energies entering in Eq. (2.68). The cluster energies CE_k for the single-body terms (i.e., for the individual adsorbates) can be taken as the corresponding formation energies E^f_k, which are essentially energy differences with respect to a reference set. The following rules are useful to decide how many reference species we need in the reference set:

- The pristine catalytic phase (e.g., surface, nanoparticle … with nothing adsorbed) has to be included
- The remaining reference species will be gas phase species, and we need as many such species as the number of different atoms encountered in our species
- The reference species must have linearly independent compositions. This means that we should not be able to write a reaction that produces one or more reference species from other reference species

Consider for instance the WGSR on Cu(111). In this case, we have the Cu surface as the catalyst and C-, H-, and O-containing species. A good reference set is $\{Cu(111), CO,\ H_2O,\ H_2\}$. The formation energy of adsorbate i, E^f_i is defined as

$$E^f_i = U_{i+slab} - U_{slab} - \sum\nolimits_j (n_j R_j) \tag{2.71}$$

where U_{i+slab} is the raw DFT energy of the slab with adsorbate i, U_{slab} is the raw DFT energy of the slab (i.e., Cu(111)), n_j is the number of atomic species j in i, and R_j is the reference energy of that atomic species, defined in our reference set as

$$R_H = \frac{1}{2} U_{H_{2(g)}} \tag{2.72}$$

$$R_O = U_{H_2O_{(g)}} - 2R_H \tag{2.73}$$

$$R_C = U_{CO_{(g)}} - R_O \tag{2.74}$$

where again $U_{i(g)}$ is a raw energy directly taken from the DFT based calculation. Let us now focus our attention on the cluster energies for the two-body terms entering the CE (i.e., the pairwise lateral interactions). In particular, consider the repulsion between two neighboring CO adsorbates. The formation energy of this figure can be calculated as

$$E^{f}_{CO-CO} = U_{CO-CO+slab} - U_{slab} - 2R_C - 2R_O \quad (2.75)$$

If these CO molecules were placed on the surface far away from each other, the formation energy would be equal to twice the formation energy of a single CO molecule, E^{f}_{CO}. However, because of the pairwise repulsive interaction between them, the formation energy of the co-adsorbed configuration is higher: $E^{f}_{CO-CO} > 2E^{f}_{CO}$. The magnitude of this pairwise interaction energy is therefore

$$CE_{CO-CO} = E^{f}_{CO-CO} - 2E^{f}_{CO} \quad (2.76)$$

As a simple example on how the CE formalism works, consider the following event shown in Figure 2.5

$$\{(10: CO, 11: O) \rightarrow (10: CO_2(1), 11: CO_2(2))\} \quad (2.77)$$

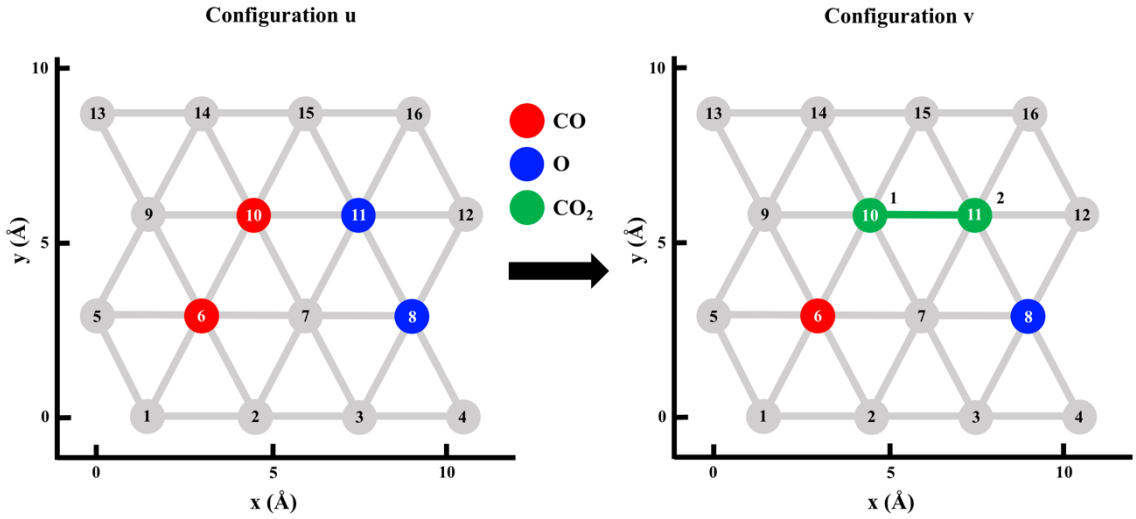

Fig. 2.5 Graph pattern representing a elementary step involving two unidentate adsorbates, species CO and O, that get converted to a bidentate CO_2 adsorbate.

This event belongs to the chemical reaction $CO + O \rightarrow CO_2$, which is one of the elementary steps included in the WGSR mechanism on Cu(111). Here, CO_2 is a bidentate adsorbate that occupies two adsorption sites, being the dentate nº 1 on site 10 and the dentate nº 2 on site 11. Now, let's assume that, in absence of lateral interactions, the energy barrier of this reaction is $\Delta E_0^{0\neq} = 0.60$ eV. The following cluster energies have been obtained from DFT calculations: $CE_{CO} = -1.10$ eV, $CE_O = 1.00$ eV and $CE_{CO_2} = -0.50$ eV. Note that, in absence of lateral interactions, the cluster expansion contains only

single-body terms. From these data, we can use Eq. (2.69) to calculate the reaction energy at zero-coverage limit

$$\begin{aligned}\Delta_r E_0^o = E(v) - E(u) &= \left(CE_{CO} + CE_O + CE_{CO_2}\right) - (2CE_{CO} + 2CE_O) \\ &= -0.40\ eV\end{aligned} \tag{2.78}$$

Let's improve now our model by incorporating nearest-neighbour pairwise additive interactions. Our cluster expansion contains now the following additional two-body terms, obtained from DFT calculations: $CE_{CO-CO} = 0.40$ eV, $CE_{CO-O} = 0.10$ eV, $CE_{O-O} = CE_{CO_2-O}$ eV $= 0$ eV and $CE_{CO_2-CO} = 0.20$ eV. The coverage-dependent reaction energy is then

$$\begin{aligned}\Delta_r E^o(u,v) &= E'(v) - E'(u) \\ &= \left(CE_{CO} + CE_O + CE_{CO_2} + CE_{CO_2-O} + CE_{CO_2-CO}\right) \\ &- (2CE_{CO} + 2CE_O + CE_{CO-CO} + CE_{CO-O} + CE_{O-O}) \\ &= -0.7\ eV\end{aligned} \tag{2.79}$$

Now, we can compute the energy barrier for that event in that particular configuration using Eq. (2.70) (we assume that $\beta = 0.5$). The result is $\Delta E^{o\neq}(u,v) = 0.45$ eV. Note that this value is 0.15 eV lower than the reaction energy at zero-coverage limit. When considering lateral interactions, the event represented on Figure 2.5 can no longer be written as $\{(10:CO, 11:O) \rightarrow (10:CO_2(1), 11:CO_2(2))\}$. Instead, the local lattice configuration includes not only the sites that change its occupation label from reactant to product configuration (i.e., sites nº 10 and 11), but also the eight neighboring sites the occupation value of which is a necessary information to determine the reaction rate of the process (i.e., sites 6-9, 12, 14-16).

2.6. References

1 D. Frenkel, B. Smit, Understanding Molecular Simulation, Academic Press, London, **2002**.

2 D. A. McQuarrie, Statistical Mechanics, Harper and Row, New York, **1976.**

3 N. Metropolis, A. W. Rosenbluth, M. N. Rosenbluth, A. H. Teller and E. Teller, Equation of state calculations by fast computing machines, *J. Chem. Phys*., **1953**, 21, 1087–1092.

4 A. C. T. van Duin, S. Dasgupta, F. Lorant and W. A. Goddard, ReaxFF: A reactive force field for hydrocarbons, *J. Phys. Chem. A*, **2001**, 105, 9396–9409.

5 L. H. Thomas, The calculation of atomic fields, *Math. Proc. Camb. Philos. Soc.*, **1927**, 23, 542–548.

6 P. a. M. Dirac, The quantum theory of the electron, *Proc. R. Soc. Lond. A*, **1928**, 117, 610–624.

7 P. a. M. Dirac, Note on exchange phenomena in the Thomas atom, *Math. Proc. Camb. Philos. Soc.*, **1930**, 26, 376–385.

8 F. Bloch, Bemerkung zur elektronentheorie des ferromagnetismus und der elektrischen leitfähigkeit, *Z. Für Phys.*, **1929**, 57, 545–555.

9 P. Hohenberg and W. Kohn, Inhomogeneous electron gas, *Phys. Rev.*, **1964**, 136, B864–B871.

10 W. Kohn and L. J. Sham, Self-consistent equations including exchange and correlation effects, *Phys. Rev.*, **1965**, 140, A1133–A1138.

11 X. Hua, X. Chen and W. A. Goddard, Generalized gradient approximation: an improved density-functional theory for accurate orbital eigenvalues, *Phys. Rev. B*, **1997**, 55, 16103–16109.

12 J. P. Perdew and Y. Wang, Accurate and simple analytic representation of the electron-gas correlation energy, *Phys. Rev. B*, **1992**, 45, 13244–13249.

13 J. P. Perdew, K. Burke and M. Ernzerhof, Generalized gradient approximation made simple, *Phys. Rev. Lett.*, **1996**, 77, 3865–3868.

14 A. E. Mattsson, R. Armiento, P. A. Schultz and T. R. Mattsson, Nonequivalence of the generalized gradient approximations PBE and PW91, *Phys. Rev. B*, **2006**, 73, 195123.

15 P. Schwerdtfeger, The pseudopotential approximation in electronic structure theory, *ChemPhysChem*, **2011**, 12, 3143–3155.

16 S. Grimme, Semiempirical GGA-type density functional constructed with a long-range dispersion correction, *J. Comput. Chem.*, **2006**, 27, 1787–1799.

17 S. Grimme, J. Antony, S. Ehrlich and H. Krieg, A consistent and accurate ab initio parametrization of density functional dispersion correction (DFT-D) for the 94 elements H-Pu, *J. Chem. Phys.*, **2010**, 132, 154104.

18 S. Grimme, Accurate description of van der Waals complexes by density functional theory including empirical corrections, *J. Comput. Chem.*, **2004**, 25, 1463–1473.

19 J. Klimeš and A. Michaelides, Perspective: Advances and challenges in treating van der Waals dispersion forces in density functional theory, *J. Chem. Phys*., **2012**, 137, 120901.

20 H. Eyring, The activated complex in chemical reactions, *J. Chem. Phys*., **1935**, 3, 107–115.

21 M. G. Evans and M. Polanyi, Some applications of the transition state method to the calculation of reaction velocities, especially in solution, *Trans. Faraday Soc*., **1935**, 31, 875–894.

22 K. J. Laidler, Chemical kinetics, Harper and Row, New York, **1987**.

23 C. Hartmann, R. Banisch, M. Sarich, T. Badowski and C. Schütte, Characterization of rare events in molecular dynamics, *Entropy*, **2013**, 16, 350–376.

24 L. Yang, A. Karim and J. T. Muckerman, Density functional kinetic Monte Carlo simulation of water–gas shift reaction on Cu/ZnO, *J. Phys. Chem. C*, **2013**, 117, 3414–3425.

25 A. F. Voter, F. Montalenti and T. C. Germann, Extending the time scale in atomistic simulation of materials, *Annu. Rev. Mater. Res*., **2002**, 32, 321–346.

26 M. Boudart, From the century of the rate equation to the century of the rate constants: a revolution in catalytic kinetics and assisted catalyst design, *Catal. Lett.*, **2000**, 65, 1–3.

27 K. A. Fichthorn and W. H. Weinberg, Theoretical foundations of dynamical Monte Carlo simulations, *J. Chem. Phys*., **1991**, 95, 1090–1096.

28 A. B. Bortz, M. H. Kalos and J. L. Lebowitz, A new algorithm for Monte Carlo simulation of Ising spin systems, *J. Comput. Phys*., **1975**, 17, 10–18.

29 J. J. Lukkien, J. P. L. Segers, P. A. J. Hilbers, R. J. Gelten and A. P. J. Jansen, Efficient Monte Carlo methods for the simulation of catalytic surface reactions, *Phys. Rev. E*, **1998**, 58, 2598–2610.

30 M. J. Hoffmann, S. Matera and K. Reuter, kmos: A lattice kinetic Monte Carlo framework, *Comput. Phys. Commun*., **2014**, 185, 2138–2150.

31 A. P. J. Jansen, An introduction to kinetic Monte Carlo simulations of surface reactions, Springer, Heidelberg, **2012**.

32 M. Stamatakis and D. G. Vlachos, A graph-theoretical kinetic Monte Carlo framework for on-lattice chemical kinetics, *J. Chem. Phys*., **2011**, 134, 214115.

33 J.I. Steinfeld, J.S. Francisco, W.L. Hase, Chemical kinetics and dynamics, Prentice Hall, Englewood Cliffs, USA, 1989.

34 H. Prats, L. Álvarez, F. Illas and R. Sayós, Kinetic Monte Carlo simulations of the water gas shift reaction on Cu(111) from density functional theory based calculations, *J. Catal*., **2016**, 333, 217–226.

35 H. Prats, P. Gamallo, F. Illas and R. Sayós, Comparing the catalytic activity of the water gas shift reaction on Cu(321) and Cu(111) surfaces: step sites do not always enhance the overall reactivity, *J. Catal*., **2016**, 342, 75–83.

36 S. Piccinin and M. Stamatakis, CO oxidation on Pd(111): A first-principles-based kinetic Monte Carlo study, *ACS Catal*., **2014**, 4, 2143–2152.

37 M. J. Hoffmann and K. Reuter, CO oxidation on Pd(100) Versus PdO(101)-($\sqrt{5}\times\sqrt{5}$)R27^{o}: first-principles kinetic phase diagrams and bistability conditions, *Top. Catal*., **2014**, 57, 159–170.

38 A. Chatterjee and A. F. Voter, Accurate acceleration of kinetic Monte Carlo simulations through the modification of rate constants, *J. Chem. Phys*., **2010**, 132, 194101.

39 E. C. Dybeck, C. P. Plaisance and M. Neurock, Generalized temporal acceleration scheme for kinetic Monte Carlo simulations of surface catalytic processes by scaling the rates of fast reactions, *J. Chem. Theory Comput*., **2017**, 13, 1525–1538.

40 R. B. Getman and W. F. Schneider, DFT-based coverage-dependent model of Pt-catalyzed NO oxidation, *ChemCatChem*, **2010**, 2, 1450–1460.

41 J. K. Nørskov, T. Bligaard, A. Logadottir, S. Bahn, L. B. Hansen, M. Bollinger, H. Bengaard, B. Hammer, Z. Sljivancanin, M. Mavrikakis, Y. Xu, S. Dahl and C. J. H. Jacobsen, Universality in heterogeneous catalysis, *J. Catal*., **2002**, 209, 275–278.

42 L. C. Grabow, A. A. Gokhale, S. T. Evans, J. A. Dumesic and M. Mavrikakis, Mechanism of the water gas shift reaction on Pt: first principles, experiments, and microkinetic modeling, *J. Phys. Chem. C*, **2008**, 112, 4608–4617.

43 J. Nielsen, M. d'Avezac, J. Hetherington and M. Stamatakis, Parallel kinetic Monte Carlo simulation framework incorporating accurate models of adsorbate lateral interactions, *J. Chem. Phys*., **2013**, 139, 224706.

44 M. Stamatakis and D. G. Vlachos, Unraveling the complexity of catalytic reactions via kinetic Monte Carlo Simulation: current status and frontiers, *ACS Catal*., **2012**, 2, 2648–2663.

45 E. Vignola, S. N. Steinmann, B. D. Vandegehuchte, D. Curulla, M. Stamatakis and P. Sautet, A machine learning approach to graph-theoretical cluster expansions of the energy of adsorbate layers, *J. Chem. Phys*., **2017**, 147, 054106.

CHAPTER THREE

Optimal faujasite structures for post-combustion CO_2 separation

3.1. Introduction

Potential applications of adsorbent materials such as MOFs, ZIFs or zeolites towards post-combustion CO_2 capture have been highlighted in Chapter 1. Among these materials, zeolites look especially adequate because of their narrow and uniform pore size, high surface area, adjustable hydrophobic and hydrophilic nature and ion exchange capacity. They are frequently used in PSA and VSA processes for removing CO_2 from air as an impurity, because of their high CO_2 selectivity and better thermal and mechanical stability[1,2]. Moreover, they are already produced on a large scale for many commercial applications[3,4].

Zeolites are molecular sieves with a 3D framework structure possessing orderly distributed micropores with diameters up to 2 nm. The zeolite framework is built from TO_4 tetrahedrals (T = Si or Al atom), and the different ways in which these tetrahedrals can be connected lead to a rich variety of zeolite structures[4–6]. In particular, faujasites (FAU) are a family of zeolites built from silicon, aluminum and oxygen atoms, with a composition that depends on the Si/Al ratio $\left(\mathrm{Na}, \mathrm{Ca}_{1/2}, \mathrm{Mg}_{1/2}\right)_{\mathrm{n}}\mathrm{Al}_{\mathrm{n}}\mathrm{Si}_{192-\mathrm{n}}\mathrm{O}_{384}$, $0 \leq n \leq 96$[7]. They consist of truncated octahedrons (also known as b-cages) and hexagonal prisms, connected in such a manner that large internal supercages are created. This results in much faster intra-crystalline diffusion rates as compared to other zeolites[8], making them good candidates for adsorbent materials in gas separation.

As shown in Section 1.2.4, the properties of zeolites depend on the nature and number of the cations (i.e., the Si/Al ratio or, equivalently, the Al content). In the present work ten FAU-type structures with different Al content have been studied (i.e., containing sodium as non-framework cations). These structures have been labelled as n-FAU, where n is the number of aluminum (or sodium) atoms per unit cell, n = 0, 6, 12, 24, 32, 48, 64, 77, 88 and 96.

Post-combustion power plants constitute the largest stationary source of CO_2 emissions. Concerning coal-fired plants, the main flue gas components in dry weight by volume are N_2 (75-80%), CO_2 (15-16%) and O_2 (4-5%), with total pressures near 1 bar and temperatures between 313 and 333K.[9] Despite the large number of adsorbent materials that have been reported in the context of CO_2 capture, the vast majority of them has relied exclusively on pure CO_2 and N_2 isotherms. Mixture results are then predicted using the Ideal Adsorbed Solution Theory (IAST) reported by Myers and Prausnitz[10].

This fact makes the selection of the best materials challenging, since phenomena as coadsorption and/or site competition are not taken into account. In addition, mixed gas adsorption measurements are often time-consuming, requiring carefully designed custom equipment and complex data analysis[11]. As a result, there is a significant lack of mixed gas adsorption data reported in the literature for mixtures with more than two components, even though many industrial gas separation involve multicomponent mixtures. Instead of having to rely on IAST, the present study is based directly on simulated mixture adsorption isotherms corresponding to the following ternary mixture: CO_2 (15%), N_2 (80%) and O_2 (5%).

The main goal of this chapter is then to assess faujasite structures in post-combustion CO_2 capture process in order to find the optimum structures and experimental conditions (i.e., P, T) for a given swing adsorption process. To this purpose, GCMC simulations are used to calculate several performance criteria (e.g., purity, working capacity, selectivity, …) for the ten different faujasite structures mentioned above. Publication 1 focuses on PSA, VSA and also combined VPSA processes. On the other hand, Publication 2 targets the TSA process and establishes a deep comparison between faujasite structures and swing adsorption processes in terms of energy.

3.2. Publication 1

Optimal Faujasite structures for post-combustion CO_2 capture and separation in different swing adsorption processes

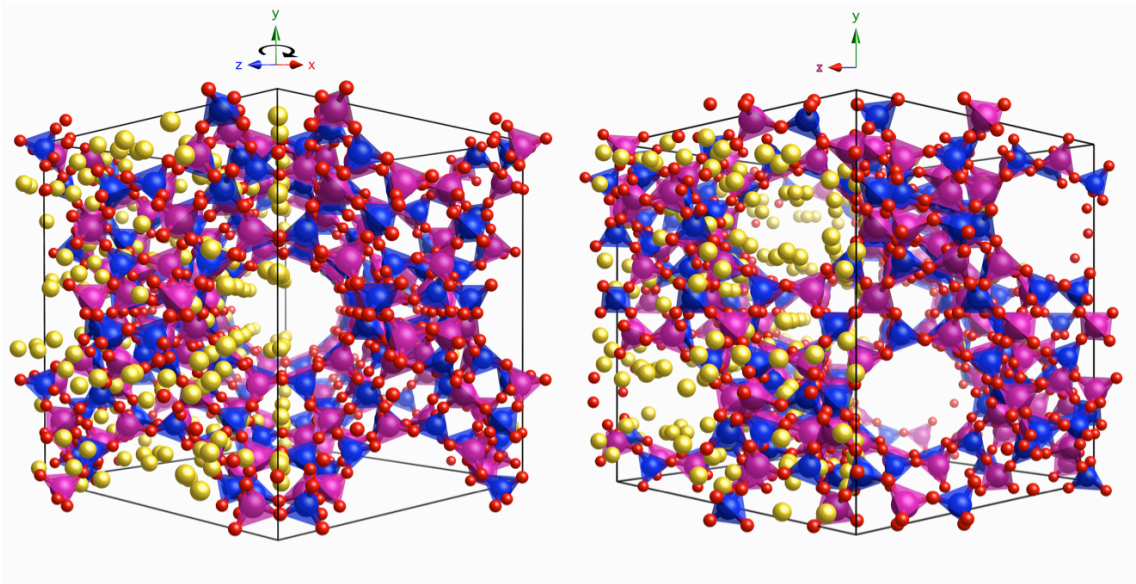

Journal of CO_2 Utilization 19 (2017) 100–111

Contents lists available at ScienceDirect

Journal of CO_2 Utilization

journal homepage: www.elsevier.com/locate/jcou

Optimal Faujasite structures for post combustion CO_2 capture and separation in different swing adsorption processes

Hèctor Prats, Daniel Bahamon, Gerard Alonso, Xavier Giménez, Pablo Gamallo*, Ramón Sayós

Departament de Ciència de Materials i Química Física & Institut de Química Teòrica i Computacional (IQTCUB), Universitat de Barcelona, C. Martí i Franquès 1, 08028 Barcelona, Spain

ARTICLE INFO

Article history:
Received 24 September 2016
Received in revised form 22 February 2017
Accepted 15 March 2017
Available online xxx

Keywords:
Zeolite
CO_2 capture
Sequestration
Molecular simulation
Swing adsorption process

ABSTRACT

Grand Canonical Monte–Carlo (GCMC) simulations are used in this work, to assess optimum faujasite structures, the well–known family of zeolites, in CO_2 capture processes. Pressure Swing Adsorption (PSA) and Vacuum Swing Adsorption (VSA) procedures have been considered to evaluate purity, working capacity and breakthrough time. To this purpose, ten faujasite structures with different Al content were selected, and the best conditions for CO_2 capture maximization have been calculated for each structure. Further results show that zeolites having intermediate Al content are the most effective for VSA processes, whereas low Al content faujasites perform better at PSA conditions. Remarkably, present work best results clearly improve Faujasite 13X VSA–PSA performances, so far considered the industrial reference in absence of water. Moreover, combined VPSA processes, in terms of working capacity and adiabatic work required for compression/expansion, have also been studied, showing that VPSA systems are more efficient than pure PSA/VSA, for structures with intermediate Al content. Finally, an improved methodology has been derived, where GCMC mixture isotherms and energetic cost calculations are combined, and a more accurate way of estimating working capacities and breakthrough times is proposed. This new approach allows more realistic evaluations of adsorbents' performances, than those found in the literature based on pure adsorption data.

1. Introduction

Carbon dioxide (CO_2) is the primary greenhouse gas generated by human activities, mainly from the combustion of fossil fuels (*e.g.*, oil, coal and natural gas) for energy and transportation [1]. Economic growth and industrial development are responsible of the increasing amount of atmospheric CO_2, and thus the resulting global warming and climate change that have attracted increasing attention in the last years [2,3].

Despite the development of alternative renewable energy sources, fossil fuels still dominate in almost all near future energy projections. Therefore, many efforts have been addressed to the development of cost-efficient technologies for separation and capture of carbon dioxide [4,5], focusing on improved Carbon Capture and Sequestration/Utilization (CCS/U) processes. The aim is to capture CO_2 emissions, and either reuse or store it, so it will not enter into the atmosphere. Moreover, these technologies should satisfy low cost energy requirements [6,7].

Post-combustion power plants constitute the largest stationary source of CO_2 emissions. Concerning coal-fired plants, the largest flue gas components in dry weight by volume are N_2 (75–80%), CO_2 (15–16%) and O_2 (4–5%), with total pressures near 100 kPa and temperatures between 40 and 60 °C (*i.e.*, 313–333 K) [8]. Aqueous amine solutions are currently the most viable absorbents for carbon capture, under the aforementioned conditions, being monoethanolamine (MEA) in water the benchmark solvent against which competing technologies are generally compared. The low solvent cost and proven effectiveness make MEA an attractive absorbent for many applications. However, it suffers from high parasitic energy consumption, over 30%, as well as adverse environmental impact, in the form of solvent losses and corrosion issues [9–11].

Alternative technologies, aimed at mitigating some of the disadvantages of these amine solutions, are an active area of research. Solid adsorbents are promising candidates, since they may reduce the energy required for regeneration, according to

* Corresponding author.
E-mail address: gamallo@ub.edu (P. Gamallo).

http://dx.doi.org/10.1016/j.jcou.2017.03.007
2212-9820/

Nomenclature

b	Constants in the Langmuir-Freundlich equation for component A ($kPa^{-\upsilon}$)
BTC	Benzene-1,3,5-tricarboxylate
C	Ideal gas concentration at the feeding-gas conditions ($kmol\,m^{-3}$)
CCS/U	Carbon capture and sequestration/utilization
EOS	Equation of state
FAU	Faujasite
GC	Grand canonical
GCMC	Grand canonical monte carlo
IAST	Ideal adsorbed solution theory
L	Length of packed bed (m)
LJ	Lennard-Jones
LSX	Low silica x
LTA	Linde type a
MC	Monte carlo
MEA	Monoethanolamine
MOF	Metal organic framework
N	Amount adsorbed per mass of adsorbent ($mol\,kg^{-1}$)
NIST	National Institute of Standards and Technology
$N_{k,sat}$	Maximum loading (saturation) of component a ($kmol\,m^{-3}$)
P	Pressure (kPa)
PSA	Pressure swing adsorption
q_i	Partial charge of atom i
q_{ST}	Isosteric heat of adsorption at infinite dilution ($kJ\,mol^{-1}$)
R	Gas constant ($8.314\,kPa\,m^3\,kmol^{-1}\,K^{-1}$)
r_{ij}	Distance between a pair of atoms i and j (m)
$S_{A/B}$	Selectivity
t	Time (s)
T	Temperature (K)
TSA	Temperature swing adsorption
u	Superficial gas velocity ($m\,s^{-1}$)
U_{ij}	Potential energy between a pair of atoms i and j ($kJ\,mol^{-1}$)
U_g	Total potential energy of an isolated guest molecule ($kJ\,mol^{-1}$)
V	Total volume of packed bed (m^3)
VOC	Volatile organic compounds
VPSA	Volume pressure swing adsorption
VSA	Volume swing adsorption
W	Adiabatic energy requirement for compression/vacuum (kJ)
WC	Working capacity of the targeted component in the mixture ($mol\,kg^{-1}$)
x_A	Mole fraction of component a in the adsorbed phase
y_A	Mole fraction of component a in the gas (bulk) phase
z	Distance along the adsorber (m)

Greek symbols

ε	Voidage of bed
ε_{ij}	Lennard-Jones potential well depth ($kJ\,mol^{-1}$)
ε_0	Vacuum permittivity ($F\,m^{-1}$)
κ	Polytropic parameter of gases
η	Feeding/vacuum blower efficiency
ρ_S	Framework density ($kg\,m^{-3}$)
σ_{ij}	Lennard-Jones potential diameter (m)
τ	Time necessary per saturation in a cycle [adim.]
μ	Chemical potential ($kJ\,mol^{-1}$)
ν	Intersticial gas velocity ($m\,s^{-1}$)

Subscripts

ads/feed	Adsorption or feeding conditions
des/regen	Desorption or regeneration conditions
k	Species in the gas mixture ($k = A, B, C, \ldots$)

their properties. This step is typically accomplished by Swing Adsorption processes, where desorption is performed by a) decreasing the pressure (Pressure Swing Adsorption, PSA, or Vacuum Swing Adsorption, VSA), b) increasing the temperature (Temperature Swing Adsorption, TSA) or c) by application of electrical current (Electric Swing Adsorption, ESA). All these processes are considered viable economic and ecological possibilities, and indeed numerous examples of commercial gas separation/purification processes, such as air fractionation, hydrogen production, carbon dioxide capture and volatile organic compounds (VOC) removal are already available, to name a few [12–17]. Focusing on pressure swing processes, the feeding gas system in VSA operates at a pressure one order of magnitude lower than in PSA air compressor, resulting in significant energy savings, because higher pressures are directly proportional to higher energy consumption [18,19].

Finding the most efficient adsorbents has attracted both experimental and theoretical research focus, and even new adsorbent materials are being synthesized in the large scale, claiming suitability for post-combustion CO_2 capture [10,20]. Zeolites, activated carbons, silicas and metal–organic frameworks (MOFs) have received significant attention as alternatives to amine solutions, demonstrating high CO_2 capacities and high selectivities for CO_2 over N_2, together with reduced regeneration energy penalties [9,21–23]. It is known that traces of water vapour in the post-combustion flow drastically reduce the CO_2 adsorption in zeolites, whereas activated carbons present good performance even in presence of water [21,24]. This fact makes an additional step for moisture removal prior to CO_2 adsorption mandatory in the case of zeolites.

Adequate, long–lasting capture materials should fulfil two main conditions. First, a potentially practical adsorbent should possess good adsorption capacity, high selectivity, as well as improved working capacity and regenerability, among other properties [11,25,26]. Second, it should be highly air-stable and be able to maintain its stability over multiple cycles [27]. Among these materials, zeolites look especially adequate because of their narrow and uniform pore size, high surface area, adjustable hydrophobic and hydrophilic nature, ion exchange capacity and strong acidity. They are frequently used in PSA and VSA processes for removing CO_2 from air, as an impurity, because of their high CO_2 selectivity [28,29]. Moreover, they offer a much better thermal and mechanical stability than other adsorbent materials recently described in the literature, such as MOFs, even though the latter possess higher pore volumes and surface areas [30,31].

Zeolites are molecular sieves with a 3D framework structure built from TO_4 tetrahedrals (T denotes tetrahedral–coordinated Si, Al, P, etc), possessing orderly distributed micropores with diameters smaller than 2 nm. Although all zeolite families are constructed from TO_4 tetrahedra, the different ways in which they can be connected lead to a rich variety of zeolite structures [32–34]. Dehydrated faujasite (FAU)-type structures are a family of zeolites built from silicon, aluminium and oxygen atoms, with a composition that depends on the Si/Al ratio, $(Na,Ca_{1/2},Mg_{1/2})_nAl_nSi_{192-n}O_{384}$, $0 \le n \le 96$ [35]. They consist of b-cages and hexagonal prisms, connected in such a manner that large internal supercages are created. The properties of the faujasites depend on the nature, number and distribution of the framework cations. As the Si/Al ratio increases, the cation content decreases, the thermal stability is higher, the surface becomes more hydrophobic and the

zeolite loses its catalytic properties. That is of supreme importance in the evaluation of energetic costs for the CO_2 capture and, obviously, in the adsorbent material regenerability [36]. Thus, FAU-type zeolites present outstanding properties for their use in adsorptive separations. Furthermore, their open three-dimensional pore system results in much faster intra-crystalline diffusion rates as compared to other zeolites [37].

In this work, the influence of the Si/Al-ratio in FAU zeolites, with sodium exchanged cations, on the gas adsorption behaviour for post-combustion CO_2 capture and separation in PSA and VSA processes, has been evaluated in detail. Ten faujasite structures with different Al content have been considered, which makes it the most extensive study to date. A more complete understanding of the separation mechanism has been gained from complementary methods, including transient breakthrough simulations, as well as an extensive analysis regarding the effect of operating conditions in capture costs. Positive results indicate that the present methodology may serve as a useful tool for adsorbent materials screening and design.

The paper is organized as follows: structure details and computational methodology are described in Section 2. Results for all the different structures are presented in Section 3, being divided in four topics: a) simulations for pure components, b) results for ternary mixtures, c) evaluation of their performance in PSA and VSA units (focusing on working capacities, energetic requirements and transient breakthrough simulations) and d) combined VPSA processes. Finally, the main conclusions are summarized in Section 4.

2. Methods and computational details

2.1. Faujasite structures

In this work, molecular simulations have been performed as a screening tool for choosing the most efficient adsorbent material among ten FAU-type structures with different Si/Al ratio (*i.e.*, containing sodium atoms as non-framework cations). These structures have been labelled as *n*-FAU, where n represents the number of aluminium or sodium atoms per unit cell, $n = 0, 6, 12, 24, 32, 48, 64, 77, 88$ and 96. These values correspond to Si/Al ratios of $+\infty$, 31, 15, 7, 5, 3, 2, 1.5, 1.2 and 1, respectively. FAU-type zeolites can be labelled either X or Y, depending on their framework aluminium density: X zeolites contain between 77 and 96 aluminium atoms per unit cell, whereas Y zeolites contain less than 77 aluminium atoms. Moreover, when the number of aluminium atoms per unit cell is greater than 88 the Si/Al ratios are lower than 1.15 and the faujasite is usually called a Low Silica X zeolite (LSX) [38]. The *n*-FAU structures with $n \neq 88$ were obtained from 88-FAU (commonly named zeolite 13X), by randomly replacing aluminium by silicon atoms and satisfying the generally accepted Löwenstein's avoidance rule [39], which states that Al-O-Al bonds cannot be found in the zeolitic framework. For the 88-FAU structure we use the atomic crystallographic position reported by Olson et al. [35] with a cubic unit cell of $a = b = c = 25.10$ Å.

Several random structures can be obtained satisfying the desired Si/Al ratio, and therefore different frameworks were constructed for each structure, finding that the distribution of Al atoms does not change considerably the main properties of the adsorbate. All FAU frameworks were treated as rigid structures with atoms fixed at their crystallographic positions. In addition, it is known that the mobility of the non-framework cations has a strong effect on the adsorption behaviour [40,41]; thus in our case the negative charge was counterbalanced by sodium atoms which were allowed to move freely along the FAU structure, adjusting their position depending on their interactions with the framework atoms, other sodium cations and the gas molecules. This represents a step further with respect to other works published in literature, in which the position of the cations is optimized, then frozen before running the GCMC simulation [10,41,42–45].

2.2. Force field and GCMC simulations

GCMC simulations exchange atoms or molecules with an imaginary ideal gas reservoir at a constant temperature *T*, volume *V* and chemical potential μ [46] Then, the amount of molecules adsorbed is calculated using a statistically averaged approach after the equilibrium stage for every single pressure point, allowing the construction of adsorption isotherms. All simulations were performed by means of LAMMPS code [47]. At every simulation step, the code attempts a number of GCMC exchanges (*i.e.*, insertions and deletions) of gas molecules between the simulation box and the imaginary reservoir, and a number of Monte Carlo movements (*i.e.*, translations and rotations) of gas molecules within the simulation box. Regarding MC exchanges, deletions and insertions were attempted with equal probability to ensure microscopic detailed balance whereas MC movements were also attempted with 50% probability. Finally, once the molecules are moved in a simulation step, an extra MC translation movement is attempted for the sodium cations. At least 4×10^6 MC equilibration steps and 8×10^6 MC production steps were used at each pressure condition.

Both pure-component and mixture isotherms were computed at 313 K, in a pressure range between 1 and 5000 kPa (except for pure CO_2 adsorption, where the pressure range was increased to 0.01–5000 kPa due to its high affinity with the adsorbent material even at very low pressures). According to the typical post-combustion gas composition, we considered the following ternary mixture in our simulations: CO_2 (15%), N_2 (80%) and O_2 (5%). As described below in Section 3.2, there is a significant lack of adsorption data reported in the literature for mixtures with more than two components. We assume that water and impurities have been previously removed from the tail gas in an earlier stage. This previous phase can be achieved using activated carbons for sulphur compounds and trace contaminant removal, silica gels for light hydrocarbon elimination, and activated aluminas, bauxite, and also silica gels for dehumidification [48].

The Peng-Robinson Equation of State (EOS) [49] was used to relate the pressure to the chemical potential required in the GCMC simulations. Pure substance parameters of the EOS were taken from the NIST database [50]. For the ternary mixtures, the van der Waals one-fluid mixing rule was used [51], and the binary parameters were taken from Vrabec et al. [52]

A potential model for CO_2, N_2 and O_2 molecules was used with rigid geometrical structures, where only the nonbonded interactions were taken into account. Moreover, we have excluded the pairwise interactions between the framework atoms, since the structure was treated as frozen, in order to save unnecessary computation time. Hence, at each simulation step, the total energy of the system was calculated as the sum of the adsorbate-faujasite and the adsorbate–adsorbate interaction energies, written as a sum of nonbonded interatomic terms modelled as a combination of Lennard Jones (LJ 12-6) and Coulomb potentials,

$$U_{ij} = 4\varepsilon_{ij}\left[\left(\frac{\sigma_{ij}}{r_{ij}}\right)^{12} - \left(\frac{\sigma_{ij}}{r_{ij}}\right)^{6}\right] + \frac{1}{4\pi\varepsilon_0}\frac{q_i q_j}{r_{ij}} \quad (1)$$

where U_{ij} is the potential energy between a pair of atoms *i* and *j* at a distance r_{ij}; q_i, q_j are the partial charge of atom *i* and *j*, respectively, ε_{ij} and σ_{ij} are the LJ potential well depth and diameter, respectively, and ε_0 is the vacuum permittivity. All the LJ and Coulomb parameters were taken from the force field developed by Calero's group [53,54]. These parameters have been proved to

accurately reproduce the experimental adsorption properties for pure CO_2, N_2 and O_2 molecules (among others) in many different zeolite framework types, at cryogenic and high temperatures. Moreover, it is applicable to all possible Si/Al ratios in a transferable manner, with sodium atoms as extra-framework cations.

Coulombic interactions were computed using the Ewald summation method [46] with a relative precision of 10^{-6}, LJ cutoff ratio was fixed at 12 Å, and van der Waals interactions between molecules were obtained from Lorentz-Berthelot mixing rules. Section I in the Supplementary information (SI) summarizes the Coulombic charges and LJ parameters used in this work, as well as the agreement between simulations and experimental data for selected structures (when available).

2.3. Parameters/Indicators for separating processes

The isosteric heat of adsorption of component A, $q_{st,A}$, is one of the most important thermodynamic quantities for understanding the thermal effects related to adsorption and the cost of desorption/regeneration. It provides information about the energy released during the adsorption process, and it depends on the temperature and surface coverage. From energy/particle fluctuations in the GC ensemble, the isosteric heat can be calculated as [55]:

$$-q_{st,A} = \frac{< U \times N > - < U >< N >}{< N^2 > - < N >^2} - < U_g > - RT \quad (2)$$

where U is the total potential energy of the system per molecule, N is the number of molecules adsorbed, U_g is the energy of an isolated guest molecule and the brackets $< \ldots >$ denote an average in the GCMC ensemble.

A helpful indicator for the mixture separation ability is the adsorption selectivity of a porous adsorbent. This selectivity ($s_{A/B}$) for component A relative to B species, is calculated as:

$$s_{A/B} = \left(\frac{x_A}{x_B}\right)\left(\frac{y_B}{y_A}\right) \quad (3)$$

where x_A and x_B are the molar fractions of species A and B in the adsorbed phase, respectively, while y_A and y_B correspond to the molar fractions of A and B in the bulk phase (*i.e.*, feeding conditions), respectively. In the present work selectivity values are obtained directly from the mixture GCMC simulations, instead from the pure isotherm data, as it is usually done in both theoretical [56–58] and experimental [15,16,29,43,59–61] works published in literature.

Apart from the adsorption selectivity, another very important property that is often used as evaluation criteria in Swing Adsorption processes is the working capacity (WC_A) of the targeted component in the mixture. This quantity is defined as:

$$WC_A = N_{A,ads} - N_{A,des} \quad (4)$$

where A is the targeted component (*i.e.*, CO_2) and $N_{A,ads}$ and $N_{A,des}$ are the uptake per mass of adsorbent under adsorption or feeding and desorption or regeneration conditions, respectively.

The working capacity is generally more relevant than the total uptake at the adsorption pressure, since it really determines the amount of A that can be recovered at each adsorption cycle. Thus, $N_{A,ads}$ corresponds to the CO_2 uptake obtained from the ternary mixture isotherms at the adsorption pressure (*i.e.*, 1000–3000 kPa and 100 kPa for PSA and VSA, respectively), whereas $N_{A,des}$ corresponds to the CO_2 uptake in the mixture obtained at the desorption step, which is more concentrated in CO_2 than the original flue gas mixture. When the material is highly selective for one component of the mixture, a good approximation is assuming pure gas recovered at the outlet of the adsorber, as have been implemented by several authors [15,62,63]. In that case, the amount of A removed from the adsorbent material is obtained from pure isotherms. However, in the present study, since carbon dioxide recovered is not completely pure, we have calculated the amount of remaining CO_2 in the adsorbent material (*i.e.,* at the desorption step) by multiplying the pure CO_2 uptake at desorption pressure by a fractional factor obtained from the composition in the adsorbed phase (using mixture isotherms data) and the molecules retained in the void volume within the adsorbent material.

There are other indicators for comparing adsorbent materials such as the Adsorption Figure of Merit [64], the solvent selection parameter [65], or the adsorbent productivity [66]. However, the first two indicators seem to be an empirical rule of thumb that works well for certain objectives, whereas the last indicator cannot be obtained from GCMC simulations that only allows getting equilibrium properties.

2.3.1. Packed bed adsorber breakthrough simulation methodology

It has been demonstrated that neither highest $s_{A/B}$ nor maximum WC_A on their own can be chosen as final criteria for adsorbent selection. However, it is the combination of them, which leads to the best adsorbent material, and also to determine the optimum energetic cost of CO_2 capture in PSA and VSA processes [11,31,67,68]. Breakthrough calculations mimic the dynamic conditions of a large-scale separation, and therefore they can be helpful to screening a variety of adsorbents for a specified separation and to evaluate the separation performance [69,70]. In this regard, it is recommended to analyse the transient breakthrough curves of gas mixtures at the outlet of the adsorber [71].

Assuming a plug flow model for the gas mixture through the fixed bed, maintained under isothermal conditions and negligible pressure drop, the composition at any position and instant of time can be obtained by performing material balances for the adsorbates, that is, by solving the partial differential Eq. (5) for each one of the k species in the gas mixture ($k = A, B, C, \ldots$).

$$\varepsilon\frac{\partial P_k}{\partial t} + (1-\varepsilon)RT\rho_S\frac{\partial N_k}{\partial t} + \frac{\partial(v \cdot P_k)}{\partial z} = 0 \quad (5)$$

In Eq. (5), the terms represent the accumulation of the adsorbate in the fluid phase, the rate of adsorption with time, and the convective flow of the adsorbate within the bed, respectively. Note that with these assumptions, intracrystalline diffusion term is negligible, and therefore, thermodynamic equilibrium prevails everywhere within the bed. Further details of the adsorber model, along with the numerical procedure used, are provided in earlier works [72–74]. Moreover, in Eq. (5), t is the time, z is the distance along the adsorber, ρ_S is the framework density, ε is the bed voidage that is the ratio of the void volume to the total volume of the bed, v is the interstitial gas velocity equal to the superficial gas velocity, u, divided by ε, and P_k the partial pressure of k-th component. Finally, the molar loadings of the species, $N_k(z,t)$, at any position and time were determined according to the Ideal Adsorbed Solution Theory (IAST) exhibited by Myers and Prausnitz [75]. The accuracy of IAST for estimating the mixture equilibrium in zeolites has been well established in literature [56].

In order to apply IAST, the excess component loadings of the pure isotherms were fitted with a Langmuir–Freundlich adsorption isotherm model,

$$N_k = \frac{N_{k,sat} b_k P_k^{v_k}}{1 + b_k P_k^{v_k}} \quad (6)$$

with $N_{k,sat}$ (kmol m^{-3}) and b_k (kPa$^{-\nu_k}$) standing for the adsorption constants of component k, and P_k the partial pressure of k-th component.

For a chosen purity of 0.5% CO_2 in the gaseous mixture exiting the adsorber, a breakthrough time (τ_{break}) was determined; this time controls the frequency of required regeneration and influences the working capacity of PSA or VSA units.

2.4. Techno-economic aspects

Isothermal PSA and VSA processes were simulated including only two fixed beds at constant temperature in parallel, according to the simplest scheme configuration. While one bed is adsorbing, the other bed is desorbing at a lower pressure. This is called Skarstrom's [76] four-step cycle, and it was selected as the baseline analysis in the present study. The shortcut method described by Chung et al. [77] was adopted for the calculations, since it is able to easily describe the characteristics of the PSA and VSA processes, including the effect of different operating conditions. The model classifies the four steps of the Skarstrom's cycle into two main groups: pressurization (step I) and adsorption (step II) are merged into "adsorption" group, while depressurization/blowdown (step III) and evacuation (step IV) are grouped into "desorption".

Desorption pressures between 5 and 10 kPa were assumed for the VSA processes, since it has been shown that these conditions can be achievable in experiments [78]. Conversely, for the high-pressure feeding operation (*i.e.*, PSA), we assumed that the desorbed stream is expanded from 1000 to 3000 kPa to atmospheric pressure.

In order to determine the energy requirements to capture and separate an amount of CO_2, it is required to calculate the work done during one cycle, involving pressurizing during adsorption step (for PSA) and vacuum during desorption step (for VSA). Therefore, the adiabatic energy requirement was calculated in a similar way of that presented by Chaffee et al. [79] and Riboldi et al. [80] using the following equations,

$$W_{feed}(kJ) = \left(\frac{k}{k-1}\right)\frac{RT}{\eta}\int_{t=0}^{t=\tau}\left(\varepsilon v_o C_{feed} + \frac{WC_{CO_2}}{y_{CO_2}^{feed}}\rho_S V(1-\varepsilon)\right)\left[\left(\frac{P_{feed}}{P_{atm}}\right)^{\frac{k-1}{k}} - 1\right]dt \quad (7)$$

$$W_{vacuum}(kJ) = \left(\frac{k}{k-1}\right)\frac{RT}{\eta}\int_{t=0}^{t=\tau}\left(\varepsilon v_o C_{feed} + N_{TOT}^{ads}\rho_S V(1-\varepsilon)\right)\left[\left(\frac{P_{atm}}{P_{vacuum}}\right)^{\frac{k-1}{k}} - 1\right]dt \quad (8)$$

where $\eta = 0.85$ (feeding/vacuum blower efficiency), k is the polytropic parameter that depends on the purity of the gas ($k = 1.28$ and 1.4 for pure CO_2 and air, respectively), τ is the time necessary per cycle, P_{atm} is the atmospheric pressure (*i.e.*, 101.375 kPa), P_{feed} corresponds to the instantaneous discharge pressure (kPa) from the feeding compressor and P_{vacuum} is the instantaneous pressure (kPa) to the vacuum pump. The term $\varepsilon v_o C_{feed}$ stands for the non-adsorbed molecules placed at the void spaces of the bed, where $\varepsilon = 0.4$ is the void fraction, C_{feed} is the concentration at the feeding conditions in kmol m^{-3} units, and v_o the velocity of the gas mixture through the bed in m s^{-1} units.

Depending on whether PSA or VSA processes are considered, the amount of pressurized or expanded substance differs. In VSA, the complete bed is subjected to a vacuum; hence the total amount adsorbed (N_{TOT}^{ads}) plus the molecules in the void space must be evacuated. Conversely, for PSA, the amount compressed will be higher and mainly depends on the working capacity of CO_2 at the feeding stream conditions, since purge has not been taken into account in this study.

3. Results and discussion

In this section, the main results for the ten different faujasite structures are presented and compared with other adsorbents for potential applications in post-combustion CO_2 capture, such as the Ca-A zeolite, and the Mg-MOF-74 and Cu-BTC metal organic frameworks. Pure component data and selectivities for these structures have been obtained from the works of Bae et al. (Ca-A) [15], Mason et al. (Mg-MOF-74) [16] and Bahamon et al. (Cu-BTC) [81]. Working capacities and CO_2 purities have been estimated from IAST calculations by fitting the pure component adsorption isotherms.

3.1. Pure components

The pure component adsorption isotherms for CO_2 on the different adsorbents evaluated are presented in Fig. 1. The corresponding fitting parameters used later for the costs evaluation are given in Section II in the SI. In all cases, the amount of CO_2 adsorbed or uptake is significantly higher at lower pressures than that of N_2 and O_2 (see Section III in the SI), indicating good selectivity towards carbon dioxide, even at lower quantities of sodium atoms within the framework.

It is generally accepted that the separation ability for CO_2 increases when increasing the electrostatic field inside the zeolite cavities, which is mainly caused by the framework charge. This charge can be varied either by the nature of the charge compensating cations or by the Al content of the zeolite framework [28]. From Fig. 1 it is clear that the CO_2 adsorption capacities at

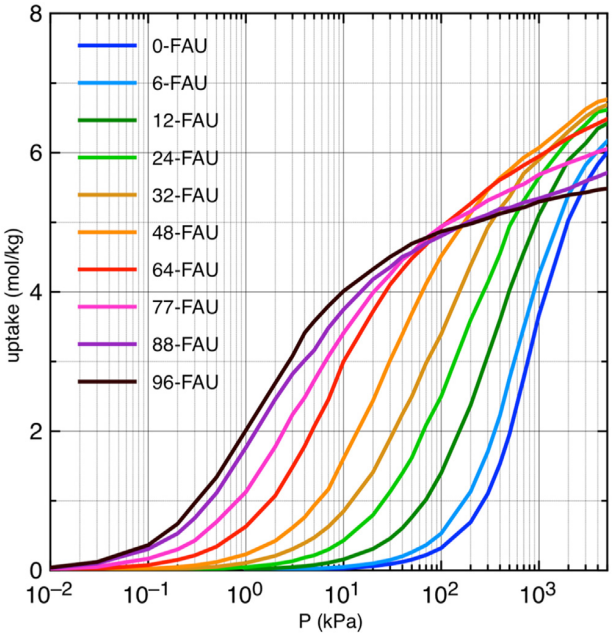

Fig. 1. CO_2 pure adsorption isotherms for ten different faujasite structures at 313 K. These structures have been labelled as n-FAU, where n is the number of aluminium or sodium atoms per unit cell. Lines are guide to the eyes, obtained from 29 equidistant single points for each structure. (For interpretation of the references to colour in this figure legend, the reader is referred to the web version of this article).

low–pressure regimes increase as the Al content does, indicating that the interaction between adsorbed molecules and the zeolite framework is stronger at high Na^+ contents. Thus, the 96-FAU structure is the first reaching saturation, whereas 0-FAU saturates the last. However, at high–pressure regimes the maximum adsorption capacity is found for structures having intermediate Al content, because the volume occupied by the cations inside the framework is not negligible, and the available pore volume for CO_2 adsorption diminishes as the Al content increases. Therefore, above 5000 kPa the maximum adsorption capacity is reached by the 48-FAU structure, whereas the most common industrially used structure 13X or 88-FAU shows a reduction of about 15% of the capacity with respect to the 48-FAU.

As above-mentioned, the isosteric heat of adsorption is an important point to be considered since the regenerability of the adsorbent material will depend on the CO_2-adsorbent interaction. A small q_{st} value implies better regeneration but lower adsorption capacity for a given pressure, and vice versa [29].

Fig. 2 shows the isosteric heat of adsorption for CO_2 as a function of the Al content. Due to the strong interaction between CO_2 molecules and the non-framework cations, the isosteric heat increases from 13 to 42 kJ mol^{-1} from the raw silica FAU to the 96-FAU zeolite, respectively. This fact has been also reported by A. Corma's group for LTA zeolites [29]. Interestingly, 96-FAU and Mg-MOF-74 show the same isosteric heat of adsorption (42 kJ mol^{-1}), and the same is observed comparing 12-FAU with Cu-BTC (25 kJ mol^{-1}). Finally, zeolite Ca-A exhibits the highest value (58 kJ mol^{-1}). The heats of adsorption remain more or less stable over the pressure range investigated for most of the structures, suggesting relatively homogeneous adsorption sites. This fact will not be discussed in more detail here as it has been previously discussed [82].

3.2. Mixture behaviour

Despite the large number of adsorbent materials that have been reported in the context of CO_2 capture, the main part of the studies has relied exclusively on pure CO_2 and N_2 isotherms. This fact makes the selection of the best materials for capturing CO_2 from an actual flue gas mixture challenging, since phenomena as co-adsorption and/or site competition are not taken into account. In addition, mixed gas adsorption measurements are often time-consuming, requiring carefully designed custom equipment and complex data analysis [83]. As a result, there is a significant lack of mixed gas adsorption data reported in the literature for mixtures with more than two components, even though many industrial gas separations involve multicomponent mixtures.

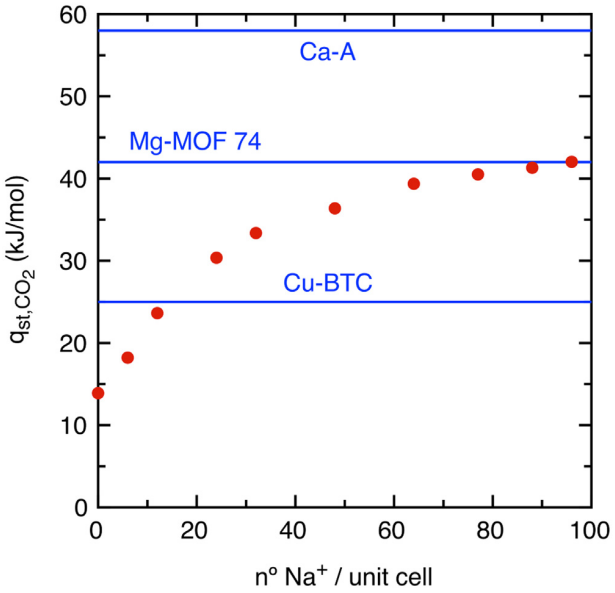

Fig. 2. Isosteric heat of adsorption for pure CO_2 at zero loading, as a function of the number of Na^+ cations per unit cell (red circles). The values for Ca-A, Mg-MOF-74 and Cu-BTC are also included as lines, for comparison, taken from the works of Bae et al. [15], Mason et al. [16] and Bahamon et al.[81], respectively.

Fig. 3 shows the adsorption isotherms at 313 K for carbon dioxide and nitrogen in four selected structures from both pure and mixture simulations, as well as the IAST mixture prediction. In this case, the *x* axis represents the total and partial pressure of *k-th* component at pure and mixture conditions, respectively. Oxygen data are omitted for the sake of clarity of the figures, but its loading is lower than that of nitrogen (see Section IV in the SI for complete isotherms).

As the amount of Na^+ ions in the structure increases, the behaviour of the CO_2 in mixtures mimic more consistently the adsorption isotherm at pure conditions, but the N_2 uptake in the mixture is much lower. IAST correctly predicts the N_2 behaviour in the mixture. However, for structures with intermediate and high Al content, the CO_2 uptake predicted by IAST is overestimated at high pressures and underestimated at low pressures (Fig. 3).

Fig. 4 shows the selectivity for CO_2 relative to N_2 for the ten structures evaluated over the entire range of pressures. As expected, 96-FAU has the highest CO_2 selectivity, ranging from 1150 to 170, at 5 and 5000 kPa, respectively, while 0-FAU has the lowest value, ranging from 4 to 6 in the same pressure range. The high selectivity values for NaX-type zeolites are even greater than those of Ca-A (250 at feeding conditions of 15 kPa CO_2, 75 kPa N_2 and 313 K) and Mg-MOF-74 (175 at feeding conditions of 15 kPa CO_2, 75 kPa N_2 and 313 K). Finally, Cu-BTC selectivity is similar to that of 12-FAU (18 at feeding conditions of 14 kPa CO_2, 86 kPa N_2 and 318 K). It is worth mentioning that, for zeolites having 64 or more Na^+ cations per unit cell, the selectivity decreases as the pressure is increased. However, it remains constant for zeolites having between 12 and 48 Na^+ atoms, and even increases slightly with the pressure whether the number of Na^+ cations per unit cell is below 12. The reason of this decreasing in selectivity with pressure for zeolites having high Na^+ content is associated with the fact that these are the first structures in reaching CO_2 saturation and it obviously occurs since no more empty space is available for CO_2 molecules, although adsorption of smaller molecules like N_2 and O_2 is still possible.

3.3. Evaluation of PSA/VSA processes

Swing adsorption cycles and conditions can be manipulated to meet a variety of demanding requirements, for instance to provide high purity CO_2, or to minimize power demands [18,84,85]. Moreover, same working capacities can be obtained by changing the adsorption/desorption pressures (*i.e.*, feeding/regeneration steps); the one with the lowest compression costs would then be the best material. The aim of this section is to test different conditions and to be able of selecting, for each faujasite structure, those conditions that minimize both the power and capital costs for CO_2 capture.

Carbon dioxide working capacity for the different FAU structures are given in Fig. 5. Four operating conditions $P_{feed.}$-$P_{regen.}$ have been considered (two for each process), which correspond to 1000–100 and 3000–100 kPa for PSA, and 100–10 and 100–5 kPa for VSA. Note that for VSA process, desorption pressures above 10 kPa imply net values of working capacities of almost zero for most of the structures.

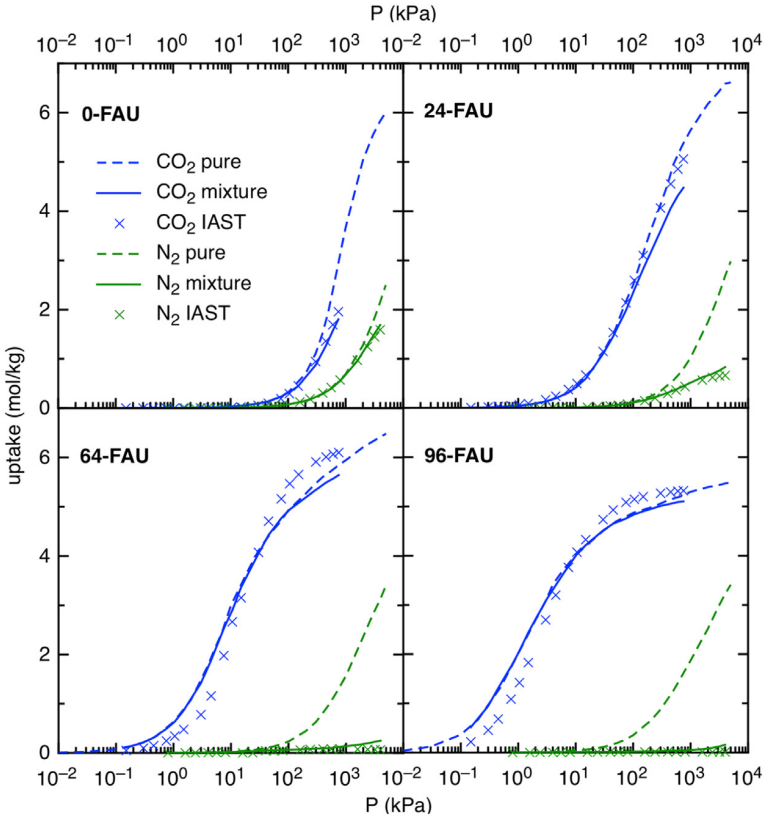

Fig. 3. Simulated adsorption isotherms for CO_2 (blue) and N_2 (green) for four selected faujasite structures at pure (dashed lines) and mixture (solid lines) conditions, at 313 K. IAST mixture prediction (cross marks) has also been included. The *x* axis represents the total and partial pressure of *k*-th component at pure and mixture conditions. (For interpretation of the references to colour in this figure legend, the reader is referred to the web version of this article.)

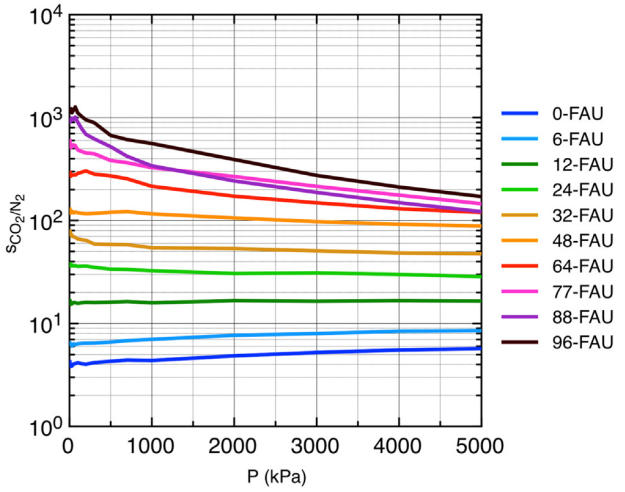

Fig. 4. Calculated selectivities for CO_2 relative to N_2 as a function of pressure, for ten different faujasite structures at 313 K. (For interpretation of the references to colour in this figure legend, the reader is referred to the web version of this article.)

Regarding the PSA process, the working capacity is almost tripled when the feeding pressure at adsorption conditions is raised from 1000 to 3000 kPa, for all the faujasite structures. Moreover, the NaY-type structures present higher working capacities than the NaX-type structures, reaching optimum values at 12–24 Na^+ cations per unit cell. As saturation conditions are approached at high pressures, the hierarchy of WC_{CO2} is dictated largely by the pore volumes and free surface areas, which are greater for faujasites with low Al content since they present a lesser amount of Na^+ cations. While NaX-type faujasites showed highest uptakes, the number of CO_2 desorbed molecules at regenerating conditions (*i.e.*, 100 kPa) is small, making them rather less interesting for the PSA process. In contrast, NaX-type faujasites present good working capacities for the VSA process, especially when the pressure at the desorption conditions is lowered to 5 kPa. In fact, working capacities for 48-FAU and 64-FAU structures operating between 100 and 5 kPa are almost as high as the value of the Ca-A zeolite, which is around 1.55 mol kg^{-1}. Conversely, MOFs are the adsorbent materials with the highest working capacities at PSA conditions, because they saturate at much higher pressures. For instance, Cu-BTC and Mg-MOF-74 present values of 4.72 and 6.06 mol kg^{-1} operating between 3000 and 100 kPa, respectively, but their values become lower operating between 100 and 10 kPa (*i.e.*, 0.27 and 0.52 mol kg^{-1}). Finally, it is important to note that experimental materials are known to be not fully activated and then, some discrepancies could appear in their performance compared to simulated perfect crystals.

The CO_2 purity at outlet of the adsorber is an important variable to consider, especially when it is possible to reuse it for other applications. Fig. 6 shows the CO_2 purity (%) exiting the adsorber at the desorption step as a function of the PSA adsorption pressure and VSA desorption pressure for all the faujasite structures, assuming a packed bed with a total volume of 0.1 m^3 (*i.e.*, L = 0.1 m, A = 1 m^2) and a void fraction of $\varepsilon = 0.4$ (ε = (bulk density)/(framework density)). The final CO_2 purity depends on the selectivity, the working capacities for $CO_2/N_2/O_2$, and also on the

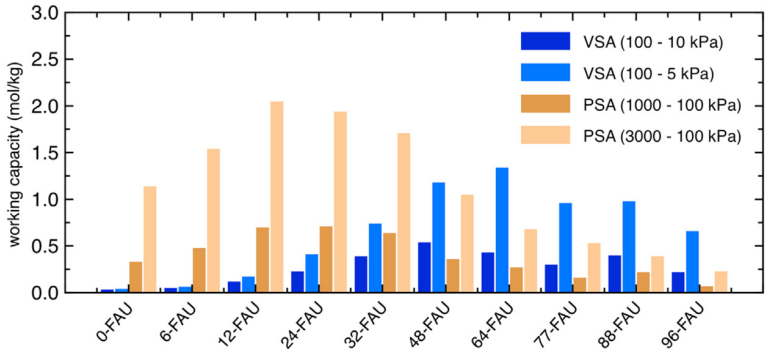

Fig. 5. Calculated CO_2 working capacities for the ten FAU structures considered corresponding to PSA and VSA processes at different $P_{feed.}$-$P_{regen.}$, and at 313 K. (For interpretation of the references to colour in this figure legend, the reader is referred to the web version of this article.)

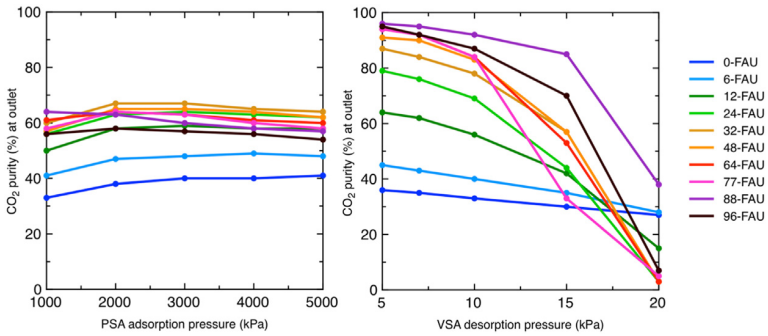

Fig. 6. CO_2 purity (%) in the gaseous mixture exiting the bed adsorber at the desorption step, as function of adsorption ($P_{feed.}$; PSA, left) and desorption ($P_{regen.}$; VSA, right) pressure, assuming a packed bed with a total volume of 0.1 m^3 (L = 0.1 m, A = 1 m^2) and a void fraction of $\varepsilon = 0.4$. Simulations performed at 313 K. (For interpretation of the references to colour in this figure legend, the reader is referred to the web version of this article.)

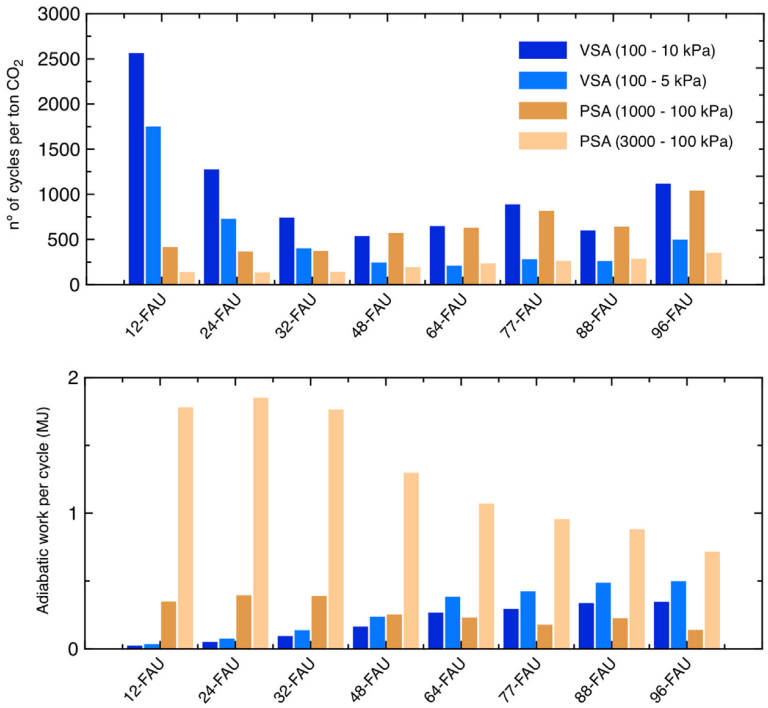

Fig. 7. Number of VSA and PSA cycles needed to remove a ton of CO_2 for each structure (up) and adiabatic work per cycle (down), assuming a packed bed with a total volume of 0.1 m^3 (L = 0.1 m, A = 1 m^2) and a void fraction of $\varepsilon = 0.4$. 0-FAU and 6-FAU structures have not been included for the clarity of the plot (the number of required PSA cycles is 7200 and 8300 for 6-FAU and 0-FAU, respectively). (For interpretation of the references to colour in this figure legend, the reader is referred to the web version of this article.)

void fraction ε. It can be seen that the VSA process allows obtaining a higher CO_2 purity than PSA ones, because the N_2 and O_2 working capacities in PSA conditions are much higher than in VSA conditions, as well as the amount of N_2 and O_2 in the empty space of the bed. Moreover, in general NaX-type structures drive to higher purities due to their high selectivity. Regarding the zeolite Ca-A, we have estimated, assuming also $\varepsilon = 0.4$, high purity values for VSA applications up to 98% at 100–5 kPa, similar to 88-FAU. However, for PSA application at 3000–100 kPa its value is only around 49%, overtaken by most of the faujasite structures considered. Finally, MOFs present lower CO_2 purity than most of the faujasite structures at VSA conditions (89% and 67% for Mg-MOF-74 and Cu-BTC, respectively) but higher than all zeolite structures at PSA process (87% and 63% for Mg-MOF-74 and Cu-BTC, respectively). Higher purity values can be achieved by reducing the void fraction or also by combining several Skarstrom cycles.

For PSA units operating at say 1000 kPa, the screening on the basis of $s_{CO2/N2}$ indicates 96-FAU as the best choice. If we use WC_{CO2} for ranking, then 12-FAU emerges as better choice. However, in terms of CO_2 purity, one should select the 88-FAU structure. A similar disagreement is also observed for VSA processes. This dilemma indicates the need to examine the PSA and VSA operations in more detail.

Fig. 7 shows the number of PSA ($P_{feed.}$ = 3000/1000 kPa) and VSA ($P_{regen.}$ = 10/5 kPa) cycles needed to remove a ton of CO_2 for each structure, and also the adiabatic work per cycle calculated by means of Eqs. (7) and (8), assuming a packed bed with a total volume of 0.1 m^3 and a void fraction of $\varepsilon = 0.4$. As the PSA feeding pressure is raised or the VSA regeneration pressure is decreased, the number of required cycles is lower, but the adiabatic work for pressurizing or swing to vacuum increases. A compromise must be found between a low number of cycles and a moderate energetic cost. Note that, as shown in Fig. 7 (bottom), decreasing the regeneration pressure in a VSA process from 10 to 5 kPa increases the adiabatic work per cycle by 40% approximately. However, Fig. 5 shows that the working capacities at 100–5 kPa are two or even three times greater than those at 100–10 kPa.

Fig. 7 also shows that for structures with low Al content the number of required VSA cycles is much higher than the number of required PSA cycles. Thus, using these structures under VSA conditions is unpractical. In contrast, structures with intermediate and high Al content require a similar number of VSA-100/5 and PSA-3000/100 cycles per ton of CO_2. However, the adiabatic work for compression is much higher than the adiabatic work for evacuating at these conditions, making them more interesting for a VSA process.

Note that in our model we only include operating costs for gas compression and evacuation at the desired pressures. We do not include capital costs of equipment and adsorbent materials. Therefore, we cannot establish a final ranking in terms of total capital costs. Moreover, the costs for previous dehumidification of the flue gas and the costs associated to post-separation (*i.e.,* compression and transport) should also be included for a full evaluation. According to the work by Leperi et al. [86] the operating costs represent close to 45% of the total requirements, while annualized capital costs around 5%, dehumidification around 10% and finally, post-compression and transport around 40%.

3.3.1. Breakthrough curves

Potentiality for CO_2 separation from the ternary mixture considered under dynamic conditions was also studied by simulated breakthrough experiments. The following parameters were used: length of packed bed, L = 0.1 m, (A = 1 m^2); voidage of packed bed, $\varepsilon = 0.4$; superficial gas velocity at inlet, $u = 0.04\ m\ s^{-1}$. When comparing among different materials, the fractional voidage was held constant, implying that the volumes of adsorbent materials used in the fixed bed are the same for all zeolites. Therefore, the total mass of the adsorbents used is governed by the framework density. The transient breakthrough simulation results are presented in terms of a dimensionless time (τ_{break}) defined by dividing the actual time (t) by the contact time, τ ($\tau = L\varepsilon \cdot u^{-1}$).

Fig. 8 presents the breakthrough times as a function of desorption or regeneration pressures, for both PSA and VSA processes. In these simulations, the working capacity of the materials has been taken into account considering saturation times from a non-clean bed, initially containing the quantity of molecules present at the desorption conditions from the previous cycle. An alternative way of performing the breakthrough simulations is considering as initial state a clean bed with no molecules within the framework. Several authors [15,16,61] commonly use the clean bed alternative, although it provides different results, with larger breakthrough times and clearly, resulting in a different adsorbent materials ranking. However, this alternative implies a system where, after each PSA or VSA cycle, a purge of the column is required to push the remaining CO_2 out of the column and hence, consuming a higher amount of energy. The comparison of breakthrough times obtained in both situations can be found in the Section V in the SI.

In PSA, the value of τ_{break} increases when increasing the adsorption pressure up to a maximum value around 1000–2000 kPa, and above that point it starts to decrease. The reason for this increment is because the working capacity of the material is increased as the pressure range is larger, and thus the time for reaching saturation becomes longer. However, at higher

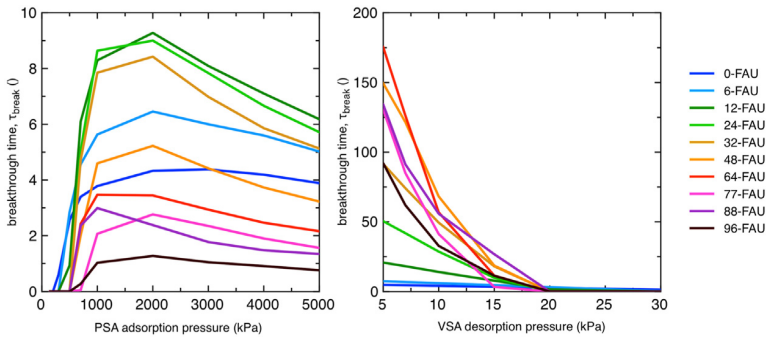

Fig. 8. Dimensionless breakthrough times for a chosen purity of 0.5% CO_2 in the gaseous mixture exiting the adsorber, as a function of adsorption (PSA, left side) and desorption (VSA, right side) pressures. Simulations performed at 313 K. (For interpretation of the references to colour in this figure legend, the reader is referred to the web version of this article.)

adsorption or feeding pressures, the adsorbent reaches saturation faster, and then an increment in the pressure range does not improve the working capacity, resulting in a lower τ_{break} value. On the other hand, in VSA the value of τ_{break} is increased when decreasing the regeneration pressure, due to the higher working capacity. For instance, if a VSA process is considered operating at 100–5 kPa, the following hierarchy for breakthrough times is obtained: 64-FAU > 48-FAU > 88-FAU > 77-FAU > 96-FAU > 32-FAU > 24-FAU > 12-FAU > 6-FAU > 0-FAU. This sequence demonstrates the better separation performance for faujasites with intermediate Al content at these conditions.

3.4. Combined VPSA processes

A convenient procedure for CO_2 adsorption could be a process in which the adsorption step takes place at moderate pressures above atmospheric conditions, where expensive compression units are not required, and desorption is performed under vacuum conditions in order to avoid heating systems [66]. This is called VPSA process, and it can have even more chances of commercial application because of the low energy demand. Fig. 9 shows the working capacity and the adiabatic work required for selected faujasite structures as a function of different $P_{feed.}/P_{regen.}$

We have selected 5 different pressure conditions ranging from 100/5 kPa (pure VSA) to 2000/100 kPa (pure PSA) in such a way that the $P_{feed.}/P_{regen.}$ ratio is constant. The reason is that the adiabatic cost of compression/expansion mostly depends on this ratio (as suggested by Eqs. (7) and (8)). It can be observed that the working capacity strongly depends on the selected conditions, with values up to 1.43–1.47 kg mol^{-1} for 24-FAU, 32-FAU and 48-FAU structures. In fact, at these conditions all three structures present higher working capacities than zeolite Ca-A, whose value at 400/20 kPa is around 0.77. Fig. 9 also shows that the separation performance for 24-FAU and 32-FAU structures operating at 1000/50 kPa is remarkably good, as well as for 48-FAU structure operating at 400/20 kPa. At these conditions, the ratio between working capacity and adiabatic cost for all the three structures is very high, with potential use in industrial applications. Moreover, it can be seen that the VPSA performance of the commonly used Faujasite 13X structure (here 88-FAU) is quite bad compared to previous ones. Apart from presenting a smaller working capacity, it requires more power consumption at these conditions. The main reason is that, for this structure, the total amount of moles adsorbed (N_{TOT}^{ads} in Eq. (8)) is very high. This increases the required adiabatic work for expansion, as seen in Fig. 9.

4. Conclusions

Results shown in the present work demonstrate the strong influence of faujasite Si/Al ratio on the post-combustion CO_2 capture by adsorption in dehumidified streams. Ten faujasite structures with different Al content have been evaluated in detail for potential application in Swing Adsorption processes, by computing both pure and mixture adsorption isotherms for CO_2, N_2 and O_2. Among the materials assessed, 96-FAU in which Si/Al ratio equals to 1, presents the highest selectivity towards CO_2 and

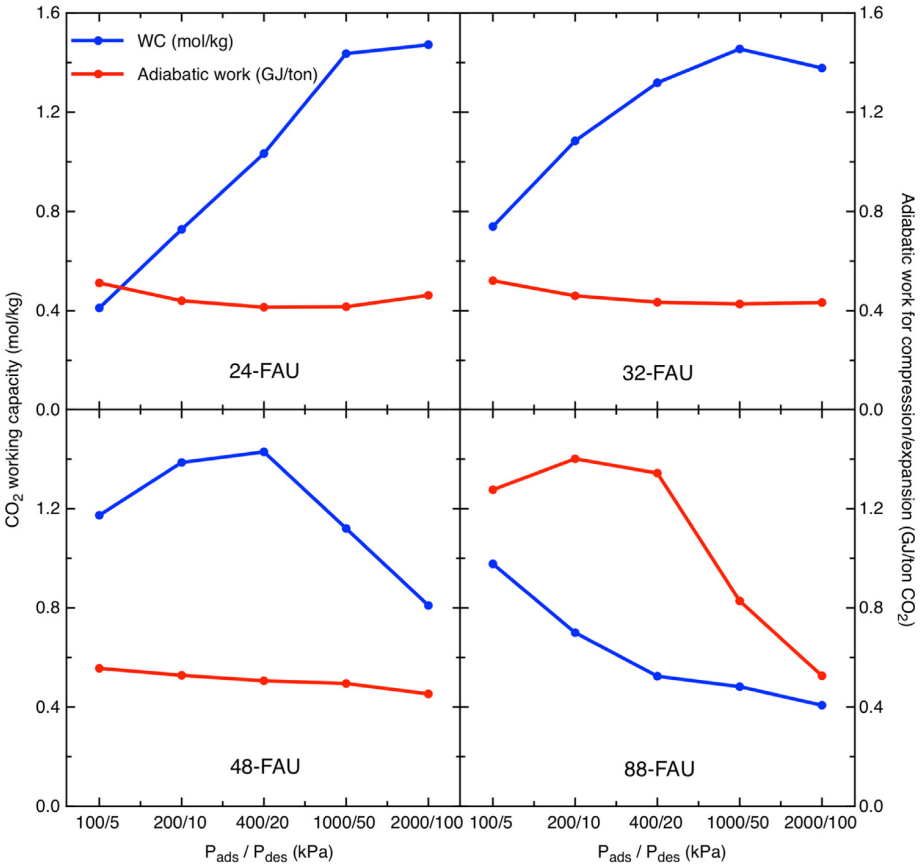

Fig. 9. Blue lines represent the CO_2 working capacity as a function of the VPSA adsorption ($P_{feed.}$) and desorption ($P_{regen.}$) pressures at 313 K. Red lines represent the adiabatic work required for compression/expansion (vacuum) to remove a ton of CO_2 assuming a packed bed with a total volume of 0.1 m^3 and void fraction of $\varepsilon = 0.4$. (For interpretation of the references to colour in this figure legend, the reader is referred to the web version of this article.)

isosteric heat of adsorption, but saturates at low pressures. Conversely, 0-FAU in which Si/Al ratio equals to ∞, presents the lowest selectivity and isosteric heat of adsorption, but allows capturing more CO_2 molecules at higher pressures. However, it turns out that structures with intermediate Al content present the greatest potential towards post-combustion CO_2 capture. Moreover, the potential separation of each structure strongly depends on the working range. For instance, in a VSA unit operating at 100–5 kPa (*i.e.*, $P_{feed.}$-$P_{regen.}$) 48-FAU and 64-FAU structures show the maximum working capacity, while in a PSA unit operating at 3000–100 kPa the best adsorbent materials in terms of working capacity are 12-FAU and 24-FAU structures. On the other hand, CO_2 purity at outlet of the adsorber may be an important variable, especially if it is necessary to reuse CO_2 in other applications. In this case, 88-FAU structure operating in a VSA system emerges as the better choice, with CO_2 purity up to 96%.

Dynamic breakthrough calculations for all the structures have been also computed both for PSA and VSA systems in a wide range of pressures. The breakthrough time obtained, that combines working capacity and selectivity, is considered as the final criterion for adsorbent selection. Our results confirm that 48-FAU and 64-FAU structures are the best adsorbent materials evaluated for VSA applications, while 12-FAU and 24-FAU structures are the top ones for PSA applications, in agreement with the analysis in terms of the working capacity.

Additionally, we have tested the separation performance for all the faujasite structures in different hybrid VPSA systems. The working capacity and the required adiabatic work for compression and expansion (vacuum) have been calculated for all structures at several pressure conditions, keeping constant the $P_{feed.}/P_{regen.}$ ratio at 20. In this way, we were able to determine which are the most optimal conditions for each structure (*i.e.*, high working capacities for low energy consumption). Our results show that 24-FAU, 32-FAU and 48-FAU present extremely good separation ability under VPSA conditions, outperforming by far the commonly used Faujasite 13X structure.

Finally, the present methodology allows the performance evaluation of different adsorbent materials at more realistic conditions than those found in literature. Selectivities and working capacities have been obtained from the ternary mixture adsorption isotherms, instead of pure adsorption ones. Additionally, for working capacity calculations, we have taken into account that at desorption conditions, the recovered CO_2 is not completely pure. Thus, instead of using the uptake at desorption pressure from the pure CO_2 adsorption isotherm, we calculate the real uptake at desorption conditions. Moreover, breakthrough simulations found in literature are usually computed starting from a clean bed with no molecules within the framework. However, at each PSA or VSA cycle, there is a remaining number of adsorbed molecules that are not desorbed during the desorption step. Thus, we have performed the dynamic breakthrough calculations by starting from a bed which already contains the quantity of molecules present at the desorption conditions. This model represents a further step for adsorbent selection and provides important guidelines for future screening and for designing novel materials.

Acknowledgments

Financial support to this research has been provided by the Spanish Ministry of Economy and Competitiveness (project number CTQ2014-53987-R) and, in part, from the Generalitat de Catalunya (project number 2014SGR1582). HPG thanks Generalitat de Catalunya for a predoctoral FI-DGR-2015 grant. PG thanks Generalitat de Catalunya for his Serra Húnter Associate Professorship. Computational resources provided by Consorci de Serveis Universitaris de Catalunya (CSUC, former CESCA) are gratefully acknowledged. With all the love PG wants to dedicate this study to his loved Pablo, Maria and Patricia, his best adsorbent materials.

Appendix A. Supplementary data

Supplementary data associated with this article can be found, in the online version, at http://dx.doi.org/10.1016/j.jcou.2017.03.007.

References

[1] D.Y.C. Leung, G. Caramanna, M.M. Maroto-Valer, An overview of current status of carbon dioxide capture and storage technologies, Renew. Sustain. Energy Rev. 39 (2014) 426–443.
[2] B.P. Spigarelli, S.K. Kawatra, Opportunities and challenges in carbon dioxide capture, J. CO_2 Util. 1 (2013) 69–87.
[3] N. MacDowell, N. Florin, A. Buchard, J. Hallett, A. Galindo, G. Jackson, C.S. Adjiman, C.K. Williams, N. Shah, P. Fennell, An overview of CO2 capture technologies, Energy Environ. Sci. 3 (2010) 1645–1669.
[4] R.M. Cuéllar-Franca, A. Azapagic, Carbon capture, storage and utilisation technologies: a critical analysis and comparison of their life cycle environmental impacts, J. CO_2 Util. 9 (2015) 82–102.
[5] N. Hedin, L. Andersson, L. Bergstrom, J. Yan, Adsorbents for the post-combustion capture of CO2 using rapid temperature swing or vacuum swing adsorption, Appl. Energy 104 (2013) 418–433.
[6] J. Čejka, H. van Bekkum, A. Corma, F. Schuth, Introduction to Zeolite Science and Practice, third ed., Elsevier, Amsterdam, 2007.
[7] S. Chu, Carbon capture and sequestration, Science 325 (2009) 1599.
[8] E.J. Granite, H.W. Pennline, Photochemical removal of mercury from flue gas, Ind. Eng. Chem. Res. 41 (2002) 5470–5476.
[9] K. Sumida, D.L. Rogow, J.A. Mason, T.M. McDonald, E.D. Bloch, Z.R. Herm, T.H. Bae, J.R. Long, Carbon dioxide capture in metal-organic frameworks, Chem. Rev. 112 (2012) 724–781.
[10] L. Lin, A.H. Berger, R.L. Martin, J. Kim, J.A. Swisher, K. Jariwala, C.H. Rycroft, A.S. Bhown, M.W. Deem, M. Haranczyk, B. Smit, In silico screening of carbon-capture materials, Nat. Mater. 11 (2012) 633–641.
[11] J.M. Huck, L. Lin, A.H. Berger, M.N. Shahrak, R.L. Martin, A.S. Bhown, M. Haranczyk, K. Reuter, B. Smit, Evaluating different classes of porous materials for carbon capture, Energy Environ. Sci. 7 (2014) 4132–4146.
[12] C.A. Grande, R.P.L. Ribeiro, E.L.G. Oliveira, A.E. Rodrigues, Electric swing adsorption as emerging CO2 capture technique, Energy Procedia 1 (2009) 1219–1225.
[13] R. Ribeiro, C.A. Grande, A.E. Rodrigues, Electric swing adsorption for gas separation and purification: a review, Sep. Sci. Technol. 49 (2014) 1985–2002.
[14] S. Sircar, Basic research needs for design of adsorptive gas separation processes, Ind. Eng. Chem. Res. 45 (2006) 5435–5448.
[15] T.H. Bae, M.R. Hudson, J.A. Mason, W.L. Queen, J.J. Dutton, K. Sumida, K.J. Micklash, S.S. Kaye, C.M. Brown, J.R. Long, Evaluation of cation-exchanged zeolite adsorbents for post-combustion carbon dioxide capture, Energy Environ. Sci. 6 (2013) 128–138.
[16] J.A. Mason, K. Sumida, Z.R. Herm, R. Krishna, J.R. Long, Evaluating metal-organic frameworks for post-combustion carbon dioxide capture via temperature swing adsorption, Energy Environ. Sci. 4 (2011) 3030–3040.
[17] M.A. Granato, T.J.H. Vlugt, A.E. Rodrigues, Molecular simulation of propane-propylene binary adsorption equilibrium in zeolite 13X, Ind. Eng. Chem. Res. 46 (2007) 7239–7245.
[18] D. Ko, R. Siriwardane, L. Biegler, Optimization of pressure swing adsorption and fractionated vacuum pressure swing adsorption processes for CO2 capture, Ind. Eng. Chem. Res. 44 (2005) 8084–8094.
[19] P. Xiao, J. Zhang, P. Webley, G. Li, R. Singh, R. Todd, Capture of CO2 from flue gas streams with zeolite 13X by vacuum-pressure swing adsorption, Adsorption 14 (2008) 575–582.
[20] I. Matito-Martos, A. Martin-Calvo, J.J. Gutierrez-Sevillano, M. Haranczyk, M. Doblare, J.B. Parra, C.O. Ania, S. Calero, Zeolite screening for the separation of gas mixtures containing SO2, CO2 and CO, Phys. Chem. Chem. Phys. 16 (2014) 19884–19893.
[21] N.A. Rashidi, S. Yusup, An overview of activated carbons utilization for the post-combustion carbon dioxide capture, J. CO_2 Util. 13 (2016) 1–16.
[22] J. Liu, P.K. Thallapally, B.P. McGrail, D.R. Brown, J. Liu, Progress in adsorption-based CO2 capture by metal-organic frameworks, Chem. Soc. Rev. 41 (2012) 2308–2322.
[23] Z. Zhang, Z.Z. Yao, S. Xiang, B. Chen, Perspective of microporous metal-organic frameworks for CO2 capture and separation, Energy Environ. Sci. 7 (2014) 2868–2899.
[24] J. Ling, A. Ntiamoah, P. Xiao, D. Xu, P.A. Webley, Y. Zhai, Overview of CO2 capture from flue gas streams by vacuum pressure swing adsorption technology, Austin J. Chem. Eng. 1 (2014) 1–7.
[25] Y. He, W. Zhou, R. Krishna, B. Chen, Microporous metal-organic frameworks for storage and separation of small hydrocarbons, Chem. Commun. 48 (2012) 11813–11831.
[26] Y.Q. Lan, H.L. Jiang, S.L. Li, Q. Xu, Mesoporous metal-organic frameworks with size-tunable cages: selective CO2 uptake, encapsulation of Ln3+ cations for luminescence, and column-chromatographic dye separation, Adv. Mater. 23 (2011) 5015–5020.

[27] H.L. Jiang, D. Feng, K. Wang, Z.Y. Gu, Z. Wei, Y.P. Chen, H.C. Zhou, An exceptionally stable, porphyrinic Zr metal-organic framework exhibiting pH-dependent fluorescence, J. Am. Chem. Soc. 135 (2013) 13934–13938.
[28] P.L. Llewellyn, G. Maurin, Chapter 17–Gas adsorption in zeolites and related materials, Stud. Surf. Sci. Catal. 168 (2007) 555–610.
[29] M. Palomino, A. Corma, F. Rey, S. Valencia, New insights on CO2-methane separation using LTA zeolites with different Si/Al ratios and a first comparison with MOFs, Langmuir 26 (2010) 1910–1917.
[30] R. Banerjee, A. Phan, B. Wang, C. Knobler, H. Furukawa, M. O'Keeffe, O.M. Yaghi, High-throughput synthesis of zeolitic imidazolate frameworks and application to CO2 capture, Science 319 (2008) 939–943.
[31] Y.S. Bae, R.Q. Snurr, Development and evaluation of porous materials for carbon dioxide separation and capture, Angew. Chem. Int. Ed. 50 (2011) 11586–11596.
[32] Y. Li, J. Yu, New stories of zeolite structures: their descriptions, determinations, predictions, and evaluations, Chem. Rev. 14 (2014) 7268–7316.
[33] M.E. Davis, Ordered porous materials for emerging applications, Nature 417 (2002) 813–821.
[34] C. Martínez, A. Corma, Inorganic molecular sieves: preparation, modification and industrial application in catalytic processes, Coord. Chem. Rev. 255 (2011) 1558–1580.
[35] D.H. Olson, The crystal structure of dehydrated NaX, Zeolites 15 (1995) 439–443.
[36] A. Corma, From microporous to mesoporous molecular sieve materials and their use in catalysis, Chem. Rev. 97 (1997) 2373–2420.
[37] D.M. Ruthven, Diffusion of linear paraffins and cyclohexane in NaX and 5A zeolite crystals, Zeolites 8 (1988) 472–479.
[38] I. Daems, P. Leflaive, A. Methivier, G.V. Baron, J.F.M. Denayer, Influence of Si:Al-ratio of faujasites on the adsorption of alkanes, alkenes and aromatics, Microporous Mesoporous Mater. 96 (2006) 149–156.
[39] W. Löwenstein, The distribution of aluminum in the tetrahedra of silicates and aluminates, Am. Mineral. 39 (1954) 92–96.
[40] S. Calero, D. Dubbeldam, R. Krishna, B. Smit, T.J.H. Vlugt, J.F.M. Denayer, J.A. Martens, T.L.M. Maesen, Understanding the role of sodium during adsorption: a force field for alkanes in sodium-exchanged faujasites, J. Am. Chem. Soc. 126 (2004) 11377–11386.
[41] A. Martin-Calvo, J.B. Parra, C.O. Ania, S. Calero, Insights on the anomalous adsorption of carbon dioxide in LTA zeolites, J. Phys. Chem. C 118 (2014) 25460–25467.
[42] A.O. Yazaydin, R.W. Thompson, Molecular simulation of water adsorption in silicalite: effect of silanol groups and different cations, Micropor. Mesopor. Mat 123 (2009) 169–176.
[43] R.S. Pillai, S.A. Peter, R.V. Jasra, CO2 and N2 adsorption in alkali metal ion exchanged X-Faujasite: grand canonical Monte Carlo simulation and equilibrium adsorption studies, Microporous Mesoporous Mater. 162 (2012) 143–151.
[44] G. Maurin, Y. Belmabkhout, G. Pirngruber, L. Gaberova, P. Llewellyn, CO2 adsorption in LiY and NaY at high temperature: molecular simulations compared to experiments, Adsorption 13 (2007) 453–460.
[45] W. Louisfrema, B. Rotenberg, F. Porcher, J.L. Paillaud, P. Massiani, A. Boutin, Cation redistribution upon dehydration of Na58Y faujasite zeolite: a joint neutron diffraction and molecular simulation study, Mol. Sim. 41 (2015) 1371–1378.
[46] D. Frenkel, B. Smit, Understanding Molecular Simulation: from Algorithms to Applications, Academic Press, London, 2002.
[47] S. Plimpton, Fast parallel algorithms for short-range molecular dynamics, J. Comp. Phys. 117 (1995) 1–19.
[48] J.A. Ritter, A.D. Ebner, Carbon Dioxide Separation Technology: R&D Needs for the Chemical and Petrochemical Industries, (2007) www.eere.energy.gov/manufacturing/pdfs/co2_separation_report_v2020.pdf, (accessed 05 September 2016).
[49] D.Y. Peng, D.B. Robinson, A new two-constant equation of state, Ind. Eng. Chem. Fundam. 15 (1976) 59–64.
[50] E.W. Lemmon, M.O. McLinden, M.L. Huber, NIST Thermodynamic Properties of Refrigerants and Refrigerants Mixtures Database (REFPROP), Version 7.0, (2002) .
[51] S.K. Shibata, S.I. Sandler, Critical evaluation of equation of state mixing rules for the prediction of high-pressure phase equilibria, Ind. Eng. Chem. Res. 28 (1989) 1893–1898.
[52] J. Vrabec, G.K. Kedia, U. Buchhauser, R. Meyer-Pittroff, H. Hasse, Thermodynamic models for vapor-liquid equilibria of nitrogen + oxygen + carbon dioxide at low temperatures, Cryogenics 49 (2009) 72–79.
[53] A. Garcia-Sánchez, C.O. Ania, J.B. Parra, D. Dubbeldam, T.J.H. Vlugt, R. Krishna, S. Calero, Transferable force field for carbon dioxide adsorption in zeolites, J. Phys. Chem. C 113 (2009) 8814–8820.
[54] A. Martin-Calvo, J.J. Gutiérrez-Sevillano, J.B. Parra, C.O. Ania, S. Calero, Transferable force fields for adsorption of small gases in zeolites, Phys. Chem. Chem. Phys. 17 (2015) 24048–24055.
[55] T.J.H. Vlugt, E. García-Pérez, D. Dubbeldam, S. Ban, S. Calero, Computing the heat of adsorption using molecular simulations: the effect of strong coulombic interactions, J. Chem. Theory Comput. 4 (2008) 1107–1118.
[56] R. Krishna, J.M. van Baten, Investigating the potential of Mg-MOF74 membranes for CO2 capture, J. Membr. Sci. 377 (2011) 249–260.
[57] A.N. Dickey, A.O. Yazaydin, R.R. Willis, R.Q. Snurr, Screening CO2/N2 selectivity in metal-organic frameworks using monte carlo simulations and ideal adsorbed solution theory, Can. J. Chem. Eng. 90 (2012) 825–832.
[58] Y.G. Chung, D.A. Gómez-Gualdrón, P. Li, K.T. Leperi, P. Deria, H. Zhang, N.A. Vermuelen, J.F. Stoddart, F. You, J.T. Hupp, O.K. Farha, R.Q. Snurr, In silico discovery of metal-organic frameworks for precombustion CO2 capture using a genetic algorithm, Sci. Adv. 2 (2016) 1–9.
[59] X. Shao, Z. Feng, R. Xue, C. Ma, W. Wang, X. Peng, D. Cao, Adsorption of CO2, CH4, CO2/N2 and CO2/CH4 in novel activated carbon beads: preparation, measurements and simulation, AIChE J. 57 (2011) 3042–3051.
[60] Z. Hu, M. Khurana, Y.H. Seah, M. Zhang, Z. Guo, D. Zhao, Ionized Zr-MOFs for highly efficient post-combustion CO2 capture, Chem. Eng. Sci. 124 (2015) 61–69.
[61] S. Xiang, Y. He, Z. Zhang, H. Wu, W. Zhou, R. Krishna, B. Chen, Microporous metal-organic framework with potential for carbon dioxide capture at ambient conditions, Nat. Commun. 3 (2012) 954.
[62] A.H. Berger, A.S. Bhown, Comparing physisorption and chemisorption solid sorbents for use separating CO2 from flue gas using temperature swing adsorption, Energy Proc. 4 (2011) 562–567.
[63] D. Wiersum, J.S. Chang, C. Serre, P.L. Llewellyn, An adsorbent performance indicator as a first step evaluation of novel sorbents for gas separations: application to metal-organic frameworks, Langmuir 29 (2013) 3301–3309.
[64] M.S.A. Baksh, F. Notaro, Method for production of nitrogen using oxygen selective adsorbents, US Patent 5735938, 1998.
[65] S.U. Rege, R.T. Yang, A simple parameter for selecting an adsorbent for gas separation by pressure swing adsorption, Sep. Sci. Technol. 36 (2001) 3355–3365.
[66] Z. Liu, C.A. Grande, P. Li, J. Yu, A.E. Rodrigues, Multi-bed vacuum pressure swing adsorption for carbon dioxide capture from flue gas, Sep. Purif. Technol. 81 (2011) 307–317.
[67] R. Kumar, Pressure swing adsorption process: performance optimum and adsorbent selection, Ind. Eng. Chem. Res. 33 (1994) 1600–1605.
[68] M.T. Ho, G.W. Allinson, D.E. Wiley, Reducing the cost of CO2 capture from flue gases using pressure swing adsorption, Ind. Eng. Chem. Res. 47 (2008) 4883–4890.
[69] L. Bastin, P.S. Barcia, E.J. Hurtado, J.A.C. Silva, A.E. Rodrigues, B. Chen, A microporous metal-organic framework for separation of CO2/N2 and CO2/CH4 by fixed-bed adsorption, J. Phys. Chem. C 112 (2008) 1575–1581.
[70] P.D. Jadhav, S.S. Rayalu, R.B. Biniwale, S. Devotta, CO2 emission and its mitigation by adsorption of zeolites and activated carbon, Curr. Sci. 92 (2007) 724–726.
[71] R. Krishna, J.R. Long, Screening metal-organic frameworks by analysis of transient breakthrough of gas mixtures in a fixed bed adsorber, J. Phys. Chem. C 115 (2011) 12941–12950.
[72] Y. He, R. Krishna, B. Chen, Metal-organic frameworks with potential for energy-efficient adsorptive separation of light hydrocarbons, Energy Environ. Sci. 5 (2012) 9107–9120.
[73] H. Wu, K. Yao, Y. Zhu, B. Li, Z. Shi, R. Krishna, J. Li, Cu-TDPAT, an rht-type dual-functional metal-organic framework offering significant potential for use in H2 and natural gas purification processes operating at high pressures, J. Phys. Chem. C 116 (2012) 16609–16618.
[74] R. Krishna, R. Baur, Modelling issues in zeolite based separation processes, Sep. Purif. Technol. 33 (2003) 213–254.
[75] A.L. Myers, J.M. Prausnitz, Thermodynamics of mixed-gas adsorption, AIChE 11 (1965) 121–127.
[76] C.W. Skarstrom, Method and apparatous for fractionating gaseous mixtures by adsorption, US Patent 2944627, 1960.
[77] Y. Chung, B.K. Na, H.K. Song, Short-cut evaluation of pressure swing adsorption systems, Comput. Chem. Eng. 22 (1998) S637–S640.
[78] W.K. Choi, T.I. Kwon, Y.K. Yeo, H. Lee, B.K. Na, H.K. Song, Optimal operation of the pressure swing adsorption (PSA) process for CO2 recovery, Korean J. Chem. Eng. 20 (2003) 617–623.
[79] A.L. Chaffee, G.P. Knowles, Z. Liang, J. Zhang, P. Xiao, P.A. Webley, CO2 capture by adsorption: materials and process development, Int. J. Green. Gas Control. 1 (2007) 11–18.
[80] L. Riboldi, O. Bolland, J.M. Ngoy, N. Wagner, Full-plant analysis of a PSA CO2 capture unit integrated in coal-fired power plants: post- and pre-combustion scenarios, Energy Procedia 63 (2014) 2289–2304.
[81] D. Bahamon, L.F. Vega, Systematic evaluation of materials for post-combustion CO2 capture in a temperature swing adsorption process, Chem. Eng. J. 284 (2016) 438–447.
[82] S. Cavenati, C.A. Grande, A.E. Rodrigues, Adsorption equilibrium of methane, carbon dioxide, and nitrogen on zeolite 13X at high pressures, J. Chem. Eng. Data. 49 (2004) 1095–1101.
[83] O. Talu, Measurements and analysis of mixture adsorption equilibrium in porous solids, Chem. Ing. Technol. 83 (2011) 67–82.
[84] V.G. Gomes, K.W.K. Yee, Pressure swing adsorption for carbon dioxide sequestration from exhaust gases, Separ. Purif. Technol. 28 (2002) 161–171.
[85] L. Joos, J.M. Huck, V. Van Speybroeck, B. Smit, Cutting the cost of carbon capture: a casa for carbon capture and utilization, Faraday Discuss. 192 (2016) 391.
[86] K.T. Leperi, R.Q. Snurr, F. You, Optimization of two-stage pressure/vacuum swing adsorption with variable dehydration level for postcombustion carbon capture, Ing. Eng. Chem. Res. 55 (2016) 3338–3359.

Supplementary Information

Optimal Faujasite structures for post combustion CO_2 capture and separation in different swing adsorption processes

Hèctor Prats, Daniel Bahamon, Gerard Alonso, Xavier Giménez, Pablo Gamallo* and Ramón Sayós

Departament de Ciència de Materials i Química Física & Institut de Química Teòrica i Computacional (IQTCUB), Universitat de Barcelona, C. Martí i Franquès 1, 08028 Barcelona, Spain.

**Corresponding author: Pablo Gamallo*
Email: gamallo@ub.edu / Tel. +34934034760

I. Force field parameters and validation

The following tables contain the force field parameters used in this work for the GCMC simulations.

Molecule		ε/k_B (K)	σ (Å)	q (e^-)	Bond length (Å)
CO_2	C_{CO2}	29.933	2.745	0.6512	1.149 (C-O)
	O_{CO2}	85.671	3.017	-0.3256	
N_2	N_{N2}	38.298	3.306	-0.4050	0.55 (N-X)
	X_{N2}	-	-	0.8100	
O_2	O_{O2}	53.023	3.045	-0.1120	0.60 (O-X)
	X_{O2}	-	-	0.2240	

Table S1. Lennard-Jones and Coulomb parameters for adsorbate-adsorbate interactions used in this work. Dummy atoms, labelled with X, are used to reproduce the quadrupole moments of the molecules. We use reported models for carbon dioxide [1] nitrogen [2] and oxygen [2] molecules.

	$O_{zeolite}$		Na^+	
	ε/k_B (K)	σ (Å)	ε/k_B (K)	σ (Å)
C_{CO2}	37.595	3.511	362.292	3.320
O_{CO2}	78.980	3.237	200.831	2.758
N_{N2}	60.58	3.261	225.568	2.766
O_{O2}	65.189	3.129	241.284	2.060
Na^+	23.000	3.400	-	-

Table S2. Lennard-Jones parameters for faujasite-adsorbate interactions used in this work. These parameters have been taken from the force field developed by Calero *et al*.[1,2]

Atom	q (e^-)
Si	0.78598
Al	0.48598
O_{Si-Si}	-0.39299
O_{Si-Al}	-0.41384
Na^+	0.38340

Table S3. Partial charges for faujasite atoms and sodium cations used in this work. These parameters have been taken from the force field developed by Calero *et al*.[1,2]

These parameters have been proved to accurately reproduce the experimental adsorption properties for CO_2, N_2 and O_2 molecules (among others) in many different zeolite framework types, at cryogenic and high temperatures. Moreover, they are applicable to all possible Si/Al ratios, with sodium atoms as extra-framework cations.

However, we have performed some preliminary calculations in order to verify that these parameters have been well implemented within the LAMMPS code. Figure S1 shows the comparison of computed and experimental adsorption isotherms taken from the works of Dunne *et al*. [3] and Maurin *et al*. [4]

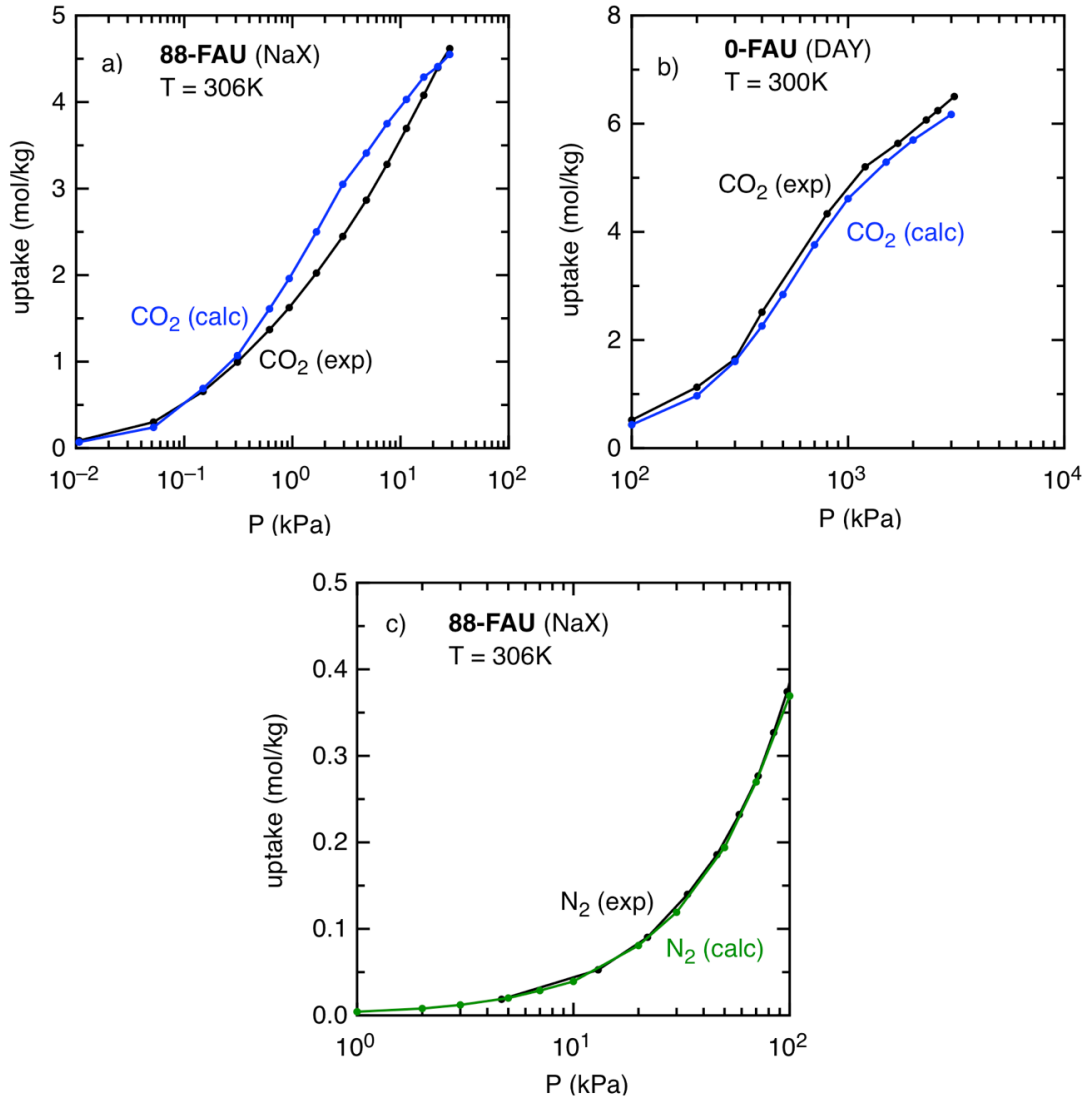

Figure S1. Comparison of our simulated (color lines) and experimental (black lines) adsorption isotherms for pure CO_2 (blue) and N_2 (green). The experimental isotherms are taken from a) Dunne *et al*., corresponding to the 88-FAU structure at 306 K, commonly named NaX in the literature; b) Maurin *et al*., corresponding to the 0-FAU structure at 300 K, commonly named DAY in the literature; and c) Dunne *et al*., from the same reference than Figure S1a).

II. Langmuir-Freundlich pure fitting parameters

CO_2	0-FAU	6-FAU	12-FAU	24-FAU	32-FAU	48-FAU	64-FAU	77-FAU	88-FAU	96-FAU
$N_{k,sat}$ (kmol·m^{-3})	7.61	7.88	8.26	8.63	8.67	8.70	8.46	8.16	7.80	7.58
b_k (kPa$^{-\nu_k}$)	0.00	0.00	0.00	0.01	0.02	0.05	0.16	0.30	0.52	0.67
ν_k	1.48	1.33	1.06	0.90	0.83	0.80	0.69	0.61	0.55	0.62
N_2	0-FAU	6-FAU	12-FAU	24-FAU	32-FAU	48-FAU	64-FAU	77-FAU	88-FAU	96-FAU
$N_{k,sat}$ (kmol·m^{-3})	7.86	7.63	7.55	6.98	7.08	6.89	6.52	6.45	6.52	6.35
b_k (kPa$^{-\nu_k}$)	0.00	0.00	0.00	0.00	0.00	0.00	0.00	0.00	0.00	0.00
ν_k	1.02	1.02	1.01	1.01	0.99	0.97	0.97	0.94	0.90	0.90
O_2	0-FAU	6-FAU	12-FAU	24-FAU	32-FAU	48-FAU	64-FAU	77-FAU	88-FAU	96-FAU
$N_{k,sat}$ (kmol·m^{-3})	10.36	9.19	9.18	8.10	8.29	8.45	7.51	7.57	6.44	6.79
b_k (kPa$^{-\nu_k}$)	0.00	0.00	0.00	0.00	0.00	0.00	0.00	0.00	0.00	0.00
ν_k	1.02	1.03	1.03	1.05	1.04	1.03	1.04	1.03	1.07	1.05

Table S4. Langmuir-Freundlich fitting parameters from the pure isotherms used for evaluating costs.

III. Pure component adsorption isotherms for N_2 and O_2

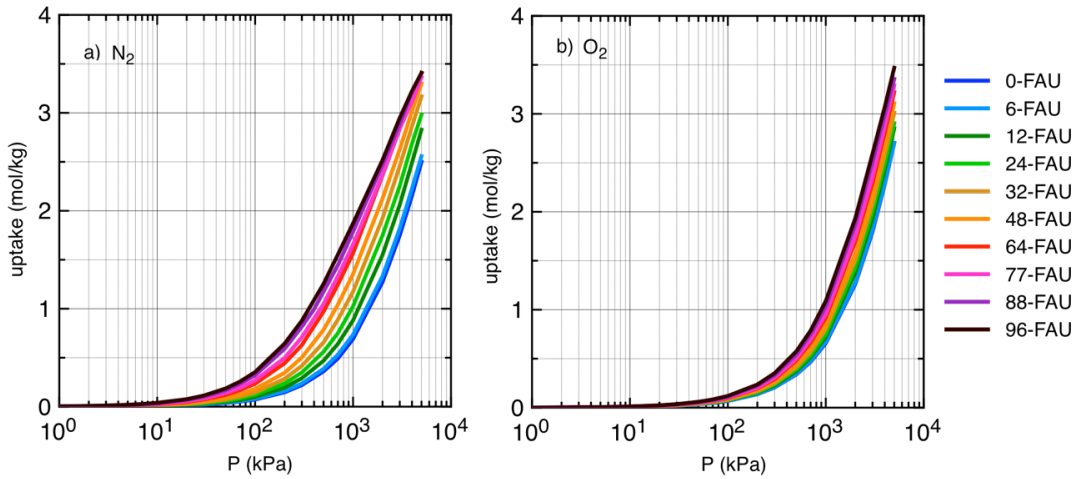

Figure S2. Pure adsorption isotherms for a) N_2 and b) O_2 for the ten different faujasite structures at 313 K studied in the present work.

IV. Ternary mixture isotherms

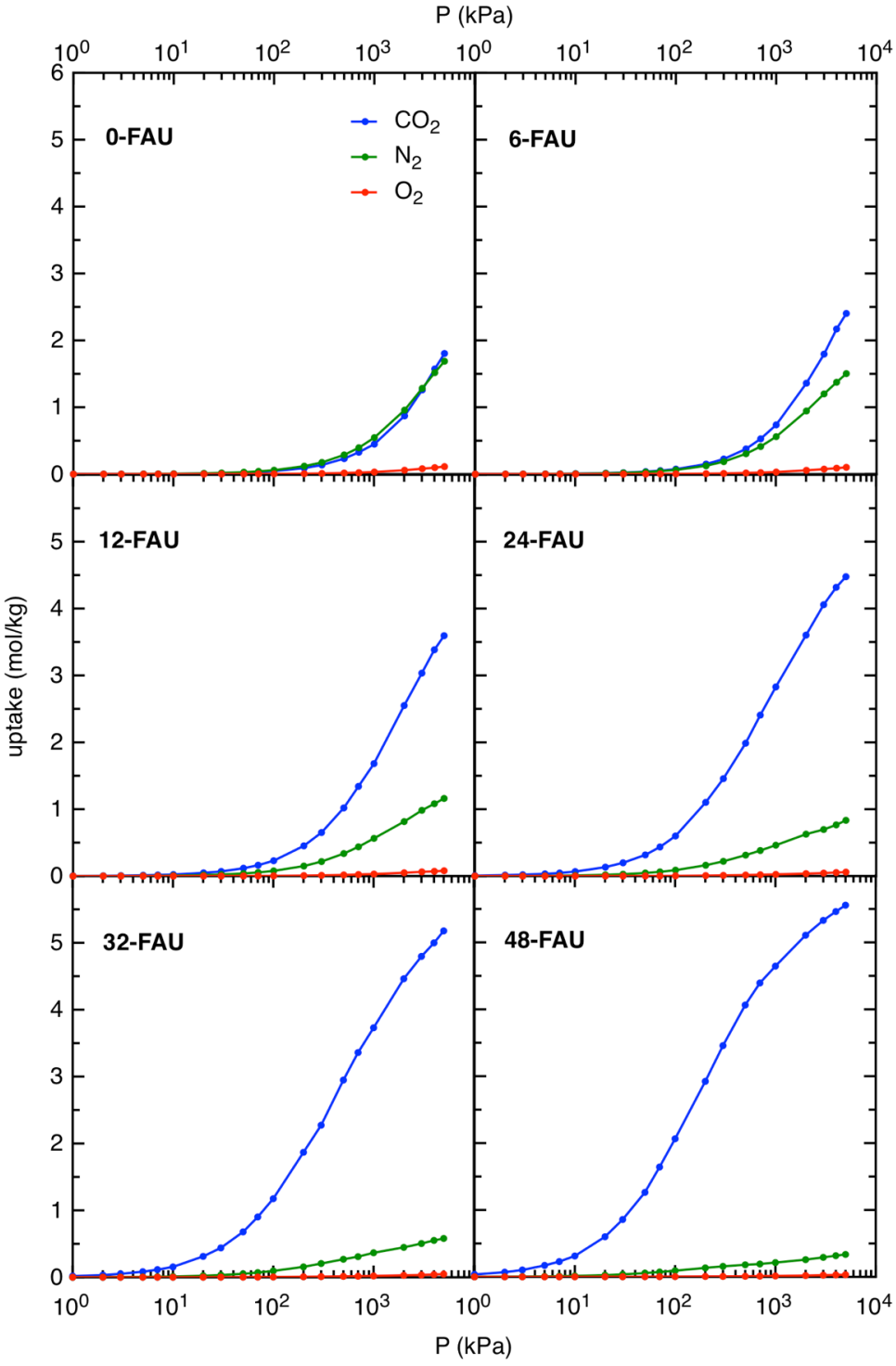

Figure S3-1. Computed adsorption isotherms for the ternary mixtures (*i.e.,* 80% N_2, 15% CO_2 and 5% O_2) in the ten different faujasite structures considered at 313 K.

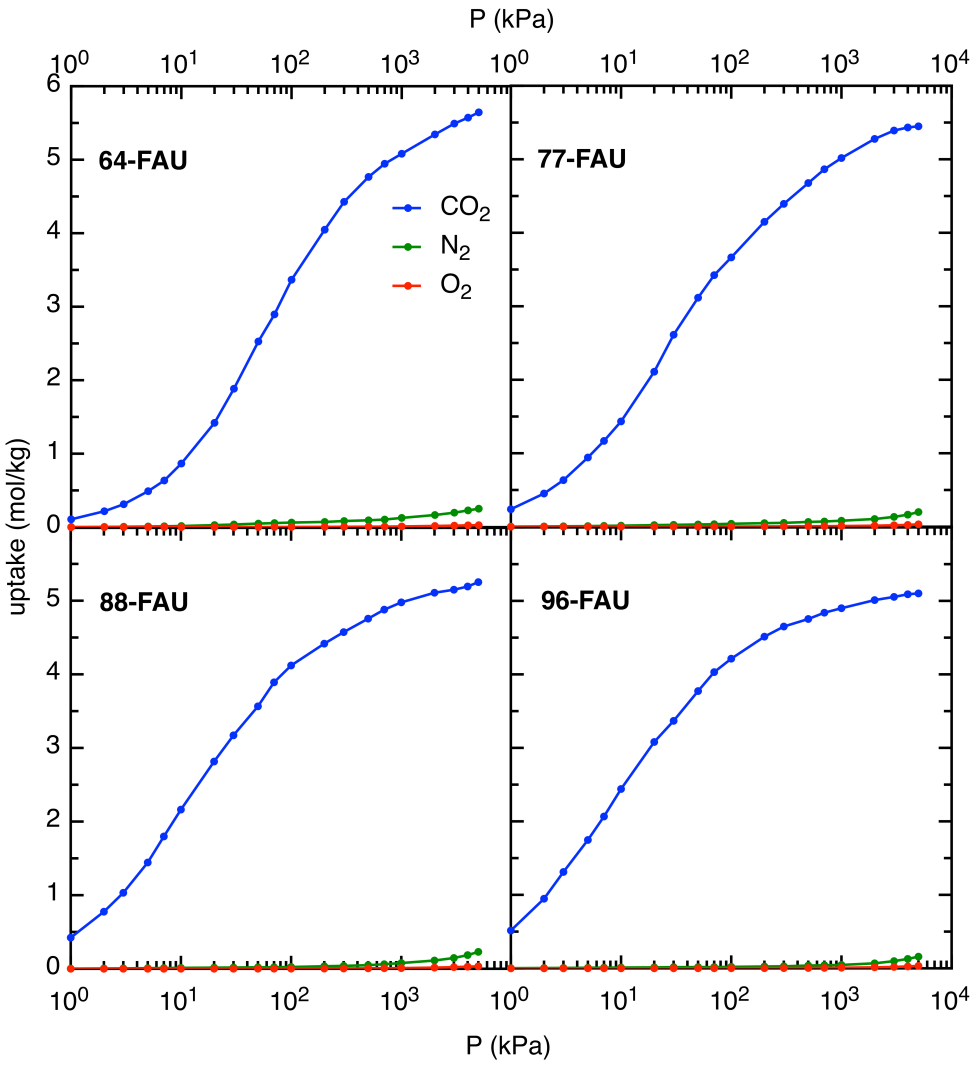

Figure S3-2. Computed adsorption isotherms for the ternary mixtures (*i.e.,* 80% N_2, 15% CO_2 and 5% O_2) in the ten different faujasite structures considered at 313 K.

V. Breakthrough curves

Breakthrough simulations found in the literature are usually computed starting from a clean bed with no molecules within the framework (Figures S4a and S5a). However, at each PSA or VSA cycle, there is a remaining number of adsorbed molecules that are not desorbed during the desorption step ($P_{regen.}$). Thus, when the next adsorption cycle starts again, the bed is not fully clean. In order to better estimate the PSA or VSA costs, we have performed those simulations by starting from a bed which contains the quantity of molecules present at the desorption conditions (Figures S4b and S5b).

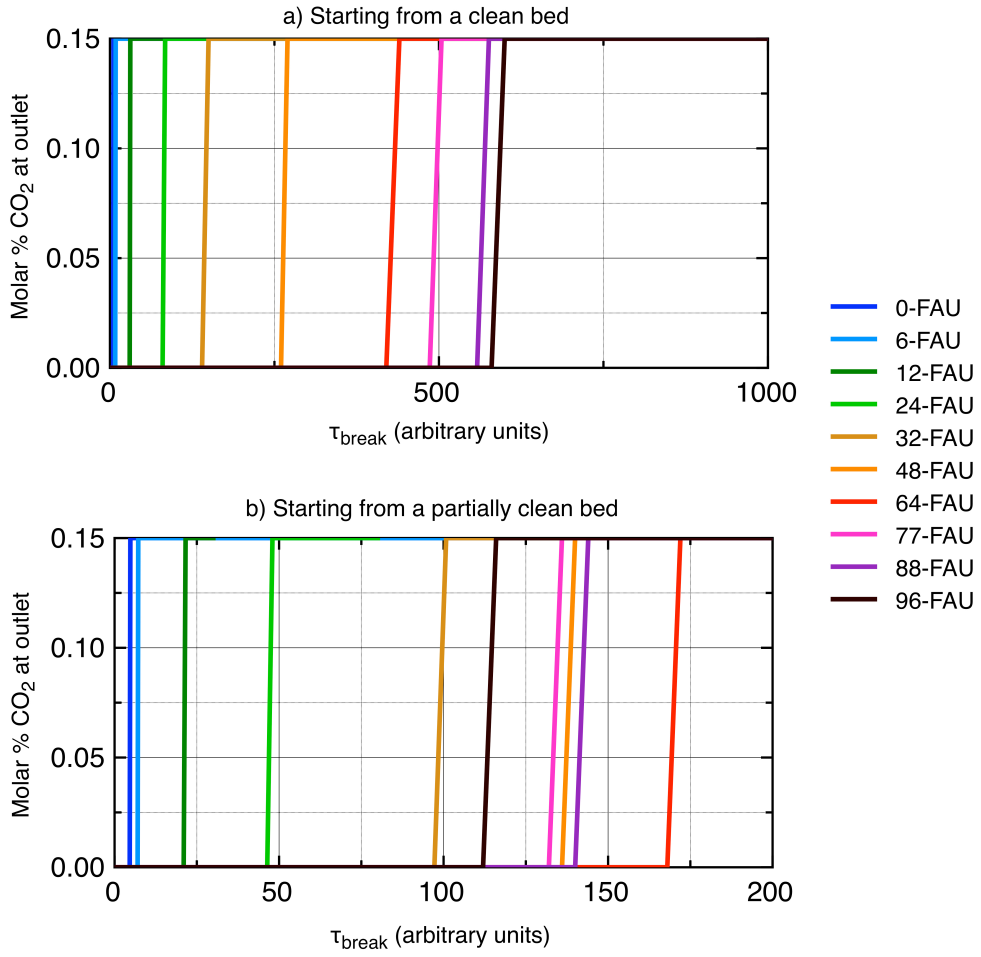

Figure S4. Breakthrough curves showing the molar % CO_2 in the gaseous mixture exiting the adsorber bed for a VSA process (100 – 5 kPa) a) starting from an empty bed and b) starting from a bed which contains the quantity of molecules present at the desorption conditions, as it is done in this work. The mixture at inlet is 80% N_2 / 15% CO_2 / 5% O_2. All simulations were performed at 313 K.

Figures S4 and S5 shows the comparison between starting from a clean or non-clean bed, for a VSA and PSA process, respectively. As it is seen, breakthrough times starting from a clean bead are much larger for both PSA and VSA processes, and even the ordering (ranking) among the ten different faujasite structures is altered.

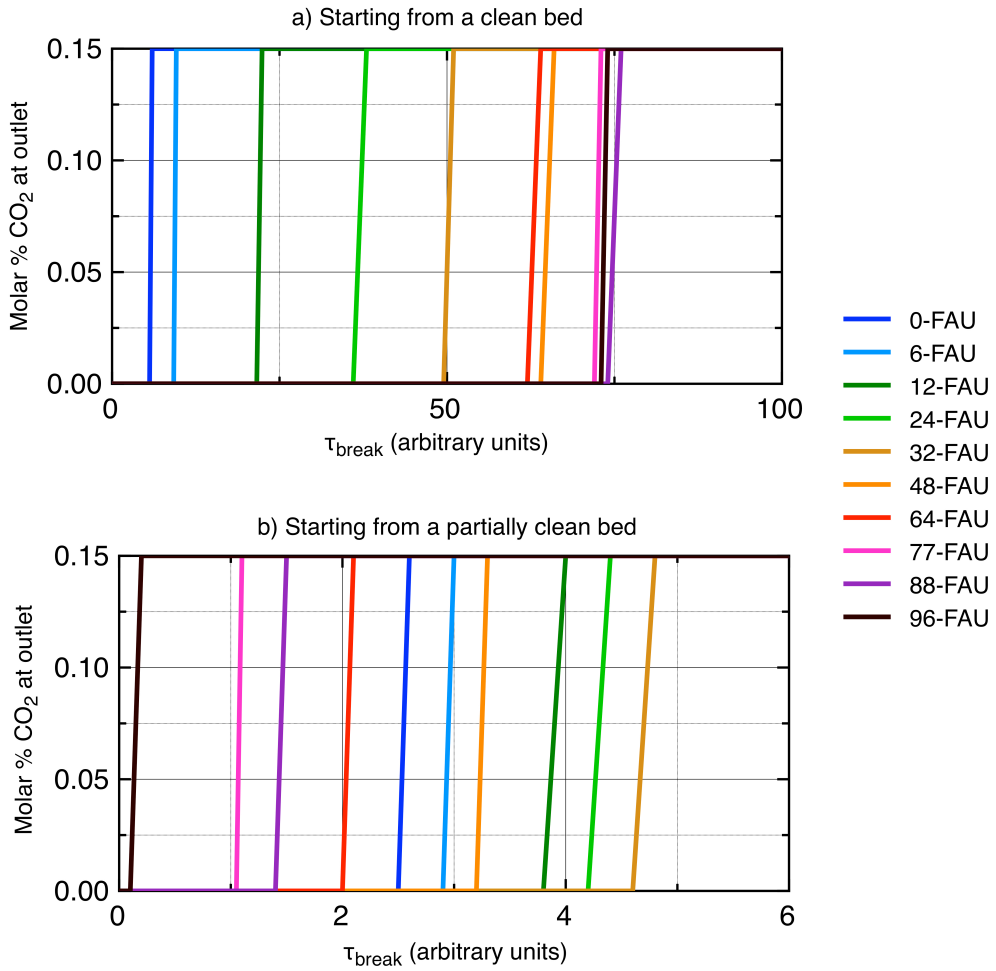

Figure S5. Breakthrough curves showing the molar % CO_2 in the gaseous mixture exiting the adsorber for a PSA process (1000 – 100 kPa) a) starting from an empty bed and b) starting from a bed which contains the quantity of molecules present at the desorption conditions, as it is done in this work. The mixture at inlet is 80% N_2 / 15% CO_2 / 5% O_2. All simulations were performed at 313 K.

[1] A. Garcia-Sánchez, C.O. Ania, J.B. Parra, D. Dubbeldam, T.J.H. Vlugt, R. Krishna, S. Calero, Transferable force field for carbon dioxide adsorption in zeolites, J. Phys. Chem. C 113 (2009) 8814-8820.

[2] A. Martin-Calvo, E. Garcia-Perez, A. Garcia-Sanchez, R. Bueno- Perez, S. Hamad, S. Calero, Effect of air humidity on the removal of carbon tetrachloride from air using Cu-BTC metal-organic framework, Phys. Chem. Chem. Phys. 13 (2011) 11165-11174.

[3] J.A. Dunne, M. Rao, S. Sircar, R.J. Gorte, A.L. Myers, Calorimetric heats of adsorption and adsorption isotherms. 2. O_2, N_2, Ar, CO_2, CH_4, C_2H_6 and SF_6 on NaX, H-ZSM-5, and Na-ZSM-5 zeolites, Langmuir 12 (1996) 5896-5904.

[4] G. Maurin, R. Bell, Adsorption of non polar and quadrupolar gases in siliceous faujasite: molecular simulations and experiments, Adsorption 11 (2005) 331-336.

3.3 Publication 2

Computational simulation study of the influence of faujasite Si/Al ratio on CO_2 capture by temperature swing adsorption

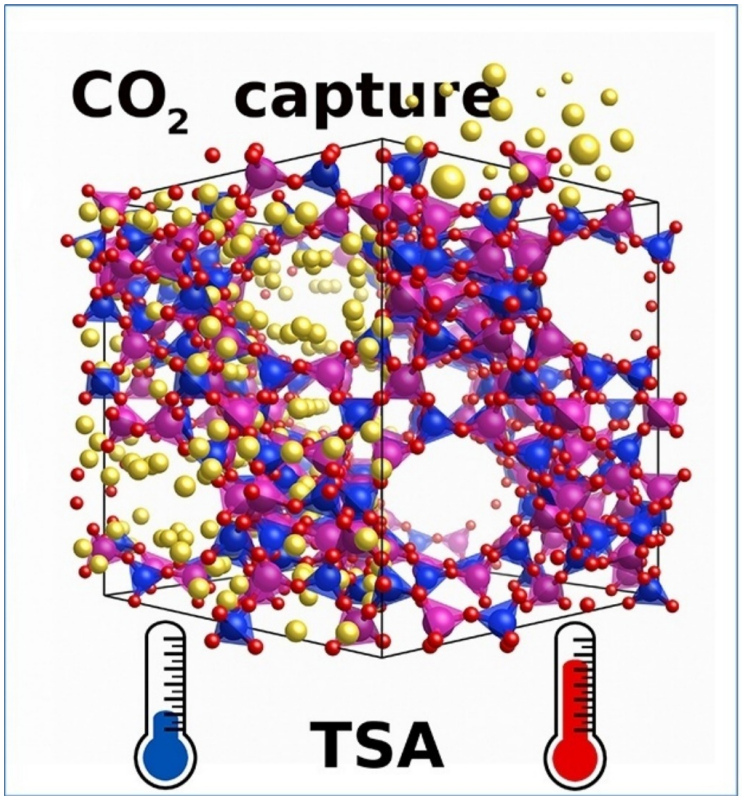

Journal of CO_2 Utilization 21 (2017) 261–269

Contents lists available at ScienceDirect

Journal of CO_2 Utilization

journal homepage: www.elsevier.com/locate/jcou

Computational simulation study of the influence of faujasite Si/Al ratio on CO_2 capture by temperature swing adsorption

Hèctor Prats, Daniel Bahamon, Xavier Giménez, Pablo Gamallo*, Ramón Sayós

Departament de Ciència de Materials i Química Física & Institut de Química Teòrica i Computacional (IQTCUB), Universitat de Barcelona, C. Martí i Franquès 1, 08028 Barcelona, Spain

ARTICLE INFO

Keywords:
Zeolites
CO_2 capture
GCMC
Faujasite
TSA

ABSTRACT

Grand Canonical Monte-Carlo simulations are used to assess ten faujasite structures, the well-known family of zeolites with different Al content in post-combustion CO_2 capture via Temperature Swing Adsorption (TSA) processes, at 313–473 K and 100 kPa. Selectivity, regenerability, purity, isosteric heat and working capacity values, for each structure, have been calculated from simulations, providing a rather complete evaluation of adsorbents' performance. Additionally, for all the structures the temperature dependence of the heat capacity has been modeled to estimate the thermal regeneration energy. Calculated heat capacities range from 0.78–0.86 kJ/kg K at 313 K to 0.98–1.15 kJ/kg K at 473 K, values considerably lower than those corresponding to aqueous amine solutions. Comparison of TSA results with previous Vacuum and Pressure Swing Adsorption (VSA and PSA) ones shows that there is no structure that works well for all three processes. Instead, each process reaches optimum conditions for certain range of Al content. Results indicate that high Al content faujasites, 64-to-96-FAU, are the most effective for TSA with working capacities above 1.7 mol/kg, doubling PSA/VSA values. Intermediate Al content 48-,64-FAU perform better at VSA conditions and low Al content 12-,24-FAU structures are more suitable for PSA processes. At moderate operative conditions (i.e., regeneration temperature of 413 K), TSA shows the highest purities (above 99% for one-stage process), followed by VSA and PSA. Finally, TSA is more effective in cleaning faujasites with 48 or more Al, compared to PSA/VSA, leading to a higher regenerability (energetic cost index range between 2.3 and 2.4 GJ/tCO_2).

1. Introduction

Economic growth and industrial development have resulted in an increased burning of fossil fuels, leading to growing emissions of atmospheric CO_2 [1]. These emissions may be reduced by a variety of measures, such as improving energy efficiency, and/or developing alternative energy sources, e.g. wind and solar power. However, the necessary transition into a sustainable energy mix, and the phasing out of fossil fuel combustion, is unlikely to occur at a sufficiently fast pace, unless additional, negative emission methods are considered.

Reduction of energy-related CO_2 emissions might be undertaken by means of Carbon Capture and Sequestration/Utilization (CCS/U) techniques. In CCS/U, carbon dioxide is separated from the flue gas of a power plant, compressed to supercritical conditions to transport it, and either stored or reused as a raw material in industry[2–6].

Separation technologies with proven adequacy for post-combustion processes are absorption, membrane use, and adsorption [7]. Whereas the membrane technology is currently waiting its application to mass production, absorption is more mature, but it results in high-energy consumption during the absorbent regeneration step [8] (*i.e.*, about 30% of the output of the power plant) [9]. Alternatively, CO_2 can be captured through adsorption in the pores of solid materials [10,11]. Adsorption technology is based on the preferential affinity of CO_2 to the adsorbent pores, compared to other flue gas components. After the adsorption step, molecules are desorbed from the solid by lowering the pressure (Pressure Swing Adsorption, PSA) or heating the solid material (Temperature Swing Adsorption, TSA) inside the column. The PSA process in which the desorption is performed below atmospheric pressure is called Vacuum Swing Adsorption (VSA). After this operation, the adsorbent is ready for a further cycle. All these methods have been used successfully for air fractionation, hydrogen production, carbon dioxide capture (CCS/U) and removal of volatile organic compounds (VOC) [12–18]. Among these methods, TSA is particularly promising, owing to difficulties with compressing or applying a vacuum to such large volumes of gas stream, as well as to the potential availability of low-grade heat in a power plant as a source of energy for regeneration [19].

Zeolites, activated carbons and metal-organic frameworks (MOFs) are promising adsorption materials, presenting high CO_2 working

* Corresponding author.
E-mail address: gamallo@ub.edu (P. Gamallo).

http://dx.doi.org/10.1016/j.jcou.2017.07.013
Received 29 April 2017; Received in revised form 29 June 2017; Accepted 16 July 2017
Available online 15 September 2017

Nomenclature

BTC	Benzene-1,3,5-tricarboxylate
C	Ideal gas concentration at the feeding-gas conditions (kmol m^{-3})
C_p^i	Heat capacity of i component (kJ kg^{-1} K^{-1})
CCS/U	Carbon capture and sequestration/utilization
dobpdc	4,4′-Dioxidobiphenyl-3,3′-dicarboxylate
en	Ethylenediamine
EOS	Equation of state
FAU	Faujasite
GC	Grand canonical
GCMC	Grand canonical Monte Carlo
IAST	Ideal adsorbed solution theory
L	Length of packed bed (m)
LJ	Lennard-Jones
LSX	Low silica X
LTA	Linde type A
MC	Monte Carlo
MEA	Monoethanolamine
mmen	*N*,*N*′-dimethylethylenediamine
MOF	Metal organic framework
N	Amount adsorbed per mass of adsorbent (mol kg^{-1})
NIST	National Institute of Standards and Technology
$N_{k,sat}$	Maximum loading (saturation) of component A (kmol m^{-3})
P_{TOT}	Total initial pressure (kPa)
PSA	Pressure swing adsorption
q_i	Partial charge of atom i (e^-)
q_{ST}	Isosteric heat of adsorption at infinite dilution (kJ mol^{-1})
R	Gas constant (8.314 kPa m^3 $kmol^{-1}$ K^{-1})
r_{ij}	Distance between a pair of atoms *i* and *j* (m)
$S_{A/B}$	Selectivity
t	Time (s)
T	Temperature (K)
TSA	Temperature swing adsorption
u	Superficial gas velocity (m s^{-1})
U_{ij}	Potential energy between a pair of atoms *i* and *j* (kJ mol^{-1})
U_g	Total potential energy of an isolated guest molecule (kJ mol^{-1})
V	Total volume of packed bed (m^3)
VOC	Volatile organic compounds
VPSA	Volume pressure swing adsorption
VSA	Volume swing adsorption
W	Adiabatic energy requirement for compression/vacuum (kJ)
WC	Working capacity of the targeted component in the mixture (mol kg^{-1})
x_A	Mole fraction of component A in the adsorbed phase
y_A	Mole fraction of component A in the gas (bulk) phase
z	Distance along the adsorber (m)

Greek symbols

ϵ	Voidage of bed
ε_{ij}	Lennard-Jones potential well depth (kJ mol^{-1})
ε_0	Vacuum permittivity (F m^{-1})
κ	Polytropic parameter of gases
η	Feeding/vacuum blower efficiency
ϕ	Adsorbed composition factor [adim.]
ρ_S	Framework density (kg·m^{-3})
σ_{ij}	Lennard-Jones potential diameter (m)
τ	Time necessary per saturation in a cycle [adim.]
μ	Chemical potential (kJ mol^{-1})
v	Intersticial gas velocity (m s^{-1})

Subscripts

ads/feed	Adsorption or feeding conditions
des/regen	Desorption or regeneration conditions
k	Species in the gas mixture ($k = A, B, C, \ldots$)
out	Mixture exiting the adsorber

capacity and selectivity for CO_2 over N_2, together with low regeneration energy [10,20–25]. In particular, zeolites are inexpensive porous materials that are already produced on a large scale for many commercial applications. Thus, they have been used successfully in PSA and TSA processes for CCS/U [26–28]. Furthermore, they present higher thermal and mechanical stability than other common adsorbents such as MOFs, although the latest often possess higher surface areas [29,30].

Zeolites are molecular sieves with a 3D framework structure possessing orderly distributed micropores with diameters up to 2 nm. The different ways in which TO_4 tetrahedrals (T = Si or Al atom) can be connected lead to a rich variety of zeolite structures [31–33]. Faujasites are a zeolite family built from Si, Al and O atoms, with a crystal composition that vary with the Si/Al ratio (*i.e.*, $(Na_2O)_{n/2}(Al_2O_3)_{n/2}(SiO_2)_{192-n}$, $0 \leq n \leq 96$) [34], and consist of sodalite cages which are connected through hexagonal prisms. The properties of the faujasites depend on the nature, number and distribution of the framework cations. As the Si/Al ratio decreases, the cation content increases, the thermal stability diminishes, the surface becomes more hydrophilic and the zeolite increases its catalytic properties. These changes are of great importance in the energetic cost of the CO_2 capture and in the regenerability of the adsorbent material [35]. Thus, the open three-dimensional pore system of FAU-type zeolites allows exceptional properties for using it in adsorptive separations compared to other zeolite families [36].

Computational methods have been employed in a complementary fashion to experimental investigations. Grand-canonical Monte Carlo (GCMC) simulations allow the prediction of adsorption isotherms, adsorption selectivities and preferred adsorption sites at a very moderate computational expense, making an important contribution to the microscopic understanding of gas adsorption and separation in porous materials [37]. In a previous work [38], we have employed GCMC simulations to study the separation of post-combustion $CO_2/N_2/O_2$ mixtures via PSA and VSA processes in FAU-type zeolites with different Si/Al ratio. An analysis of the influence of the Si/Al ratio on the CO_2 capture performance revealed that faujasites having intermediate Al content are the most effective for P/VSA processes. In the present work, we have performed new GCMC simulations for all faujasite structures considered in Ref. [38] to study the separation of post-combustion $CO_2/N_2/O_2$ mixtures via TSA processes. Thus, we have calculated selectivities, working capacities and purities at TSA conditions and then, compared the results obtained with those for PSA and VSA processes. Moreover, we have calculated the thermal regeneration energy (*i.e.,* the energy required for heating and desorb) and compare it with the adiabatic work for expansion/compression required in VSA/PSA processes.

This document is structured as follows: Section 2 describes the methodology, the computational details and the evaluation criteria used to rank all the faujasite structures simulated. Section 3 reports the

values for all the properties calculated and gives the comparison of TSA versus PSA and VSA processes. Finally, Section 4 provides the main conclusions obtained.

2. Methods and computational details

2.1. Faujasite structures

Ten different Si/Al Faujasite structures have been studied in the present work. Since the full set of Faujasite structures are the same that those used in our previous work [38], here only a few details are given. These structures have been labeled as *n*–FAU, where *n* signifies the number of sodium or aluminum atoms per unit cell (*i.e.*, n = 0, 6, 12, 24, 32, 48, 64, 77, 88 and 96, which correspond to Si/Al ratio of $+\infty$, 31, 15, 7, 5, 3, 2, 1.5, 1.2 and 1, respectively). All the structures were obtained from 88-FAU (*i.e.*, also named zeolite 13X), by randomly replacing Al by Si atoms and satisfying the Löwenstein's avoidance rule [39].

We considered all faujasites under study as rigid models. Nevertheless, the non-framework sodium cations were allowed to move freely along the zeolite structure, changing their position depending on their interactions within the rigid structure, other Na^+ cations and the adsorbed gas molecules, as recommended in previous studies [40,41].

2.2. Force field and simulation details

Carbon dioxide, nitrogen and oxygen molecules were modelled rigid. The potential of the system was calculated as the sum of the guest-host and the guest–guest interaction energies, modeled as a combination of Lennard-Jones (LJ 12-6) and Coulomb potentials

$$U_{ij} = 4\varepsilon_{ij}\left[\left(\frac{\sigma_{ij}}{r_{ij}}\right)^{12} - \left(\frac{\sigma_{ij}}{r_{ij}}\right)^{6}\right] + \frac{1}{4\pi\varepsilon_0}\frac{q_i q_j}{r_{ij}} \quad (1)$$

where U_{ij} is the total potential energy between atoms i and j at distance r_{ij}; q_i, q_j are the partial charges of atoms i and j, respectively, ε_{ij} is the LJ potential well depth, σ_{ij} is the LJ potential diameter, and finally ε_0 is the vacuum permittivity. All the force field parameters were taken from Calero et al.[42,43]. These parameters are applicable to all Si/Al ratios, both at cryogenic and high temperatures.

Ewald summation was used to calculate Coulombic interactions [44] with a relative precision of 10^{-6}. A cutoff distance of 12 Å was used, and Lorentz-Berthelot mixing rules were used to calculate the van der Waals interactions between molecules. A summary of the Coulombic charges and LJ parameters used in this work, as well as the agreement between simulations and experimental data for selected structures (when available), can be found in the Supplementary data from our previous study [38].

Pure and ternary mixture adsorption isobars were computed using GCMC simulations by means of LAMMPS code [44]. At every simulation step, the GCMC algorithm attempts a number of insertions/deletions of guest molecules between the simulation cell and the imaginary reservoir, and a number of translations/rotations of guest molecules within the simulation box. Simulations have been run for at least 4×10^6 GCMC equilibration steps and 8×10^6 GCMC production steps for each temperature value. The number of molecules adsorbed was calculated using a statistically averaged approach after the equilibrium stage for every single point, allowing the construction of the adsorption isobars [45].

Both pure and ternary mixture isobars were computed at a pressure of 1 bar, in a temperature range between 313 and 473 K. The separation efficiency of the ternary mixture $CO_2/N_2/O_2$ was studied, with a typical post-combustion gas composition of 15%/80%/5% [46] (*i.e.*, we assume that water and other impurities have been removed from the tail gas in earlier stages).

To relate the chemical potential to the pressure in the present simulations the Peng-Robinson Equation of State (EOS) [47] was used, taking the pure substance parameters from NIST database [48]. The van der Waals one-fluid mixing rule was used in mixture simulations [49], taking the binary parameters from Vrabec et al. [50]. Additional details regarding the GCMC simulations and force-field parameters can be found in our previous work [38].

2.3. Adsorbent evaluation criteria

Five different evaluation criteria were considered in this work to analyze the CO_2 capture and separation performance for each faujasite under the studied conditions: selectivity (s_{CO_2/N_2}), CO_2 working capacity (WC_{CO_2}), regenerability (R_{CO_2}), purity at outlet (X_{CO_2}) and thermal regeneration energy ($Q_{thermal}$). All of them can be obtained, respectively, from the following expressions:

$$s_{CO_2/N_2} = \left(\frac{x_{CO_2}}{x_{N_2}}\right)/\left(\frac{y_{CO_2}}{y_{N_2}}\right) \quad (2)$$

$$WC_{CO_2} = N_{CO_2}^{ads} - \phi N_{CO_2}^{des} \quad (3)$$

$$R_{CO_2} = \left(WC_{CO_2}/N_{CO_2}^{ads}\right) \times 100\% \quad (4)$$

$$X_{CO_2} = \frac{N_{CO_2}^{out}}{N_{gas}^{out}} = \frac{\frac{P_{CO_2}V\varepsilon}{RT} + WC_{CO_2}\rho V(1-\varepsilon)}{\frac{P_{TOT}V\varepsilon}{RT} + (WC_{CO_2} + WC_{N_2} + WC_{O_2})\rho V(1-\varepsilon)} \quad (5)$$

$$Q_{thermal} = \int_{T_{des}}^{T_{ads}} C_p^{FAU}\,dT + \sum_k q_{ST_k} WC_k \quad (6)$$

where x_i is the molar fraction of *i*-component in the adsorbed phase and y_i is the molar fraction of *i*-component in the bulk/gas phase, and WC_{CO_2} is calculated from the difference between the CO_2 uptake under adsorption and desorption conditions per kg of adsorbent material and per cycle. The usual procedure of estimating the working capacity experimentally in TSA processes [51] consists in calculating $N_{CO_2}^{ads}$ from ternary mixture adsorption data and $N_{CO_2}^{des}$ from pure CO_2 adsorption data. However, this procedure assumes that after adsorption step the composition inside the bed is 100% CO_2, which is only valid for high selective materials, as in Ref. [51]. However, faujasites structures with low Al content (*i.e.,* 0-FAU to 24-FAU) also contain a non-negligible fraction of N_2 and O_2 molecules adsorbed. Thus, for these structures, at desorption conditions the value of $N_{CO_2}^{des}$ which has been calculated from pure CO_2 adsorption data at 100 kPa must be corrected because P_{TOT} does not equal P_{CO_2}. The correction is done by the ϕ factor [38] that varies between 0 and 1 and considers the molar fraction x_{CO_2} in the adsorbed phase, providing a more realistic method of estimating the number of molecules that will remain adsorbed after the desorption step. As above-mentioned, this approach is necessary for low Al content structures where other uptakes are not negligible, and it makes results more realistic than those found in the literature based on pure adsorption data [14,52], which are only valid when the material is highly selective for one component. The values of ϕ used in this study correspond to 1.00, 0.99, 0.99, 0.98, 0.96, 0.93, 0.87, 0.75, 0.54 and 0.44 for *n*-FAU structures with n = 96, 88, 77, 64, 48, 32, 24, 12, 6 and 0, respectively.

Regeneration of CO_2, Eq. (4), represents the fraction in percentage of carbon dioxide that can be desorbed by heating up the adsorbent material from the total uptake of gas species. On the other hand, the CO_2 purity at the outlet of the bed, Eq. (5), is an important variable to consider, especially when is possible to reuse the captured CO_2 for other applications. In Eq. (5), the ratio $N_{CO_2}^{out}/N_{gas}^{out}$ indicates the molar fraction of CO_2 in the mixture exiting the adsorbent material. This ratio is calculated considering the void fraction of the bed (*i.e.,* the ratio of the void volume to the total volume of the bed), ε = 0.4, the feed composition, P_{CO_2} = 15 kPa and P_{TOT} = 100 kPa, the volume of the packed bed, V = 0.1 m^3, the working capacity of component i at desorption

temperature T, WC_i and the framework density, ρ.

The total thermal regeneration energy ($Q_{thermal}$) per unit mass of adsorbent has two main contributions: (i) the energy required for heating the adsorbent material, and (ii) the energy required to overcome the endothermic desorption process. According to Sculley et al. [53] this energy can be calculated per kg of adsorbent in one cycle from Eq. (6) where C_p^{FAU} is the heat capacity of the adsorbent, T_{ads} and T_{des} are the adsorption and desorption temperatures, respectively and finally, q_{ST_k} and WC_k are the isosteric heat of adsorption and working capacity of k-component in the mixture, respectively. q_{ST_k} is a thermodynamic quantity that characterizes the enthalpy change associated with the adsorption of one molecule onto the surface. According to the energy/particle fluctuations in the GC ensemble, the isosteric heat of adsorption (q_{st_k}) corresponds to [54]:

$$q_{st_k} = -\frac{<U \times N> - <U><N>}{<N^2> - <N>^2} + <U_g> + RT \quad (7)$$

where U is the total potential energy of the N adsorbed molecules and the brackets $< \ldots >$ denote an average in the GC ensemble. The bracket terms have been obtained from GCMC simulations by averaging over 10.000 different values for each loading. Moreover, we have assumed that the isosteric heat remains constant throughout the desorption step at the value corresponding to the adsorption uptake. This is a good approximation due to the flatness of the isosteric heat curves as a function of the CO_2 uptake (Fig. 1). Finally, $< U_g >$ is the average energy of an isolated adsorbate molecule in the ideal-gas state. For rigid molecules, this term vanishes.

On the other hand, C_P is an important parameter for the energy requirements calculation, since materials with low heat capacity would lead to lower energy penalties for the regeneration step, Eq. (6). Unfortunately, only a limited number of specific heat capacities have already been measured and reported in literature for cation-exchanged faujasites [55–57]. In the present work, heat capacities for all the structures have been computed by means of the predictive model from Vieillard [58], based on the oxide summation technique. This method considers that the thermodynamic properties of silicate minerals can be described as a linear combination of the fractional properties of their constituent polyhedral, where only the crystallography of the mineral needs to be known. The C_P value of our FAU structures were calculated in the following way:

$$C_p^{FAU}(T) = n_{SiO_2} \cdot C_p^{SiO_2}(T) + n_{Al_2O_3} \cdot C_p^{Al_2O_3}(T) + n_{Na_2O} \cdot C_p^{Na_2O}(T) \quad (8)$$

where C_p^i are the heat capacities of the i-polyhedral, n_i is the total number of i-polyhedrals present in a unit cell, and the $C_p^i(T)$ values are obtained from a polynomial correlation with temperature. Calculated heat capacities range from 0.78-0.86 kJ/kg K at 313 K to 0.98–1.15 kJ/kg K at 473 K. Interestingly, there is a nearly linear relationship between the heat capacity and temperature for all the faujasite structures (see Fig. S1 in Supplementary data). These values of $C_p^i(T)$ are considerably lower than those conventionally employed in aqueous amine solutions since the presence of water in which the amine molecules are dissolved must also be heated until desorption temperature. For example, the heat capacity for 30% wt monoethanolamine (MEA) solution at 298 K is 3.73 kJ/kg K, more than four times larger [59]. These results highlight one of the main advantages of employing zeolites or other porous solid materials such as MOFs when TSA process is adopted. Details regarding the heat capacity calculation can be found in Section I of the Supplementary data.

In the present work, we consider TSA processes in their simplest configuration including only two fixed beds in parallel by the so-called Skarstrom cycle [60]. When comparing among the different faujasite structures, both the total volume of the column and the fractional voidage were held constant, implying that the volumes of adsorbent materials used in the fixed beds are equal for all faujasite structures.

Moreover, it needs to be mentioned that the different adsorption criteria used in the present work should be used with caution when aiming to predict the best material for post-combustion CO_2 capture. Our results provide key insights regarding the performance of different faujasites structures, but they must always be accompanied by kinetic studies under realistic process conditions. In fact, there have been a few works investigating the capability of adsorbent metrics to screen potential adsorbents [61,62]. These studies indicated that adsorbent criteria could identify the adsorbents that eventually performed poorly. However, the relative ranking provided by various metrics can be different.

3. Results and discussion

3.1. Isosteric heat of adsorption

Isosteric heat of adsorption (q_{st}) is an important thermodynamic quantity for understanding the possible thermal effects related to adsorption. It can be used to compare the interaction strength of the adsorbates with various adsorbent materials. The isosteric heats of adsorption at different CO_2 uptakes for the different faujasite structures analyzed in this work are plotted in Fig. 1.

The isosteric heats of adsorption of CO_2 at zero coverage increase from 14 to 42 kJ mol^{-1} from the pure silica zeolite (with a Si/Al ratio of $+\infty$) to the 96-FAU zeolite (with a Si/Al ratio of 1), respectively. This fact comes from the increasing number of strong interactions between Na^+ cations and gas molecules from 0-FAU to 96-FAU structures. This tendency is also observed for CO_2 uptakes up to 5 mol/kg. Above this loading value, different adsorption behaviors start to appear, especially for faujasites with a high Al content.

The flatness of the isosteric heat curves observed for intermediate Al content faujasites (*i.e.,* from 12-FAU to 64-FAU) indicates that solid-gas interactions are dominant along the whole adsorption process until high loadings. Conversely, the increase of the adsorption heat with the loading for low Al content faujasites (*i.e.*, 0-FAU and 6-FAU) suggests that the adsorption regime at low CO_2 coverage is dominated by solid-gas interactions, while this interaction becomes less important as the CO_2 loading increases due to the formation of new gas–gas interactions, which are stronger. However, high Al content structures (from 77-FAU to 96-FAU) show a different behavior and the heat of adsorption decreases upon reaching a certain value. Above this value, the CO_2 molecules and the Na^+ cations are so close together that the gas–gas and Na^+-gas interactions become more repulsive (*i.e.*, the structure reaches saturation). Fig. 1 shows that 96-FAU structure is the one that presents the isosteric heat decay at a lower loading, since it contains a higher number of Na^+ cations than the other structures. A similar behavior has been reported previously for LTA structures with different Si/Al ratios

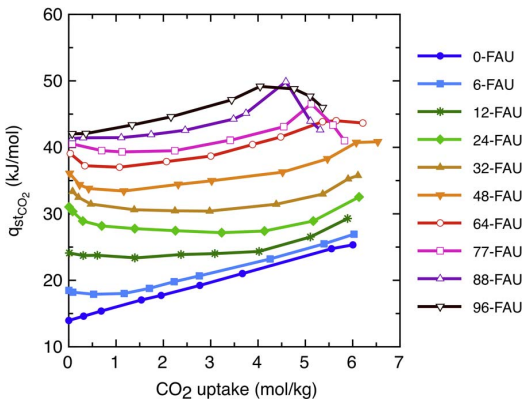

Fig. 1. Isosteric heat of adsorption (q_{st,CO_2}) as a function of the CO_2 uptake per kg of adsorbent material obtained for the ten faujasite structures with different Si/Al ratio at T = 313 K. Lines are guide to the eye.

[28]. The values of the isosteric heat at different loadings will be used to calculate the thermal regeneration energy.

3.2. Selectivity, purity and regenerability

Fig. 2 shows the selectivity for CO_2 relative to N_2 for the ten structures evaluated as a function of temperature according to Eq. (2). As expected, 96-FAU has the highest CO_2 selectivity in all the temperatures considered, ranging from 1150 (313 K) to 46 (473 K), while 0-FAU has the lowest value, between 4.1-2.1 in the same temperature range. This is due to the strong interactions between CO_2 and Na^+ cations and the increasing value of the isosteric heat of adsorption, which are dominant in structures with high Al content. Moreover, as the thermal energy of the gas molecules increases, the difference in adsorption between CO_2 and N_2 becomes less significant, so decreasing the selectivity. The drop in selectivity with temperature is more pronounced for structures with higher selectivity (*e.g.*, a factor of 25 for 96-FAU compared to a factor of 2 for 0-FAU in the same temperature range). The fact that systems with large selectivity are more sensitive to temperature has been observed also in MOFs [63].

Selectivity values in Fig. 2 have been obtained directly from ternary mixture isotherms obtained from GCMC simulations. In addition, selectivity has been also evaluated using adsorption isotherm fits for pure components followed by IAST calculations (Section II in Supplementary data). Selectivity values obtained from IAST calculations are substantially larger than those values obtained directly from ternary mixture isotherms, specially for low Al-content faujasites, as reported previously in Ref. [38] since IAST does not consider the interaction among all the species in the mixture, as GCMC does.

Fig. 3 shows calculated values of CO_2 purity at outlet and regenerability as a function of desorption temperature for all the faujasite structures, assuming a packed bed with a total volume of 0.1 m^3 (*i.e.,* L = 0.1 m, A = 1 m^2) and a void fraction of $\varepsilon = 0.4$. The highest purities are obtained for high Al-content structures, with values above 90% for structures containing more than 48 Na^+ atoms per unit cell. This degree of purity agrees with real feed experimental value of 94% of purity at outlet obtained in Ref. [18] for 13X (FAU-88) performing TSA processes with a smaller amount of CO_2 (10%) and a bit different operative conditions (T_{ads} = 288 K, T_{des} = 423 K). Purity values corresponding to 77-FAU, 88-FAU and 96-FAU structures are coincident, and therefore they cannot be distinguished in the plot. Conversely, purity values for 0-FAU, 6-FAU and 12-FAU structures are very low, making them not attractive for the process. Note that the final CO_2 purity depends on the selectivity, the working capacities for $CO_2/N_2/O_2$, and on the void fraction ε. Higher purity values can be achieved by reducing the void fraction.

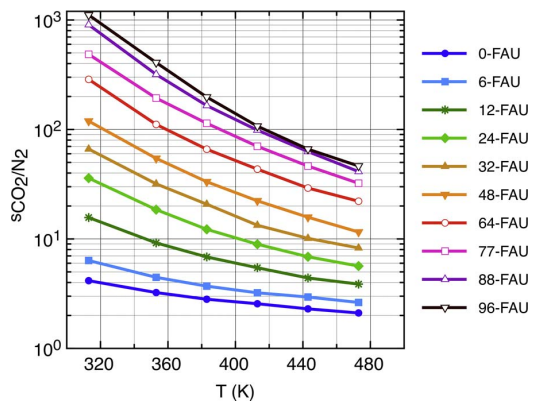

Fig. 2. Calculated selectivities for CO_2 relative to N_2 as a function of temperature, for ten different n-FAU structures (P_{TOT} = 100 kPa).

Unlike purity, maximum regenerability values are obtained for intermediate Al content structures, with 48-FAU having the highest value at all temperatures explored. Even though, it should be noted that although certain structures such as 12-FAU and 24-FAU present moderately high regenerability, their uptake is so low that the amount of recovered CO_2, in absolute terms, is small. It can be expected that regenerability will be even higher at temperatures above 473 K. Purity and regenerability values corresponding to lower desorption temperatures have not been plotted in Fig. 3, since the working capacity at these conditions is nearly zero for most of the structures, and hence the CO_2 purity and regenerability tend to 15% and 0%, respectively.

Pure adsorption isobars for CO_2 and ternary mixture isobars for CO_2 and N_2 can be found in Section III and Section IV in the Supplementary data, respectively.

3.3. Working capacity, thermal regeneration energy and optimal desorption temperature

Desorption temperature can significantly affect both the CO_2 working capacity and the thermal regeneration energy, which are the two main parameters to study the performance of the adsorbent materials for carbon capture and sequestration [53]. Fig. 4 shows the variations of these two quantities as a function of desorption temperature in the range 353–473 K.

As it can be seen in Fig. 4a, the working capacity initially increases quickly with increasing temperature and then nearly reaches a plateau for most of the structures. The initial sharp increase can be attributed to the fact that the influence of temperature on the gas/solid interactions is more remarkable at low temperatures [63], and can be also deduced from the shape of the CO_2 adsorption isobars (see Section IV in the Supplementary data). Low and intermediate Al content structures reach the plateau at temperature values around 473 K, whereas for high Al content structures this plateau is beyond the temperature range considered in the present work.

In post-combustion CO_2 capture, the solid adsorbent will likely be packed into a large fixed bed, and, as such, the volumetric working capacity in units of mol/dm^3 is also a vital consideration from the perspective of minimizing the size of the column towers, which may affect the heating efficiency during the regeneration step. Alternatively, the bed porosity or void fraction ($\varepsilon = 0.4$) could be used to estimate the bed densities and use those values to obtain a volumetric working capacity values that are related to the size of the fixed beds. For the faujasite structures considered in the present work, both mass capacity and volumetric capacity analysis lead to the same ranking due to their similar density. However, when comparing between different materials, a volumetric capacity ranking is more useful. Framework density was used to convert from mass-specific to volume-specific working capacity. Table 1 compares our results for mass capacity and volumetric capacity with those for promising adsorbent materials found in literature. We found that high Al-content faujasite structures have competitive capacity values beating the vast majority of the other zeolites and being only surpassed in volumetric capacity by zeolite CaA, although it presents a higher heat of adsorption of 58 kJ/mol [51], which may imply more energy required to overcome the endothermic desorption process. In the case of MOFs, some of them also present higher working capacities. To name a few, Mg-MOF-74 [14] and mmen-Mg_2(dobpdc) [65] present higher mass capacity and similar volumetric capacity than high Al-content faujasites at T_{ads} = 313 K − T_{des} = 443 K, 413 K, respectively. Additionally, it is important to note that experimental materials are not fully activated and then some discrepancies could appear in their performance compared to simulated perfect crystals. Moreover, small temperature changes can occur during the adsorption and desorption steps due to the exothermic and endothermic processes that take place, respectively.

In contrast, Fig. 4b shows that there is a nearly linear relationship between the required thermal regeneration energy per cycle and the

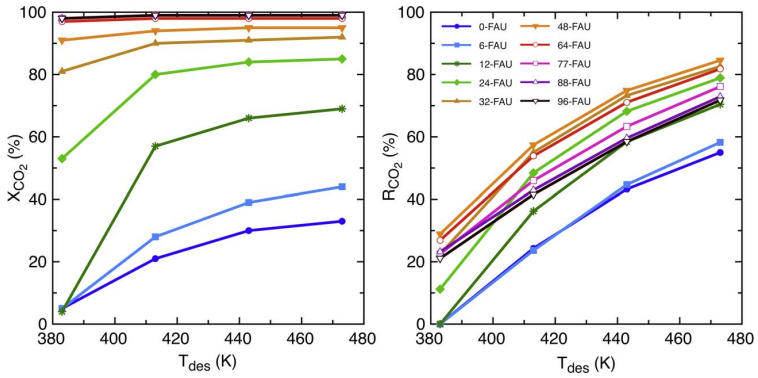

Fig. 3. CO_2 purity at outlet (%) in the gaseous mixture exiting the bed (left) and regenerability (right) as a function of desorption temperature, assuming a packed bed with a total volume of 0.1 m^3 (L = 0.1 m, A = 1 m^2) and a void fraction of ε = 0.4. Simulations performed at T_{ads} = 313 K and P_{TOT} = 100 kPa.

desorption temperature. This fact can be explained analyzing both terms in Eq. (6) separately. Both terms increase with temperature, however, the first one increases in a concave manner while the second increases in a convex manner, resulting in a total increase that is almost constant with temperature.

To seek out the optimal desorption temperature, both contributions should be considered. Hence, by calculating the required thermal regeneration energy per unit mass of CO_2 recovered as a function of desorption temperature (presented in Fig. 5) it is possible to estimate the optimal desorption temperature. According to Sculley et al. [53], this simplest ratio will be the most telling, as it will give a true direct comparison between materials, independent of assumptions about the process. Of course, the values obtained in GJ/kg do not represent the real cost for the whole capture process. There are other factors that will come into play during the industrial process, such as the efficiency of types of heat exchangers, capital costs of equipment and adsorbent materials and costs associated to post-separation (*e.g.,* compression and transport), among others.

Fig. 5 shows that the optimum desorption temperature is between 413 and 443 K. In addition, it can be observed that TSA process is only profitable for faujasites with more than 48 Al atoms per unit cell. The low working capacity for structures with lower Al content does not compensate their lower heat capacity. Moreover, the values obtained for 64-, 77-, 88- and 96-FAU structures are very similar in all the temperature range considered. This is due to similar values of density, heat capacity, isosteric heat and working capacity. Among these structures, 64-FAU has the minimum thermal regeneration energy per unit mass of CO_2 recovered at 413 K, with a value of 2.42 GJ/tCO_2. This value is in line with the real feed experimental value of 2.02 GJ/tCO_2 reported in Ref. [17] using PTSA at operative conditions T_{ads} = 323 K − T_{des} = 373 K, at pressures 15% below atmospheric conditions, with 11.5% of CO_2 at feeding and using CaX zeolites (same as FAU-88 with Ca^{2+} instead of Na^+ cations). On the other hand,

Table 1
Mass and volumetric working capacity values per cycle for selected faujasite structures from this work and other promising adsorbents found in literature. The temperature range considered is T_{ads} = 313 K − T_{des} = 443 K and P_{TOT} = 100 kPa for all the materials except for en-M(dobpdc) MOFs. [a,b] Values for X-FAU structures correspond to a ternary CO_2 (15%)/N_2(80%)/O_2(5%) mixture, whereas the other values correspond to a binary CO_2(15%)/N_2(85%) mixture.

Material	Working capacity		Ref.
	(mol/kg)	(mol/dm^3)	
64-FAU	2.40	3.20	This work
88-FAU	2.45	3.41	This work
96-FAU	2.46	3.47	This work
CaX	2.20	3.14	[61]
MgX	2.37	3.38	[61]
PS-MFI	0.36	0.67	[61]
CaA	2.79	4.22	[51]
CuBTC	0.88	0.84	[61]
Ni-MOF-74	1.71	2.05	[61]
Zn-MOF-74	1.13	1.38	[61]
Mg-MOF-74	4.25	3.36	[14]
ZIF-68	0.21	0.19	[61]
PPN-6-SO_3Li	0.62	0.32	[53]
PPN-6-SO_3H	0.36	0.12	[53]
en-Mg_2(dobpdc)[a]	0.60	0.52	[64]
mmen-Mg_2(dobpdc)[b]	3.60	3.13	[65]
mmen-Mn_2(dobpdc)[b]	2.80	2.35	[65]

[a] Temperature range: T_{ads} = 298 K − T_{des} = 423 K.
[b] Temperature range: T_{ads} = 313 K − T_{des} = 413 K.

Ref. [18] reports a real feed value of 8.8 GJ/tCO_2 for TSA, FAU-88 although for 10% of CO_2 in the incoming mixture. This value is higher than that obtained here but they operated at larger range of temperatures T_{ads} = 288 K − T_{des} = 423 K. As they stated the adiabatic estimate of the thermal regeneration energy halves the previous value to 4.4 GJ/tCO_2.

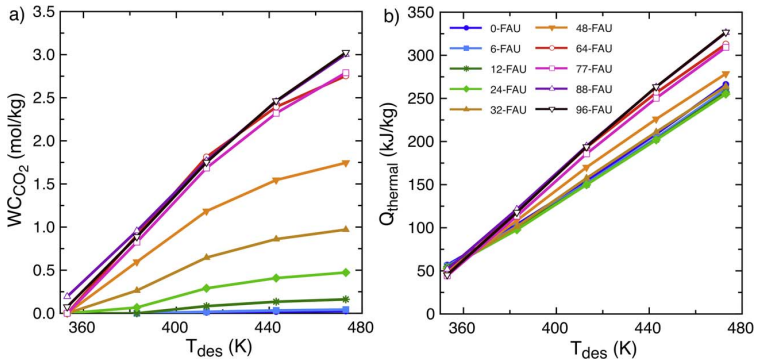

Fig. 4. Influence of TSA desorption temperature on the CO_2 working capacity (a) and required thermal regeneration energy (b) for the different faujasite structures (T_{ads} = 313 K, CO_2 (15%), N_2 (80%), O_2 (5%) and P_{TOT} = 100 kPa). WC_{CO_2} and $Q_{thermal}$ values plotted are per cycle.

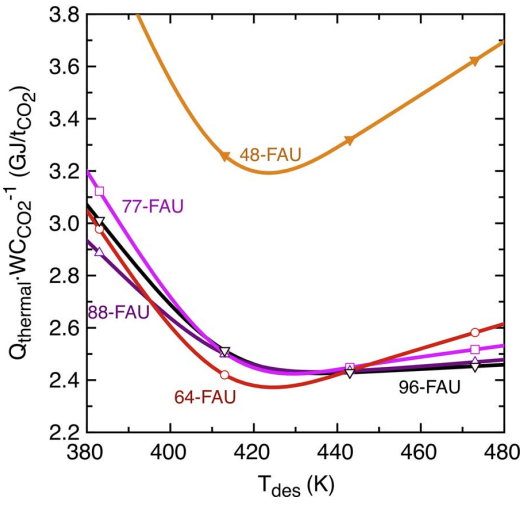

Fig. 5. Thermal regeneration energy per ton of CO_2 recovered as a function of desorption temperature at P_{TOT} = 100 kPa. Lines are guide to the eyes.

Finally, flue gas can be used directly from the stack stream to preheat the bed at the desorption step, allowing to reduce the regeneration thermal energy for the process [66]. For instance, assuming a stack temperature of 400 K, a reduction of 10% could be achieved.

3.4. Comparison of TSA separation performance versus PSA and VSA processes

In Sections 3.2 and 3.3 we have shown that the best faujasite structures to be used in TSA processes for post-combustion CO_2 capture are those with a higher Al content, from 64-FAU to 96-FAU. These structures stand out in all the five different evaluation criteria considered, especially when the temperature of desorption is raised between 413 and 473 K. In order to determine whether TSA is more effective in separating CO_2 than PSA and VSA processes, the calculated values of purity, regenerability, working capacity and energetic requirement for the ten different faujasite structures are plotted in Fig. 6. For comparison, moderate conditions were selected for TSA (P = 100 kPa, T_{ads} = 313 K, T_{des} = 413 K), PSA (T = 313 K, P_{ads} = 1000 kPa, P_{des} = 100 kPa) and VSA (T = 313 K, P_{ads} = 100 kPa, P_{des} = 10 kPa). Fig. 6a shows that TSA presents the highest purity values for almost all the structures, followed by VSA and PSA. Even reducing the vacuum in VSA process to 5 kPa such high purity provided by TSA is not achieved. In addition, TSA is more effective in cleaning faujasites with 24 or more Al atoms per unit cell compared to PSA and VSA (see Fig. 6b), leading to a higher value of regenerability. These differences in regenerability are more pronounced in structures with high Al content, where the values obtained for PSA and VSA are extremely low. Moreover, Fig. 6c shows that TSA far surpasses PSA and VSA in working capacity for intermediate and high Al content structures. For faujasite structures like 0-FAU to 24-FAU, with a low Henry coefficient (10^{-5} to 10^{-4} mol kg^{-1} Pa^{-1}), the working capacity under TSA conditions is very small (red solid bars in Fig. 6c). This fact requires heating up the entire sorbent to relatively high temperatures to get the capture of a small amount of CO_2, resulting in a very expensive heating cost. In this case, the energy required for heating the system is much greater than the energy required for overcoming the endothermic desorption process (*i.e.,* first and second terms in Eq. (6), respectively). Thus, materials with low Henry coefficient are not suitable for operating under TSA conditions. However, in a PSA process, these materials present high working capacities due to their low CO_2 uptake at the desorption step (*i.e.,* atmospheric pressure). On the contrary, 64-FAU to 96-FAU structures present higher Henry coefficients (around 10^{-3} mol kg^{-1} Pa^{-1}) due to the electrostatic interactions with the guest molecules and the Na^+ cations, resulting in much higher working capacities under TSA conditions. For these materials, it is worth investing energy in heating the system due to the large amount of CO_2 desorbed. Therefore, we expect that these results could be generalized to some extent at least for zeolite structures.

Finally, Fig. 6d shows that TSA process allows to obtain much higher values of purity, regenerability and working capacity for 64-, 77-, 88- and 96-FAU structures at a very similar energetic cost compared to P/VSA. Nevertheless, the thermal regeneration energy per ton CO_2 captured for low Al content structures is extremely high, even out of the scale, due to the poor working capacity. Therefore, although TSA process is not appropriated for low Al content faujasites, it is highly recommended against PSA and VSA for high Al content structures. To complement the study, these three processes have been also evaluated at different operative conditions. The resultant metrics for TSA, VSA and PSA (*i.e.,* purity, working capacity and thermal regeneration energy or adiabatic work) at these conditions are available in Sections V, VI and VII of the Supplementary data.

Note that for a true comparison between thermal energy and adiabatic work, it is necessary to consider a conversion coefficient, which would reduce the energetic requirements plotted for TSA.

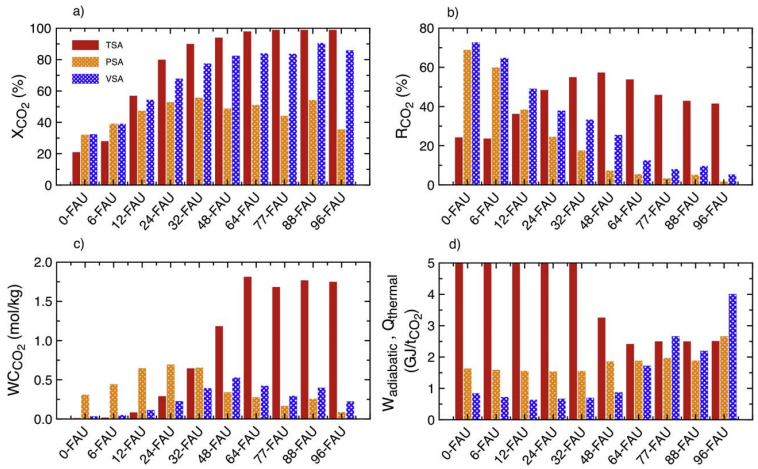

Fig. 6. Comparison for a) CO_2 purity at outlet, b) regenerability, c) working capacity per cycle, and d) energetic requirement per ton CO_2 between TSA (red solid bars, T_{ads} = 313 K, T_{des} = 413 K), PSA (orange tiny dotted bars, T = 313 K, P_{ads} = 1000 kPa, P_{des} = 100 kPa) and VSA (blue thick dotted bars, T = 313 K, P_{ads} = 100 kPa, P_{des} = 10 kPa) processes. The Y-axis in (d) represents the thermal regeneration energy (for TSA process) or the adiabatic work for expansion/compression (for VSA/PSA processes). Calculated values for PSA and VSA processes are taken from our previous work [38]. (For interpretation of the references to colour in this figure legend, the reader is referred to the web version of this article.)

4. Conclusions

Five different evaluation criteria are considered in this work to analyze the CO_2 capture performance for each faujasite under the studied conditions: selectivity, working capacity, regenerability, purity and thermal regeneration energy, considering the difference between the uptake under adsorption and desorption conditions.

The total thermal regeneration energy is obtained considering both the energy required for heating the adsorbent material and the energy required to overcome the endothermic desorption process. To this end, the heat capacity of the adsorbent material is needed. Since only a limited number of specific heat capacities have already been measured and reported in literature for cation-exchanged faujasites, the heat capacities for all the structures were calculated by means of the oxide summation technique. The calculated heat capacities for all the structures range from 0.78-0.86 kJ/kg·K at 313 K to 0.98-1.15 kJ/kg·K at 473 K. These values are considerably lower than those conventionally employed in aqueous amine solutions, highlighting one of the main advantages of employing zeolites or other porous solid materials in TSA processes.

The 96-FAU structure presents the highest CO_2 selectivity at all the temperatures considered, ranging from 1150 (313 K) to 46 (473 K), while 0-FAU has the lowest values. Highest purities are obtained for high Al-content structures, with values above 90% for structures containing more than 48 Na^+ atoms per unit cell. Purity values corresponding to 77-FAU, 88-FAU and 96-FAU structures are coincident. Conversely, purity values for 0-FAU, 6-FAU and 12-FAU structures are very low, making them not attractive for TSA. Maximum regenerability values are obtained for intermediate Al content structures, with 48-FAU having the highest value at all temperatures explored. Even though, it should be noted that although certain structures such as 12-FAU and 24-FAU present moderately high regenerability, their uptake is so low that the amount of recovered CO_2, in absolute terms, is small.

The results for mass capacity and volumetric capacity are compared with those for promising adsorbent materials found in literature. Thus, high Al-content faujasite structures present competitive capacity values, beating the clear majority of the other materials and being only surpassed in volumetric capacity by zeolite CaA.

The optimal desorption temperature for the ten faujasite structures evaluated varies in the range 413–443 K whereas the minimum value of thermal energy per ton of CO_2 recovered at 413 K is for the 64-FAU framework with a value of 2.42 GJ/tCO_2.

Comparison of present TSA results with our recent PSA and VSA ones shows that there is no structure that works well for all three processes. Thus, each process reaches optimum conditions for certain range of Al content. The best faujasite structures to be used in TSA processes for post-combustion CO_2 capture in the range 413 K–473 K are those with a higher Al content, from 64-FAU to 96-FAU. Intermediate Al content 48-,64-FAU perform better at VSA conditions, and low Al content 12-,24-FAU structures are more suitable for PSA processes.

Moreover, at moderate operative conditions, TSA presents the highest purity values for almost all the structures, followed by VSA and PSA. Even reducing the vacuum in VSA process the TSA purity is not reached. In addition, TSA is more effective in cleaning faujasites with 24 or more Al atoms per unit cell compared to PSA and VSA leading to a higher value of regenerability. These differences in regenerability are more pronounced in structures with high Al content, where the values obtained for PSA and VSA are extremely low.

Finally, the forgoing results demonstrate that from a thermodynamic point of view, TSA processes can be an excellent choice for high Al content faujasites structures, due to the good compromise between high working capacity and moderate thermal regeneration energy. However, it should be noted that these results are based purely on equilibrium properties. Kinetic studies of diffusion coefficients and full process simulations are necessary to unequivocally determine whether TSA performance is better than V/PSA for these materials. In fact, although TSA processes are easier to implement and can benefit from the low-grade heat in a power plant as a source of energy for regeneration, the variation (swing) of temperature is much slower than the pressure change, requiring longer step times than V/PSA. Hence, further investigations need to be conducted to get more reliable predictions including kinetic effects and real flue gas conditions.

Acknowledgements

Financial support to this research has been provided by the Spanish Ministry of Economy and Competitiveness (project number CTQ2014-53987-R) and, in part, from the Generalitat de Catalunya (project number 2014SGR1582). HPG thanks Generalitat de Catalunya for a predoctoral FI-DGR-2015 grant. PG thanks Generalitat de Catalunya for his Serra Húnter Associate Professorship. Computational resources provided by Consorci de Serveis Universitaris de Catalunya (CSUC, former CESCA) are gratefully acknowledged.

Appendix A. Supplementary data

Supplementary data associated with this article can be found, in the online version, at http://dx.doi.org/10.1016/j.jcou.2017.07.013.

References

[1] M.M.F. Hasan, E.L. First, C.A. Floudas, Cost-effective CO_2 capture based on in silico screening of zeolites and process optimization, Phys. Chem. Chem. Phys. 15 (2013) 17601–17618.
[2] N. MacDowell, N. Florin, A. Buchard, J. Hallett, A. Galindo, G. Jackson, C.S. Adjiman, C.K. Williams, N. Shah, P. Fennell, An overview of CO_2 capture technologies, Energy Environ. Sci. 3 (2010) 1645–1669.
[3] S. Chaemchuen, N.A. Kabir, K. Zhou, F. Verpoort, Metal-organic frameworks for upgrading biogas via CO_2 adsorption to biogas green energy, Chem. Soc. Rev. 42 (2013) 9304–9332.
[4] J. Wang, L. Huang, R. Yang, Z. Zhang, J. Wu, Y. Gao, Q. Wang, D. O'Hare, Z. Zhong, Recent advances in solid sorbents for CO_2 capture and new development trends, Energy Environ. Sci. 7 (2014) 3478–3518.
[5] N. Hedin, L. Andersson, L. Bergstrom, J. Yan, Adsorbents for the post-combustion capture of CO_2 using rapid temperature swing or vacuum swing adsorption, Appl. Energy 104 (2013) 418–433.
[6] S. Chu, Carbon capture and sequestration, Science 325 (2009) 1599.
[7] N. MacDowell, N. Florin, A. Buchard, J. Hallett, A. Galindo, G. Jackson, C.S. Adjiman, C.K. Williams, N. Shah, P. Fennell, An overview of CO_2 capture technologies, Energy Environ. Sci. 3 (2010) 1645–1669.
[8] Ch.-H. Yu, Ch.-H. Huang, Ch.-S. Tan, Review of CO_2 capture by absorption and adsorption, Aerosol Air Qual Res. 12 (2012) 745–769.
[9] J.D. Figueroa, T. Fout, S. Plasynski, H. McIlvried, R.D. Srivastava, Advances in CO_2 capture technology, Int. J. Greenh. Gas Control 2 (2008) 9–20.
[10] K. Sumida, D.L. Rogow, J.A. Mason, T.M. McDonald, E.D. Bloch, Z.R. Herm, T.H. Bae, J.R. Long, Carbon dioxide capture in metal–organic frameworks, Chem. Rev. 112 (2012) 724–781.
[11] J.M. Huck, L.-Ch. Lin, A.H. Berger, M.N. Shahrak, R.L. Martin, A.S. Bhown, M. Haranczyk, K. Reuter, B. Smit, Evaluating different classes of porous materials for carbon capture, Energy Environ. Sci. 7 (2014) 4132–4146.
[12] R. Ribeiro, C.A. Grande, A.E. Rodrigues, Electric swing adsorption for gas separation and purification: a review, Sep. Sci. Technol. 49 (2014) 1985–2002.
[13] S. Sircar, Basic research needs for design of adsorptive gas separation processes, Ind. Eng. Chem. Res. 45 (2006) 5435–5448.
[14] J.A. Mason, K. Sumida, Z.R. Herm, R. Krishna, J.R. Long, Evaluating metal-organic frameworks for post-combustion carbon dioxide capture via temperature swing adsorption, Energy Environ. Sci. 4 (2011) 3030–3040.
[15] M.A. Granato, T.J.H. Vlugt, A.E. Rodrigues, Molecular simulation of propane-propylene binary adsorption equilibrium in zeolite 13X, Ind. Eng. Chem. Res. 46 (2007) 7239–7245.
[16] C. Shen, Z. Liu, P. Li, J. Yu, Two-stage VPSA process for CO_2 capture from flue gas using activated carbon beads, Ind. Eng. Chem. Res. 51 (2012) 5011–5021.
[17] M. Ishibashi, H. Ota, N. Akutsu, S. Umeda, M. Tajika, J. Izumi, A. Yasutake, T. Kabata, Y. Kageyama, Technology for removing carbon dioxide from power plant flue gas by the physical adsorption method, Energy Convers. Manag. 37 (1996) 929–933.
[18] J. Merel, M. Clausse, F. Meunier, Experimental investigation on CO_2 post-combustion capture by indirect thermal swing adsorption using 13X and 5A zeolites, Ind. Eng. Chem. Res. 47 (2008) 209–215.
[19] K.Z. House, C.F. Harvey, M.J. Aziz, D.P. Schrag, The energy penalty of post-combustion CO_2 capture & storage and its implications for retrofitting the U.S. installed base, Energy Environ. Sci. 2 (2009) 193.
[20] L. Lin, A.H. Berger, R.L. Martin, J. Kim, J.A. Swisher, K. Jariwala, C.H. Rycroft,

A.S. Bhown, M.W. Deem, M. Haranczyk, B. Smit, In silico screening of carbon-capture materials, Nat. Mater. 11 (2012) 633–641.
[21] I. Matito-Martos, A. Martin-Calvo, J.J. Gutierrez-Sevillano, M. Haranczyk, M. Doblare, J.B. Parra, C.O. Ania, S. Calero, Zeolite screening for the separation of gas mixtures containing SO_2, CO_2 and CO, Phys. Chem. Chem. Phys. 16 (2014) 19884–19893.
[22] N.A. Rashidi, S. Yusup, An overview of activated carbons utilization for the post-combustion carbon dioxide capture, J. CO_2 Util. 13 (2016) 1–16.
[23] J. Liu, P.K. Thallapally, B.P. McGrail, D.R. Brown, J. Liu, Progress in adsorption-based CO_2 capture by metal-organic frameworks, Chem. Soc. Rev. 41 (2012) 2308–2322.
[24] Z. Zhang, Z.Z. Yao, S. Xiang, B. Chen, Perspective of microporous metal-organic frameworks for CO_2 capture and separation, Energy Environ. Sci. 7 (2014) 2868–2899.
[25] J. Ling, A. Ntiamoah, P. Xiao, D. Xu, P.A. Webley, Y. Zhai, Overview of CO_2 capture from flue gas streams by vacuum pressure swing adsorption technology, Austin J. Chem. Eng. 1 (2014) 1–7.
[26] J.A. Dunne, M. Rao, S. Sircar, R.J. Gorte, A.L. Myers, Calorimetric heats of adsorption and adsorption isotherms. 2. O_2, N_2, Ar, CO_2, CH_4, C_2H_6 and SF_6 on NaX, H-ZSM-5, and Na-ZSM-5 zeolites, Langmuir 12 (1996) 5896–5904.
[27] P.L. Llewellyn, G. Maurin, Chapter 17—Gas adsorption in zeolites and related materials, Stud. Surf. Sci. Catal. 168 (2007) 555–610.
[28] M. Palomino, A. Corma, F. Rey, S. Valencia, New insights on CO_2-methane separation using LTA zeolites with different Si/Al ratios and a first comparison with MOFs, Langmuir 26 (2010) 1910–1917.
[29] R. Banerjee, A. Phan, B. Wang, C. Knobler, H. Furukawa, M. O'Keeffe, O.M. Yaghi, High-throughput synthesis of zeolitic imidazolate frameworks and application to CO_2 capture, Science 319 (2008) 939–943.
[30] Y.S. Bae, R.Q. Snurr, Development and evaluation of porous materials for carbon dioxide separation and capture, Angew. Chem. Int. Ed. 50 (2011) 11586–11596.
[31] Y. Li, J. Yu, New stories of zeolite structures: their descriptions, determinations, predictions, and evaluations, Chem. Rev. 14 (2014) 7268–7316.
[32] M.E. Davis, Ordered porous materials for emerging applications, Nature 417 (2002) 813–821.
[33] C. Martínez, A. Corma, Inorganic molecular sieves: preparation, modification and industrial application in catalytic processes, Coord. Chem. Rev. 255 (2011) 1558–1580.
[34] D.H. Olson, The crystal structure of dehydrated NaX, Zeolites 15 (1995) 439–443.
[35] A. Corma, From microporous to mesoporous molecular sieve materials and their use in catalysis, Chem. Rev. 97 (1997) 2373–2420.
[36] M. Eic, D.M. Ruthven, Diffusion of linear paraffins and cyclohexane in NaX and 5A zeolite crystals, Zeolites 8 (1988) 472–479.
[37] B. Smit, T.L.M. Maesen, Molecular simulations of zeolites: adsorption, diffusion, and shape selectivity, Chem. Rev. 108 (2008) 4125–4184.
[38] H. Prats, D. Bahamon, G. Alonso, X. Giménez, P. Gamallo, R. Sayós, Optimal faujasite structures for post combustion CO_2 capture and separation in different swing adsorption processes, J. CO_2 Util. 19 (2017) 100–111.
[39] W. Löwenstein, The distribution of aluminum in the tetrahedra of silicates and aluminates, Am. Mineral. 39 (1954) 92–96.
[40] S. Calero, D. Dubbeldam, R. Krishna, B. Smit, T.J.H. Vlugt, J.F.M. Denayer, J.A. Martens, T.L.M. Maesen, Understanding the role of sodium during adsorption: a force field for alkanes in sodium-exchanged faujasites, J. Am. Chem. Soc. 126 (2004) 11377–11386.
[41] A. Martin-Calvo, J.B. Parra, C.O. Ania, S. Calero, Insights on the anomalous adsorption of carbon dioxide in LTA zeolites, J. Phys. Chem. C 118 (2014) 25460–25467.
[42] A. Garcia-Sánchez, C.O. Ania, J.B. Parra, D. Dubbeldam, T.J.H. Vlugt, R. Krishna, S. Calero, Transferable force field for carbon dioxide adsorption in zeolites, J. Phys. Chem. C 113 (2009) 8814–8820.
[43] A. Martin-Calvo, J.J. Gutiérrez-Sevillano, J.B. Parra, C.O. Ania, S. Calero, Transferable force fields for adsorption of small gases in zeolites, Phys. Chem. Chem. Phys. 17 (2015) 24048–24055.
[44] S. Plimpton, Fast parallel algorithms for short-range molecular dynamics, J. Comp. Phys. 117 (1995) 1–19.
[45] D. Frenkel, B. Smit, Understanding Molecular Simulation: from Algorithms to Applications, Academic Press, London, 2002.
[46] E.J. Granite, H.W. Pennline, Photochemical removal of mercury from flue gas, Ind. Eng. Chem. Res. 41 (2002) 5470–5476.
[47] D.Y. Peng, D.B. Robinson, A new two-constant equation of state, Ind. Eng. Chem. Fundam. 15 (1976) 59–64.
[48] E. W. Lemmon, M. O. McLinden, M. L. Huber, NIST thermodynamic properties of refrigerants and refrigerants mixtures database (REFPROP), version 7.0, 2002.
[49] S.K. Shibata, S.I. Sandler, Critical evaluation of equation of state mixing rules for the prediction of high-pressure phase equilibria, Ind. Eng. Chem. Res. 28 (1989) 1893–1898.
[50] J. Vrabec, G.K. Kedia, U. Buchhauser, R. Meyer-Pittroff, H. Hasse, Thermodynamic models for vapor-liquid equilibria of nitrogen + oxygen + carbon dioxide at low temperatures, Cryogenics 49 (2009) 72–79.
[51] T.H. Bae, M.R. Hudson, J.A. Mason, W.L. Queen, J.J. Dutton, K. Sumida, K.J. Micklash, S.S. Kaye, C.M. Brown, J.R. Long, Evaluation of cation-exchanged zeolite adsorbents for post-combustion carbon dioxide capture, Energy Environ. Sci. 6 (2013) 128–138.
[52] M. Wiedt, J.P. Sculley, W.M. Verdegaal, A.A. Yakovenko, H. Zhou, Unprecedented activation CO_2 capture properties of an elastic single-molecule trap, Chem. Commun. 49 (2013) 9612–9614.
[53] J.P. Sculley, W.M. Verdegaal, W.G. Lu, M. Wriedt, H. Zhou, High-throughput analytical model to evaluate materials for temperature swing adsorption processes, Adv. Mater. 25 (2013) 3957–3961.
[54] T.J.H. Vlugt, E. García-Pérez, D. Dubbeldam, S. Ban, S. Calero, Computing the heat of adsorption using molecular simulations: the effect of strong coulombic interactions, J. Chem. Theory Comput. 4 (2008) 1107–1118.
[55] W. G. Allinson, M. T. Ho, P. R. Neal, D. E. Wiley, The methodology used for estimating the costs of CCS, Conference 8th International Conference on Greenhouse Gas Control Technologies (GHGT-8), At Trondheim, Norway.
[56] J. Boerio-Goates, R. Stevens, B.K. Hom, B.F. Woodfield, P.M. Piccione, M.E. Davis, A. Navrotsky, Heat capacities third-law entropies and thermodynamic functions of SiO_2 molecular sieves from T = 0 K to 400 K, J. Chem. Therm. 34 (2002) 205–227.
[57] A. Findikakis, Heat Capacity Analysis Report, U.S. Department of Energy. November 2004. 10.2172/838658.
[58] P. Vieillard, A predictive model for the entropies and heat capacities of zeolites, Eur. J. Mineral 22 (2010) 823–836.
[59] R.H. Weiland, J.C. Dingman, D.B. Cronin, Heat capacity of aqueous monoethanolamine, diethanolamine N-methyldiethanolamine, and N-methyldiethanolamine-based blends with carbon dioxide, J. Chem. Eng. Data 42 (1997) 1004–1006.
[60] C. W. Skarstrom, Method and apparatus for fractionating gaseous mixtures by adsorption, US Patent 2944627 A, 1960.
[61] M. Khurana, S. Farooq, Adsorbent screening for post?combustion carbon capture: a method relating equilibrium isotherm characteristics to optimum VSA process performance, Ind. Eng. Chem. Res. 55 (2016) 2447–2460.
[62] A.K. Rajagopalan, A.M. Avila, A. Rajendran, Do adsorbent screening metrics predict process performance? A process optimization based study for post-combustion capture of CO_2, Int. J. Greenh. Gas Control 46 (2016) 76–85.
[63] H. Huang, W. Zhang, D. Liu, B. Liu, G. Chen, C. Zhong, Effect of temperature on gas adsorption and separation in ZIF-8: A combined experimental and molecular simulation study, Chem. Eng. Sci. 66 (2011) 6297–6305.
[64] W.R. Lee, S.Y. Hwang, D.W. Ryu, K.S. Lim, S.S. Han, D. Moon, J. Choide, C.S. Hong, Diamine-functionalized metal-organic framework: exceptionally high CO_2 capacities from ambient air and flue gas, ultrafast CO_2 uptake rate, and adsorption mechanism, Energy Environ. Sci. 7 (2014) 744–751.
[65] T.M. McDonald, J.A. Mason, X. Kong, E.D. Bloch, D. Gygi, A. Dani, V. Crocellà, F. Giordanino, S.O. Odoh, W.S. Drisdell, B. Vlaisavljevich, A.L. Dzubak, R. Poloni, S.K. Schnell, N. Planas, K. Lee, T. Pascal, L.F. Wan, D. Prendergast, J.B. Neaton, B. Smit, J.B. Kortright, L. Gagliardi, S. Bordiga, J.A. Reimer, J.R. Long, Cooperative insertion of CO_2 in diamine-appended metal-organic frameworks, Nature 519 (2015) 303–308.
[66] M. Zaman, J.H. Lee, Carbon capture from stationary power generation sources: a review of the current status of the technologies, Korean J. Chem. Eng. 30 (2013) 1497–1526.

Supplementary Data

Computational Simulation Study of the influence of Faujasite Si/Al ratio on CO_2 capture by Temperature Swing Adsorption

Hèctor Prats, Daniel Bahamon, Xavier Giménez, Pablo Gamallo* and Ramón Sayós

Departament de Ciència de Materials i Química Física & Institut de Química Teòrica i Computacional (IQTCUB), Universitat de Barcelona, C. Martí i Franquès 1, 08028 Barcelona, Spain.

**Corresponding author: Pablo Gamallo*
Email: gamallo@ub.edu / Tel. +34934039308

I. Heat capacity calculation

The heat capacities for all structures have been computed by means of the predictive model from Vieillard[i], based on summation techniques. This model has been devised for all zeolites, both hydrated and anhydrous, and has been proven to give deviations between measured and predicted values below 3%, for all temperatures between 298 and 500 K. This method is based on the previous oxide summation technique methods from Robinson & Hass[ii], Berman & Brown[iii] and Van Hinsberg *et al.*[iv], which consider that the thermodynamic properties of silicate minerals can be described as a linear combination of the fractional properties of their constituent polyhedral. Thus, given the thermodynamic properties of these polyhedral, the thermodynamic properties of minerals can be estimated, where only the crystallography of the mineral needs to be known. The Vieillard method improves the prediction of heat capacity of zeolites using a multiple linear regression method, which exclusively targets zeolites, and limits the range of minerals used as a basis for the model.

In the present work, we predict the unit cell heat capacity of our faujasite structures in the following way:

$$C_p^{FAU}(T) = n_{SiO_2} \cdot C_p^{SiO_2}(T) + n_{\mathrm{Al_2O_3}} \cdot C_p^{\mathrm{Al_2O_3}}(T) + n_{\mathrm{Na_2O}} \cdot C_p^{\mathrm{Na_2O}}(T)$$

where C_p^i is are the heat capacities of the i polyhedral, and n_i is the total number of i polyhedral present in a unit cell, and the values C_p^i are obtained from the Maier-Kelley equation:

$$C_p^i(T) = a_i + b_i T + c_i T^{-2}$$

The parameter values used in the Vieillard method are listed in the following table:

	a ($J \cdot K^{-1} \cdot mol^{-1}$)	b ($J \cdot K^{-2} \cdot mol^{-1}$)	$c \times 10^{-5}$ ($J \cdot K \cdot mol^{-1}$)
SiO_2	23.5	0.1045	-9.0
Al_2O_3	117.347	-1.1860	-0.190
Na_2O	55.612	1.1149	0.190

Table S1. Maier-Kelley parameters taken from Viellard used in the present work.

Table S2 shows the density and the different number of polyhedrals per unit cell for the ten faujasite structures studied.

	0-FAU	6-FAU	12-FAU	24-FAU	32-FAU	48-FAU	64-FAU	77-FAU	88-FAU	96-FAU
Na+	0	6	12	24	32	48	64	77	88	96
nº SiO_2	192	186	180	168	160	144	128	115	104	96
nº Al_2O_3	0	3	6	12	16	24	32	38.5	44	48
nº Na_2O	0	3	6	12	16	24	32	38.5	44	48
ρ (kg/m^3)	1183.1	1197.0	1211.0	1238.8	1257.4	1294.6	1331.7	1361.9	1387.5	1406.1

Table S2. Density values and number of polyhedrals corresponding to each faujasite structure.

Finally, Figure S1 shows the calculated values of heat capacity for the ten different faujasite structures considered in the present study. Interestingly, there is a nearly linear relationship between the heat capacity and the temperature. Additionally, the slope of the function decreases as we increase the number of Al atoms of the structure, presumably due to the negative value of *b* parameter for Al_2O_3. Thus, at temperature below 360 K the maximum heat capacity if found for 96-FAU, whereas 0-FAU presents the maximum heat capacity above 360 K.

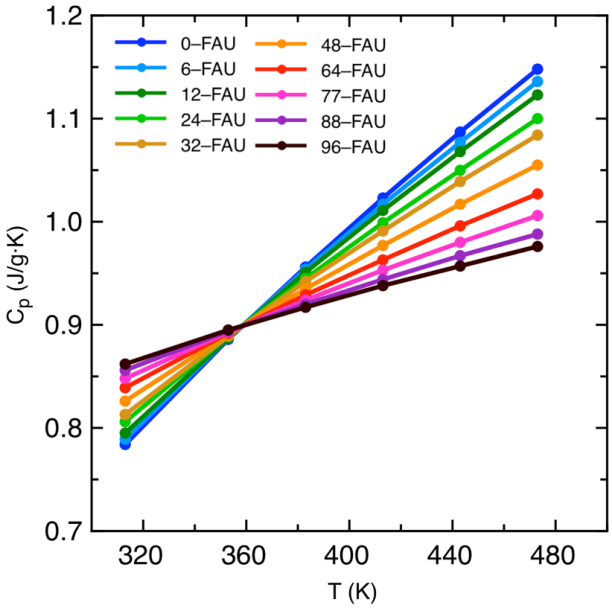

Figure S1. Calculated heat capacity as function of temperature for the ten different faujasite structures. Lines are guide to the eyes.

II. Selectivity with IAST

Selectivity values obtained from IAST calculations using pure isotherm data are substantially larger than those values obtained directly from ternary mixture isotherms (Figure 2), as shown in Figure S2.

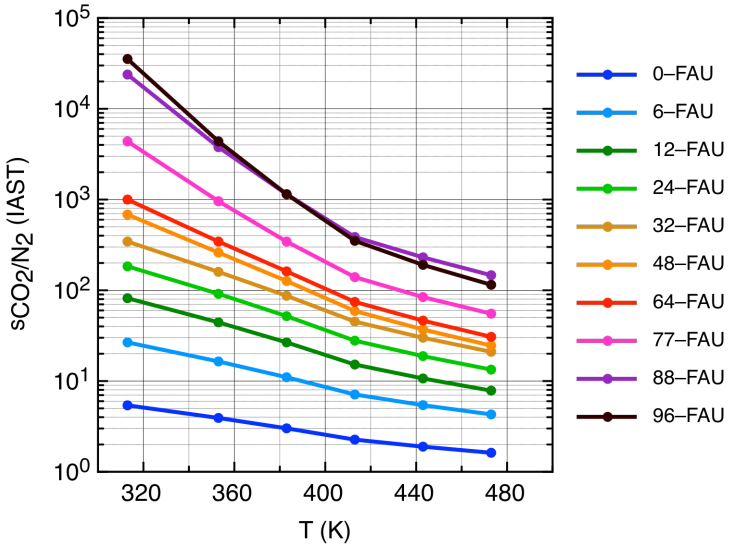

Figure S2. Calculated IAST selectivities for CO_2 relative to N_2 as a function of temperature, for ten different n-FAU structures (P = 100 kPa).

III. Pure component adsorption isobars for CO_2.

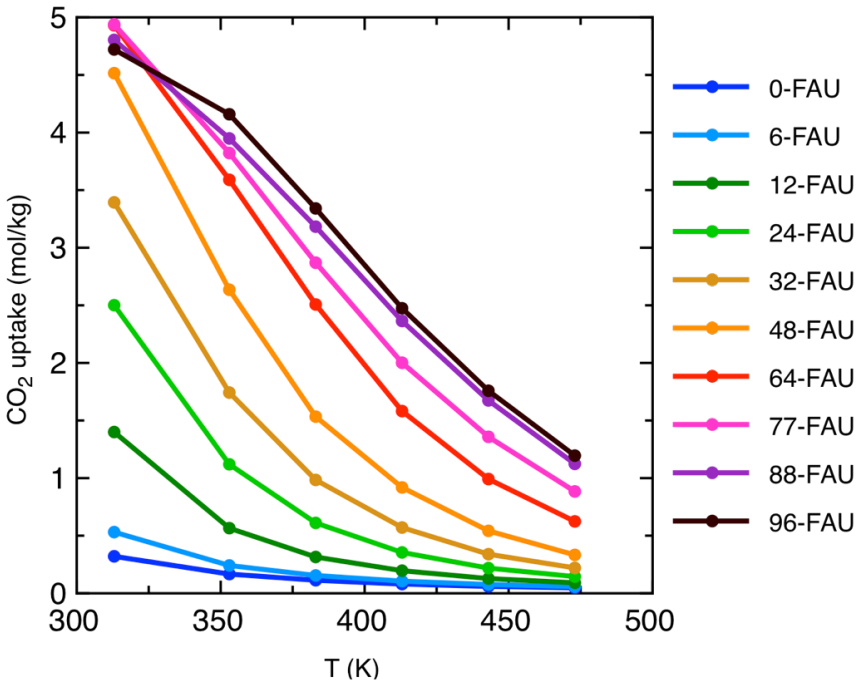

Figure S3. CO_2 pure adsorption isobars for the ten different faujasite structures at P = 100 kPa. These structures have been labelled as n-FAU, where n is the number of aluminium or sodium atoms per unit cell. Lines are guide to the eyes.

IV. Mixture adsorption isobars for CO_2 and N_2.

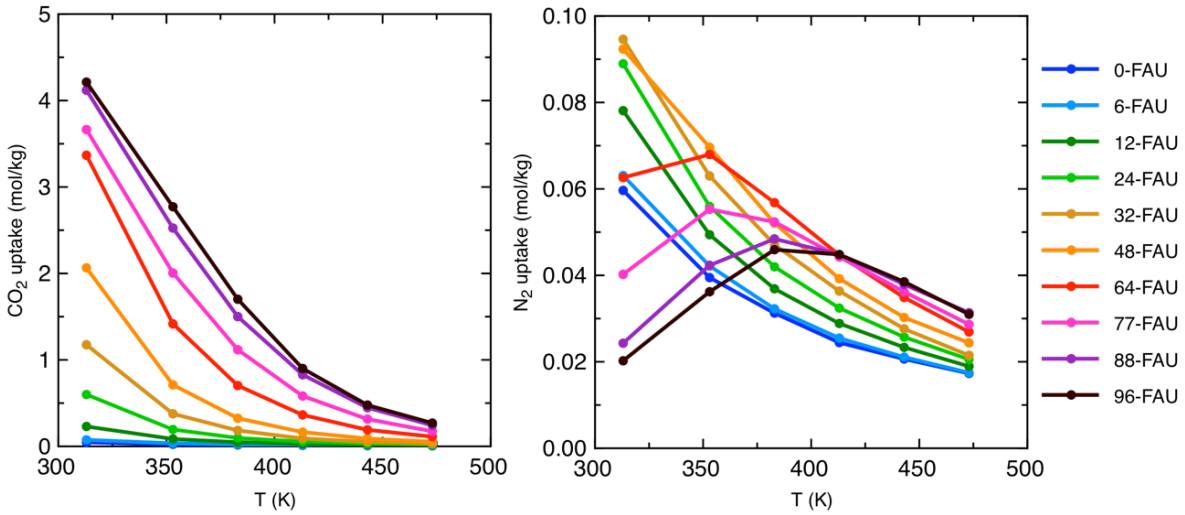

Figure S4. CO_2 (left) and N_2 (right) adsorption isobars for the ten different faujasite structures corresponding to the following mixture: CO_2 (15%), N_2 (80%) and O_2 (5%) at P = 100 kPa. Lines are guide to the eyes.

As the temperature rises, the loading of CO_2 falls monotonously for all adsorbents. At high Al content structures, this decrease is very pronounced. As a consequence, the void adsorption sites increase and more N_2 molecules will enter inside the pores. When the temperature further increases, the remarkable thermal motion emerges, which results in a higher desorption of N_2 molecules. Thus, for high Al content structures the loading of N_2 show a trend of first rising and then declining.

V. Purity comparison (TSA, PSA and VSA)

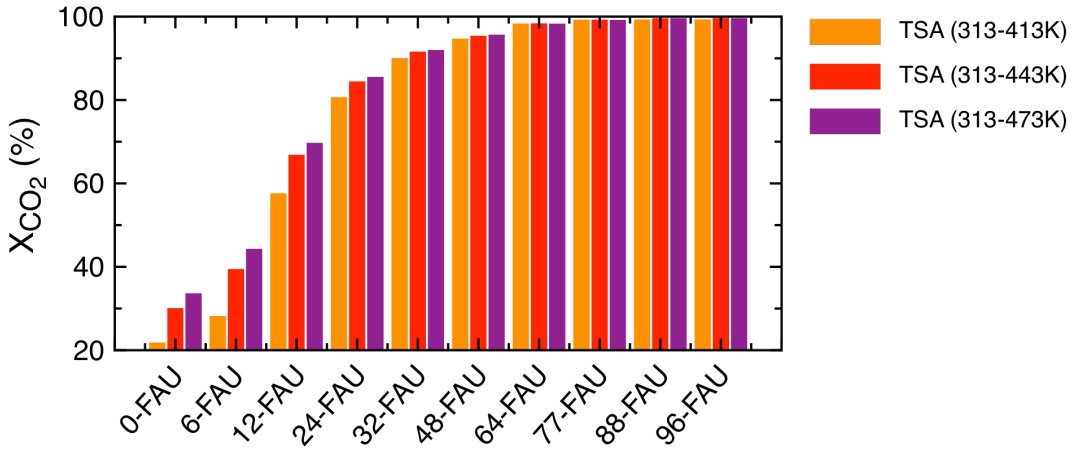

Figure S5. Comparison of CO_2 purity at outlet for TSA process operating at three different desorption temperatures (P = 100 kPa).

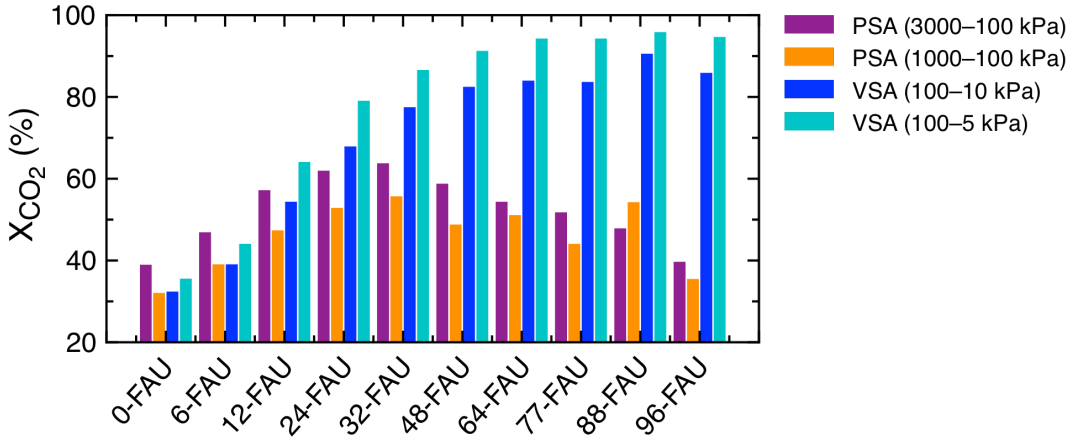

Figure S6. Comparison of CO_2 purity at outlet for PSA and VSA processes operating different conditions (T = 313 K).

VI. Working capacity comparison (TSA, PSA and VSA)

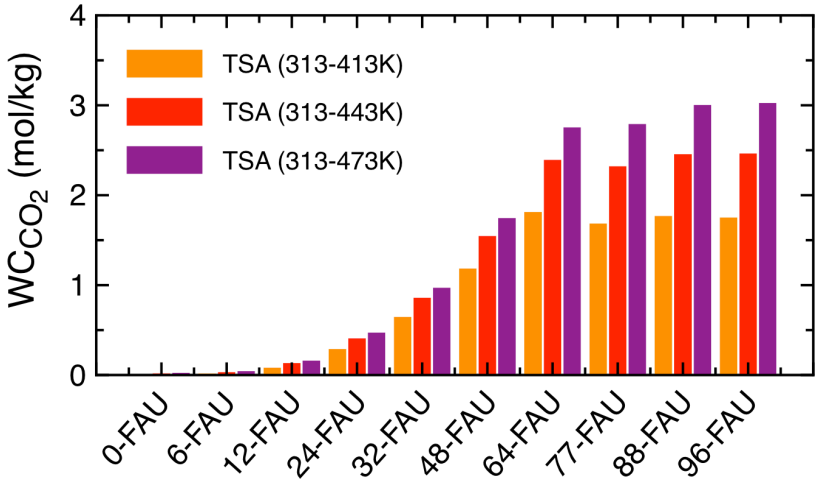

Figure S7. Comparison of CO_2 working capacity for TSA process operating at three different desorption temperatures (P = 100 kPa).

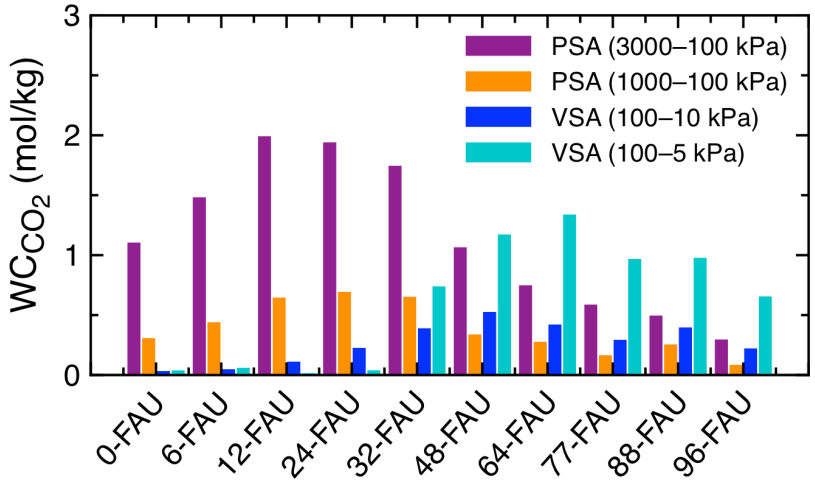

Figure S8. Comparison of CO_2 working capacity for PSA and VSA processes operating different conditions (T = 313 K).

VII. Thermal regeneration energy (TSA) and adiabatic work for expansion (VSA) or compression (PSA)

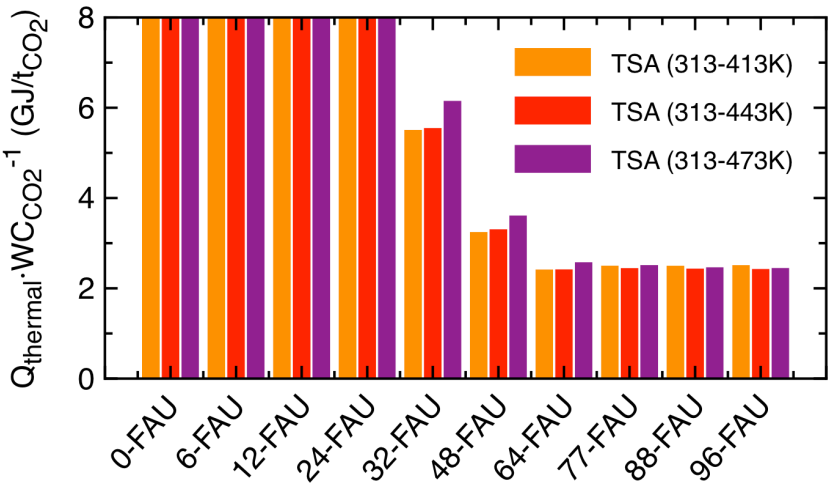

Figure S9. Comparison of thermal regeneration energy per ton CO_2 for TSA process operating at three different desorption temperatures (P = 100 kPa).

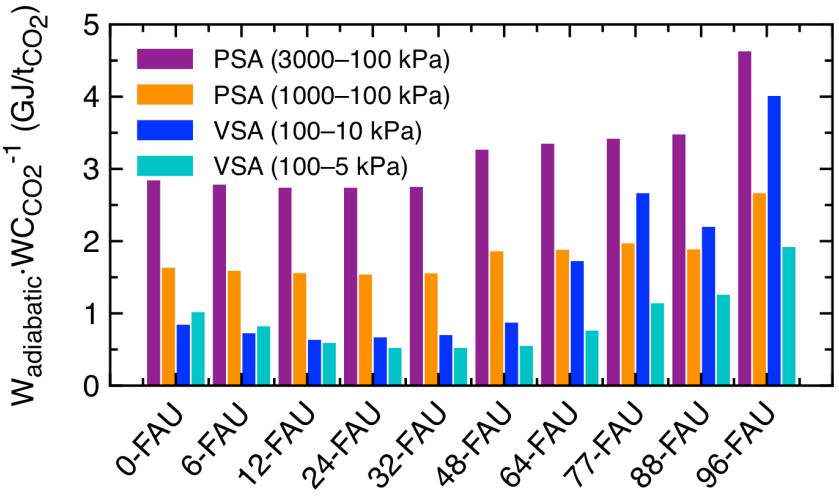

Figure S10. Comparison of adiabatic work for expansion/compression per ton CO_2 for VSA/PSA processes operating different conditions (T = 313 K).

[i] P. Vieillard, A predictive model for the entropies and heat capacities of zeolites, Eur. J. Mineral. 22(2010) 823-836.

[ii] G. R. Robinson, J. L. Hass, Heat capacity, relative enthalpy, and calorimetric entropy of silicate minerals: An empirical method of prediction, Am. Mineral. 68 (1983) 541-553.

[iii] R. G. Berman, T. H. Brown, Heat capacity of minerals in the system Na_2O-K_2O-CaO-MgO-FeO-Fe_2O_3-Al_2O_3-SiO_2-TiO_2-CO_2: representation, estimation, and high temperature extrapolation, Contrib. Mineral. Petrol. 89 (1985) 168-183.

[iv] V. J. Van Hinsberg, S. P. Vriend, J. C. Schumacher, A new method to calculate end-member thermodynamic properties of minerals from their constituent polyhedra I: enthalpy, entropy and molar volume, J. Metamorphic Geol. 23 (2005) 165-179.

3.4. Summary and conclusions

The performance of ten faujasite structures with different Al content towards post-combustion CO_2 capture have been studied and presented in this chapter. Pure gas adsorption isotherms obtained from GCMC simulations show that CO_2 molecules interact strongly with the Na^+ cations. Since the number of Na^+ cations and the number of Al atoms coincide, high Al content faujasite structures present the higher uptakes (see Figure 1 from Publication 1). Thus, the 96-FAU structure (i.e., the faujasite structure with the highest possible Al content) is the first reaching saturation, whereas 0-FAU saturates the last. However, the volume occupied by the cations inside the framework is not negligible, and the available pore volume for CO_2 adsorption decreases as the Al content increases. Therefore, at high-pressure regimes the maximum uptake is found for faujasites having intermediate Al content. In all pure gas adsorption isotherms, the CO_2 uptake is significantly higher than that of N_2 or O_2 at the same conditions, suggesting a good selectivity towards CO_2. The isosteric heat of adsorption for CO_2 as function of the Al content follows the same trend than the CO_2 uptake. Due to the strong interaction between CO_2 and Na^+, the isosteric heat increases from 13 to 42 $kJ \cdot mol^{-1}$ from the 0-FAU to the 96-FAU structure, respectively.

Ternary mixture simulations show that 96-FAU structure is really the one presenting the highest CO_2 selectivity (see Figure 4 from Publication 1), especially at low pressures, with values up to 1150, surpassing other popular adsorbent materials such as zeolite Ca-A, Mg-MOF-74 and MOF Cu-BTC. The selectivity decreases when lowering the Al content, with 0-FAU structure presenting the lowest values (i.e., ranging from 4 to 6, at 5 and 5000 kPa, respectively).

At this point, one might think that high Al content structures are the best faujasites for post-combustion CO_2 capture, due to their high uptake and selectivity. But this is true in practice? The crucial issue in this context is the energy required to separate a given amount of CO_2, commonly expressed in GJ per ton of CO_2. This energy depends on the amount of CO_2 extracted per cycle, the operating cost for an adsorption/desorption cycle (which in turn depend on the type of Swing Adsorption process chosen and the operating conditions: compression in PSA, expansion in VSA or heating in TSA), as well as the capital costs of equipment and adsorbent materials, the costs for previous dehumidification of the flue gas and the costs for final compression and transport.

Assuming that most of these costs are independent of the chosen faujasite and Swing Adsorption process, we can focus on two main factors: 1) the amount of CO_2 extracted per cycle, also known as the *working capacity*, and 2) the amount of energy needed per adsorption/desorption cycle. The ratio between the first and the second term will determine the performance of a given structure under chosen operating conditions.

We begin with our attention focusing on the working capacity. This quantity can be computed directly from GCMC simulations as the difference between the CO_2 uptake at adsorption and desorption (or regeneration) conditions. It turns out that there is no best structure. Instead, depending on the selected Swing Adsorption process and the operating conditions (i.e., P_{feed}, P_{regen}, T_{feed} and T_{regen}), one or another structure should be chosen in order to maximize the working capacity. While high Al content structures present the highest working capacities for TSA, intermediate and low Al content structures are better candidates for VSA and PSA, respectively (see Figure 6c in Publication 2).

What about the energy requirements? The amount of power required per adsorption cycle on a PSA or VSA unit can be calculated as the adiabatic work for compression or expansion, respectively, which mainly depends on the feeding and regeneration pressures and the working capacity (see Eqs. (7) and (8) in Publication 1). These quantities can be compared with the thermal regeneration energy required per adsorption cycle on a TSA unit. The latter depends on the heat capacity of the adsorbent material, the isosteric heat of adsorption and the working capacity (see Eq. (6) in Publication 2). Of course, if we reduce the feeding pressure on a PSA unit, or we reduce the regeneration temperature on a TSA unit, or we increase the regeneration pressure on a VSA unit, the energy required per adsorption/desorption cycle will be lower. However, the working capacity will lower as well, so a good compromise is needed.

The present study shows that, in general, TSA processes using faujasites as adsorbent material are more expensive than those based on PSA or VSA, except for high Al content structures (see Figure 6d in Publication 2). Note that, however, for a true comparison between thermal energy (cheap) and adiabatic work (expensive), a conversion coefficient should be considered, which would reduce the energetic requirements for TSA. Interestingly, intermediate Al content FAU structures working on a VSA unit present the lowest energetic cost per ton of CO_2 captured.

3.5. References

1 P. L. Llewellyn and G. Maurin, Studies in surface science and catalysis, eds. J. Čejka, H. van Bekkum, A. Corma and F. Schüth, Elsevier, **2007**.

2 M. Palomino, A. Corma, F. Rey and S. Valencia, New insights on CO_2−methane separation using LTA zeolites with different Si/Al ratios and a first comparison with MOFs, *Langmuir*, **2010**, 26, 1910–1917.

3 M. Pera-Titus, Porous inorganic membranes for CO_2 capture: present and prospects, *Chem. Rev.*, **2014**, 114, 1413–1492.

4 Y. Li and J. Yu, New stories of zeolite structures: their descriptions, determinations, predictions, and evaluations, *Chem. Rev*., **2014**, 114, 7268–7316.

5 M. E. Davis, Ordered porous materials for emerging applications, *Nature*, **2002**, 417, 813.

6 C. Martínez and A. Corma, Inorganic molecular sieves: preparation, modification and industrial application in catalytic processes, *Coord. Chem. Rev*., **2011**, 255, 1558–1580.

7 D. H. Olson, The crystal structure of dehydrated NaX, *Zeolites*, **1995**, 15, 439–443.

8 M. Eic and D. M. Ruthven, Diffusion of linear paraffins and cyclohexane in NaX and 5A zeolite crystals, *Zeolites*, **1988**, 8, 472–479.

9 E. J. Granite and H. W. Pennline, Photochemical removal of mercury from flue gas, *Ind. Eng. Chem. Res*., **2002**, 41, 5470–5476.

10 A. L. Myers and J. M. Prausnitz, Thermodynamics of mixed-gas adsorption, *AIChE Journal*, **1965**, 11, 121–127.

11 O. Talu, Measurement and analysis of mixture adsorption equilibrium in porous solids, *Chem. Ing. Tech*., **2011**, 83, 67–82.

CHAPTER FOUR

The WGSR on Cu(111) surface

4.1. Introduction

The previous chapter was devoted to gas separation of a typical post-combustion mixture. However, it should be noted that the results of the previous chapter were based purely on equilibrium properties. Now we enter the world of catalysis, the second main topic of the present thesis. To this end we study the WGSR, a well-known chemical reaction of great interest. In this context, one cannot focus only in thermodynamic properties. Instead, one has to consider also the kinetics of the system. In the previous GCMC study, we give probabilities for GCMC movements (i.e., insertion, deletion, translation and rotation) to occur. Analogously, in this chapter we give probabilities for processes such as adsorption, desorption, diffusion or chemical reaction to occur. This is the basis of the kMC method, which provides information about surface coverages and turnover frequencies that ultimately are required for reactor level modeling. Applications of the WGSR have been highlighted in the introduction of this thesis (Chapter 1).

Due to its exothermicity, several catalysts that are active at relatively low temperatures are being investigated. In fact, several theoretical and experimental studies have been undertaken aimed at disclosing the molecular mechanism and thus obtaining the necessary knowledge for potential improvement through a rational design. Among the different types of systems that have been explored one can highlight those involving well-defined metallic surfaces (e.g., Pd(111)[1], Pt(111)[1,2], Pt(211)[2], Pt(322)[2], Cu(321)[3], Cu(111)[4,5]…), inverse catalysts constituted by metal oxide nanoparticles supported on metals (e.g., CeO_x/Cu(111), CeO_x/Au(111)[6]…), metallic nanoparticles supported on oxides (e.g., Cu/ZnO(0001)[7], Cu/TiO_2(110), Au/TiO_2(110)[8]…) or more recently carbides as in the novel Au/TiC(001) system[9].

Nevertheless, in spite of the progress in the search of more efficient WGSR catalysts, Cu continues to be at present the main ingredient of the industrially used catalysts. Not surprisingly a huge effort has been devoted to understand the microscopic molecular mechanism of the WGSR catalyzed by Cu containing systems. The work of Hadden *et al.*[10] presented evidence that the activity of the CuO/ZnO/Al_2O_3 catalysts on the WGSR can be closely correlated to the copper surface area. Since in these catalysts large Cu particles are present, predominantly exhibiting (111) facets, the Cu(111) surface has been usually taken as a typical benchmark for WGSR studies.

Thus, in this chapter a systematic first-principles kMC study of the WGSR on Cu(111) is presented, including a total of 34 elementary steps with all reaction rates obtained from periodic DFT based calculations.

4.2. Publication 3

Kinetic Monte Carlo simulations of the water gas shift reaction on Cu(111) from density functional theory based calculations

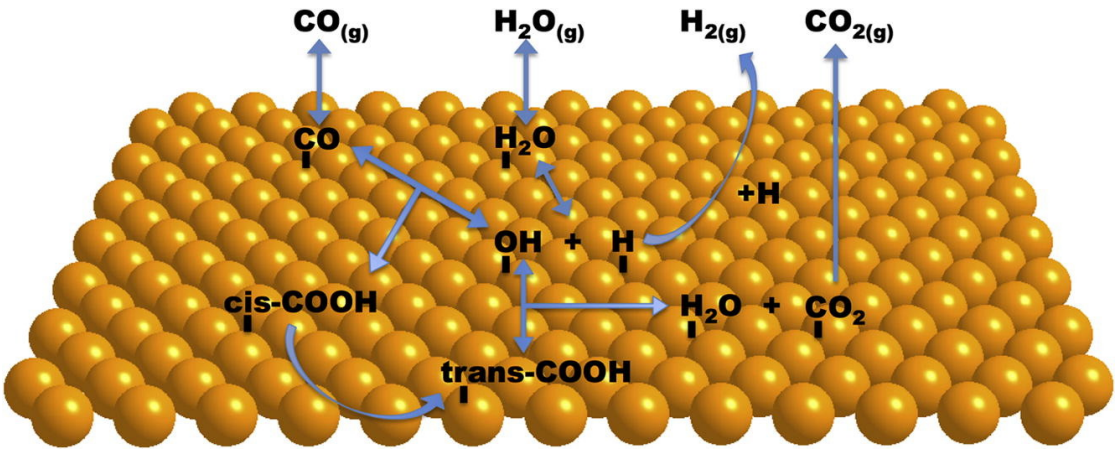

Journal of Catalysis 333 (2016) 217–226

Contents lists available at ScienceDirect

Journal of Catalysis

journal homepage: www.elsevier.com/locate/jcat

Kinetic Monte Carlo simulations of the water gas shift reaction on Cu (1 1 1) from density functional theory based calculations

Hèctor Prats, Leny Álvarez, Francesc Illas, Ramón Sayós *

Departament de Química Física and Institut de Química Teòrica i Computacional (IQTCUB), Universitat de Barcelona, C. Martí i Franquès 1, 08028 Barcelona, Spain

ARTICLE INFO

Article history:
Received 30 May 2015
Revised 30 October 2015
Accepted 31 October 2015

Keywords:
Kinetic Monte Carlo
Water gas shift reaction
Density functional theory
Mechanisms
Redox
Associative
Carboxyl
Copper(1 1 1) surface
Microkinetic model
Simulations

ABSTRACT

A systematic first-principles kinetic Monte Carlo study of the water gas shift reaction taking place on the Cu(1 1 1) surface is presented including adsorption/desorption, diffusion and other elementary chemical reactions, totalling 34 elementary steps with all reaction rates obtained from periodic density functional theory based calculations. The kinetic Monte Carlo simulations were carried out at different partial pressures and temperatures. The results show that the diffusion processes cannot be neglected and that the reaction proceeds predominantly through an associative mechanism via a carboxyl intermediate. The analysis of temperature dependence shows an Arrhenius behaviour with an apparent activation energy of 0.5–0.8 eV in agreement with experiments and with previous microkinetic studies. The effect of H_2O/CO ratio on this reaction shows that mixtures with higher CO proportion enhance the reactivity, also in accordance with previous studies. The present work allows one to ascertain the relative importance of the different steps in the mechanism of water gas shift reaction over Cu(1 1 1) at several conditions as well as to see the coverage evolution of the surface.

1. Introduction

The water gas shift reaction (WGSR) involves CO and H_2O to produce CO_2 and H_2. It is an exothermic reaction

$$CO + H_2O \rightarrow CO_2 + H_2, \quad \Delta_r H^0_{298.15\ K} = -0.43\ eV$$

constituting an important industrial process involved in the production of high purity hydrogen [1]. Hence, this at first sight simple reaction is relevant to the synthesis of ammonia and methanol. It is also involved in the town gas purification and in other important industrial and technologically relevant processes. The interest in the WGSR has been renewed due to the stringent requirements of high purity hydrogen needed in fuel cells [2], where CO concentration below 0.5% is needed to prevent poisoning of the Pt anode, a key component of these devices. Industrially, the WGSR is typically carried out in two stages: a first one at quite high temperature (300–450 °C) and second one at a lower temperature (200–300 °C). The high temperature stage uses iron oxide–chromium oxide based catalysts ($Fe_2O_3/Cr_2O_3/MgO$) [3] while copper based catalysts with inclusion of Zn, Cr and Al oxides [4] and $CuO/ZnO/Al_2O_3$ [5] are used in low temperature reactors [6]. Nevertheless, it is worth pointing out that these catalysts usually require lengthy and quite complex activation steps before usage.

Several alternatives are being investigated to find WGSR catalysts that are active at relatively low temperatures. To this end several theoretical and experimental studies have been undertaken aimed at disclosing the molecular mechanism and thus obtaining the necessary knowledge for potential improvement through a rational design. Two main reaction mechanisms, redox and associative, have been proposed for different catalytic surfaces. The two mechanisms start from H_2O dissociation, but the former continues with OH dissociation to produce adsorbed O atoms whereas in the latter CO_2 is produced through a carboxyl (COOH) intermediate. Among the different types of systems that have been explored one can highlight those involving well-defined metallic surfaces Pd(1 1 1) [7], Pt(1 1 1) [7,8], Pt(2 1 1) [8], Pt(3 2 2) [8], Cu (3 2 1) [9], Cu(1 1 1) [10,11], inverse catalysts constituted by metal oxide nanoparticles supported on metals CeO_x/Cu(1 1 1), CeO_x/Au (1 1 1) [12], metallic nanoparticles supported on oxides Cu/ZnO $(0\,0\,0\bar{1})$ [13], $Cu/TiO_2(1\,1\,0)$ and $Au/TiO_2(1\,1\,0)$ [14] or, more recently carbides as in the novel Au/TiC(0 0 1) system [15]. A series of systems based on other supported gold nanocatalysts have recently been reviewed [16]. Based on the information extracted from experiments on model catalysts and on theoretical models, more complex systems have been proposed involving a metallic

* Corresponding author.
E-mail address: r.sayos@ub.edu (R. Sayós).

http://dx.doi.org/10.1016/j.jcat.2015.10.029
0021-9517/

nanoparticle supported on CeO_x nanoparticles which, in turn, are supported in TiO_2(1 1 0) [17]. The resulting catalysts have been proven to significantly increase the H_2 production rate [18].

Nevertheless, in spite of the progress in the search of more efficient WGSR catalysts, Cu continues to be at present the main ingredient of the industrially used catalysts. Not surprisingly a huge effort has been devoted to understand the microscopic molecular mechanism of the WGSR catalysed by Cu containing systems. The work of Hadden et al. [19] presented evidence that the activity of the CuO/ZnO/A1$_2$O$_3$ catalysts on the WGSR can be closely correlated to the copper surface area. Since in these catalysts large Cu particles are present, predominantly exhibiting (1 1 1) facets, the Cu(1 1 1) surface has been usually taken as a typical benchmark for WGSR studies. In particular, previous studies used Density Functional Theory (DFT) calculations to investigate the WGSR mechanisms on Cu(1 1 1) surface, determining the energy barriers of all elementary processes [10,11] and showing that the associative mechanism via carboxyl species dominates over the redox mechanism via the oxidation of CO by atomic O. This picture was also confirmed by a microkinetic model including in all 32 elementary processes with transition state theory derived reaction rate constants at a temperature of 463 K and pressure of 1 bar, using DFT energy barriers and partition functions [10]. The microkinetic analysis carried out by Gokhale et al. [10] showed as well that water dissociation was the rate-limiting step for WGSR on Cu (1 1 1). Nevertheless, in this microkinetic model some reaction rate parameters had to be modified to better match the WGSR experimental data.

In order to reach a more detailed picture beyond the mean field approximation inherent to the microkinetic approach, we present a comprehensive first-principles kinetic Monte Carlo (kMC) study of the WGSR over Cu(1 1 1) surface and we analyse the results obtained from kMC simulations at several temperatures and partial pressures. A total of 34 elementary processes are considered, including also CO, OH, H and O surface diffusion processes. Reaction rates for all processes are obtained from DFT data along with transition state theory or collision theory. Some additional DFT calculations were also carried out to complete data missing in the literature. The results of the present kMC study are compared to those from the microkinetic model abovementioned and to other available experimental and theoretical studies.

The rest of paper is organized as follows. Section 2 includes the description of the lattice-gas model chosen and outlines the set of elementary processes taken into account, and it also reports the details of the kMC method and contains important details about the calculation of the different reaction rates, which represents the key ingredient of the whole approach. Section 3 presents the kMC simulations for several temperatures and partial pressures discussing their effect on the WGSR mechanism and H_2 production. Finally, Section 4 summarizes the main conclusions of the present investigation.

2. Theory

2.1. Lattice-gas model

In order to carry out the kinetic Monte Carlo simulations, a suitable model of the surface of interest is needed. In the present work, the Cu(1 1 1) surface is represented by a two-dimensional hexagonal periodic grid of $L \times L$ points, where each point represents one catalytically active (1 1 1) surface site. The convergence with the lattice size has been tested by computing the final (i.e., steady-state) H_2 production for several surface models with different L numbers (i.e., 8–64), concluding that the results for the 25×25 lattice model virtually coincide with those obtained using larger surface models. Periodic boundary conditions have been applied to provide an adequate representation of the periodicity exhibited by the Cu(1 1 1) surface. In this way, surface species jumping across the boundary reappear at the opposite side of the lattice. All sites are considered equally probable for adsorption of both reactants species (i.e., CO and H_2O) and it is assumed that an adsorbed species in a given site can interact with its six nearest neighbours in the hexagonal periodic grid. Moreover, all other possible intermediates adsorbed species (e.g., OH, H, COOH,...) will use only one adsorption site, excepting the bidentate formate (HCOO) that needs two sites, as previous DFT calculations have shown [10].

For the present kMC simulations the initial state corresponded to an experiment with a fresh reactants mixture of CO and H_2O with P_{CO} and P_{H2O} partial pressures, continuously impinging on an empty thermalized Cu(1 1 1) surface, where the heterogeneous reaction takes place and afterwards the final gas products (i.e., CO_2 and H_2) leave the surface region (i.e., in a nonequilibrium thermodynamic state). A total of 34 elementary processes were considered for the molecular mechanism of the WGSR, which are described in Table 1. These include all elemental steps considered in a previous microkinetic study of this reaction [10] but with some important refinements in the calculation of the reaction rates as explained in detail below. Thus, the overall mechanism includes adsorption and desorption of reactants (steps ±1 and ±3, where + stands for forward and − for backward for all elementary steps in Table 1), desorption of products (steps −2 and −4) and several surface reactions (steps ±5 to ±16). In addition, four processes involving diffusion of CO, OH, H and O adsorbed species have been considered (steps 17 to 20) because these are the most mobile adsorbates and were also considered in a previous and similar kMC study of the WGSR on a Cu/ZnO supported model catalyst [13].

2.2. Kinetic Monte Carlo

The kMC method has been used to numerically solve the master equation (ME) by generating an ensemble of trajectories, usually referred to as Poisson processes. ME is the starting point for a stochastic description of the system [20]:

$$\frac{dP_\alpha}{dt} = \sum_\beta [W_{\beta\alpha} P_{\beta-} W_{\alpha\beta} P_\alpha] \tag{1}$$

where the summation runs over all possible configurations, P_α is the probability that the system is in a α configuration at time t, and $W_{\alpha\beta}$ is the transition probability per unit time that the system will undergo the $\alpha \rightarrow \beta$ configuration transition due to reactions and other processes. This is a lost-gain equation, which can be derived from first-principles. In the kMC procedure, each generated trajectory propagates the system correctly from configuration to configuration in such a way that the average over the entire ensemble of trajectories yields probability density functions for all states fulfilling the ME. A C^{++} code has been written to solve the ME by means of the most widely used rejection-free algorithm, which leads to the so-called direct kMC method [21,22], a type of the variable step size procedure [20].

Once the list of all possible elementary processes on the different lattice sites is obtained, the transition probability (W) of the i^{th} process at j^{th} site (i.e., r_{ij} rate) is calculated and normalized to the total rate r_{tot}

$$\frac{r_{ij}}{\sum_{i=1}^{N_p}\sum_{j=1}^{N_L} r_{ij}} = \frac{r_{ij}}{r_{tot}} \tag{2}$$

where N_P stands for the total number of processes that can occur at the j^{th} site and N_L corresponds to the total number of sites. Then, a (I,J) pair process of the list is selected, proportionally to its relative rate, when fulfils the following condition:

Table 1
Energy barriers (E_b in eV) and reaction rates (r_i in s^{-1}) for all the elementary processes included in the simulation (T = 625 K, P_{CO} = 26 Torr, P_{H2O} = 10 Torr). Energy barriers with zero point energy correction from (a) Ref. [10], (b) Ref. [13] and (c) Ref. [10] along with additional present DFT calculations.

ID	Elementary process	Forward		Reverse	
		E_b	r_i	E_b	r_i
1	$CO\ (g) \leftrightarrow CO^*$	0.00[a]	4.00×10^{6}	0.51[a]	1.02×10^{10}
2	$H_2\ (g) \leftarrow 2H^*$	–	–	0.96[a]	1.51×10^{5}
3	$H_2O\ (g) \leftrightarrow H_2O^*$	0.00[a]	1.92×10^{6}	0.18[a]	1.08×10^{8}
4	$CO_2\ (g) \leftarrow CO_2^*$	–	–	0.09[a]	1.67×10^{8}
5	$H_2O^* \leftrightarrow OH^* + H^*$	1.01[c]	4.55×10^{5}	1.15[a]	1.18×10^{4}
6	$OH^* \leftrightarrow O^* + H^*$	1.60[c]	2.30×10^{0}	1.19[a]	3.17×10^{3}
7	$2OH^* \leftrightarrow H_2O^* + O^*$	0.68[c]	1.86×10^{8}	0.00[a]	2.75×10^{13}
8	$CO^* + O^* \leftrightarrow CO_2^*$	0.79[a]	8.07×10^{6}	1.57[c]	4.88×10^{0}
9	$CO^* + OH^* \leftrightarrow cis\text{-}COOH^*$	0.70[c]	4.99×10^{7}	0.55[a]	3.38×10^{8}
10	$cis\text{-}COOH^* \leftrightarrow trans\text{-}COOH^*$	0.48[a]	1.23×10^{9}	0.70[c]	2.65×10^{7}
11	$trans\text{-}COOH^* \leftrightarrow CO_2^* + H^*$	1.18[a]	5.57×10^{3}	1.69[c]	3.19×10^{-1}
12	$trans\text{-}COOH^* + OH^* \leftrightarrow CO_2^* + H_2O^*$	0.38[a]	1.31×10^{10}	0.75[c]	1.45×10^{7}
13	$CO_2^* + H^* \leftrightarrow HCOO^*$	1.00[c]	1.05×10^{5}	0.54[a]	8.44×10^{8}
14	$HCOO^* \leftrightarrow HCOO^{**}$	0.04[a]	6.11×10^{12}	0.48[c]	1.82×10^{9}
15	$CO_2^* + H_2O^* \leftrightarrow HCOO^{**} + OH^*$	1.61[a]	1.18×10^{0}	1.71[c]	2.12×10^{-1}
16	$CO_2^* + OH^* \leftrightarrow HCOO^{**} + O^*$	2.09[c]	1.84×10^{-4}	1.71[a]	2.38×10^{-1}
17	$CO^* + * \rightarrow * + CO^*$	0.08[b]	2.18×10^{10}	0.08[b]	2.18×10^{10}
18	$OH^* + * \rightarrow * + OH^*$	0.12[b]	1.06×10^{10}	0.12[b]	1.06×10^{10}
19	$H^* + * \rightarrow * + H^*$	0.15[b]	6.77×10^{9}	0.15[b]	6.77×10^{9}
20	$O^* + * \rightarrow * + O^*$	0.38[b]	8.31×10^{7}	0.38[b]	8.31×10^{7}

Reaction rates were calculated using TST equations excepting for processes 1 and 3, where collision theory and detailed balance principle were used.
The optimum scaling factor α for diffusion processes (17–20) was taken to be 0.01.

$$\frac{\sum_{i=1}^{I-1}\sum_{j=1}^{J} r_{ij}}{r_{tot}} < \rho \leqslant \frac{\sum_{i=1}^{I}\sum_{j=1}^{J} r_{ij}}{r_{tot}} \tag{3}$$

ρ is a random number generated from a uniform distribution on the unit interval ($\rho \in [0,1]$) at each step of the simulation. Obviously, a process with a large rate will have a higher chance of being chosen in this way, and this probability-weighted selection is precisely provided by the partial sums in Eq. (3). By executing the selected process the system is moved to a new configuration, and the time is advanced by

$$t \rightarrow t + \frac{1}{r_{tot}} \tag{4}$$

Next, the code computes all the new r_{ij} and r_{tot} values and repeats the previous steps until a sufficiently large number of steps have been considered. This typically involves hundreds of millions and is high enough to ensure that the system achieves a steady-state.

The correctness and performance of the present code have been validated by comparing several simulations with those obtained using ZACROS 1.0.1 package, a first-reaction kMC software developed by Stamatakis et al. [23,24]; for instance, calculating the logarithm of the number of H_2 or CO_2 products formed per site and second (hereafter referred to as turnover frequency (TOF)) for T = 625 K and partial pressures of CO and H_2O of 26 and 10 Torr (i.e., 34.7 and 13.3 mbar), respectively. The present algorithm predicts a TOF of $10^{3.89}$ s^{-1} whereas ZACROS prediction is of $10^{3.92}$ s^{-1}. The two results are sufficiently close to claim good agreement. Moreover, differences in calculated surface coverage of several adsorbed species using both codes were also checked, showing only a small increase in the OH coverage, going from ~0.20 in our code to ~0.22 in ZACROS; also a very small decrease in the H coverage from ~0.12 to ~0.10 was observed, respectively. The surface coverage for other species was almost the same. The main reason for having developed the present code is to allow for a considerable saving of computational time with respect to ZACROS, which also includes many options, which are not used here.

2.3. Reaction rates

The rate of a surface elementary process, defined as the number of times this process occurs per site and time unit, can be calculated by using either the transition state theory (TST) or the collision theory (CT) [20,25]. Usually, TST values from DFT results constitute a better choice. For a surface Langmuir–Hinshelwood type reaction or an atomic or molecular diffusion, this rate can be calculated as

$$r_i \equiv r_{ij} = \frac{k_b T}{h}\frac{Q_i^{\neq}}{Q_R} e^{\frac{-\Delta E_i^{0\neq}}{k_b T}} \tag{5}$$

where h denotes Planck's constant, k_b the Boltzmann's constant, and $Q_i^{\neq}$ and Q_R are partition functions (dimensionless) of the transition state and the reactants, respectively. $\Delta E_i^{0\neq}$ stands for the energy barrier for the i^{th} process, including the zero-point energy (ZPE) correction. Moreover, r_i should be multiplied by a statistical factor $l^{\neq}$ (sometimes ignored), which accounts for the several equivalent ways to achieve the transition state, as it is explained in standard kinetic textbooks [25]. In fact, this factor was 2 (default value $l^{\neq}$ = 1) only for reactions 5, 7 and −8, shown in Table 1. It is also worth pointing out that in microkinetic studies, where classical kinetics differential equations are written for all the elementary steps and numerically integrated (see for instance Ref. [10] and references therein) a similar expression to Eq. (5) is used for the rate constant calculation, but including also as a factor the area of the adsorption site (e.g., units for LH rate constants: m^2 s^{-1}).

The rate of adsorption processes of a gas with species of mass m_i at a given temperature T and partial pressure p_i can be calculated from the flux of incident species through the well-known Hertz–Knudsen equation as

$$r_i^{ad} = S_{0,i} \cdot A_{site} \frac{p_i}{\sqrt{2\pi m_i k_b T}} \tag{6}$$

where at a given temperature $S_{0,i}$ stands for the initial sticking coefficient and A_{site} corresponds to the area of a single site. Rigorously speaking, $S_{0,i}$ is introduced to take into account the fact that only a fraction of the incoming molecules will be adsorbed. Nevertheless, in the present study $S_{0,i}$ is taken as the unity for both gas reactants CO [26] and H_2O [27] as in previous studies. A_{site} was calculated always as the total area divided by the number of sites. For Cu, the calculated DFT/PW91 bulk lattice parameter is 3.66 Å [10] (exp. 3.62 Å [28]), and the corresponding surface unit cell

parameter for (1 1 1) face turns out to be 2.59 Å, which implies an A_{site} value of 5.80 Å^2.

The rate of desorption processes (i.e., r_i^{des} for $i = -1$, -3 and -4) can be determined from TST assuming an early 2D gas-like transition state [23] or simply by applying the microscopic reversibility and detailed balance principles [25,29], although the two approaches produce identical values. The first method implies the use of Eq. (5) with

$$\frac{Q_i^{\neq}}{Q_R} = \frac{Q_{vib}^{gas} \cdot Q_{rot}^{gas} \cdot Q_{tras,2D}^{gas}}{Q_{vib}^{ad}} \tag{7}$$

$$Q_{tras,2D}^{gas} = A_{site} \frac{2\pi m_X k_b T}{h^2} \tag{8}$$

The effect of repulsive lateral interactions for CO on Cu(1 1 1) on WGSR [13] has been previously included by correcting their desorption energy barriers through the following equation:

$$\Delta E_{i,lat}^{0\neq} = \Delta E_i^{0\neq} + n\Delta E_{lat} \tag{9}$$

where n indicates the number of nearest neighbours CO adsorbed molecules and $\Delta E_{lat} = -0.15$ eV. Nevertheless, their effect in the present work was negligible, due to the low CO surface coverage observed (see next section).

For the diffusion processes 17, 18, 19 and 20 (see Table 1), the rate was calculated assuming a typical constant pre-exponential factor of 10^{13} s^{-1} [20], its corresponding DFT calculated energy barrier [13] and a scaling factor ($0 \leqslant \alpha \leqslant 1$), which decreases the diffusion to reduce the computational cost but without affecting the results of the simulations [13], as it will be clearly shown in the next section. Hence, diffusion rates were obtained as

$$r_i^{dif} = \alpha \cdot 10^{13} (s^{-1}) e^{\frac{-\Delta E_{i,dif}^{0\neq}}{k_b T}} \tag{10}$$

Finally, it is necessary to point out that since some of the elementary processes involve hydrogen atom transfer, one needs to introduce a one-dimensional tunnelling correction factor ($\kappa \geqslant 1$) in the calculation of reaction rates of these processes (i.e., steps ±5, ±6, ±11, ±13 and 19, Table 1). The tunnelling correction factor is computed from the expression derived from a symmetrical Eckart barrier [30] as

$$\kappa(T) = 1 + \frac{1}{24} \left| \frac{h\nu_{img}}{k_b T} \right|^2 \left(1 + \frac{k_b T}{\Delta E_i^{0\neq}} \right) \tag{11}$$

where ν_{img} is the imaginary frequency of the transition state. In spite of the fact that the observed effect was very small, all the calculated rates of the abovementioned processes include this correction.

All rates used in the present kMC simulations were calculated from first-principles using available DFT data [10,13] and the set of equations outlined above. It is important to point out that the ZPE-corrected energy barriers for the exothermic reactions were taken from a previous microkinetics study of the WGSR on Cu(1 1 1) [10]. However, for the endothermic ones the ZPE-correction was missing. Thus, harmonic vibrational frequencies to be used both in these missing ZPE-corrected energy barriers and also in the necessary vibrational partition functions were determined from pertinent DFT calculations. Therefore, additional DFT calculations on some gas phase species (i.e., $H_2O_{(g)}$, $CO_{2(g)}$, $OH_{(g)}$, $CO_{(g)}$, $H_{2(g)}$, *trans*-$COOH_{(g)}$ and *cis*-$COOH_{(g)}$) and on several adsorbed species were performed by means of VASP code [31–33]. A four-layer Cu relaxed slab, periodically repeated in a 2×2 supercell with 20 Å of vacuum between any two successive metal slabs was used to model Cu(1 1 1). The valence electron density was expanded in a plane-wave basis set with a cut-off of 415 eV for the kinetic energy. The effect of core electrons in the valence electron density was taken into account through the projector augmented wave method [34] as implemented in VASP [35]. The surface Brillouin zone was sampled with a $5 \times 5 \times 1$ Monkhorst–Pack grid of special k-points [36] and the exchange–correlation energy and potential were described by the generalized gradient approximation (GGA-PW91) [37], using the same functional as in previous study [10].

To facilitate the comparison of the different competitive processes, Table 1 summarizes all reaction rates at $T = 625$ K. Note, however, that these rates can be also easily obtained for different temperatures, and this is possible due to the use of the additional calculated DFT data.

The PW91 DFT data were used earlier to derive the reaction rates used in a microkinetic model for WGSR on Cu(1 1 1) [10]. Later the same DFT data were also used to derive other set of reaction rates for a kMC study of the WGSR on a Cu/ZnO supported model catalyst [13]. In the present study, we use also these DFT data along with some extra calculations to improve more the quality of the reaction rates, especially for all endothermic reactions. However, one may wonder whether the PW91 method is accurate enough to provide physically meaningful results in the present study. Playing the advocate devils' game one can even compare the standard change free energy (ΔG_r^o) of the WGSR in gas phase to experimental data [38], although the present study corresponds really to an open system in a nonequilibrium state. Assuming a closed system, where the WGSR achieves a thermodynamic equilibrium at a given pressure and temperature is possible to derive the equilibrium constant (K) at several temperatures. Table 2 shows some calculations carried out by means of the GAUSSIAN code [39] for ΔG_r^o and K at two temperatures (298.15 and 600 K), using different methods and a near Hartree–Fock basis set [40]. It is observed that PW91 poorly describes the thermochemistry of this reaction in gas phase at low temperature although the agreement with experiment is much better at high temperature. The results also show that the broadly used B3LYP method designed precisely to improve the thermochemistry of reaction in gas phase [40,41] does not perform so well, and even the golden standard CCSD(T) method exhibits some inaccuracy. At this point one can perhaps argue that results obtained for the mechanism of the WGSR reaction on the Cu(1 1 1) surface are doubtful and the doubts would have to be extended to all published articles dealing with DFT calculations of reactions taking place at metal surfaces. However, this claim is incorrect because, differently from gas phase chemistry, when the reaction takes place above a metal surface the electrons in the reacting spaces are largely screened by the electrons in the conduction band and, in addition, constitute a fraction of the total number of electrons. In this situation, PW91 and related GGA type functionals provide a very good description of the properties of the metals [42–44], where hybrid approaches, working well to describe the thermochemistry in gas phase, fail [45,46] because of the failure to attain the exact homogeneous

Table 2
Calculated standard change of free energy (kcal/mol) of the WGSR at 298.15 K and 600 K with different DFT functionals and with the post-HF CCSD(T) method, using the aug-cc-pVTZ basis set, compared with the experimental value Ref. [38]. Equilibrium constant ($\Delta G_r^o = -RTlnK$) is also reported for comparison.

	$\Delta G_{r,298}^o$	$\Delta G_{r,600}^o$	K_{298}	K_{600}
PBE	−17.36	−14.52	5.3×10^{12}	1.9×10^5
PW91	−16.99	−9.98	2.8×10^{12}	4.0×10^3
B3LYP	−11.51	−8.64	2.7×10^8	1.4×10^3
CCSD(T)	−5.56	−2.69	1.2×10^4	9.6
Exp.	−6.85	−3.99	1.0×10^5	28

electron gas limit [47]. This view is supported by the large body of literature comparing DFT calculations at the GGA level (e.g., PBE or PW91) with experimental values for adsorption and reaction energies [48,49], and is reinforced by the evidence that for reactions catalysed by (non-magnetic) metals the transition states do not evidence any spin polarization [50]. Therefore, even if calculated results for reaction rates and related properties calculated here are by no means exact, it is very likely that the overall physical description is correct. This also supported by the excellent agreement between theory and experiment in the landmark paper of Gokhale et al. [10] reporting a microkinetic model precisely for the WGSR reaction on Cu(1 1 1).

3. Results and discussion

In this study, the effect of diffusion rates, the temperature and the reactants partial pressures on the WGSR on Cu(1 1 1) have been investigated in detail. Each kMC simulation was allowed to achieve a steady-state (typically reached between 70 and 200 million kMC steps) in which surface coverage for all intermediates reached constant values, with the exception of small fluctuations resulting from the stochastic nature of the simulation. From that point, the overall macroscopic kinetic values, such as the TOF, were calculated. For $T = 625$ K the total reaction rate (r_{tot}) was somewhere between 10^9 and 10^{12} s^{-1}, which means that each kMC step takes place in the sub-nanosecond timescale.

3.1. Scaled diffusion rates

Even if the diffusion processes are not rate-limiting steps in WGSR reaction, it is necessary to include them into the reaction mechanism to reach a realistic description including all possible elementary steps [20]. In the system studied here, diffusion processes have energy barriers substantially lower than those corresponding to other elementary chemical reactions (see Table 1). Consequently, most kMC steps correspond to diffusion with a small number of steps corresponding to other chemical reactions. This implies that very large simulations are required to obtain meaningful results. Using a scaling factor as shown in Eq. (10) can significantly increase the efficiency of kMC simulation without affecting the results [51]. Nevertheless, it is important to appropriately choose the scaling factor which requires a few additional simulations, an effort largely compensated by the gain in speeding up the overall study. Fig. 1 reports the change of the TOF with respect to the scaling factor, and shows that selecting $\alpha = 10^{-2}$, which reduces the diffusion rates by two orders of magnitude, speeds up the simulation considerably but producing almost the same TOF value as for $\alpha = 1$. A similar optimum value was taken as scaling factor in a previous kMC study of the WGSR on a model of the Cu/ZnO $(000\bar{1})$ catalyst surface [13] containing 0.2 ML Cu coverage. Thus, all simulations in the present work have been carried out by selecting $\alpha = 10^{-2}$.

3.2. Temperature effects

The effect of temperature on the WGSR catalysed by Cu(1 1 1) has been investigated within the temperature range 463–625 K, where some experimental data are available for Cu(1 1 1) single-crystal catalyst [52] and $CuO/ZnO/Al_2O_3$ catalysts [5,53]. Most of the theoretical studies of the WGSR on Cu surfaces are also within this temperature range [10,11,13,23]. We observe that raising the temperature within this range increases the value of the reaction rates and hence one would expect an increase of the TOF too. However, the overall kinetics is controlled not only by the reaction rates, but also by the surface coverage of the different species.

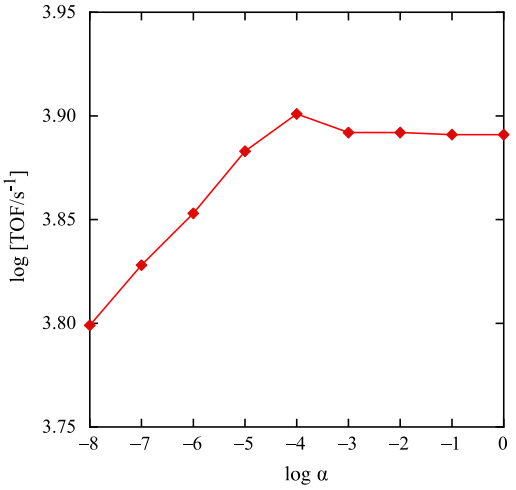

Fig. 1. H_2 productivity as a function of the scaling α factor. Simulations performed at $T = 625$ K, $P_{CO} = 26$ Torr and $P_{H2O} = 10$ Torr.

Plotting the logarithm of the simulated TOF as function of $1000/T$ leads to an Arrhenius behaviour (see Fig. 2) in two temperature intervals, with apparent activation energies of 0.5 eV (525–625 K) and 0.8 eV (463–525 K). A very similar behaviour was observed for WGSR on Pt(1 1 1) (see Supplementary material on Ref. [23]). The experimental value reported of the apparent activation energy of WGSR on a clean Cu(1 1 1) single-crystal surface with 10 Torr (1.33 mbar) H_2O and 26 Torr (34.7 mbar) CO was 0.7 eV at 563–683 K [39], which is very close to the present calculated values; other reported values of the apparent activation energies of Cu-based catalysts fall within the interval 0.7 ± 0.2 eV [5,53], supporting that the metallic Cu seems to be the active phase for WGSR. A more recent kinetic study for WGSR at 1 atm of total pressure and a temperature close to 463 K [5] reports an apparent activation energy of 0.8 eV for a Cu-based catalyst (i.e., $CuO/ZnO/Al_2O_3$), in excellent agreement also with the present kMC calculated value. However, it is important to point out that a direct comparison with the apparent activation energies reported in the literature is rather complicated by the fact that most studies were carried out under

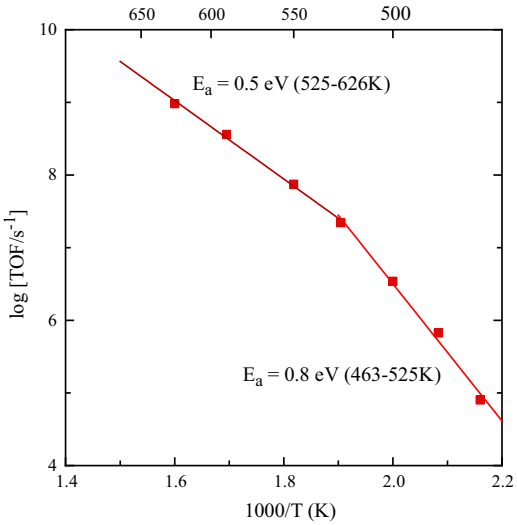

Fig. 2. Arrhenius plot of the WGSR TOF in the temperature range 460–625 K. Simulations performed at $P_{CO} = 26$ Torr and $P_{H2O} = 10$ Torr.

different conditions. For instance, CO_2 and H_2 were also included into the reactants mixture to study their inhibitory effects (i.e., negative reaction orders, see Table 4 in Ref. [5]) whereas in the present study these products leave the surface region.

Fig. 3 shows the statistics of the most important elementary processes at T = 463 K (left) and 625 K (right), showing the number of events per site and per time unit for the forward and reverse processes. At low temperatures, the system spends a considerable amount of time just in adsorption and desorption processes of both reactants. When water molecules start to dissociate according to process +5 (see Table 1), OH adsorbed species become available on the surface and processes +7 and −7 begin to occur. If a CO molecule is adsorbed besides an OH, it immediately oxidizes CO to form the *cis*-carboxyl intermediate, changing then to the more stable *trans* conformation (i.e., processes +9 and +10) until it finds another OH to form CO_2 through an associative route (i.e., processes +12). Thus, the reaction is mainly controlled by processes +5 and +12.

At higher temperatures (625 K) the system also spends some time with adsorption/desorption of both reactants, but the frequency of water dissociation is much higher, lowering the surface coverage of water and greatly increasing the number of adsorbed OH intermediates (see Fig. 4). Thus, processes +7 and −7 occur with a much higher frequency (see Fig. 3, right). In addition, processes −5, −9 and −12 also increase significantly their frequencies. Therefore, in these conditions the processes +10 and +12 seem to control the reaction. The observed change in the rate-limiting steps with the temperature increment may be related with the decrease of the apparent activation energy shown in Fig. 2.

It is important to mention that, despite the high number of elementary processes, the stoichiometry of the global reaction is preserved, except for the first simulation steps, where the $CO_{2(g)}$ production is faster than the $H_{2(g)}$ production. Interestingly enough, this fact is also experimentally observed [52]. The present kMC simulations also confirm that the associative mechanism mediated by carboxyl (COOH) intermediate provides the dominant reaction path, and that the redox or the formate mediated mechanisms do not play a significant role, in agreement with previous microkinetic models [10,54,55]. The same conclusion was found in the theoretical study of Tang et al. [11]. However, on the WGSR catalysed by Cu nanoparticles supported on a ZnO surface, where two types of active sites (edges and (1 1 1) terraces) were used to model Cu nanoparticles, both redox and COOH-mediated mechanisms are competing, because edge sites favour the former [13].

An important piece of information coming out from the kMC simulations can be obtained from inspection of the average surface coverage for the main species, which are plotted in Fig. 4. First, note that carboxyl species are very reactive and its coverage is almost insignificant. From this plot one can also clearly see that

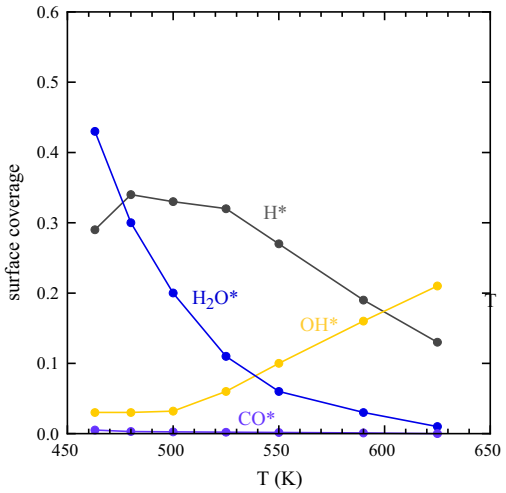

Fig. 4. Surface coverage of several species as a function of temperature for P_{CO} = 26 Torr and P_{H2O} = 10 Torr.

H_2O and H are the dominant species at low temperatures, occupying an important part of surface sites (i.e., 72% at 463 K) whereas OH and H are dominant at high temperatures but with a lower total coverage (i.e., 44% at 625 K); the higher the reaction temperature, the lower the total coverage. As shown in this figure, CO lateral interactions will not play an important role in the WGSR due to the negligible CO coverage at the final steady-state.

Unfortunately, calculated surface coverage values are very difficult to compare with results in the literature, mainly because they are very different depending on the experimental working conditions such as pressure, temperature and catalysts employed. A similar situation occurs for previous theoretical studies where surface coverage values depend on the model and methodology used. Thus, a previous microkinetic model of the WGSR on Cu(1 1 1) [56] predicts that under most reaction conditions surface coverage by reaction intermediates is small, although water is found to be the most abundant species on the surface for low H_2O/CO ratios. Another microkinetic model [55] confirms this small coverage, finding also H_2O, CO and H as the main species, with H_2O and CO coverage decreasing and H coverage slightly increasing when temperature is augmented. Nevertheless, the more recent microkinetic model from Mavrikakis et al. [10] for WGSR on Cu(1 1 1) shows that at high pressures (1–20 bar) bidentate formate and atomic H are the most abundant surface species, whereas CO and H_2O coverages are very low. In other kMC study of the WGSR on Pt(1 1 1) [51] it was observed that CO coverage was dominant (∼70–80% for

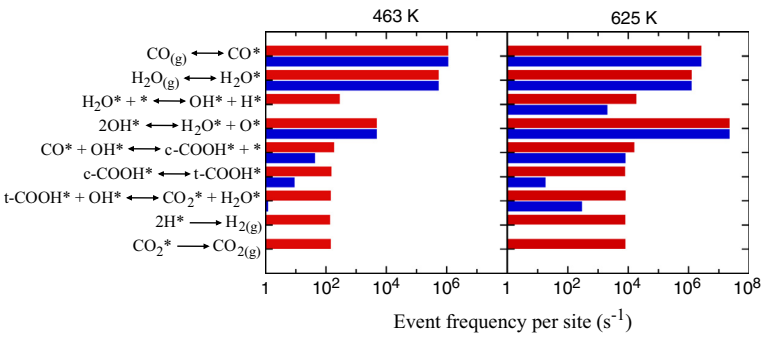

Fig. 3. Main elementary processes (direct in red and reverse in blue) and their frequencies for the WGSR at Cu(111) at P_{CO} = 26 Torr, P_{H2O} = 10 Torr and T = 463 K (left) and 625 K (right).

650 K P_{H2O} = 0.1 bar and P_{CO} = 0.05 bar) while water coverage was very low, a behaviour quite different from that corresponding to the WGSR on Cu(1 1 1), either from experimental or from theoretical simulations.

In the present study, we observe high water coverage at the lowest temperature studied (i.e., 0.43 at 463 K, Fig. 4), which becomes very low at the highest temperature (i.e., $1 \cdot 10^{-2}$ at 625 K, Fig. 4). This latter value compares quite well with the low experimental value for H_2O coverage at 612 K (i.e., $5 \cdot 10^{-4}$ [52]), which should be taken rather qualitatively because it includes several assumptions and parameters for the Cu(1 1 0) surface. The reason for the high water coverage at 463 K can be understood by analysing the water adsorption/desorption rates. At low temperature the adsorption reaction rate is almost twice larger than that for desorption, leading to a higher final water coverage, whereas at high temperatures the desorption reaction rate is two orders of magnitude larger than that for adsorption and thus the water coverage is very low as could be expected.

One of the aspects that makes kMC method such a powerful tool is that one can obtain information regarding the structure of the adlayer at any moment of the simulation. Fig. 5 shows snapshots of the Cu(1 1 1) surface at the beginning of the simulation (left) and once the steady-state (SS) is reached (right), at 463 K (top) and 625 K (bottom) for a given reactants mixture (P_{H2O} = 10 Torr and P_{CO} = 26 Torr). The time to reach the SS depends heavily on the temperature: at 463 K the SS is typically reached after 2 ms (about 70 million kMC steps), whereas at 625 K it takes 60 μs (about 200 million kMC steps). Although the total time needed to reach the SS is lower when the temperature is increased, longer simulations are required because the number of kMC steps is increased too. These snapshots apart from confirming the main adsorbed species implied in the SS (Fig. 4), also show that the assumption from macroscopic rate equations that the adsorbates are randomly distributed is not always correct. At low temperatures (Fig. 5b) there is a correlation in the occupation of neighbouring sites, and at very low temperatures may even result in island formation of ordered adlayers [20]. However, this correlation seems to be negligible at higher temperatures (Fig. 5d).

In order to see whether the formation of H/H_2O islands, as no adsorbate interactions were included in the kMC simulations, could be perhaps related with the inclusion of a scaling factor for diffusion derived for higher temperatures, we carried out additional simulations at 463 K, concluding that selecting $\alpha = 0.01$ still produces almost the same TOF than for $\alpha = 1$ (i.e., $10^{2.16}$ and $10^{2.15}$ for $\alpha = 0.01$ and 1, respectively). Thus, the formation of H/H_2O islands was not a result of the use of an unreliable scaling factor. In fact, this behaviour can be explained as a consequence of a correlation due to the reactions (see Ref. [20], pg. 2–3): at 463 K the water coverage at the initial steps of the simulation is very high (Fig. 5a); when water molecules dissociate, they generate OH + H pairs, and H_2O/OH/H islands start growing. Adsorbed CO molecules rapidly consume the adsorbed OHs (i.e., leading to a low OH coverage) forming COOHs, which in turn react rapidly with other OHs to form more water and CO_2 (that rapidly desorb) and the cycle is repeated. So, at the end what remains are the H/H_2O islands observed in Fig. 5b. Moreover, surface H atoms are accumulated due to the low reaction rate for H_2 formation at 463 K (i.e., $2.8 \cdot 10^2\ s^{-1}$) compared with the other processes. At 625 K this reaction rate is much higher ($1.5 \cdot 10^5\ s^{-1}$ in Table 1) and those H-islands are almost not observed (Fig. 5d).

3.3. Partial pressure effects

The effect of reactants mixture composition on the overall H_2 production has been examined carrying out simulations by varying the partial pressure of one of the reactants from 1 to 25 Torr while keeping constant the partial pressure of the other reactant (i.e., fixing 26 Torr for CO or 10 Torr for H_2O). The results summarized in Fig. 6 indicate that at low total pressures the partial orders for CO and H_2O are 0.7 and 0.6, respectively. For a similar pressure range and temperature (612 K) for the WGSR on Cu(1 1 1), Campbell et al. [52] found a partial order in water between 0.5 and 1, in agreement with the present result, but surprisingly they reported a zero value for the partial order in CO. However, usually positive and similar partial orders of both reactants have been found in other previous microkinetic models of the WGSR on Cu (1 1 1) (e.g., 0.90 and 0.85 for 1 bar of total pressure [10], 0–0.8 and 0.8–1 depending on temperature for total pressures until 30 bar [54], ~0 and 0.9–1 depending on temperature for a total pressure of 1.5 atm [55], for CO and H_2O, respectively) and in several experiments (e.g., 0.8 and 0.8 for 1 atm of total pressure and a temperature close to 463 K [5], 1 (assumed) and 1.4 for 5 bar of

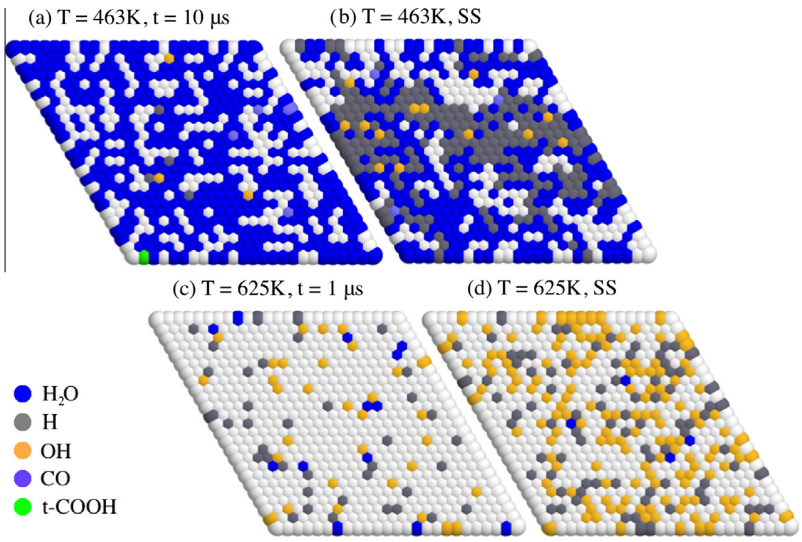

Fig. 5. Snapshots of the surface coverage at the beginning and once achieved the steady-state at two temperatures and P_{H2O} = 10 Torr and P_{CO} = 26 Torr. Surface Cu atoms are shown in white colour.

total pressure and a temperature close to 463 K [55], for CO and H_2O, respectively). Since both calculated reaction orders are lower than 1, TOF converges to a constant value for very high pressures of CO and H_2O, limited by the available number of free sites in the catalyst and maybe by the repulsive lateral interactions between CO adsorbates.

The H_2O/CO ratio in the initial reactants mixture plays a very important role in the WGSR. Thus, a series of kMC simulations were performed at H_2O/CO ratios ranging from 0.1 to 9.0 for a total pressure of 100 Torr and for a temperature of 625 K (Fig. 7). It can be seen that TOF passes through a maximum around a H_2O/CO ratio of 0.43–0.66, close to the experimental selected conditions (i.e., 0.38 for 10 Torr H_2O and 26 Torr CO in [52]). This need for a higher pressure of CO can be explained using the information of the reaction rates (Table 1); at 625 K the rate for CO desorption is two orders of magnitude larger than for water; therefore, a higher pressure of CO should be used to compensate its larger desorption. This result is also in agreement with the slightly higher reaction order found for CO compared to H_2O at the low total pressures used in Fig. 6.

There is a clear relationship between TOF and H coverage as can be seen from Fig. 7. The larger the amount of H adsorbed at the surface, the higher the probability to form molecular hydrogen via process −2; this is also true for CO_2 formation. For all of these initial conditions the stoichiometry of the WGSR is perfectly maintained, except in the initial steps of the simulations with high H_2O/CO ratios, where hydrogen is firstly produced with a high TOF and then its rate decays slowly until a lower value at the same instant at which begins the production of CO_2.

Finally, it is also observed that as the H_2O/CO initial ratio increases the concentration of adsorbed OH increases. This effect was also observed in the rather old kinetic model of Ovesen et al. [56]. For very high H_2O/CO ratios, the TOF of the reaction would drop rapidly because of OH poisoning of the surface. Likewise, in a more recent study [57] it was found that copper catalysts retain their high activity and selectivity for the WGSR when the reactants' feeding operates a low H_2O/CO ratio at low temperatures.

We have also made a study of the increase of the total pressure on the WGSR. Thus, we have considered 1 bar of pressure (P_{CO} = P_{H2O} = 375 Torr = 0.5 bar) and a temperature of 625 K. In these conditions TOF was $7.1 \cdot 10^4\ s^{-1}$, larger than the value obtained for lower pressure ($P_{CO} = P_{H2O}$ = 10 Torr) and the same H_2O/CO ratio (TOF = $5.2 \cdot 10^3\ s^{-1}$) as could be expected because reactants

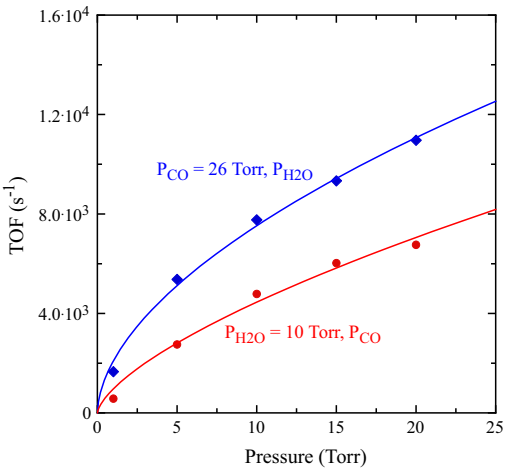

Fig. 6. H_2 formation at T = 625 K as a function of reactants partial pressures. Red line (circles) corresponds to the variation of P_{CO} when P_{H2O} = 10 Torr and blue line (squares) corresponds to the variation of P_{H2O} when P_{CO} = 26 Torr.

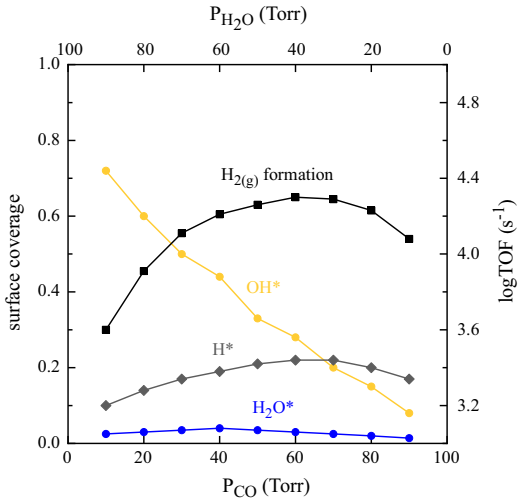

Fig. 7. Surface coverage of several species (coloured lines) and TOF based on $H_{2(g)}$ formation (black line) as a function of the partial pressures of reactants for a total pressure of 100 Torr. Simulations performed at T = 625 K.

pressure/concentration increases; larger coverages for H and H_2O were also obtained, and a small presence of adsorbed formate was observed. Probably, formate formation could be more enhanced when working with partial pressures of CO_2 and H_2 different from zero (i.e., products participating in the initial reactants mixture); in this case, processes +15 and +16 (see Table 1), although with low reaction rates, would be more important due to the major presence of CO_2^* and would explain formate formation.

4. Conclusions

In this work, we present a first-principles based kMC simulation of the water gas shift reaction on Cu(1 1 1) surface including a total of 34 elementary processes, such as adsorption/desorption, diffusion and other elementary surface chemical reactions. Reactions rates were obtained by application of both transition state theory and collision theory, with also an inclusion of one-dimensional tunnelling correction for reactions involving hydrogen atom transfer. Diffusion reaction rates were scaled enough to accelerate those simulations without affecting the final results. Earlier density functional theory results along with additional calculations were used for the computation of reaction rates at several temperatures.

The effect of temperature on WGSR was studied in the 463–625 K range, showing an Arrhenius behaviour with an activation energy of 0.8 eV at lower temperatures and a smaller value of 0.5 eV for higher ones. This behaviour can be explained due to the change in the rate-limiting step from low (water dissociation) to high (carboxyl isomerization) temperature. In both cases the associative mechanism mediated by carboxyl (COOH) intermediate provides the dominant reaction path, and the redox or the formate mediated mechanisms do not play a significant role.

Surface coverage was also analysed, indicating that H_2O and H are the main adsorbed species at low temperatures whereas OH and H are the dominant at high temperatures.

The effect of reactants initial mixture composition (i.e., H_2O/CO ratio) was also studied, observing that mixtures with higher CO proportion enhance the production of H_2 in the WGSR.

In spite of the fact that present simulations have been carried out for the Cu(1 1 1) surface, which in principle could be assumed as an ideal catalyst, previous studies confirm that the metallic Cu seems to be the active phase for WGSR catalysed with different Cu-based catalysts. However, further kMC studies with Cu-stepped surfaces are

in progress to ascertain the effect of possible lower energy barriers in some of the elementary steps (e.g., for water dissociation) and its influence into the final WGSR mechanism and TOF, which will allow to give more chemical insights to design more efficient catalysts.

We further demonstrated the capabilities of the kMC method to model complex surface reactions, providing a large amount of information, like apparent activation energies, surface coverage as function of temperature or reactants partial pressure, optimum reactants mixture composition, and the structure of the adlayer at atomic scale, among other data, which cannot be obtained all together from previous theoretical approaches or experiments.

Acknowledgments

The authors are indebted to Prof. Manos Mavrikakis for sending unpublished DFT data from Ref. [10] and for useful comments. The authors acknowledge support from the Spanish MINECO CTQ2012-30751 and CTQ2014-53987-R grants and, in part, from the Generalitat de Catalunya – Catalonia, Spain grants 2014SGR97, 2014SGR1582 and XRQTC. Leny Álvarez is grateful to the *Secretaría de Ciencia y Tecnología e Innovación del Distrito Federal de la Ciudad de México* for the financial support to her postdoctoral research at the Institute of Theoretical and Computational Chemistry of *Universitat de Barcelona* (IQTCUB).

References

[1] M. Flytzani-Stephanopoulos, Gold atoms stabilized on various supports catalyze the water–gas shift reaction, Acc. Chem. Res. 47 (2014) 783–792.
[2] J.R. Ladebeck, J.P. Wagner, in: W. Vielstich, A. Lamm, A.H. Gasteiger (Eds.), Handbook of Fuel Cells: Fundamentals, Technology and Applications, vol. 3, John Wiley & Sons, Chichester, UK, 2003, pp. 190–201.
[3] D.S. Newsome, The water–gas shift reaction, Catal. Rev. Sci. Eng. 21 (1980) 275–318.
[4] D.W. Jeong, W.J. Jang, J.O. Shim, W.B. Han, H.S. Roh, U.H. Jung, W.L. Yoon, Low-temperature water–gas shift reaction over supported Cu catalysts, Renew. Energy 65 (2014) 102–107.
[5] N.A. Koryabkina, A.A. Phatak, W.F. Ruettinger, R.J. Farrauto, F.H. Ribeiro, Determination of kinetic parameters for the water–gas shift reaction on copper catalysts under realistic conditions for fuel cell applications, J. Catal. 217 (2003) 233–239.
[6] D. Falleiros, F. Ademar, M. Kaminski, P. Matar, in: V. Patel (Ed.), Petrochemicals, Intech, Rijeka, Croatia, 2012 (Chapter 4).
[7] J.P. Clay, J.P. Greely, F.H. Ribeiro, W.N. Delgass, W.F. Schneider, DFT comparison of intrinsic WGS kinetics over Pd and Pt, J. Catal. 320 (2014) 106–117.
[8] M. Stamatakis, Y. Chen, G. Vlachos, First-principles-based kinetic Monte Carlo simulation of the structure sensitivity of the water–gas shift reaction on platinum surfaces, J. Phys. Chem. C 115 (2011) 24750–24762.
[9] J.L.C. Fajín, M.N.D.S. Cordeiro, F. Illas, J.R.B. Gomes, Influence of step sites in the molecular mechanism of the water gas shift reaction catalysed by copper, J. Catal. 268 (2009) 131–141.
[10] A.A. Gokhale, A.J. Dumesic, M. Mavrikakis, On the mechanism of low-temperature water gas shift reaction on copper, J. Am. Chem. Soc. 130 (2008) 1402–1414.
[11] Q. Tang, Z. Chen, X. He, A theoretical study of the water–gas shift reaction mechanism on Cu(111) model system, Surf. Sci. 603 (2009) 2138–2144.
[12] K. Mudiyanselage, S.D. Senanayake, L. Feria, S. Kundu, A.E. Baber, J. Graciani, A. B. Vidal, S. Agnoli, J. Evans, R. Chang, S. Axnanda, Z. Liu, J.F. Sanz, P. Liu, J.A. Rodriguez, D.J. Stacchiola, Importance of the metal-oxide interface in catalysis: in situ studies of the water–gas shift reaction by ambient-pressure X-ray photoelectron spectroscopy, Angew. Chem. 125 (2013) 5205–5209.
[13] L. Yang, A. Karim, J.T. Muckerman, Density functional kinetic Monte Carlo simulation of water–gas shift reaction on Cu/ZnO, J. Phys. Chem. C 117 (2013) 3414–3425.
[14] J.A. Rodriguez, J. Evans, J. Graciani, J.B. Park, J. Hrbek, J.F. Sanz, High water–gas shift activity in TiO_2(110) supported Cu and Au nanoparticles: role of the oxide and metal particle size, J. Phys. Chem. C 113 (2009) 7364–7370.
[15] J.A. Rodriguez, P.J. Ramírez, G.G. Asara, F. Viñes, J. Evans, P. Liu, J.M. Ricart, F. Illas, Charge polarization at a Au-TiC interface and the generation of highly active and selective catalysts for the low-temperature water–gas shift reaction, Angew. Chem., Int. Ed. 53 (2014) 11270–11274.
[16] F. Tao, Z. Ma, Water–gas shift on gold catalysts: catalyst systems and fundamental studies, Phys. Chem. Chem. Phys. 15 (2013) 15260–15270.
[17] J.B. Park, J. Graciani, J. Evans, D. Stacchiola, S.D. Senanayake, L. Barrio, P. Liu, J.F. Sanz, J. Hrbek, J.A. Rodriguez, Gold, copper, and platinum nanoparticles dispersed on CeO_x/TiO_2(110) surfaces: high water–gas shift activity and the nature of the mixed-metal oxide at the nanometer level, J. Am. Chem. Soc. 132 (2010) 356–363.
[18] J. Graciani, J.F. Sanz, Designing a new generation of catalysts: water gas shift reaction example, Catal. Today 240 (2014) 214–219.
[19] R.A. Hadden, P.D. Lambert, C. Ranson, Relationship between the copper surface area and the activity of $CuO/ZnO/Al_2O_3$ water–gas shift catalysts, Appl. Catal., A: Gen. 122 (1995) L1–L4.
[20] A.P.J. Jansen, An introduction to kinetic Monte Carlo simulations of surface reactions, Lecture Notes in Physics, vol. 856, Springer-Verlag, Heidelberg, Germany, 2012.
[21] A. Chatterjee, D.G. Vlachos, An overview of spatial microscopic and accelerated kinetic Monte Carlo methods, J. Comput. Aided Mater. Des. 14 (2007) 253–308.
[22] K. Reuter, in: O. Deutschmann (Ed.), Modeling and Simulation of Heterogeneous Catalytic Reactions, Wiley-VCH Verlag GmbH and Co. KGaA, Weinheim, Germany, 2011, pp. 71–111.
[23] M. Stamatakis, D.G. Vlachos, A graph-theoretical kinetic Monte Carlo framework for on-lattice chemical kinetics, J. Chem. Phys. 134 (2011) 214115.
[24] J. Nielsen, M. d'Avezac, J. Hetherington, M. Stamatakis, Parallel kinetic Monte Carlo simulation framework incorporating accurate models of adsorbate lateral interactions, J. Chem. Phys. 139 (2013) 224706.
[25] K.J. Laidler, Chemical Kinetics, Harper & Row Publishers, New York, USA, 1987.
[26] I. Bönicke, W. Kirstein, S. Spinzig, F. Thieme, CO adsorption studies on a stepped Cu(111) surface, Surf. Sci. 313 (1994) 231–238.
[27] B.J. Hinch, L.H. Dubois, Water adsorption on Cu(111): evidence for Volmer–Weber film growth, Chem. Phys. Lett. 181 (1991) 10–15.
[28] D.R. Lide (Ed.), CRC Handbook of Chemistry and Physics, 88th ed., CRC Press, Boca Raton, USA, 2008.
[29] K. Reuter, M. Scheffler, First-principles kinetic Monte Carlo simulations for heterogeneous catalysis: application to the CO oxidation at RuO_2(110), Phys. Rev. B 73 (2006) 045433.
[30] J.I. Steinfeld, J.S. Francisco, W.L. Hase, Chemical Kinetics and Dynamics, Prentice Hall, Englewood Cliffs, USA, 1989.
[31] G. Kresse, J. Hafner, Ab initio molecular dynamics for liquid metals, Phys. Rev. B 47 (1993) 558–561.
[32] G. Kresse, J. Furthmüller, Efficiency of ab-initio total energy calculations for metals and semiconductors using a plane-wave basis set, Comput. Mater. Sci. 6 (1996) 15–50.
[33] G. Kresse, J. Furthmüller, Efficient iterative schemes for ab initio total-energy calculations using a plane-wave basis set, Phys. Rev. B 54 (1996) 11169–11186.
[34] P.E. Blöchl, Projector augmented-wave method, Phys. Rev. B 50 (1994) 17953.
[35] G. Kresse, D. Joubert, From ultrasoft pseudopotentials to the projector augmented-wave method, Phys. Rev. B 59 (1999) 1755–1758.
[36] H.J. Monkhorst, J.D. Pack, Special points for Brillouin-zone integrations, Phys. Rev. B 13 (1976) 5188–5192.
[37] J.P. Perdew, J.A. Chevary, S.H. Vosko, K.A. Jackson, M.R. Pederson, D.J. Singh, C. Fiolhais, Atoms, molecules, solids, and surfaces: applications of the generalized gradient approximation for exchange and correlation, Phys. Rev. B 46 (1992) 6671–6687.
[38] M.W. Chase Jr., NIST-JANAF Thermochemical Tables, J. Phys. Chem. Ref. Data Monograph 9, fourth ed., American Institute of Physics, New York, 1998.
[39] Gaussian 09, Revision D.01, M.J. Frisch, G.W. Trucks, H.B. Schlegel, G.E. Scuseria, M.A. Robb, J.R. Cheeseman, G. Scalmani, V. Barone, B. Mennucci, G.A. Petersson, H. Nakatsuji, M. Caricato, X. Li, H.P. Hratchian, A.F. Izmaylov, J. Bloino, G. Zheng, J.L. Sonnenberg, M. Hada, M. Ehara, K. Toyota, R. Fukuda, J. Hasegawa, M. Ishida, T. Nakajima, Y. Honda, O. Kitao, H. Nakai, T. Vreven, J.A. Montgomery Jr., J.E. Peralta, F. Ogliaro, M. Bearpark, J.J. Heyd, E. Brothers, K.N. Kudin, V.N. Staroverov, R. Kobayashi, J. Normand, K. Raghavachari, A. Rendell, J. C. Burant, S.S. Iyengar, J. Tomasi, M. Cossi, N. Rega, J.M. Millam, M. Klene, J.E. Knox, J.B. Cross, V. Bakken, C. Adamo, J. Jaramillo, R. Gomperts, R.E. Stratmann, O. Yazyev, A.J. Austin, R. Cammi, C. Pomelli, J.W. Ochterski, R.L. Martin, K. Morokuma, V.G. Zakrzewski, G.A. Voth, P. Salvador, J.J. Dannenberg, S. Dapprich, A.D. Daniels, Ö. Farkas, J.B. Foresman, J.V. Ortiz, J. Cioslowski, D.J. Fox, Gaussian Inc, Wallingford, CT, 2013.
[40] A.D. Becke, Density-functional thermochemistry. III. The role of exact exchange, J. Chem. Phys. 98 (1993) 5648–5652.
[41] S.F. Sousa, P.A. Fernandes, M.J. Ramos, General performance of density functionals, J. Phys. Chem. A 111 (2007) 10439–10452.
[42] P. Janthon, S. Luo, S.M. Kozlov, F. Viñes, J. Limtrakul, D.G. Truhlar, F. Illas, Bulk properties of transition metals: a challenge for the design of universal density functionals, J. Chem. Theory Comput. 10 (2014) 3832–3839.
[43] P. Janthon, S.M. Kozlov, F. Viñes, J. Limtrakul, F. Illas, Establishing the accuracy of broadly used density functionals in describing bulk properties of transition metals, J. Chem. Theory Comput. 9 (2013) 1631–1640.
[44] A. Notario-Estévez, S.M. Kozlov, F. Viñes, F. Illas, Electronic-structure-based material descriptors: (in)dependence on self-interaction and Hartree-Fock exchange, Chem. Commun. 51 (2015) 5602–5605.
[45] Y. Zhao, D.G. Truhlar, Comparative assessment of density functional methods for 3d transition-metal chemistry, J. Chem. Phys. 124 (2006) 224105.
[46] N.E. Schultz, Y. Zhao, D.G. Truhlar, Density functionals for inorganometallic and organometallic chemistry, J. Phys. Chem. A 109 (2005) 11127–11143.
[47] J. Paier, M. Marsman, G. Kresse, Why does the B3LYP hybrid functional fail for metals?, J Chem. Phys. 127 (2007) 024103.
[48] L. Grabow, W. Schneider, M.J. Janik, T. Manz, A. van Duin, S. Sinnott, D. Scholl, in: A. Asthagiri (Ed.), J. Spivey (Series Ed.), Computational Catalysis, RSC Books, 2013.

[49] J.K. Nørskov, F. Studt, F. Abild-Pedersen, T. Bligaard, Fundamental Concepts in Heterogeneous Catalysis, John Wiley and Sons, Hoboken, 2014.
[50] J.L.C. Fajín, M.N.D.S. Cordeiro, J.R.B. Gomes, F. Illas, On the need for spin polarization in heterogeneously catalyzed reactions on nonmagnetic metallic surfaces, J. Chem. Theory Comput. 8 (2012) 1737–1743.
[51] M. Stamatakis, D.G. Vlachos, Equivalence of on-lattice stochastic chemical kinetics with the well-mixed chemical master equation in the limit of fast diffusion, Comput. Chem. Eng. 35 (2011) 2602–2610.
[52] T.C. Campbell, A.K. Daube, A surface science investigation of the water–gas shift reaction on Cu(1 1 1), J. Catal. 104 (1987) 109–119.
[53] C.V. Ovesen, B.S. Clausen, B.S. Hammershøi, G. Steffensen, T. Askgaard, I. Chorkendorff, J.K. Nørskov, P.B. Rasmussen, P. Stoltze, P. Taylor, A microkinetic analysis of the water–gas shift reaction under industrial conditions, J. Catal. 158 (1996) 170–180.
[54] I. Fishtik, R. Datta, A UBI-QEP microkinetic model for the water–gas shift reaction on Cu(1 1 1), Surf. Sci. 512 (2002) 229–254.
[55] C. Callaghan, I. Fishtik, R. Datta, M. Carpenter, M. Chmielewski, A. Lugo, An improved microkinetic model for the water gas shift reaction on copper, Surf. Sci. 541 (2003) 21–30.
[56] C.V. Ovesen, P. Stoltze, J.K. Nørskov, T.C. Campbell, A kinetic model of the water–gas shift reaction, J. Catal. 134 (1992) 445–468.
[57] E. Xue, M. O'Keeffe, J.R.H. Ross, Water–gas shift conversion using a feed with a low steam to carbon monoxide ratio and containing sulphur, Catal. Today 30 (1996) 107–118.

4.3. Summary and conclusions

The mechanism of the WGSR on Cu(111) has been assessed by means of kMC simulations. The reaction rates have been mainly taken from already published DFT data,[4,7] although some additional calculations have been performed at the same level of theory to obtain the missing parameters.

As explained in Section 2.5.5, one of the main challenges for kMC simulations is to deal with processes with very dissimilar reaction rates. In the present study, the diffusion processes for CO, OH and H species have energy barriers substantially lower than those corresponding to other elementary chemical reactions (see Table 1 from Publication 3). This implies that diffusion processes dominate and extremely long kMC simulations must be performed to observe some evolution of the overall chemical process. Since these diffusion steps are not rate-determining steps (RDS), we found that we can reduce their rates by two orders of magnitude, speeding up the simulation and producing the same TOF value. However, if their reaction rates are lowered by four or more orders of magnitude, the system enters to a slow-diffusion regime where the kMC simulation results are affected.

After finding the appropriate scaling factor for diffusion processes, we investigated both the effects of reaction temperature and reactant partial pressures. The first effect was studied in the temperature range 463-625 K, showing an Arrhenius behavior in two temperature intervals, and finding a good agreement between the computed apparent activation energy and the experimental one. The slope change can be explained due to a change of a RDS (see below). Regarding the effect of the reactants mixture composition, we observed that the H_2 production is enhanced with CO-rich mixtures (i.e., P_{CO}:P_{H2O} = 60:40, P_{TOT} = 100 Torr). The reason is that the desorption rate for CO is about two orders of magnitude larger than for H_2O; therefore, a higher partial pressure of CO must be used to compensate.

The steps that control the activity of the WGSR on Cu(111) were investigated by looking at the turnover frequency of all elementary steps (i.e., the number of times a given process is selected per time unit, see Figure 3 in Publication 3). Here, we are assuming that the RDSs will be those with small TOF in the forward direction and almost zero frequency in the reverse direction (i.e., non-equilibrated). This analysis shows that COOH isomerization and CO_2 formation by reaction between COOH and OH are the RDSs at high temperatures (i.e., 625 K), while water dissociation is the limiting step at low

temperatures (i.e., 463 K). The change in the RDS when lowering the temperature is probably the reason why there are two different slopes in the Arrhenius plot.

Finally, we found that the associative mechanism (i.e., the one involving the COOH intermediate) provides the dominant reaction path at all reaction conditions studied, while the redox mechanism (i.e., the formation of CO_2 by CO and O reaction) and the formate mechanism (i.e., the one involving the HCOO intermediate) do not play a significant role.

4.4. References

1 J. P. Clay, J. P. Greeley, F. H. Ribeiro, W. N. Delgass and W. F. Schneider, DFT comparison of intrinsic WGS kinetics over Pd and Pt, *J. Catal*., **2014**, 320, 106–117.

2 M. Stamatakis, Y. Chen and D. G. Vlachos, First-principles-based kinetic Monte Carlo simulation of the structure sensitivity of the water–gas shift reaction on platinum surfaces, *J. Phys. Chem. C*, **2011**, 115, 24750–24762.

3 J. L. C. Fajín, M. N. D. S. Cordeiro, F. Illas and J. R. B. Gomes, Influence of step sites in the molecular mechanism of the water gas shift reaction catalyzed by copper, *J. Catal*., **2009**, 268, 131–141.

4 A. A. Gokhale, J. A. Dumesic and M. Mavrikakis, On the mechanism of low-temperature water gas shift reaction on copper, *J. Am. Chem. Soc*., **2008**, 130, 1402–1414.

5 Q.-L. Tang, Z.-X. Chen and X. He, A theoretical study of the water gas shift reaction mechanism on Cu(111) model system, *Surf. Sci*., **2009**, 603, 2138–2144.

6 K. Mudiyanselage, S. D. Senanayake, L. Feria, S. Kundu, A. E. Baber, J. Graciani, A. B. Vidal, S. Agnoli, J. Evans, R. Chang, S. Axnanda, Z. Liu, J. F. Sanz, P. Liu, J. A. Rodriguez and D. J. Stacchiola, Importance of the metal–oxide interface in catalysis: in situ studies of the water–gas shift reaction by ambient-pressure X-ray photoelectron spectroscopy, *Ang. Chem. Int. Ed*., **2013**, 52, 5101–5105

7 L. Yang, A. Karim and J. T. Muckerman, Density functional kinetic Monte Carlo simulation of water–gas shift reaction on Cu/ZnO, *J. Phys. Chem. C*, **2013**, 117, 3414–3425.

8 J. A. Rodríguez, J. Evans, J. Graciani, J.-B. Park, P. Liu, J. Hrbek and J. F. Sanz, High water−gas shift activity in TiO2(110) supported Cu and Au nanoparticles: role of the oxide and metal particle size, *J. Phys. Chem. C*, **2009**, 113, 7364–7370.

9 J. A. Rodriguez, P. J. Ramírez, G. G. Asara, F. Viñes, J. Evans, P. Liu, J. M. Ricart and F. Illas, Charge polarization at a Au-TiC interface and the generation of highly active and selective catalysts for the low-temperature water-gas shift reaction, *Ang. Chem. Int. Ed*., **2014**, 53, 11270–11274.

10 R. A. Hadden, P. J. Lambert and C. Ranson, Relationship between the copper surface area and the activity of $CuO/ZnO/Al_2O_3$ water-gas shift catalysts, *Appl. Catal. A: General*, **1995**, 122, L1–L4.

CHAPTER FIVE

Impact of vdW interactions: the WGSR on Cu(321)

5.1. Introduction

Van der Waals (also known as dispersion) interactions play an important role in chemical and physical processes involving biomolecules and their role in conformational related problems and in thermochemistry have been studied in detail[1]. Also, it has been shown that dispersion terms are dominant in the case of aromatic molecule interactions with the basal plane of MoS_2[2], hydrocarbons interacting with zeolites[3] or graphene on metallic surfaces[4]. In spite of the large number of articles devoted to study the importance of dispersion terms in adsorbate-surface interactions, there is almost no information on the effect of dispersion terms in the energy profile of heterogeneously catalyzed reactions, especially for complex reaction mechanisms involving many elementary steps.

The aim of this chapter is to study the impact of van der Waals interactions on the WGSR, an important catalyzed reaction with special technological relevance. Concretely, periodic DFT calculations have been performed to obtain the adsorption energies, energy barriers and reaction rates of the main elementary steps of the WGSR on the stepped Cu(321) surface. The vdW interactions have been included by adding the dispersion term from the D2 method of Grimme[5] to the PBE[6] calculated energy (PBE-D2). The present results are compared with: 1) published DFT data on the same reaction that does not include dispersion corrections, and 2) DFT results reported for the flat Cu(111) surface not including dispersion terms. Finally, the present results will be used in Chapter 6 to study the WGSR on Cu(321) with the kMC method.

5.2. Publication 4

Unexpectedly large impact of van der Waals interactions on the description of heterogeneously catalyzed reactions: the water gas shift reaction on Cu(321) as a case example

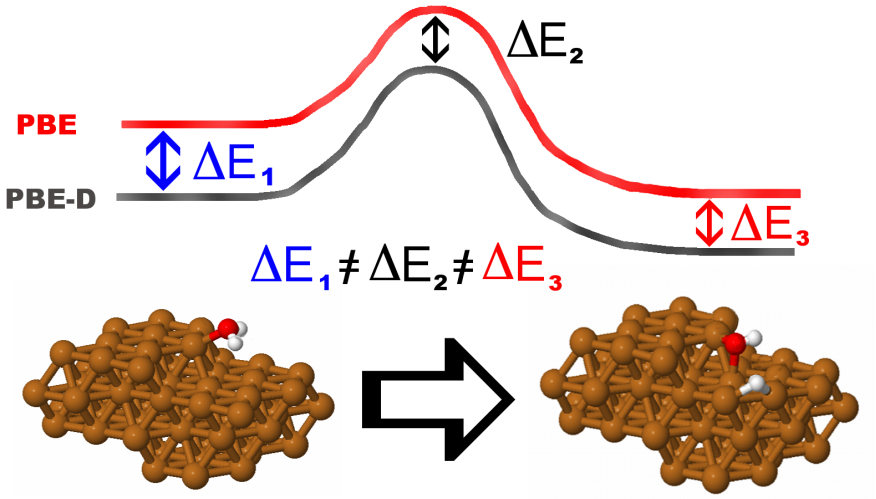

PCCP

PAPER

Cite this: *Phys. Chem. Chem. Phys.*, 2016, **18**, 2792

Unexpectedly large impact of van der Waals interactions on the description of heterogeneously catalyzed reactions: the water gas shift reaction on Cu(321) as a case example

Hèctor Prats, Pablo Gamallo, Ramón Sayós and Francesc Illas*

Received 10th November 2015,
Accepted 17th December 2015

DOI: 10.1039/c5cp06863k

www.rsc.org/pccp

The molecular mechanisms of the water gas shift reaction on Cu(321) have been chosen to investigate the effect of dispersion terms on the description of the energy profile and reaction rates. The present study based on periodic DFT calculations shows that including dispersion terms does not change the qualitative picture of the overall reaction, maintaining the rate determining step and the predominant route. However, the effect of dispersion is different for different adsorbates – reactants, intermediates or products – with a clear net effect and with no compensation of errors. Thus, in the OH + OH → H_2O + O process the dispersion effects imply up to three orders of magnitude in the calculated reaction rates; the formation of carboxyl is highly disfavoured when dispersion terms are explicitly included and finally, the reaction rate for CO_2 production (at 463 K) through *cis*-COOH dissociation is enhanced by three orders of magnitude by including dispersion terms in the calculation of the energy barrier. Consequently, the inclusion of dispersion terms largely affects the overall potential energy profile and produces tremendous changes in the predicted reaction rates. Therefore, dispersion terms must be included when aiming at obtaining information from macroscopic simulations employing for instance microkinetic or kinetic Monte Carlo approaches, where these effects should be clearly shown.

Introduction

Density functional theory (DFT) based calculations carried out on suitable periodic surface models have enormously contributed to our understanding of heterogeneously catalyzed reactions at the molecular level to the point that they have nowadays become a rather standard tool as illustrated in recently published books.[1,2] This type of computational methodology allowed us to take into account environmental effects into the equilibrium structure of surfaces exposed to gases,[3] determining rather accurate energy profiles for many heterogeneously catalyzed reactions thus unveiling the molecular mechanism behind complex processes involving many elementary steps[4] and helped us to derive useful concepts as descriptors allowing for a rational design of potential new and improved catalysts.[5,6] The information extracted from the DFT based calculations often includes transition state theory (TST) reaction rate constants for the elementary steps which can be used in subsequent macroscopic simulations of complex reactions. For instance, the microkinetic modeling[7] of the water gas shift reaction (WGSR) catalyzed by Cu(111) by Gokhale *et al.*[8] and the kinetic Monte Carlo simulations by Yang *et al.*[9] and Prats *et al.*,[10] both based on DFT calculated rates, constitute an excellent example of the interpretative and predictive power of this computational approach. Moreover, the increasing use of models involving stepped surfaces[11–16] or large metallic nanoparticles[17] provides more realistic models of the catalytic active sites. Yet, one of the remaining problems in this field concerns the accuracy of the calculated total energy defining the potential energy surface. In fact, commonly used Generalized Gradient Approach[18,19] (GGA) forms of the exchange–correlation potential such as PW91[20] or PBE[21] provide a balanced and rather accurate description of the bulk properties of the three series of transition metals whereas other broadly used functionals such as RPBE exhibit a poorer behavior and excessively stabilize surface energies.[22,23] Nevertheless, these GGA functionals do not provide accurate enough results for main group elements containing molecules[24] and, as already pointed out by Kristyan and Pulay twenty years ago,[25] neglect dispersion terms which may play a non-negligible role in the molecular picture of heterogeneously catalyzed reactions.

The first of the two shortcomings of DFT mentioned above has precisely triggered the development of new and more accurate functionals such as the widely used B3LYP hybrid functional[26] or the series of Minnesota hybrid meta-GGA functionals.[27–29]

Departament de Química Física & Institut de Química Teòrica i Computacional (IQTCUB), Universitat de Barcelona, C/Martí i Franquès 1, 08028 Barcelona, Spain. E-mail: francesc.illas@ub.edu

These are, however, seldom used in computational studies in heterogeneous catalysis due to the difficulty that these methods face when applied to metals.[30–32] Because of their good performance, hybrid functionals are surely the most well-known functionals in molecular chemistry and homogeneous catalysis.[33] However, for extended systems they have large, and often excessive, computational demands as compared to GGA type functionals. This is due to the long range of the exchange interactions when making use of programs working in the real space and due to the requirement for dense Brillouin zone sampling when relying on programs using plane wave basis sets.[34] Nevertheless, it is often argued that, for chemical reactions taking place at metal surfaces, calculated relative energies are much less affected than absolute energies by the inherent errors of GGA type functionals[2,4,35,36] and this is surely one of the keys to success of this type of calculations.

The effect of van der Waals (also known as dispersion) interactions on adsorption properties has been the focus of an intense research in the past few years, especially after the landmark contributions of Grimme and coworkers,[37–39] which has triggered many new theoretical developments and the appearance of a plethora of new functionals aiming to account for these terms in an accurate and non-empirical way as recently critically reviewed by Klimes and Michaelides.[40] Dispersion terms play an important role in chemical and physical processes involving biomolecules and their role in conformational related problems and in thermochemistry have been recently reviewed.[41] These terms largely affect the adsorption properties of molecules at surfaces and can even be the dominant term as in the case of aromatic molecule interaction with the basal plane of MoS_2,[42] hydrocarbons interacting with zeolites[43] or graphene on metallic surfaces;[44] a review on the role of dispersion terms in adsorption properties has been recently published.[45]

In spite of the large number of articles devoted to study the importance of dispersion terms in adsorbate–surface interactions, there is almost no information on the effect of dispersion terms in the energy profile of heterogeneously catalyzed reactions, especially for complex mechanisms involving several elementary steps. An important catalyzed reaction with special technological relevance[46] is the WGSR transforming CO and H_2O into CO_2 and H_2. This process takes place in two stages, at high and low temperatures, respectively. The catalyst for the low temperature stage involves Cu nanoparticles supported on different oxides[47] although other metals and supports have also been proposed.[48,49] The molecular mechanism for the low temperature catalyzed WGSR involves a rather large number of elementary steps and two possible routes, redox or carboxyl, are possible.[8] These have been studied in depth for the Cu(111)[8] and Cu(321)[13] surfaces; the latter one, containing different low-coordinated sites, offers a more realistic model of the catalyst. Moreover in the latter case, there is detailed information regarding the structure of many transition state structures involved in the mechanism and thus constitutes an excellent system to check the effect of the dispersion terms on the overall energy profile and rate constants. This is precisely the goal of the present paper. We will provide compelling evidence that while the qualitative picture of the overall reaction scheme is not largely affected by the inclusion of the dispersion terms, there are significant differences in the calculated reaction rates, which have important implications in the macroscopic description of the overall process *via* microkinetic or kinetic Monte Carlo simulations.

Elementary steps in the water gas shift reaction

In this section we will briefly summarize the most salient features of the reaction mechanisms proposed for the WGSR. These can be grouped in two general mechanisms, namely redox and associative, although with at least two variants in each route. Both mechanisms share the first three elementary steps, which correspond to CO and H_2O adsorption and subsequent dissociation of adsorbed H_2O into adsorbed H and OH, and also share formation of adsorbed H_2 through recombination of H adsorbed atoms and, eventually, subsequent desorption of adsorbed H_2 and CO_2 products. However, there are notable differences in the formation of adsorbed CO_2. Hereafter, we will assume that any reaction species is in the adsorbed state omitting the usual convention to denote any adsorbed A species as A*. To avoid confusion, any B species in the gas phase will be explicitly denoted as B(g).

The two possible variants along the redox route are direct hydroxyl dissociation ($OH \rightarrow O + H$) and hydroxyl disproportionation ($OH + OH \rightarrow O + H_2O$) although both involve CO_2 formation through direct reaction between adsorbed CO and O ($CO + O \rightarrow CO_2$). Hence, the two variants differ in the way O is produced. On the other hand, the associative mechanism is based on the formation of a carboxyl intermediate following $CO + OH \rightarrow COOH$. The decomposition of this intermediate yields CO_2 either through direct dehydrogenation ($COOH \rightarrow CO_2 + H$) or assisted dehydrogenation ($COOH + OH \rightarrow CO_2 + H_2O$). In addition, monodentate and bidentate formate (HCOO) species are also possible reaction intermediates. These species are formed by CO_2 hydrogenation but solely have a spectator role.

The study of Fajín *et al.*[13] evidenced that the presence of steps increases the water adsorption energy and decreases the energy barrier of water dissociation and atomic hydrogen recombination steps which on Cu(321) are found to constitute the rate-determining steps (rds). Interestingly, these two elementary steps are also the rds for the WGSR on Cu(111) but on the stepped Cu(321) they have similar energy barriers and reaction rates while on the flat Cu(111) surface water dissociation has an energy barrier considerably larger than hydrogen recombination.

In the present work, the effect of van der Waals interactions will be explicitly taken into account for all adsorption, reaction and desorption steps outlined above using Cu(321) as a catalyst model as described in the next section.

Surface model and computational details

The interaction of different reactants, intermediates and products involved in the WGSR catalysed by the Cu(321) surface has been

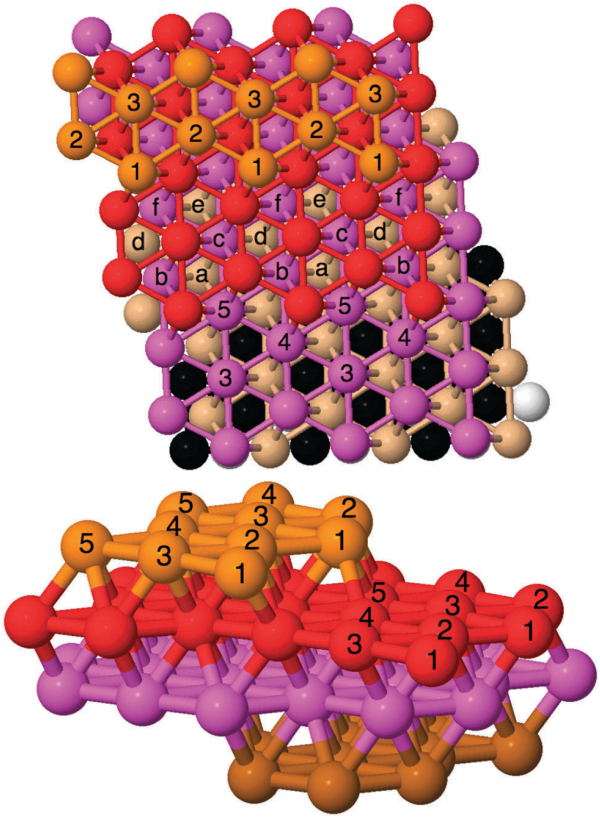

Fig. 1 Top (upper panel) and side view (bottom panel) of the 2 × 2 × 1 supercell used to represent the Cu(321) surface. Labels a, b, c, d, e and f refer to the hollow positions, whereas labels 1, 2, 3, 4 and 5 refer to the top positions.

obtained from periodic DFT calculations modelled through the usual repeated slab approach with a 2 × 2 × 1 supercell constructed using the optimum lattice parameter of 3.63 Å for the computational method chosen here and described in detail below; note that this is sufficiently close to the experimental value of 3.62 Å.[50] It is also worth pointing out that, in order to minimize lateral interactions, the unit cell for the Cu(321) slab model thus defined is larger than the one previously used by Fajín *et al.*[13] The 2 × 2 × 1 supercell used in the present work contains 60 Cu atoms distributed in four atomic layers as schematically shown in Fig. 1 and consists of a monoclinic prism with an angle of 104.96° between the x and y axes and of 90° for the angles between x and z or y and z axes. Furthermore, the unit cell vectors along the x, y and z directions have different lengths. The corresponding fractional coordinates of the atoms in this unit cell were obtained using the Materials Studio computer code (version 8.0).[51] The unit cell for the two-dimensional slab thus obtained was modified by adding a vacuum region of 12 Å and scaling the fractional coordinates conveniently so as to obtain a unit cell that can be replicated in three dimensions as required when using a plane-wave periodic DFT approach. The resulting slab was further modified by allowing full relaxation of the position of the uppermost 28 Cu atoms within the computational approach described below.

In order to investigate the impact of the dispersion terms in the calculated energy profile we compare results from two series of periodic DFT calculations, both carried out using the VASP code.[52–54] For the first series we rely on the PW91 calculation of Fajín *et al.*[13] whereas in the second one the effect of the van der Waals interactions has been included by adding the dispersion term obtained from the D2 method of Grimme[38] to the PBE calculated energy (PBE-D2). Note in passing that in spite of its semiempirical flavor, the D2 method has been shown to properly describe the physisorption and chemisorption states of graphene with Ni(111).[44] Nevertheless, to validate the present results some key calculations have been carried out by D3 parameterization of Grimme[39] (PBE-D3) and using the more physically grounded method proposed by Tkatchenko *et al.*[55] (DFT-T). Note also that PW91 and PBE results for bulk properties of transition metals[22,23] and also for the description of the adsorption energy of WGSR species are very similar.[56]

The valence electron density was expanded in a plane-wave basis set with a cut-off of 415 eV for the kinetic energy. The effect of core electrons in the valence electron density was taken into account using the projector augmented wave (PAW) method[57] as implemented in VASP.[58] Numerical integration in the reciprocal space was carried out by employing a 5 × 5 × 1 Monkhorst–Pack grid of special k-points.[59] The energy cut-off and k-point grid values were chosen after a systematic study of the geometry and energy convergence. Spin polarization is taken into account whenever species with a possible radical character are involved even if, as shown by Fajín and coworkers,[60] the open-shell character is likely to be quenched by the metallic character of the substrate.

The geometry optimization calculations carried out to locate the most stable structure of adsorbed species started from the structures reported by Fajín *et al.*,[13] the positions of the ions and the nearest surface Cu atoms (defined as those having distances to adsorbate atoms lesser than 3 Å) were relaxed using the conjugate-gradient algorithm. The convergence thresholds were 10^{-6} eV for the total energy and 10^{-3} eV Å^{-1} for the forces acting on the cores. The transition states for different elementary steps were determined using the improved Dimer method by Heyden *et al.*[61] with the same relaxation criteria. A proper frequency analysis indicating the presence of single imaginary frequencies ensured that the structures located using the Dimer method correspond to true transition states. Adsorption energies, co-adsorption energies, and energy barriers have been corrected for the zero-point vibrational energy (ZPE) within the harmonic oscillator approximation and, therefore, the subsequent presentation and discussion of results always consider ZPE-corrected energies.

The adsorption energies (E_{ads}) for all the isolated species on the slab surface model have been calculated as

$$E_{ads} = E_{slab\text{-}m} - E_{slab} - E_{m} \quad (1)$$

where $E_{slab\text{-}m}$ and E_{slab} refer to the total energy of the slab model representing the Cu(321) surface with and without the m adsorbate and E_{m} corresponds to the total energy of the molecule in the gas phase computed, as usual, by placing it in a box with the same size of the unit cell for the slab.

For situations with two adsorbates above the surface unit cell the co-adsorption energy is calculated as

$$E_{coad} = E_{slab\text{-}m1\text{-}m2} - E_{slab} - E_{m1} - E_{m2} \quad (2)$$

where $E_{slab\text{-}m1\text{-}m2}$ stands for the total energy of the system formed by the two species adsorbed on the slab and E_{slab}, E_{m1} and E_{m2} are as in eqn (1).

Results and discussion

Adsorption and co-adsorption of reactants, intermediates and products

In this subsection we discuss the effect of dispersion on the most favourable adsorption and co-adsorption configurations of the species involved in the WGSR mechanism catalysed by the Cu(321) surface. A summary of calculated results regarding adsorption energy is reported in Tables 1 and 2 whereas Fig. 2 and 3 report the equilibrium geometry of the adsorbed and co-adsorbed states for all involved species, respectively.

In agreement with the previous study of Fajín *et al.*,[13] water prefers to be adsorbed in the step region with the O atom linked to the Cu(1) surface atom and the two H atoms pointing to the lower terrace. The PBE-D2 adsorption energy for this configuration is −0.66 eV, which is very close to the PW91 result for the same surface (−0.58 eV) and 3–4 times larger than the reported value for the flat Cu(111) surface (−0.18 eV),[8] confirming the importance of the low-coordinated Cu atoms in the stabilization of the adsorbates. For adsorbed CO, the most stable configuration is also in the step region with a PBE-D2 calculated E_{ads} of −1.11 eV, again in very good agreement with the PW91 result of Fajín *et al.* (−0.95 eV) and twice larger than on the Cu(111) surface (−0.51 eV).[8] For the OH and COOH intermediates the PBE-D2 values are again very close to the PW91 ones and significantly larger than for the Cu(111) surface. Note that both intermediates are more stable when adsorbed at the bridge sites between Cu(1) and Cu(2) atoms (Fig. 2b and d) and that while the OH intermediate is clearly more stable on this stepped surface (−3.35 eV *versus* −2.77 eV for the Cu(111) surface), the adsorption energy for the COOH adsorbate is only 0.20 eV larger. Finally, both reaction products, CO_2 and H_2, interact weakly with the Cu(321) surface with PBE-D2 E_{ads} values of −0.28 and −0.12 eV only. It is worth pointing out that on the flat Cu(111) the CO_2 adsorption energy is even lower (−0.09 eV) and H_2 does not adsorb at all.[8] However, a close inspection of Table 1 shows that while the PW91 and PBE-D2 E_{ads} values for H_2O, OH, CO, COOH and H_2 are very similar, a significant difference is found for CO_2. In fact, the inclusion of the van der Waals interactions using the D2 method of Grimme[37] has a strong effect on the adsorption energy of the CO_2 molecule; the PW91 value reported by Fajín *et al.*[13] is of −0.06 eV only, much lower than the present PBE-D2 value. In order to validate the present result and to exclude a possible artefact of D2 parameterization two other vdW corrections, namely D3[39] and Tkatchenko *et al.*[55] methods, have been used giving E_{ads} values of −0.22 and −0.32 eV, respectively, in agreement with the D2 method (see also discussion at the end of the results section). Clearly, neither PBE nor PW91 functionals can properly describe the physisorption of the quite stable CO_2 molecule and vdW corrections should be included. This effect is also observed for the CO molecule, although to a lesser extent: from −0.95 to −1.11 eV. Note that this discrepancy does not come from the change in the functional because, as already discussed, PBE and PW91 essentially provide similar results. Hence, the worst possible scenario emerges where dispersion does not affect all species in a similar way.

Table 1 Adsorption energies for the adsorption of the WGSR species on Cu(321) as predicted from PBE-D2 and PW91 calculations. The different adsorption sites are indicated with numbers referring to the labels in Fig. 1 and with b indicating bridge sites. All values are in eV and ZPE corrected

Species	Adsorption site	PBE-D2	PW91[13]
H_2O	Top1-step	−0.66	−0.58
OH	$b_{2\text{-}1}$	−3.35	−3.40
CO	Top1	−1.11	−0.95
COOH	$b_{2\text{-}1}$	−2.05	−1.95
CO_2	Top1-step	−0.28	−0.06
H_2	Top1	−0.12	−0.12

Table 2 Co-adsorption energies for the adsorption of the WGSR species on Cu(321) as predicted from PBE-D2 and PW91 calculations. Sites are defined as in Table 1. All values are in eV and ZPE corrected

Species	Adsorption sites	PBE-D2	PW91
$OH_a + H_b$	$b_{4\text{-}1}$/hole "a"	−5.51	−5.47
$CO_a + OH_b$	Top1/hole "a"	−4.43	−4.05
$OH_a + OH_b$	$b_{2\text{-}1}/b_{3\text{-}1}$	−6.28	−6.40
O + H	Hole "a"/$b_{4\text{-}1}$	−7.35	−7.31
$CO_a + O_b$	Top1/hole "a"	−5.91	−5.84
$H_2O_a + O_b$	Top1-step/hole "b"	−5.82	−5.67
$H_a + H_b$	Hole "a"/hole "f"	−4.77	−4.81
$CO_aO_bH + O_cH$	$b_{2\text{-}1}$/top4	−5.20	—
$CO_2 + H$	Top1-step/hole "b"	−2.72	−2.47
$CO_2 + H_2O_a$	$b_{2\text{-}4}$/top1-step	−0.91	−0.70

Co-adsorption energies of the most stable configuration of reactant and product pairs for different elementary steps in the WGSR mechanism are listed in Table 2 and the corresponding geometries are shown in Fig. 3. All co-adsorption energies involving radicals have been obtained from spin polarized calculations for all the possible spin arrangements approaching multiplet (singlet, doublet, triplet...) states and the results show that for an even total number of electrons (H + H, OH + H, CO + O...) the most stable state is the global closed shell singlet, although the energy differences with the first most stable triplet state are only of the order of ∼0.05 eV. Analysing the most stable adsorption sites for different adsorbate pairs (Fig. 3) one can readily see that the atomic species (H and O) are typically found at the threefold-coordinated hollow sites, whereas OH prefers the bridge sites, and finally CO and the largest adsorbates are usually found in the step region, again evidencing the importance of the low-coordinated Cu atoms in the stabilization of the adsorbates. Results in Table 2 also evidence that the effect of dispersion is different for different adsorbate pairs which, as we will show in the next sections, must have an influence on several energy barriers and on the resulting TST reaction rates. In fact, the effect is almost negligible (∼0.05 eV) for some cases

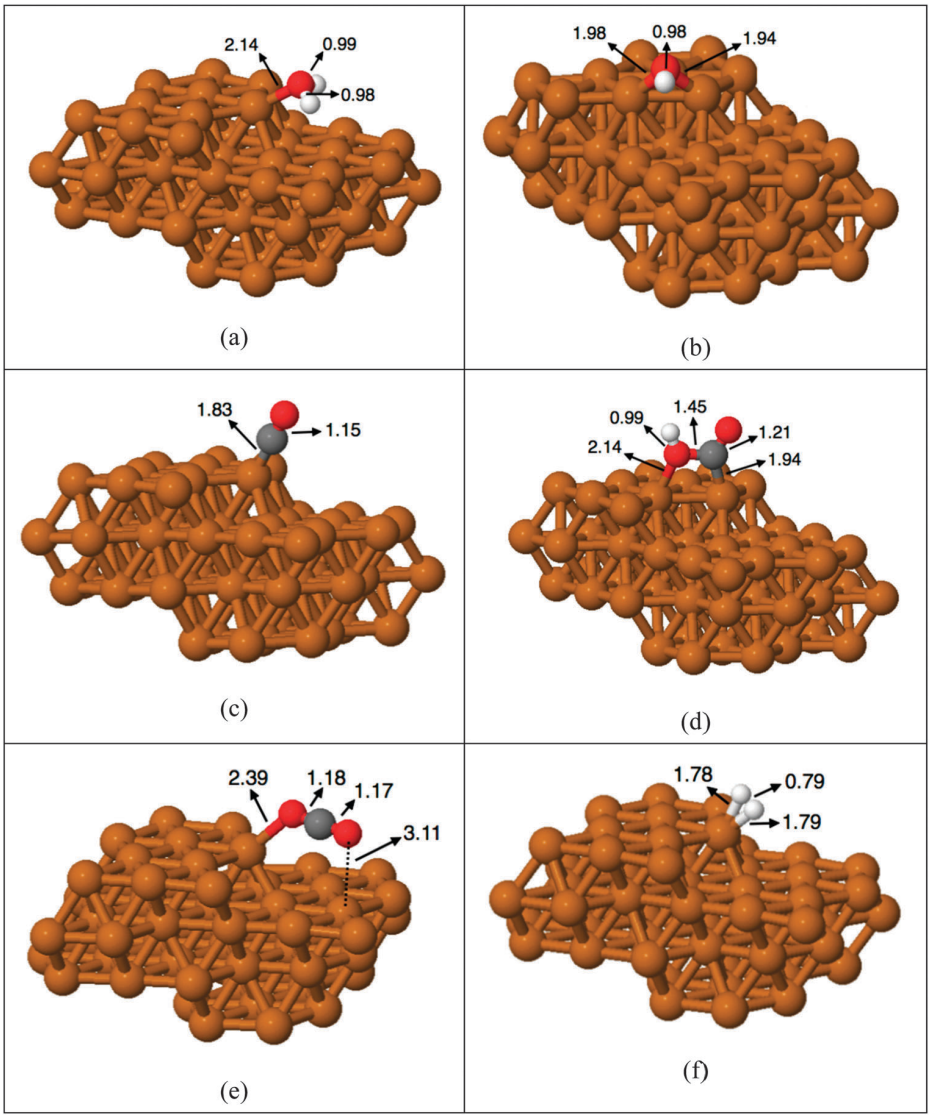

Fig. 2 Most stable configuration for H_2O (a), OH (b) CO (c), COOH (d), CO_2 (e) and H_2 (f) adsorbed species on the Cu(321) surface. Brown is used for Cu, grey for C, red for O and white for H. All the distances are in Å.

such as $OH_a + H_b$, O + H, or $H_a + H_b$, intermediate (<0.15 eV) for some others such as $OH_a + OH_b$ or $CO_a + O_b$ and quite large (>0.25 eV) in a few cases such as $CO_a + OH_b$ or CO_2 + H. The differences are large enough to be significant and likely to be present if other methods are used to estimate the dispersion contribution to the total energy.

Energy barriers of the elementary steps

Now we come to the most important part of the present work, namely the description of the calculated energy barriers for different elementary steps in the WGSR on Cu(321). The energy barrier for each individual step of the reaction mechanism has been calculated as the energy difference between the transition state, located using the improved Dimer method[61] and that of the most stable adsorption (or co-adsorption) configuration for the reactant(s). For the transition state (TS) calculations, the first step involved the search for the first order saddle point with the slab structure fixed and, in a second step, the atoms in the slab uppermost layers were allowed to relax out to refine the geometry and quantify the effect of the surface relaxation in the calculated energy barriers. ZPE corrected values, for the energy barriers obtained from PBE-D2 in the forward and reverse directions, are given in Table 3 where equivalent ZPE corrected PW91 values have been included for comparison. Schematic representations of the transition state geometries are given in Fig. 4. For product desorption (*i.e.*, $H_2 \rightarrow H_{2(g)}$ and $CO_2 \rightarrow CO_{2(g)}$) the TSs are assumed to be their final states, that is, H_2 and CO_2 in the gas phase. Thus, the energy barriers for these processes are equal to their adsorption energies in the absolute value (*i.e.*, 0.12 and 0.28 eV, respectively) and, consequently,

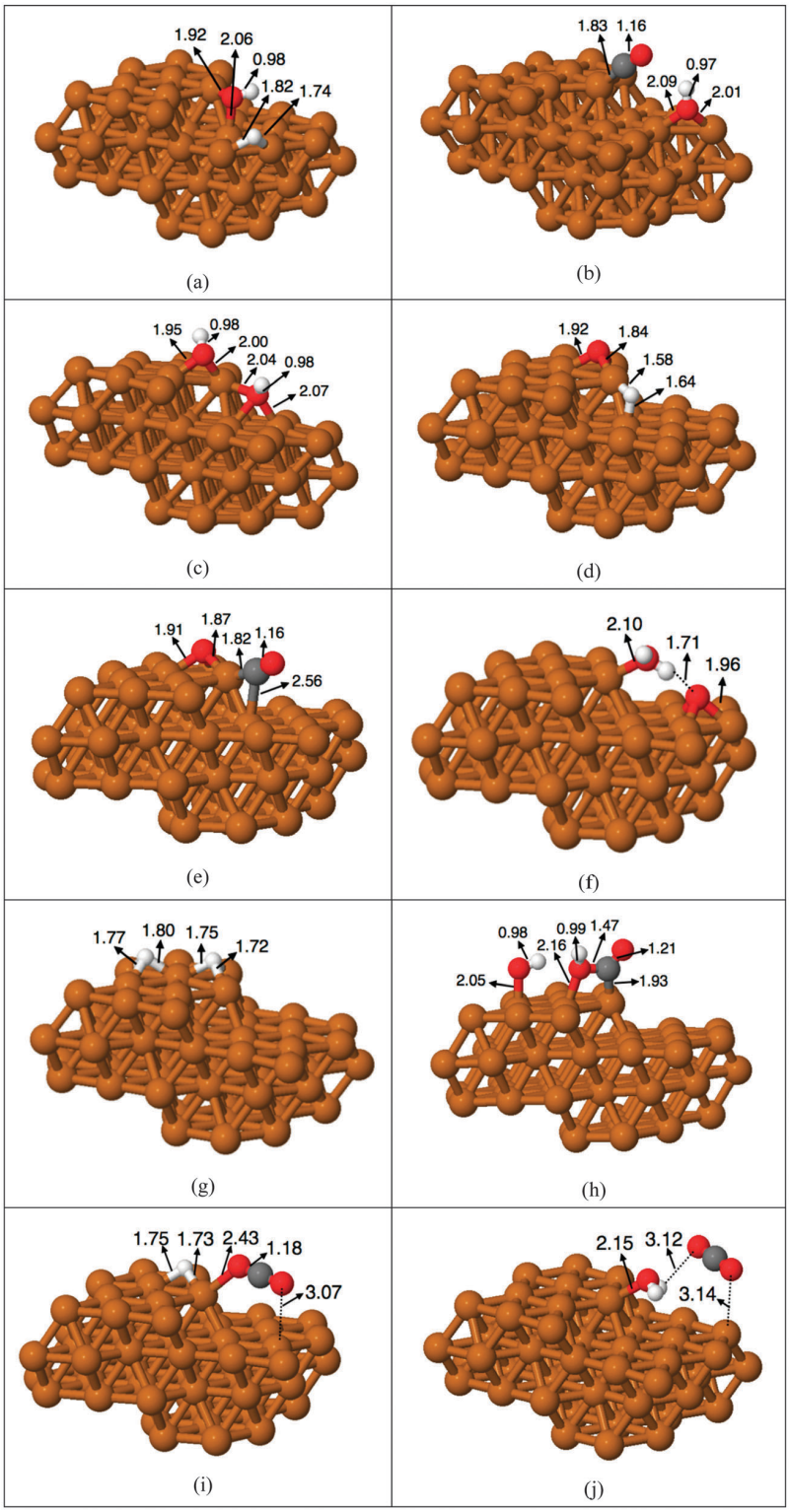

Fig. 3 Most stable configuration for OH + H (a), CO + OH (b), OH + OH (c), O + H (d), CO + O (e), H_2O + O (f), H + H (g), COOH + OH (h), CO_2 + H (i) and CO_2 + H_2O (j) co-adsorbed on the Cu(321) surface. Brown is used for Cu, grey for C, red for O and white for H. All the distances are given in Å.

Table 3 Elementary step characterization of the WGSR on the Cu(321) surface: imaginary frequencies associated with the transition state structure (ν_i in cm^{-1}), ZPE corrected energy barriers (E_b in eV) and reaction rates at 463 K (r in s^{-1}) for the forward and reverse reactions of the elementary steps as predicted from PBE-D2 calculations. ZPE corrected PW91 values from Fajín *et al.*[13] for the forward reaction are given in parenthesis for comparison

		Forward		Reverse	
Elementary step	ν_i	E_b	r	E_b	r
$H_2O \rightarrow OH + H$	919i	0.78 (0.71)	7.94×10^3 (3.6×10^4)	0.58	6.38×10^6
$OH \rightarrow O + H$	1046i	1.51 (1.55)	1.16×10^{-4} (4.1×10^{-5})	1.03	6.22×10^1
$OH + OH \rightarrow H_2O + O$	909i	0.46 (0.78)	4.51×10^7 (1.47×10^4)	0.56	5.66×10^6
$CO + O \rightarrow CO_2$	207i	0.68 (0.60)	8.25×10^4 (5.58×10^5)	1.17	1.25×10^{-2}
$CO + OH \rightarrow$ *cis*-COOH	224i	0.84 (0.46)	1.78×10^4 (2.33×10^7)	0.24	2.12×10^{10}
cis-COOH $\rightarrow CO_2 + H$	1395i	0.80 (1.10)	5.03×10^4 (9.67×10^1)	1.32	2.43×10^{-2}
cis-COOH + OH $\rightarrow CO_2 + H_2O$	248i	0.33 (0.55)	3.22×10^8 (9.72×10^6)	0.96	1.04×10^{-1}
$H + H \rightarrow H_{2(g)}$	649i	0.78 (0.80)	6.88×10^4 (3.91×10^4)	0.47	1.61×10^7

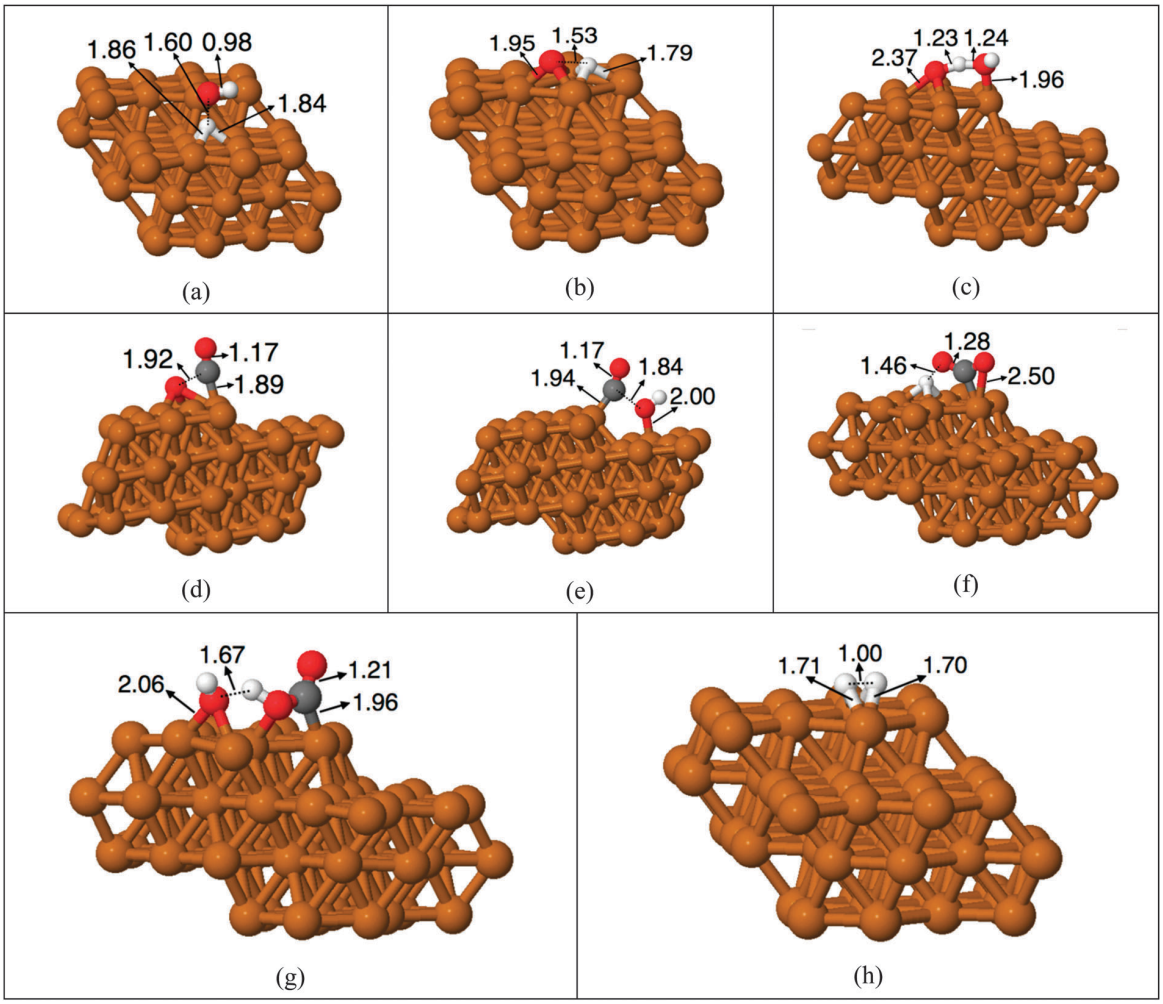

Fig. 4 Schematic representation of the transition state structures for the $H_2O \rightarrow OH + H$ (a), $OH \rightarrow O + H$ (b), $OH + OH \rightarrow H_2O + O$ (c), $CO + O \rightarrow CO_2$ (d), $CO + OH \rightarrow COOH$ (e), $COOH \rightarrow CO_2 + H$ (f), $COOH + OH \rightarrow CO_2 + H_2O$ (g) $H + H \rightarrow H_2$ (h) elementary steps in Table 3 as obtained from PBE-D2 calculations. Brown is used for Cu, grey for C, red for O and white for H. All the distances are given in Å.

are not included in Table 3. In the following we will discuss the effect of dispersion in different steps by comparing the results reported by Fajín *et al.*[13] with appropriate comparison to the results reported for Cu(111) not including dispersion terms[8] whenever needed. Hence, the appropriate comparison involves different steps on the Cu(321) with and without dispersion or on the Cu(321) and Cu(111) surfaces both without dispersion terms being included.

Water dissociation. This step is endoergic by 0.20 eV with an energy barrier of 0.78 eV (Table 3), significantly lower than the 1.01 eV value for the Cu(111) surface, and very similar to the ZPE corrected PW91 value obtained by Fajín of 0.71 eV. To further validate the present result, the energy barrier corresponding to this step has been calculated also including the vdW interactions using the DFT-T method obtaining a value of 0.79 eV, in very good agreement with the PBE-D2 results. Here including the vdW correction has a minor effect. It is worth pointing out that the lower energy barrier for this surface implies a greater reaction rate for water dissociation and hence, in principle, a concomitant enhancement of the reactivity towards WGSR. However, the reaction rate for the reverse process has been increased even more, because, while here the reaction is endoergic, on the flat Cu(111) surface this step is practically isoergic (ΔE = 0.01 eV). Therefore, the reactivity depends on whether forward reaction rates of the other processes can compete with the formation of water.

OH dissociation. This step is endoergic by 0.48 eV, almost the same value as for the Cu(111) surface, and has an energy barrier of 1.51 eV (Table 3), higher than that for the flat surface (1.19 eV)[8] and, as the previous step, very similar to the value obtained without including vdW corrections (1.55 eV).[13] The high energy barrier for this reaction implies that CO_2 formation *via* the redox mechanism through direct OH dissociation on the Cu(321) surface will surely be the least frequent route among all.

OH disproportionation. This is an alternative path for producing atomic oxygen; it is exoergic by −0.10 eV with an energy barrier of only 0.46 eV, becoming the main route of the redox mechanism. Surprisingly, this value is increased by 0.32 eV when vdW interactions are not considered (Table 3).

CO oxidation by atomic O. This step is exoergic by −0.48 eV, a value significantly different from that on the Cu(111) surface (−0.78 eV). The PBE-D2 energy barrier for this process is 0.68 eV, almost the same as obtained from PW91 (0.60 eV) even if the latter does not include the effect of dispersion. The high exoergicity of this process implies that the reverse hardly occurs.

Carboxyl formation through CO oxidation by OH. Direct CO oxidation by OH to produce surface carboxyl species represents a viable alternative to the previous step, with a PBE-D2 energy barrier of 0.84 eV, slightly higher than the value reported for the Cu(111) surface (*i.e.*, 0.70 eV). On the flat surface this process is endoergic by only 0.15 eV, the endoergicity is heavily increased on the Cu(321) surface. Note that this value is also different from the value reported by Fajín *et al.*[13] (0.22 eV), where the energy barrier reported was of 0.46 eV. The reason of this difference is that the CO + OH pair is significantly stabilized by inclusion of vdW interactions (Table 2).

Carboxyl dehydrogenation. This is an exoergic step (−0.52 eV) with an energy barrier of 0.80 eV (Table 3), again significantly lower than for the flat Cu(111) surface (1.18 eV) and also lower than that of the PW91 value obtained (1.10 eV).[13] Since the inclusion of vdW interactions stabilizes both the transition state and the final products, CO_2 formation through the carboxyl intermediate will probably play a more important role in the WGSR over Cu(321) than in Cu(111).

Carboxyl disproportionation by hydroxyl. This step involving *cis*-COOH is also exoergic by −0.64 eV, more than for the Cu(111) surface (−0.37 eV). The energy barrier for this process is 0.33 eV compared to 0.55 eV without vdW correction, which in turn needs to be compared with the result obtained for the flat surface (0.38 eV).

H recombination. This step is common to the four investigated routes. According to the present result, H atoms are not provided only by water dissociation but also by carboxyl dehydrogenation. Another possible process for H production is OH dissociation which is very unfavourable even on this stepped surface. Although H_2 does not adsorb molecularly on Cu(111) it does on the Cu(321) surface by −0.12 eV (see Table 1). This reaction is endoergic by 0.31 eV, with an energy barrier of 0.78 eV, again smaller than the ZPE corrected 0.96 eV value for the Cu(111) surface.

Reaction rates of the elementary steps

From the calculated zero point corrected energy barriers and vibrational frequencies one can readily obtain the corresponding transition state theory rates at the temperature of interest. Table 3 reports the calculated rates for the elementary steps at 463 K; this is the same temperature used in previous work regarding the WGSR mechanism on the Cu(111)[8] and Cu(321)[13] surfaces, where dispersion terms were not included in the calculations.

As discussed above and in agreement with Fajín *et al.*,[13] the presence of low-coordinated Cu atoms plays an important role in the stabilization of the reactants, with adsorption energies twice or even three times larger than that on the flat Cu(111) surface but with significant differences in the results corresponding to the Cu(321) surface depending on whether dispersion terms are neglected or included. Nevertheless, the difference to Cu(111) is very large, implying a reduction of seven and five orders of magnitude for the reaction rates of CO and H_2O desorption at T = 463 K, respectively. This is likely to be due to the coverage of these species leading to higher H_2 production although macroscopic simulations are needed to further check if this strong stabilization of reactants enhances the reactivity.

The dissociation of adsorbed water defines the rds in all cases and all results seem to indicate that the associative mechanism is clearly preferred. Nevertheless, the rates predicted by the present PBE-D2 calculations for the rds are one order of magnitude smaller than the values reported from PW91 not including dispersion terms. Here it is worth mentioning that the low energy barrier for the reverse process leads to a reaction rate of 6.38×10^6 s^{-1}, six orders of magnitude larger than that on the flat surface (5.25×10^0 s^{-1}) and greater than the rate for the forward process. Clearly, it is not possible to extract reliable conclusions from the energy barrier for the rate-determining step in the forward direction only.

Results in Table 3 show that the effect of dispersion on all elementary steps is very different. In some cases including or not these effects show a variation of barely one order of magnitude at the calculated rates for the forward reactions. This is for instance the case of $H_2O \rightarrow OH + H$, $OH \rightarrow O + H$, $CO + O \rightarrow CO_2$, *cis*-$COOH + OH \rightarrow CO_2 + H_2O$, and $H + H \rightarrow H_2$ steps. However, in

some other steps the effect of dispersion implies up to three orders of magnitude in the calculated reaction rates, as this is the case for OH + OH → H_2O + O, which now appears as the dominant source of adsorbed O. This is especially relevant since including dispersion affects the reaction rate of the main step in CO_2 production also by three orders of magnitude but in the opposite sense. The formation of carboxyl is highly disfavoured when dispersion terms are explicitly included. The reaction rate for CO_2 production (at 463 K) through *cis*-COOH dissociation is enhanced by three orders of magnitude by including dispersion terms in the calculation of the energy barrier. Finally, it is worth mentioning that, not surprisingly, dispersion terms largely affect the reaction rates for adsorption and desorption steps (not reported).

At this point, one may still argue that semiempirical dispersion treatments based on atom pairwise potentials may be inadequate for metallic systems and question the overall validity of the present results. The selected adsorption energy values reported above calculated using the D3 and Tatchenko methods would indicate that this is not the case. Nevertheless, to reach a firm conclusion it is convenient to inspect energy barriers as well. To this end, a new series of calculations has been carried out using the method recently proposed by Andersson consisting of a smart yet simple modification of the DFT-D2 method of Grimme which provides good results for metallic systems.[62] This method takes into account screening of the dispersion forces by the conducting valence electrons in the metal, includes the main physics and reproduces a wide variety of experimental data for both bulk metallic systems and adsorption onto metal surfaces. The main idea is to introduce a hard cutoff to the dispersion interaction and to conveniently replace the C_6 coefficients for metal atoms. Using this approach, all adsorption energies for reactants and products and energy barriers for two of the most important elementary steps (*i.e.* H_2O → OH + H and CO + O → CO_2) have been calculated. The ZPE corrected adsorption energy values of CO, H_2O, CO_2 and H_2 calculated in this way (−1.03, −0.57, −0.19 and −0.08 eV, respectively) are very close to the PBE-D2 values in Table 2 to the point that the changes are within the incertitude of DFT methods. The equilibrium geometries calculated using PBE-D2 and PBE-Anderson methods are almost the same and the calculated surface reaction energy barriers differ by less than 0.05 eV. Consequently, one can firmly claim that the conclusion arising from the PBE-D2 calculations reported in the present work is physically meaningful.

Conclusions

The effect of dispersion terms on the description of the energy profile and reaction rates of a complex heterogeneously catalysed process has been studied in detail taking the water gas shift reaction on Cu(321) as a case example. This is a convenient case study because of a rather large number of elementary steps and the existence of previous results regarding the molecular mechanism of the overall reaction on this surface[13] and on the flat Cu(111) surface,[8] but both neglecting dispersion effects.

Including dispersion terms does not change the qualitative picture of the overall reaction; the rate determining step and the predominant route are not affected by including or neglecting these terms. However, the present results show that, in spite of the rather small size of the species involved in the molecular mechanism of the WGSR, the contribution of dispersion to the overall picture is important and should not be ignored. The effect of dispersion is different for several adsorbates – reactants, intermediates or products – with a clear net effect and with no compensation of errors. Dispersion terms affect adsorption structures and adsorption energies but also contribute to determine the transition state and the energy barriers with differential effects on final forward and reverse values of up to 0.4 eV. This seemingly small value has a huge effect on the transition state theory computed reaction rates.

One must admit that the present results have been obtained from a particular choice of the method used to estimate dispersion terms. Nevertheless, calculations for the key steps have also been carried out including dispersion with two alternative methods indicating that the conclusions of the present work are sound and not biased.

To summarize, while the inclusion of dispersion terms does not change the qualitative description of the WGSR catalysed by Cu(321), their presence largely affects the overall potential energy profile and produces tremendous changes in the predicted reaction rates. Consequently, dispersion terms must be included when aiming at obtaining information from macroscopic simulations employing for instance microkinetic or kinetic Monte Carlo approaches, where these effects should be clearly shown.

Acknowledgements

Financial support to this research has been provided by the Spanish MINECO CTQ2012-30751 and CTQ2014-53987-R grants and, in part, from the Generalitat de Catalunya grants 2014SGR97, 2014SGR1582 and XRQTC. HPG thanks Generalitat de Catalunya for a predoctoral FI-DGR-2015 grant. Computational resources provided by Consorci de Serveis Universitaris de Catalunya (CSUC, former CESCA) are gratefully acknowledged.

References

1 L. Grabow, W. Schneider, M. J. Janik, T. Manz, A. van Duin, S. Sinnott and D. Scholl, *Computational Catalysis*, Royal Society of Chemistry Books, 2013.
2 J. K. Nørskov, F. Studt, F. Abild-Pedersen and T. Bligaard, *Fundamental Concepts in Heterogeneous Catalysis*, John Wiley & Sons, Inc., 2014, ISBN: 978-1-118-88895-7.
3 K. Reuter and M. Scheffler, *Phys. Rev. B: Condens. Matter Mater. Phys.*, 2002, **65**, 035406.
4 K. Honkala, K. Hellman, I. N. Remediakis, A. Logadottir, A. Carlsson, S. Dahl, C. H. Christensen and J. K. Nørskov, *Science*, 2005, **307**, 555–558.
5 J. K. Nørskov, T. Bligaard, J. Rossmeisl and C. H. Christensen, *Nat. Chem.*, 2009, **1**, 37–46.

6 J. K. Nørskov, F. Abild-Pedersen, F. Studt and T. Bligaard, *Proc. Natl. Acad. Sci. U. S. A.*, 2011, **108**, 937–943.
7 J. A. Dumesic, D. F. Rudd, L. L. Aparicio, J. E. Rekoske and A. A. Treviño, *The Microkinetics of Heterogeneous Catalysis*, American Chemical Society, Washington, DC, 1993.
8 A. A. Gokhale, A. J. Dumesic and M. Mavrikakis, *J. Am. Chem. Soc.*, 2008, **130**, 1402–1414.
9 L. Yang, A. Karim and J. T. Muckerman, *J. Phys. Chem. C*, 2013, **117**, 3414–3425.
10 H. Prats, L. Álvarez-Falcón, F. Illas and R. Sayos, *J. Catal.*, 2016, **333**, 217–225.
11 Z. P. Liu and P. Hu, *J. Am. Chem. Soc.*, 2003, **125**, 1958–1967.
12 S. Gonzalez, D. Loffreda, P. Sautet and F. Illas, *J. Phys. Chem. C*, 2007, **111**, 11376–11383.
13 J. L. C. Fajín, M. N. D. S. Cordeiro, F. Illas and J. R. B. Gomes, *J. Catal.*, 2009, **268**, 131–141.
14 J. Rempel, J. Greeley, L. B. Hansen, O. H. Nielsen, J. K. Norskov and M. Mavrikakis, *J. Phys. Chem. C*, 2009, **113**, 20623–20631.
15 J. L. C. Fajín, M. N. D. S. Cordeiro and J. R. B. Gomes, *J. Catal.*, 2012, **289**, 11–20.
16 S. Lin, J. Y. Ma, L. S. Zhou, C. J. Huang, D. Q. Xie and H. Guo, *J. Phys. Chem. C*, 2013, **117**, 451–459.
17 F. Viñes, J. R. B. Gomes and F. Illas, *Chem. Soc. Rev.*, 2014, **43**, 4922–4939.
18 D. D. Langreth and M. J. Mehl, *Phys. Rev. B: Condens. Matter Mater. Phys.*, 1983, **28**, 1809–1834.
19 J. P. Perdew and Y. Wang, *Phys. Rev. B: Condens. Matter Mater. Phys.*, 1986, **33**, 8800–8802.
20 J. P. Perdew and Y. Wang, *Phys. Rev. B: Condens. Matter Mater. Phys.*, 1992, **45**, 13244–13249.
21 J. P. Perdew, K. Burke and M. Ernzerhof, *Phys. Rev. Lett.*, 1996, **77**, 3865–3868.
22 J. Janthon, S. M. Kozlov, F. Viñes, J. Limtrakul and F. Illas, *J. Chem. Theory Comput.*, 2013, **9**, 1631–1640.
23 J. Janthon, S. J. Luo, S. M. Kozlov, F. Viñes, J. Limtrakul, D. G. Trulhar and F. Illas, *J. Chem. Theory Comput.*, 2014, **10**, 3832–3839.
24 Y. Zhao, N. E. Schultz and D. G. Truhlar, *J. Chem. Theory Comput.*, 2006, **2**, 364–382.
25 S. Kristyan and P. Pulay, *Chem. Phys. Lett.*, 1995, **229**, 175–180.
26 A. D. Becke, *J. Chem. Phys.*, 1993, **98**, 5648–5652.
27 R. Peverati, Y. Zhao and D. G. Truhlar, *J. Phys. Chem. Lett.*, 2011, **2**, 1991–1997.
28 Y. Zhao and D. G. Truhlar, *J. Chem. Phys.*, 2006, **125**, 194101.
29 R. Peverati and D. G. Truhlar, *Phys. Chem. Chem. Phys.*, 2012, **14**, 13171.
30 N. E. Schultz, Y. Zhao and D. G. Truhlar, *J. Phys. Chem. A*, 2005, **109**, 11127–11143.
31 J. N. Harvey, *Annu. Rep. Prog. Chem., Sect. C: Phys. Chem.*, 2006, **102**, 203–226.
32 N. E. Schultz, Y. Zhao and D. G. Truhlar, *J. Phys. Chem. A*, 2005, **109**, 4388–4403.
33 S. F. Sousa, P. A. Fernandes and M. J. Ramos, *J. Phys. Chem. A*, 2007, **111**, 10439–10452.
34 J. Paier, M. Marsman, K. Hummer, G. Kresse, I. C. Gerber and J. G. Ángyán, *J. Chem. Phys.*, 2006, **124**, 154709.
35 C. H. Christensen and J. K. Nørskov, *J. Chem. Phys.*, 2008, **128**, 182503.
36 P. Strasser, Q. Fan, M. Devenney, W. H. Weinberg, P. Liu and J. K. Nørskov, *J. Phys. Chem. B*, 2003, **107**, 11013–11021.
37 S. Grimme, *J. Comput. Chem.*, 2004, **25**, 1463–1473.
38 S. Grimme, *J. Comput. Chem.*, 2006, **27**, 1787–1799.
39 S. Grimme, J. Antony, S. Ehrlich and H. Krieg, *J. Chem. Phys.*, 2010, **132**, 154104.
40 J. Klimes and A. Michaelides, *J. Chem. Phys.*, 2012, **137**, 120901.
41 S. Grimme, *Comput. Mol. Sci.*, 2011, **2**, 211–228.
42 P. G. Moses, J. J. Mortensen, B. I. Lundqvist and J. K. Nørskov, *J. Chem. Phys.*, 2009, **130**, 104709.
43 B. A. De Moor, M. F. Reyniers, M. Sierka, J. Sauer and G. B. Marin, *J. Phys. Chem. C*, 2008, **112**, 11796–11812.
44 P. Janthon, F. Viñes, S. M. Kozlov, J. Limtrakul and F. Illas, *J. Chem. Phys.*, 2013, **138**, 244701.
45 J. P. P. Ramalho, J. R. B. Gomes and F. Illas, *RSC Adv.*, 2013, **3**, 13085–13100.
46 D. S. Newsome, *Catal. Rev.: Sci. Eng.*, 1980, **21**, 275–318.
47 N. Schumacher, A. Boisen, S. Dahl, A. A. Gokhale, S. Kandoi, L. C. Grabow, J. A. Dumesic, M. Mavrikakis and I. Chorkendorff, *J. Catal.*, 2005, **229**, 265–275.
48 A. Bruix, J. A. Rodriguez, P. J. Ramírez, S. D. Senanayake, J. Evans, J. B. Park, D. Stacchiola, P. Liu, J. Hrbek and F. Illas, *J. Am. Chem. Soc.*, 2012, **134**, 8968–8974.
49 J. A. Rodriguez, P. J. Ramírez, G. G. Asara, F. Viñes, J. Evans, P. Liu, J. M. Ricart and F. Illas, *Angew. Chem., Int. Ed.*, 2014, **53**, 11270–11274.
50 D. R. Lide, *CRC Handbook of Chemistry and Physics*, ed. D. R. Lide, CRC Press, Boca Raton, USA, 88th edn, 2008.
51 Materials Studio, Accelrys Software Inc., San Diego, 2011.
52 G. Kresse and J. Hafner, *Phys. Rev. B: Condens. Matter Mater. Phys.*, 1993, **47**, 558–561.
53 G. Kresse and J. Furthmüller, *Comput. Mater. Sci.*, 1996, **6**, 15–50.
54 G. Kresse and J. Furthmüller, *Phys. Rev. B: Condens. Matter Mater. Phys.*, 1996, **54**, 11169–11186.
55 A. Tkatchenko, R. A. Di Stasio, R. Car and M. Scheffler, *Phys. Rev. Lett.*, 2012, **108**, 236402.
56 J. L. C. Fajín, F. Illas and J. R. B. Gomes, *J. Chem. Phys.*, 2009, **130**, 224702.
57 P. E. Blöchl, *Phys. Rev. B: Condens. Matter Mater. Phys.*, 1994, **50**, 17953–17979.
58 G. Kresse and D. Joubert, *Phys. Rev. B: Condens. Matter Mater. Phys.*, 1999, **59**, 1758–1775.
59 H. J. Monkhorst and J. D. Pack, *Phys. Rev. B: Condens. Matter Mater. Phys.*, 1976, **13**, 5188–5192.
60 J. L. C. Fajín, M. N. D. S. Cordeiro, J. R. B. Gomes and F. Illas, *J. Chem. Theory Comput.*, 2012, **8**, 1737–1743.
61 A. Heyden, A. T. Bell and F. J. Keil, *J. Chem. Phys.*, 2005, **123**, 224101.
62 M. P. Andersson, *J. Theor. Chem.*, 2013, **2013**, 327839.

5.3. Summary and conclusions

The effect of vdW interactions on the adsorption energies, energy barriers and reaction rates of a complex heterogeneously catalyzed reaction has been studied in detail, taking the WGSR on Cu(321) as a case example. As shown in Table 1 from Publication 4, the inclusion of dispersion interactions has an almost negligible effect on the adsorption energies of most species, except for the special case of CO_2, where the calculated value of -0.28 eV is much higher than the reported value of -0.06 eV without dispersion. In order to validate this result and to exclude a possible artefact of D2 parameterization, two other vdW corrections, namely D3[7] and Tkatchencko *et. al*.[8] methods, have been used giving adsorption energy values in agreement with the D2 method. Clearly, the physisorption of the quite stable CO_2 molecule can only be described when vdW corrections are included. This effect is also observed for the CO molecule, although to a lesser extent: from -0.95 to -1.11 eV.

However, effect of vdW is not only limited to stabilizing some adsorbed molecules, but it can also modify the energy barriers of surface processes. For instance, consider the carboxyl formation (i.e., CO+OH→COOH). In absence of dispersion interactions the energy barrier is only 0.46 eV, but if we include those interactions the CO+OH pair is stabilized by almost 0.4 eV (see Table 2 from Publication 4) and the energy barrier increases to 0.84 eV. Apart from carboxyl formation, other surface processes such as OH disproportionation (i.e., OH+OH→H_2O+O) and COOH dissociation (i.e., COOH→ CO_2+H) also experience an important modification of their energy barriers. On the remaining surface processes, the vdW terms in the total energies for reactant, transition state and product configurations are similar, leading to a small net effect when calculating the energy barriers as total energy differences.

In spite of the rather small size of the species involved in the molecular mechanism of the WGSR, the present results show that the contribution of dispersion to the overall picture is important, with a clear net effect and with no compensation of errors on several reaction steps, and therefore should not be ignored. Note that, if one wants to study the kinetics of the reaction at the operating conditions (e.g., through a microkinetic model or kMC simulations), neglecting the effect of vdW can lead to tremendous changes in the computed reaction rates, with differences up to 4 orders of magnitude (see Table 3 in Publication 5). These errors in the reaction rates might result in wrong turnover frequencies and coverages.

Finally, a quick comparison between the energy profiles of the flat Cu(111) surface and the stepped Cu(321) surface shows that the low-coordinated Cu atoms from the latter lead to a strong adsorption of the adsorbed species. The effect of step sites is especially relevant in the case of the reactants, with adsorption energies two and three times larger for CO and H_2O, respectively. Regarding the effect of low coordinated sites on the energy barriers, there is no clear trend. Some of them decrease (e.g., water dissociation and carboxyl dissociation), but others increase (e.g., carboxyl disproportionation by OH). With the results presented on this chapter, it is not possible to make any reliable prediction regarding the effect of step sites on the kinetics of the WGSR on copper. Thus, subsequent kMC simulations are needed, and will be presented in the next chapter.

5.4. References

1 S. Grimme, Density functional theory with London dispersion corrections, *Wiley Interdiscip. Rev. Comput. Mol. Sci.*, **2011**, 1, 211–228.

2 P. G. Moses, J. J. Mortensen, B. I. Lundqvist and J. K. Norskov, Density functional study of the adsorption and van der Waals binding of aromatic and conjugated compounds on the basal plane of MoS_2, *J. Chem. Phys*., **2009**, 130, 104709.

3 B. A. De Moor, M.-F. Reyniers, M. Sierka, J. Sauer and G. B. Marin, Physisorption and chemisorption of hydrocarbons in H-FAU using QM-Pot(MP2//B3LYP) calculations, *J. Phys. Chem. C*, **2008**, 112, 11796–11812.

4 P. Janthon, F. Viñes, S. M. Kozlov, J. Limtrakul and F. Illas, Theoretical assessment of graphene-metal contacts, *J. Chem. Phys*., **2013**, 138, 244701.

5 S. Grimme, Semiempirical GGA-type density functional constructed with a long-range dispersion correction, *J. Comp. Chem*., **2006**, 27, 1787–1799.

6 J. P. Perdew, K. Burke and M. Ernzerhof, Generalized gradient approximation made simple, *Phys. Rev. Lett*., **1996**, 77, 3865–3868.

7 S. Grimme, J. Antony, S. Ehrlich and H. Krieg, A consistent and accurate ab initio parametrization of density functional dispersion correction (DFT-D) for the 94 elements H-Pu, *J. Chem. Phys.*, **2010**, 132, 154104.

8 A. Tkatchenko, R. A. DiStasio, R. Car and M. Scheffler, Accurate and efficient method for many-body van der Waals interactions, *Phys. Rev. Lett.*, **2012**, 108, 236402.

CHAPTER SIX

Effect of step sites on the WGSR on Cu surfaces

6.1. Introduction

To complete our study of the WGSR, once having studied its mechanism on the flat Cu(111) surface in Chapter 4 and also having quantified the effect of vdW interactions in Chapter 5, we focus on the effect of step sites on the activity of the WGSR catalyzed by copper.

Step sites play an important role in heterogeneous catalysis[1–3]. For instance, they allow different types of binding to the catalyst surface[4], and facilitate bond breaking of reactants.[5] It is generally assumed that the presence of steps enhances the catalytic activity towards a complex reaction by increasing the adsorption energies for reactants and decreasing the energy barriers, as shown by Honkala *et al*.[6] for the case of NH_3 synthesis over a model of a Ru catalyst. However, this assumption may not be general. Even if the energy barriers for the RDS at step sites are lower than for regular sites, one cannot conclude that the presence of steps is beneficial without studying the reaction in more detail. For instance, step sites may also result in the lowering of the energy barriers for RDSs also in the reverse direction, increasing reverse reaction rates over the forward ones with a concomitant decrease in the catalytic activity. Moreover, a strong chemisorption of reactants, products or impurities on the step sites may cause surface poisoning[7].

Previous studies for the reverse WGSR[8] and for the WGSR[9] on Cu(hkl) surfaces conclude that catalytic activity follows the order Cu(110) > Cu(100) > Cu(111). However, these claims are based on comparing energy barriers of some assumed RDSs only. Note that the use of reaction rates would include at least entropic and temperature effects. Clearly, a more rigorous approach would imply to introduce temperature, pressure, reverse processes and surface coverage effects, which also would allow a much better estimate of the RDSs. This can be done by using either microkinetic modelling or kMC simulations. Usually, the RDS for a complex reaction, as the case of the WGSR, depends on catalyst along with the T and P conditions[10]. Within a microkinetic model or kMC simulations, a rather rigorous determination of the RDSs (i.e., often there are several ones) can be done, for instance through the evaluation of the degree of rate control defined by Campbell[11].

In Chapter 5, the energy profile of the WGSR on the stepped Cu(321) surface was obtained by means of periodic DFT calculations and compared with the results reported by Gokhale *et al*.[12] for the flat Cu(111) surface. However, to answer the question of

whether the step sites will enhance the WGSR activity on copper requires additional studies. The adsorption energies for reactants, for instance, are larger on the Cu(321) surface. This will result in a higher adsorption rate and lower desorption rate, which seems positive, but a very strong adsorption may cause surface poisoning. Also, it is not clear what will be the effect of the possible reduction of energy barriers for surface processes due to the step sites on the overall TOF. Consider for instance the water dissociation, one of the main processes of the overall reaction mechanism. The forward energy barriers on Cu(111) and Cu(321) are 1.01 and 0.78 eV, respectively. This reduction suggests an improved catalytic activity on the stepped surface. Nevertheless, the reverse energy barrier is decreased even more: from 1.15 to 0.60 eV. Hence, the main goal of the present chapter is to study the effect of step sites in the WGSR catalyzed by copper.

6.2. Publication 5

Comparing the catalytic activity of the water gas shift reaction on Cu(321) and Cu(111) surfaces: Step sites do not always enhance the overall reactivity

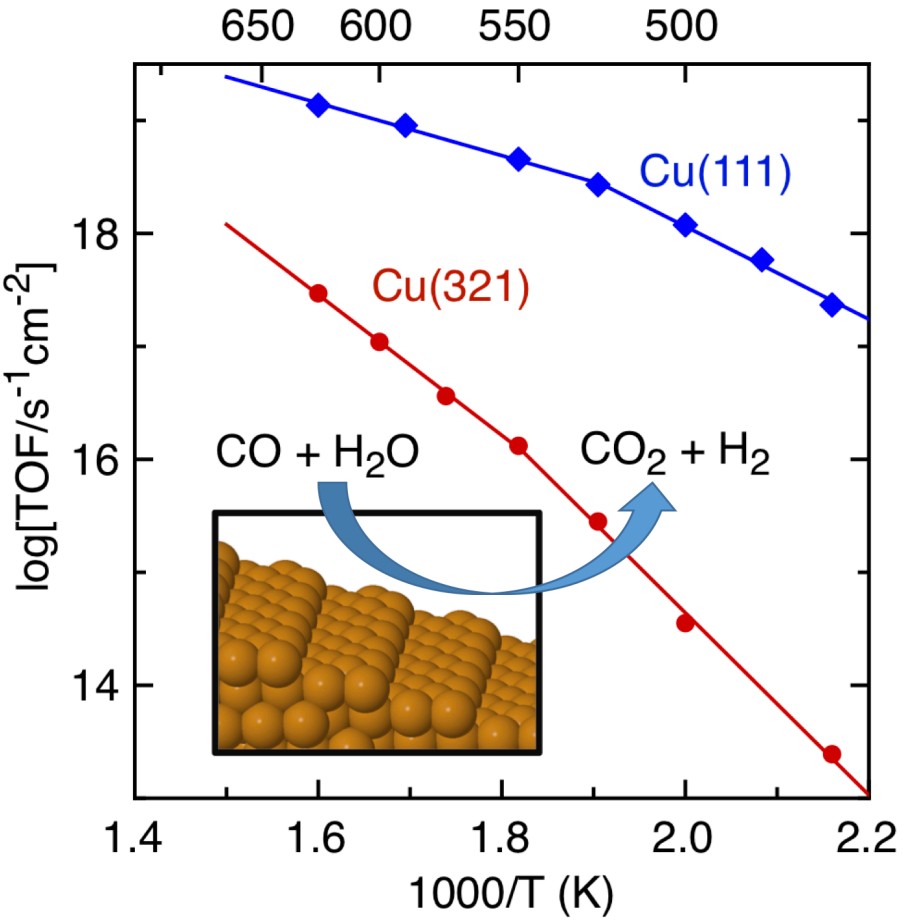

Journal of Catalysis 342 (2016) 75–83

Contents lists available at ScienceDirect

Journal of Catalysis

journal homepage: www.elsevier.com/locate/jcat

Comparing the catalytic activity of the water gas shift reaction on Cu(3 2 1) and Cu(1 1 1) surfaces: Step sites do not always enhance the overall reactivity

Hèctor Prats, Pablo Gamallo, Francesc Illas, Ramón Sayós *

Departament de Ciència de Materials i Química Física & Institut de Química Teòrica i Computacional (IQTCUB), Universitat de Barcelona, C. Martí i Franquès 1, 08028 Barcelona, Spain

ARTICLE INFO

Article history:
Received 27 May 2016
Revised 19 July 2016
Accepted 19 July 2016

Keywords:
Kinetic Monte Carlo
Water gas shift reaction
Copper (3 2 1) surface
Density functional theory
Associative COOH mechanism
Surface redox mechanism
Rate-determining step
Catalytic activity

ABSTRACT

A Density Functional Theory based first-principles kinetic Monte Carlo (kMC) study of the water gas shift reaction on the stepped Cu(3 2 1) surface is presented. We use the recently developed graph-theoretical kMC approach coupled with cluster expansion Hamiltonians to model the coverage-dependent energy barriers for the different surface processes, including adsorption/desorption, diffusion and other elementary chemical reactions, totalling 36 elementary steps, which allow two possible competitive mechanisms: surface redox and associative COOH. All results are compared to a previous kMC study on Cu (1 1 1). Both mechanisms are observed for Cu(3 2 1) surface with different extensions, whereas the associative COOH one was the dominant for Cu(1 1 1). The present study shows that, in spite of encompassing lower activation energy barriers, stepped surfaces do not necessarily have an overall larger catalytic activity. Coverage effects and the significant contribution of some of the reverse processes are behind this behaviour.

1. Introduction

Low coordinated sites play an important role in many heterogeneously catalysed reactions [1–3]. In particular, step sites are often crucial since, for instance, they allow different types of binding to the catalyst surface [4], and facilitate bond breaking of reactants [5]. It is generally assumed that the presence of steps enhances the catalytic activity towards a complex reaction by increasing the reactant adsorption energies and decreasing the energy barriers as shown by Honkala et al. [6] for the case of NH_3 synthesis over models of a Ru catalyst. However, even if the energy barriers for the rate-determining steps (RDS) at step sites are lower than for regular sites, it is not always possible to conclude that the presence of these sites is beneficial. In fact, a strong chemisorption of reactants, products or impurities may cause surface poisoning [7], and may also result in the lowering of the energy barriers for RDSs also in the reverse direction, increasing reverse reaction rates over the forward ones with a concomitant decrease in the catalytic activity.

An important catalysed reaction with special technological relevance [8] is the water gas shift reaction (WGSR) that transforms CO and H_2O into CO_2 and H_2. It is an equilibrium-limited reaction, where CO conversion is favoured at low temperatures due to its exergonicity (*i.e.*, $\Delta_r G^0_{298.15K} = -0.30$ eV). As the temperature increases, the equilibrium constant and the final conversion inherently decrease. Hence, this process is usually carried out in two stages: a first one at quite high temperature (300–450 °C) favouring fast CO consumption, and a second one at a lower temperature (200–300 °C) to reach higher conversions, which are limited by the thermodynamic equilibrium [9]. Copper based catalysts with inclusion of Zn, Cr and Al oxides [10] and $CuO/ZnO/Al_2O_3$ [11] are used in low temperature reactors [12], although other metals and supports have also been proposed [13,14].

The molecular mechanism for the low temperature catalysed WGSR involves a rather large number of elementary steps defining the two possible main routes, usually referred to as surface redox and associative COOH mechanisms [15]. Both start from H_2O dissociation; however, in the former CO_2 is produced by direct reaction between adsorbed CO and O, whereas in the latter it is generated through a COOH intermediate.

Following the initial work of Fajin et al. [16], we have recently studied the role of step sites in the WGSR catalysed by Cu surfaces using Density Functional Theory (DFT) calculations including the contribution of dispersion terms [17]. Thus, we compared the energy barriers for all the different pathways involved in the two

* Corresponding author.
E-mail address: r.sayos@ub.edu (R. Sayós).

http://dx.doi.org/10.1016/j.jcat.2016.07.013
0021-9517/

molecular routes for both the stepped Cu(321) surface and the flat Cu(111) one [18]. Although the presence of step sites increases the water adsorption energy and decreases the energy barriers of different processes (*e.g.*, the water dissociation and CO_2 formation from CO oxidation, among others) one cannot rigorously claim that the catalytic activity of the stepped surface is going to be superior to that of the flat Cu(111) surface, where the COOH formation is faster and the water formation (*i.e.*, the rate-determining step in the reverse direction) has an energy barrier much higher than on the stepped Cu(321) surface [17]. In fact, some previous studies, for instance, for the reverse WGSR [19] and for the WGSR [20] on Cu(hkl) surfaces conclude that catalytic activity follows the order Cu(110) > Cu(100) > Cu(111). However, these claims are based on comparing only energy barriers of some assumed RDSs. Note that the use of rate constants would include at least entropic and temperature effects. Clearly, a more rigorous approach would imply to introduce temperature, pressure, reverse processes and surface coverage effects on the overall reaction, which also would allow a much better estimate of the RDSs. This can be done by using either microkinetic modelling or kMC simulations. Usually, the RDS for the same global reaction involving a complex mechanism, as the case of the WGSR, can depend on the type of catalytic surface along with the T and P conditions [21]. Within a microkinetic model, a rather rigorous determination of a RDS (often several ones) can be done through the evaluation of the degree of rate control for the proposed step as defined by Campbell [22], or by doing a most sophisticated reaction-route graph analysis based on an equivalent electrical circuit [21,23]. Other similar methods are also available [24,25].

In the current study, we present kinetic Monte Carlo simulations of the WGSR over the Cu(321) surface, based on earlier DFT calculations [17], to ascertain its catalytic activity in comparison with a previous kMC study over the flat Cu(111) surface [18]. Moreover, we apply the Campbell's degree of rate control in kMC simulations in an attempt to accurately establish the main RDSs, also applied in a previous work [26]. By comparing the Campbell factors obtained with the analysis of the different frequencies of the main elementary processes involved in the WGSR mechanism, we provide compelling evidence of the usefulness of this important concept in kMC simulations and its general validity beyond microkinetic models.

2. Computational methods

2.1. DFT calculations

The optimized geometries, energy barriers and the corresponding vibrational frequencies for the reactants, products and transition states involved in the different reaction pathways of the WGSR over the Cu(321)-stepped surface have been computed and characterized at DFT level in a previous study, using a standard generalized gradient approximation (GGA) type functional and accounting explicitly for dispersion terms [17], as explained in detail below. Moreover, we have performed additional DFT calculations in order to obtain the corresponding diffusion barriers of those species that could diffuse easily over the surface, as well as to determine the main lateral interactions between the different coadsorbed reactant pairs.

All periodic DFT calculations in the present work were performed by means of VASP code [27–29]. The slab was modelled through a $2 \times 2 \times 1$ supercell constructed using the optimum lattice parameter of 3.63 Å (experimental value 3.62 Å [30]). The GGA type DFT calculations were carried out with the PBE functional [31]. The effect of van der Waals interactions was included by adding the dispersion term obtained from the D2 method of Grimme [32] to the PBE calculated energy (PBE-D2) as in our previous work [17]. The valence electron density was expanded in a plane-wave basis set with a cut-off of 415 eV for the kinetic energy. The effect of core electrons in the valence electron density was taken into account using the projector augmented wave (PAW) method [33] as implemented in the VASP code [34]. Numerical integration in the reciprocal space was carried out by employing a $5 \times 5 \times 1$ Monkhorst-Pack grid of special *k*-points [35]. The convergence thresholds were 10^{-6} eV for the total energy and 10^{-3} eV Å^{-1} for the forces acting on the cores. Additional details about the periodic DFT calculations are reported in our previous work [17].

2.2. kMC simulations

We use the full set of DFT data described above to perform kMC simulations at the molecular level. The coupling of kMC with DFT calculations renders the simulation a truly first-principles approach. From an efficiency perspective, kMC can simulate reactions with a computational expense that is much lower than that needed for ab initio molecular dynamics, and represents an improvement compared to the existing mean-field microkinetic models that, among other issues, cannot take into account the detailed structure of stepped surfaces such as the Cu(321).

The kMC method simulates the time evolution of a system at the molecular level, in which all the possible reactions or processes that can occur have an associated reaction rate [36]. In the present study, we use the recently developed graph-theoretical kMC approach [37] coupled with cluster expansion (CE) Hamiltonians [38,39] for the adlayer energetics by means of ZACROS code [34,35]. As in previous kMC schemes, a simulation is initialized with a given lattice configuration (in our case an empty lattice), and a list is generated containing all the possible lattice processes for the given configuration. Then, the algorithm enters a loop where, at each step, the most imminent process in the queue is executed (*i.e.*, the one with the smallest time of occurrence according to the first-reaction method [40]), until the stop conditions are fulfilled. Finally, a stochastic trajectory is obtained containing all the information about the lattice configuration as well as the number of gas-phase molecules produced or consumed at every time step. This trajectory can be analysed to get information such as the equilibrium surface coverage, the final CO_2 and/or H_2 production or the contribution of each possible reaction channel.

2.2.1. Lattice-gas model

The Cu(321)-stepped surface has different low-coordinated atoms and includes a high heterogeneity of adsorption sites such as terraces, nearby kinks and steps. Although it is less stable than the Cu(111) or Cu(100) low Miller index surfaces, its study is interesting to better understand the grounds of the catalytic activity and the contribution of the featured sites likely to be present in a real polycrystalline catalyst, formed by several facets. We distinguish five different top sites (named 1, 2, 3, 4 and 5) and six different hollow sites (named *a*, *b*, *c*, *d*, *e* and *f*). Moreover, a molecule adsorbed in a bridge position between top sites *i* and *j* is labelled as b_{i-j}. Fig. 1 shows the location of those sites over the surface.

In order to carry out the kMC simulations, a suitable model of the surface is needed. In the present work, the Cu(321) surface is represented by a two-dimensional periodic grid of points, where each point represents one catalytically active surface site. For simplicity, only top sites are explicitly defined in our lattice model. In that way, a molecule adsorbed in a bridge site b_{i-j} is labelled as occupying two neighbouring *top i* and *top j* sites. In an equivalent manner, molecules adsorbed on hollow sites (*i.e.*, H and OH) involve some of the surrounding top sites (see Section II in the Supplementary Information for more details). *Top 5* sites are located at

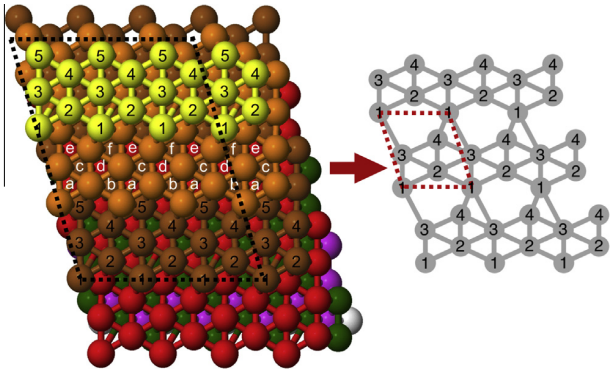

Fig. 1. Top view of the Cu(3 2 1) surface (left) and scheme of a 3 × 3 lattice model (right). Labels a, b, c, d, e and f refer to the hollow sites, whereas labels 1, 2, 3, 4 and 5 refer to the top sites. Grey lines in the lattice model represent the neighbouring connections between sites, and dotted red lines denote the 1 × 1 unit cell in.

the bottom of the step, a region displaying a large Pauli (steric) repulsion. Thus, they have not been included in the lattice model because adsorption at these sites is very improbable. Accordingly, the model unit cell has a total of 4 top sites (*i.e.*, *top 1*, *top 2*, *top 3* and *top 4*). Note that even though all lattice sites in the grid are on a plane, the real surface is not planar (Fig. 1) and the difference in bonding at the different sites is accounted for in the DFT calculated data serving as input for the kMC simulations.

The convergence of kMC simulations with respect to the lattice size has been tested by computing the final (*i.e.*, steady-state) H_2 production for several surface models with different $L \times L$ number of unit cells in the range $5 \leqslant L \leqslant 40$, concluding that the results for the 10×10 lattice model (including a total of 400 sites) virtually coincide with those obtained using larger surface models.

2.2.2. Reaction network

A full set of 36 elementary processes were considered for the molecular mechanism of the WGSR, which are described in Table 1, where "+" and "−" signs stand for forward and reverse processes, respectively (schemes of the energy profiles for most of the processes are reported in Section I of the Supplementary Information). These processes include the most important elementary steps, previously characterized by using DFT calculations [17], but adding also 14 new possible diffusion processes for H, O and OH. In this study, the adsorption of CO molecules is restricted to the step sites (*i.e.*, *top* 1) because of the higher binding energy compared to the other top sites (*i.e.*, around 0.60 eV larger); thus, diffusion of CO molecules to the other top sites has not been included. In spite of the present network including only the most favourable reaction pathways, involving a given selection of sites, the numerous diffusion processes available in kMC simulations allow adsorbed species to reach the most stable configurations and then evolve through the processes considered in the present network.

In the graph-theoretical kMC approach, each elementary step is represented as a graph pattern, with specific initial and final states. This choice enables the representation of complex elementary steps involving multidentate adsorbates in specific binding configurations and neighbouring patterns. This approach has been used recently (without coupling with cluster expansion Hamiltonians) by Stamatakis et al. to investigate the WGSR on platinum surfaces [41].

In order to "translate" an elementary step into ZACROS's input, it is instructive to make use of drawings like the one sketched in Fig. 2. There, for instance, an adsorbed H in hollow "a" site is

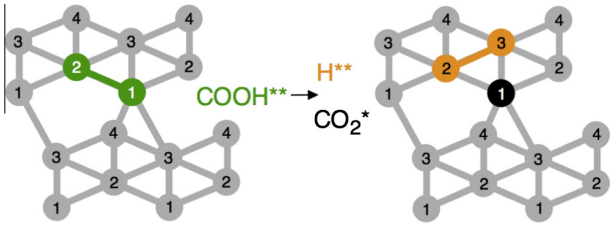

Fig. 2. Schematic representation of the process +10 in Table 1 (*i.e.*, *c*-$COOH_{b1\text{-}2}$ → $CO_{2\ top1}$ + $H_{hole"a"}$). Labels (*) and (**) are used for species occupying one or two top sites in the present lattice model, respectively.

Table 1
Elementary step characterization of the WGSR catalysed by the Cu(3 2 1) and Cu(1 1 1) surfaces: energy barriers ($E^0_{fwd,i}(0)$) and reaction energies ($\Delta E_i(0)$) at zero-coverage limit. Unless otherwise specified, species are adsorbed; label (g) is used for gas species. All values are in eV and include the ZPE correction.

ID	Elementary step	$E^0_{fwd,i}(0)$ infinite separation (coadsorbed [17])		$\Delta E_i(0)$ infinite separation (coadsorbed [17])	
		Cu(3 2 1)	Cu(1 1 1) [18]	Cu(3 2 1)	Cu(1 1 1) [18]
1	$CO_{(g)} \leftrightarrow CO_{top1}$	0.00	0.00	−1.11	−0.51
2	$H_{2(g)} \leftarrow H_{2\ top1}$	–	–	−0.12	–[a]
3	$H_2O_{(g)} \leftrightarrow H_2O_{top1}$	0.00	0.00	−0.66	−0.18
4	$CO_{2(g)} \leftarrow CO_{2\ top1}$	–	–	−0.28	−0.09
5	$H_2O_{top1} \leftrightarrow OH_{b1\text{-}4} + H_{hole"b"}$	0.78 (0.78)	1.01	0.20 (0.18)	−0.14
6	$OH_{b1\text{-}2} \leftrightarrow O_{hole"a"} + H_{b1\text{-}4}$	1.61 (1.51)	1.60	0.48 (0.86)	0.41
7	$OH_{b1\text{-}2} + OH_{b1\text{-}3} \leftrightarrow H_2O_{top1} + O_{hole"b"}$	0.60 (0.46)	0.68	0.34 (−0.10)	0.68
8	$CO_{top1} + O_{hole"a"} \leftrightarrow CO_{2\ top1}$	0.68 (0.68)	0.79	−0.49 (−0.49)	−0.78
9	$CO_{top1} + OH_{hole"a"} \leftrightarrow$ *c*-$COOH_{b1\text{-}2}$	0.86 (0.84)	0.70	0.62 (0.60)	0.15
10	*c*-$COOH_{b1\text{-}2} \leftrightarrow CO_{2\ top1} + H_{hole"a"}$	0.80 (0.80)	1.18	−0.55 (−0.52)	−0.51
11	*c*-$COOH_{b1\text{-}2} + OH_{b1\text{-}4} \leftrightarrow CO_{2\ top1} + H_2O_{top1}$	0.25 (0.33)	0.38	−0.77 (−0.63)	−0.37
12	$H_{hole"a"} + H_{hole"f"} \leftrightarrow H_{2\ top1}$	0.78 (0.78)	–[a]	0.31 (0.31)	–[a]
13	H diffusion (general)	–	0.15	–	0.00
13a	$H_{b1\text{-}4} \leftrightarrow H_{hole"a"}$	0.05	–	−0.28	–
13b	$H_{hole"a"} \leftrightarrow H_{hole"f"}$	0.20	–	0.15	–
13c	$H_{hole"f"} \leftrightarrow H_{b1\text{-}4}$	0.13	–	0.13	–
14	O diffusion (general)	–	0.38	–	0.00
14a	$O_{hole"a"} \leftrightarrow O_{hole"b"}$	0.44	–	0.00	–
15	OH diffusion (general)	–	0.12	–	0.12
15a	$OH_{b1\text{-}4} \leftrightarrow OH_{b1\text{-}3}$	0.11	–	0.06	–
15b	$OH_{b1\text{-}3} \leftrightarrow OH_{hole"a"}$	0.12	–	−0.30	–
15c	$OH_{hole"a"} \leftrightarrow OH_{b1\text{-}2}$	0.07	–	−0.05	–

[a] In the flat Cu(1 1 1) surface H_2 adsorption is dissociative (*i.e.*, $H_{2(g)} \leftrightarrow H + H$) [15,18].

labelled as occupying *top 2* and *top 3* sites, and an adsorbed *c*-COOH in a bridge $b_{1\text{-}2}$ site is labelled as occupying *top 1* and *top 2* sites. Section III of the Supplementary Information contains the schematic drawings for all reaction steps. Note that all steps are reversible excepting CO_2 and H_2 desorption.

2.2.3. Reaction rates

The reaction rate of a surface elementary process, defined as the number of times this process occurs per site and time unit, can be calculated by using either the transition state theory (TST) or the collision theory (CT) [37,42]. For a surface Langmuir-Hinshelwood type reaction, a desorption process or an atomic or molecular diffusion process, the reaction rate can be calculated as

$$r_i = \frac{k_B \cdot T}{h} \frac{Q_i^{\neq}}{Q_R} exp\left(-\frac{E_i^0(\sigma)}{k_B \cdot T}\right) \tag{1}$$

where h denotes Planck's constant, k_B is the Boltzmann's constant, and $Q_i^{\neq}$ and Q_R are the partition functions (dimensionless) of the transition state and the reactants, respectively, which are calculated from standard statistical mechanical expressions [43]. Finally, $E_i^0(\sigma)$ stands for the coverage-dependent energy barrier for the ith process, including the zero-point energy (ZPE) correction. In order to quantitatively model the configuration-dependent energetics, the formulation of CEs expands the energy of a configuration of adsorbates σ as a sum of cluster energies [44–48]:

$$H(\sigma) = \sum_{k=1}^{N_C} \frac{ECI_k}{GM_k} \cdot NCE_k(\sigma) \tag{2}$$

where $H(\sigma)$ is the Hamiltonian of the system (*i.e.*, energy of a lattice configuration); N_C is the total number of figures/clusters specified in the energetic model; ECI_k is the effective cluster energy of figure k; GM_k is the graph-multiplicity of that figure (*i.e.*, to avoid over-counting contributions, equivalent to a symmetry number); and NCE_k is the number of times that pattern of figure k appears in the lattice. Then, the reaction energy for ith process is given as in Eq. (3), which follows the formulation of Nielsen et al. [35]

$$\Delta E_i(\sigma) = H(\sigma') - H(\sigma) + \Delta E_i^{gas} \tag{3}$$

where σ and σ' refer to the initial and final configurations of the overall lattice, respectively, and ΔE_i^{gas} is the change in the energy of gas species whenever they are involved in the process (*i.e.*, $E_{i,prod}^{gas} - E_{i,reac}^{gas}$). Microscopic reversibility dictates that the difference between forward and reverse energy barriers is equal to the reaction energy

$$\Delta E_i(\sigma) = E_{fwd,i}^0(\sigma) - E_{rev,i}^0(\sigma) \tag{4}$$

In the above expression, $\Delta E_i(\sigma)$ can be calculated from the CE Hamiltonian. The forward energy barrier can be parameterized in terms of a Brønsted–Evans–Polanyi (BEP) relationship [49,50]

$$E_{fwd,i}^0(\sigma) = max(0, \Delta E_i(\sigma), E_{fwd,i}^0(0) + \omega(\Delta E_i(\sigma) - \Delta E_i(0))) \tag{5}$$

where the *max* operator filters negative values, as well as values lesser than $\Delta E_i(\sigma)$, if the latter is positive. Moreover, $E_{fwd,i}^0(0)$ and $\Delta E_i(0)$ are the energy barriers and reaction energies at the zero-coverage limit (*i.e.*, only reactants existing on the surface), and ω is the so-called proximity factor [51] ranging from 0.0 for a reactants-like transition state, to 1.0 for a products-like transition state. In that way, selecting $\omega = 0$ keeps the forward barrier fixed at the zero-coverage limit DFT value and the reverse barrier is chosen to be thermodynamically consistent, whereas in the limit $\omega = 1$ the reverse barrier is fixed to the DFT value and the forward one is adjusted. Assuming that the transition states can have both reactant and product state characters, we assume $\omega = 0.5$ for all elementary steps. The reverse energy barrier is then

$$E_{rev,i}^0(\sigma) = max(0, -\Delta E_i(\sigma), E_{rev,i}^0(0) - (1-\omega) \cdot (\Delta E_i(\sigma) - \Delta E_i(0))) \tag{6}$$

where

$$E_{rev,i}^0(0) = E_{fwd,i}^0(0) - \Delta E_i(0) \tag{7}$$

Unlike other kMC studies for simpler systems like NO oxidation on Pt(1 1 1) [45] or CO oxidation on Pd(1 1 1) [52], where CE was used in order to fit a data set of 50 and 92 DFT calculations for different surface configurations, respectively, our parameters are fitted in order to reproduce properly both the energy profile for reactants at infinite separation and coadsorbed states for all the elementary steps of the WGSR mechanism (Table 1), including lateral interactions for all reactant and product pairs (*i.e.*, 15 cases). Although this alternative is not as accurate as the one used in the above-mentioned studies, it represents a step forward compared to the traditional kMC simulations, where only one energy barrier is used for each process. This fact is especially important for a correct description of the diffusion processes, where the energy barriers strongly depend on the local environment. As an example, consider the diffusion process of a single O atom moving from hollow "b" to hollow "a" site (*i.e.*, process −14a); if the O atom has no neighbours neither at the initial nor at the final state, its energy barrier will be 0.44 eV (*i.e.*, zero-coverage limit, see Table 1). However, if it is initially coadsorbed next to a H_2O molecule, the energy barrier for that process will be larger (*i.e.*, 0.59 eV, Eq. (5)). Section IV on the Supplementary Information shows the graph patterns for all the figures/clusters included in the CE Hamiltonian and used in our calculations as input.

Due to the high number of species and site types present in the WGSR on Cu(3 2 1), it is impossible to fit a complete data set of DFT energies for all possible lateral interactions, which could appear through the reaction (*i.e.*, at higher coverages), like was done in other but simpler works mentioned above. Thus, lateral interactions for non-reactant pairs (e.g., H_2O and OH) were not considered in the present study, like neither were included for Cu(1 1 1) in the previous study [18].

The rate of adsorption processes is given by the well-known Hertz-Knudsen equation as

$$r_i^{ad} = S_{0,i} \cdot A_{site} \cdot \frac{p_i}{\sqrt{2\pi m_i k_B T}} \tag{8}$$

where $S_{0,i}$ stands for the initial sticking coefficient, A_{site} correspond to the area of a single site, p_i is the gas partial pressure and m_i is the mass of the gas molecule. In the present study $S_{0,i}$ is taken as the unity for both gas reactants, as in previous studies over the Cu(1 1 1) surface [18,53,54].

In the current system, diffusion processes have energy barriers substantially lower than those corresponding to other elementary chemical reactions (Table 1). Consequently, in practice, most kMC steps in the simulation would correspond to diffusion processes with a small number of them corresponding to the chemical processes of interest. This fact implies that very large simulations would be required to obtain meaningful results. Thus, we have artificially reduced the diffusion rates of the fastest processes (*i.e.*, steps ±13b, ±15a and ±15c from Table 1) by three orders of magnitude. A sufficiently large number of additional simulations have been performed to check that this scaling factor speeds up the overall study without affecting the results. This approach has been also applied in previous kMC studies of WGSR over Cu(1 1 1) [18,55] leading to negligible errors in the different calculated properties [56].

3. Results and discussion

For the present kMC simulations the initial conditions correspond to an experiment with a fresh reactants mixture of CO and H_2O with P_{CO} and P_{H2O} partial pressures, continuously impinging on an empty thermalized Cu(321) surface, where the heterogeneous reaction takes place and afterwards the final gas products (*i.e.*, CO_2 and H_2) desorb and leave the surface region (*i.e.*, in a nonequilibrium thermodynamic state). The partial pressure and temperature values have been chosen to allow a direct comparison between the flat Cu(111) and the stepped Cu(321) surfaces. Each kMC simulation was allowed to achieve a steady state in which surface coverage for all intermediates remains constant in time, with the exception of small fluctuations resulting from the stochastic nature of the method. From that point, the overall macroscopic kinetic properties were calculated, such as the turnover frequency (TOF), defined as the number of product species formed per area and unit time (*i.e.*, $s^{-1}\cdot cm^{-2}$). The total number of kMC steps performed depends on the reaction temperature, ranging from 10^9 to 10^{10} kMC steps at $T = 625$ K and 463 K, respectively.

We also made an estimate of the effect of missing some lateral interactions for non-reactant pairs in our reaction network. Thus, for the H_2O/OH interactions, we carried out new DFT calculations to determine this kind of interactions (the 5 most favourable configurations were included in kMC simulations at 625 K with P_{CO} = 26 Torr and P_{H2O} = 10 Torr) and we observed that there was only a small decrease in the TOF (the log [TOF] passed from 17.47 to 17.35) and an increase in only the water coverage (passed from 7% to 14%), but these changes do not affect the comparison of the Cu(321) vs. Cu(111) WGSR activities.

3.1. Temperature effects

Plotting the logarithm of the computed H_2 TOF as a function of 1000/T leads to an Arrhenius behaviour in two temperature intervals, with apparent activation energies of 1.2 eV (550–625 K) and 1.6 eV (463–550 K, see Fig. 3). Noticeably, these values are higher than those corresponding to the flat Cu(111) surface (*i.e.*, $E_a = 0.5 - 0.8$ eV [18]), but the plots exhibit a similar shape. Moreover, within the 463–625 K temperature range, the TOF for the overall reaction at the stepped Cu(321) surface is between two

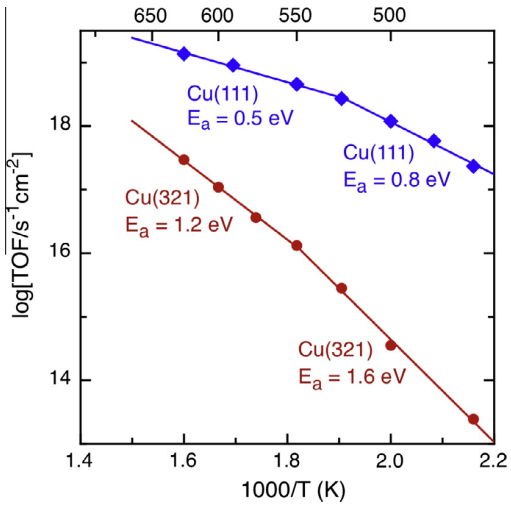

Fig. 3. Arrhenius plot of the WGSR on Cu(321) (red circles, this work) and on Cu (111) (blue squares, taken from Ref. [18]) in the temperature range 463–625 K. Partial pressures of 26 and 10 Torr were used for CO and H_2O, respectively.

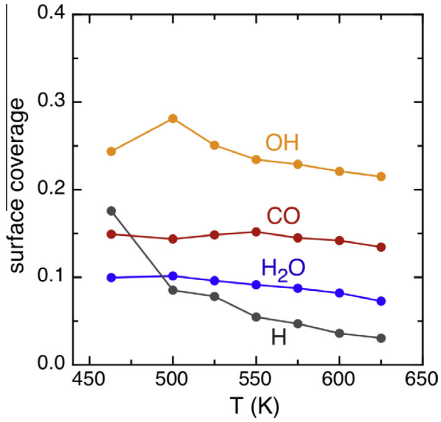

Fig. 4. Surface coverage for different adsorbates as a function of temperature for reactant partial pressures P_{CO} = 26 Torr and P_{H2O} = 10 Torr.

(at 625 K) and four (at 463 K) orders of magnitude lower than when it takes place at the Cu(111) surface. It is important to mention that, despite the high number of elementary processes involved, the stoichiometry of the global reaction is preserved, except for the first simulation steps, where the $H_{2(g)}$ production is faster than the $CO_{2(g)}$ production.

For P_{CO} = 26 Torr and P_{H2O} = 10 Torr, Fig. 4 shows that adsorbed OH is the most dominant species at the surface in all the temperature ranges, followed by CO, H_2O and finally atomic H. On the contrary, at the Cu(111) surface, the H coverage presents the largest value, excepting at the highest temperature where OH also becomes the dominant surface species (*e.g.*, $\theta_H > \theta_{OH} > \theta_{H2O} > \theta_{CO}$ at 550 K). Another striking difference with respect to the Cu (111) surface is that the coverage of the different species at the Cu(321) surface is much less temperature-dependent, with the exception of H coverage, which decreases with increasing temperature as on the flat surface. Note that the coverage of carboxyl species and atomic O is almost insignificant, because these species are very reactive.

Regarding the reaction mechanism, the associative COOH route (*i.e.*, processes 9, 10 and 11) is the dominant pathway in all the studied conditions (Fig. 5a), even when we change the ratio of partial pressures for both reactants. This point is in agreement with previous observations using mean-field microkinetic modelling [15] and kMC simulations [18] for the flat Cu(111) surface. However, at the Cu(321) surface, the surface redox route (*i.e.*, processes 6, 7 and 8), which does not play any role in the flat surface, becomes also important at high temperatures, contributing around a 12% of the overall TOF. On the flat Cu(111) surface, this process is severely hindered, because when atomic O is formed by process +7 it rapidly goes towards the opposite direction forming OH again since the forward process is highly endoergic and exhibits a very low energy barrier in the reverse direction. Nevertheless, on the stepped surface process +7 is more favoured since it is practically isoergic and the probability that a CO molecule finds an atomic O becomes greater.

Looking at the associative COOH route in some more detail, one finds that the energy barrier for direct carboxyl dehydrogenation (*i.e.*, process +10) on the Cu(111) surface is 1.18 eV, considerably higher than on the Cu(321) surface, where its value at zero-coverage limit is 0.80 eV. This fact causes that this process is not observed in the flat surface, but instead, is one of the main routes for CO_2 production on the stepped surface (Fig. 5a). On the other hand, the energy barrier for carboxyl disproportionation by hydroxyl (*i.e.*, process +11) is much lower compared to the direct carboxyl dehydrogenation for both surfaces (*i.e.*, 0.38 eV and 0.25 eV

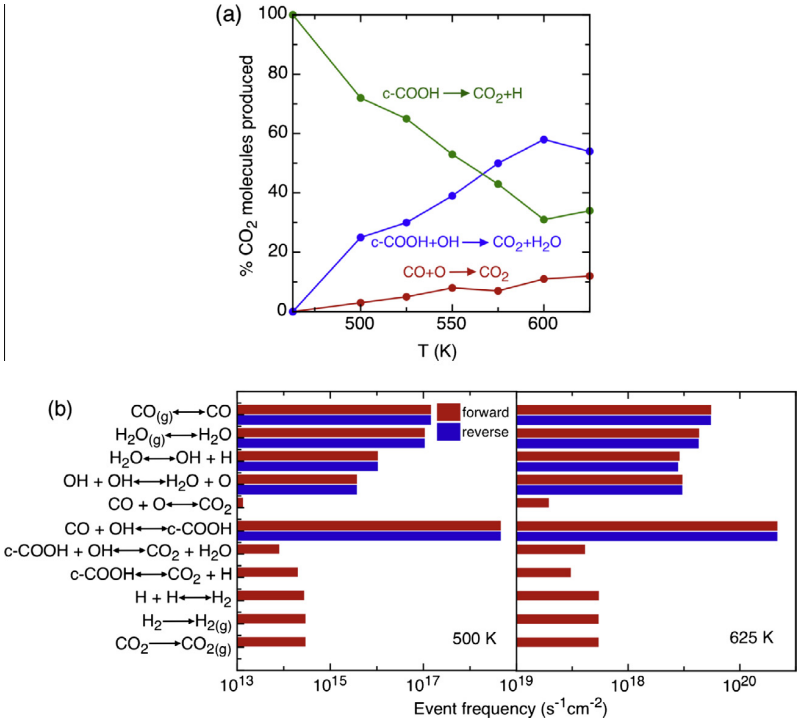

Fig. 5. (a) Relative contribution of each elementary step to the overall TOF as function of reaction temperature. Blue and green lines correspond to the associative COOH route, whereas red line corresponds to the surface redox route. (b) Frequencies of the main elementary processes at T = 500 K (left) and T = 625 K (right). Simulations performed at P_{CO} = 26 Torr and P_{H2O} = 10 Torr.

in Cu(1 1 1) and Cu(3 2 1), respectively). Nevertheless, on the Cu (3 2 1) surface both processes happen in a similar proportion. This is because carboxyl disproportionation by hydroxyl requires that a neighbouring OH reaches a b_{1-4} position and this adsorbed species is usually located at hollow "a" or b_{1-2} sites (see the diffusion energy profile in Section I of the Supplementary Information). Moreover, the direct carboxyl dehydrogenation is unimolecular.

The statistics of the most important elementary steps at low and high temperature for the reaction on Cu(3 2 1) are shown in Fig. 5b. In this figure, each pair of bars represents the event frequency per second and cm^2 for the forward (red) and reverse (blue) elementary reactions. It is worth noting that the CO and H_2O adsorption/desorption are partially equilibrated reactions, along with water dissociation, OH disproportionation and carboxyl formation; all other elementary reactions are practically irreversible. In contrast, on the Cu(1 1 1) surface only reactants adsorption/desorption and OH disproportionation processes were found to be partially equilibrated. The RDSs at both temperatures appear to be the formation of CO_2 through the associative COOH route (*i.e.*, process +10 at low temperatures and process +11 at high temperatures), since these are the first steps in the sequence that are not partially equilibrated, and the TOF for these steps is several orders of magnitude lower than for the previous steps. This finding is contrary to the prediction by Fajin et al., based purely on energy profiles obtained from DFT calculations, that the RDSs on the Cu(3 2 1) surface should be the water dissociation and the hydrogen recombination [16]. Interestingly enough, the RDS found in the present work was also suggested by Grabow et al. in a previous microkinetic model of the WGSR over Pt(1 1 1) [48]. In spite of the fact that processes +10 and +11 do not present a very high energy barrier, they cannot compete against the carboxyl dissociation (*i.e.*, process −9), which has an energy barrier at zero-coverage limit of only 0.24 eV and it is specially favoured at high temperatures due to its endoergicity. The observed change in the slope of the Arrhenius plots for the two surfaces (Fig. 3) suggests that the RDS can vary with temperature (*i.e.*, process +10 at low temperature and process +11 at high temperature, or vice versa).

The statistical analysis of Fig. 5b also shows that at 500 K, one water molecule dissociates on average for every 10 water molecules adsorption, whereas at 625 K the ratio is increased to 1:2 (the water dissociation process is endoergic, being more favoured at high temperature). This feature enhances the frequency of OH recombination (*i.e.*, process +7), producing more atomic oxygen and thus promoting the surface redox mechanism, which is negligible at low temperatures (Fig. 5a).

At this point, one may wonder why the computed H_2 TOF for the Cu(3 2 1) surface, where three different processes for CO_2 formation are participating, is lower than for the Cu(1 1 1) surface, where direct carboxyl dehydrogenation and CO oxidation do not occur. The reason is very simple. On the one hand, carboxyl formation (*i.e.*, process +9) is endoergic by 0.62 eV on the stepped surface, whereas on the flat surface becomes endoergic by only 0.15 eV. This change implies that the energy barrier in the reverse direction is much lower in the stepped surface (*i.e.*, 0.24 eV) than in the Cu(1 1 1) surface (*i.e.*, 0.55 eV). On the other hand, something similar happens with water dissociation: whereas in the flat surface this process is exoergic and has an energy barrier of 1.15 eV in the reverse direction, and it is endoergic in the stepped surface, with an energy barrier of 0.60 eV for the reverse direction (*i.e.*, the equilibrium constant for the stepped surface at 625 K is only 5.90×10^{-3}). Moreover, the poisoning of top 1 step sites by CO and, to a lesser extent, by water, prevents some elementary reactions to occur: this is the case for carboxyl disproportionation or H_2 formation (*i.e.*, within all the temperature ranges considered, the sum of H_2O and CO coverage is around 19–24%, which means that the percentage of occupied top 1 sites is between 76% and

96%, and only the remaining free sites may be available for other reactions). In fact, the lower H_2 production rate on Pt(2 1 1) compared to Pt(1 1 1) reported in the work of Stamatakis et al. [38] was attributed to the same effect.

The present results confirm that the catalytic activity of surfaces containing low-coordinated sites is not always higher, even if they present higher adsorption energies for reactants or lower energy barriers for the main elementary steps. Therefore, establishing a ranking of the most efficient crystal surfaces for catalysing a complex reaction (*e.g.*, WGSR) based only on the energy barriers of forward processes is not always correct, although this is often done [20,57,58]. Moreover, the RDSs may change from one catalyst to another, and these steps may not coincide with the processes having the highest energy barriers, as checked by performing kMC simulations or microkinetic modelling.

As an additional corroboration of the observed RDSs for the WGSR on Cu(3 2 1), derived from the analysis of the frequencies of all steps, we have investigated whether the Campbell's degree of rate control [22] (*i.e.*, $X_{rc,i}$ for step i), applied earlier and extensively in microkinetic modelling studies, could also be valid for kMC simulations, where there is an earlier similar study for CO oxidation at RuO_2(1 1 0) surface [25]. This parameter, mainly intended for kinetics where a steady state or quasi-steady state rate is achieved, should take significant but less than 1 values for RDSs and negligible values for other steps. Table 2 shows calculated $X_{rc,i}$ values for four processes at several temperatures and partial pressures. Results in Table 2 show that processes +10 and +11 are clearly the RDSs for partial pressures of 26 and 10 Torr for CO and H_2O, respectively. This is in agreement with the results derived from the analysis of the frequencies of the steps. The increase in

Table 2
Campbell's degree of rate control ($X_{rc,i}$) for main candidates to be RDSs at two temperatures and three reactant mixtures.

		$X_{rc,i}$[a]			
		625 K P_{CO} = 26 Torr P_{H2O} = 10 Torr	500 K P_{CO} = 26 Torr P_{H2O} = 10 Torr	625 K P_{CO} = 10 Torr P_{H2O} = 90 Torr	625 K P_{CO} = 90 Torr P_{H2O} = 10 Torr
5	$H_2O \leftrightarrow OH + H$	0.03	0.03	0.14	0.04
10	c-COOH $\leftrightarrow CO_2 + H$	0.24	0.11	0.14	0.42
11	c-COOH + OH $\leftrightarrow CO_2 + H_2O$	0.18	0.30	0.54	0.26
12	$H + H \leftrightarrow H_2$	0.03	0.00	0.05	0.18

[a] Campbell's degree of rate control [22] defines the degree at rate control for step i as

$$X_{rc,i} = \frac{k_i}{R}\frac{\delta R}{\delta k_i}$$

where R is the overall rate (*i.e.*, H_2 TOF) and k_i the rate constant (r_i for kMC simulations). In the present study, changes of at least 10% in both r_i and r_{-i} were necessary to achieve significant and converged values. Moreover, diffusion rates were decreased to facilitate a faster although reliable calculation.

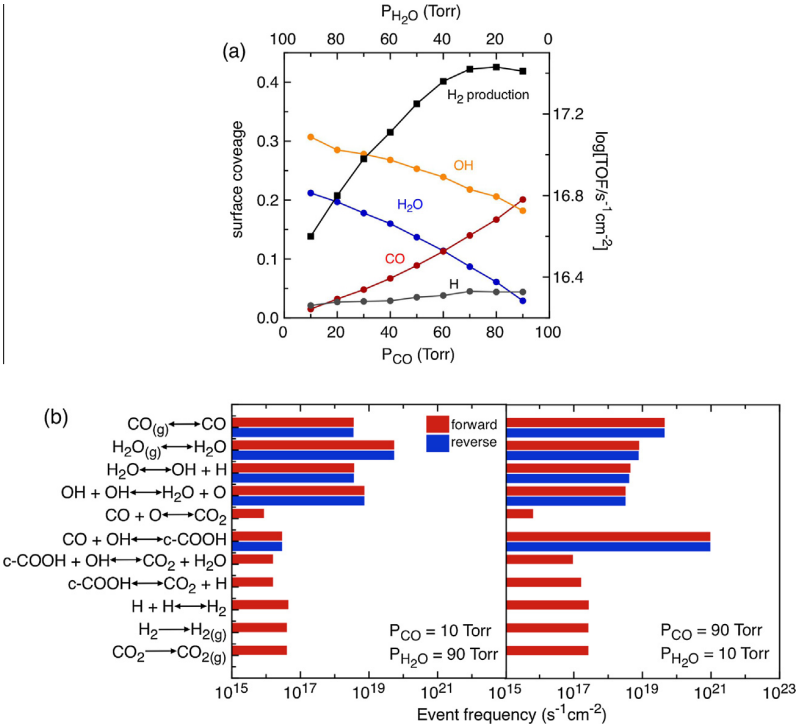

Fig. 6. (a) TOF (black line, squares) and surface coverage for different adsorbates (coloured lines, circles) as function of the reactant partial pressures for a constant total pressure of 100 Torr. (b) Frequencies of the main elementary processes for a total pressure of 100 Torr: P_{CO}/P_{H2O} equal to 10/90 (left) and 90/10 (right). All simulations were performed at T = 625 K.

temperature also indicates a change in the relative importance of both elementary steps, although contrary to the previous trend. Another important conclusion is that neither water dissociation (RDS for WGSR on Cu(1 1 1)) nor H recombination are RDSs for these conditions.

3.2. Pressure effects

The effects of reactant mixture composition on the overall H_2 TOF have been examined carrying out a series of kMC simulations with different H_2O/CO ratios ranging from 0.11 to 9.0 for a total pressure of 100 Torr and a reaction temperature of 625 K (Fig. 6). The RDSs for all these reactant mixtures are still the formation of CO_2 through the carboxyl intermediate, being processes +10 and +11 equally likely. Campbell's degree of rate control (Table 2) corroborates this conclusion, although process +11 is more important as RDS for P_{H2O}/P_{CO} = 10/90 Torr and process +10 for P_{H2O}/P_{CO} = 90/10 Torr. Thus, the associative COOH mechanism seems to be again the dominant reaction pathway. In spite of that, changes in the partial pressures increase also somewhat the importance of water dissociation or H recombination.

The maximum H_2 TOF corresponds to a H_2O/CO ratio between 0.25 and 0.40, slightly lower than for the Cu(1 1 1) surface, where the optimum value is between 0.43 and 0.66 [18]. This result can be explained by examining the coverage of the different adsorbates as a function of reactant partial pressures (Fig. 6a) and the frequencies of the main elementary processes for H_2O/CO ratios of 10/90 and 90/10 (Fig. 6b). As discussed in the previous section, carboxyl formation is a very endoergic process, with a small equilibrium constant of 2.50×10^{-5} at 625 K. This value implies that a high concentration of adsorbed CO and OH is required to shift the equilibrium towards the carboxyl intermediate, which is achieved working at low H_2O/CO ratios. However, at P_{H2O}/P_{CO} = 90/10 Torr, CO coverage is so small that the TOF for carboxyl formation is four orders of magnitude lower than the value at P_{H2O}/P_{CO} = 10/90 Torr, with a concomitant lowering the overall H_2 TOF of the reaction. Finally, Fig. 6 reveals that the total percentage of CO_2 molecules formed through the surface redox route (*i.e.*, process 8) is slightly favoured at high P_{H2O}/P_{CO} ratios, since it is easier to find atomic oxygen produced from OH disproportionation. This increment in the activity of the surface redox mechanism under an excess of water has been also observed by Stamatakis et al. for the WGSR on the Pt(1 1 1) and Pt(2 1 1) surfaces [38].

4. Conclusions

In the present work, we report first-principles based kMC simulations of the WGSR on the stepped Cu(3 2 1) surface, including a total of 36 elementary steps such as adsorption/desorption, diffusion and other elementary surface chemical reactions, which allow to reach a clear picture of the overall reaction and to differentiate between surface redox and associative COOH mechanisms.

Reactions rates were obtained by combining transition state theory and collision theory. Diffusion reaction rates were scaled to speed up simulations but without affecting the final results. Recently published DFT results including dispersion were used for the computation of reaction rates at several temperatures. We consider a reliable lattice model for the Cu(3 2 1) surface, which allows discriminating different kind of sites: hollows, bridges and tops, which are involved in the most favourable elementary steps.

Temperature effects on WGSR were studied within the 463–625 K interval, showing a two-interval Arrhenius behaviour with apparent activation energies of 1.2 and 1.6 eV, much higher than the values observed for the Cu(1 1 1) surface (*i.e.*, 0.5–0.8 eV). The overall TOFs for the stepped Cu(3 2 1) surface were between two (at 625 K) and four (at 463 K) orders of magnitude lower than for the flat Cu(1 1 1) surface. Therefore, the stepped Cu(3 2 1) surface is catalytically less active than the Cu(1 1 1) one. This fact constitutes a new and unexpected conclusion, which possibly cannot be anticipated by inspection of the energy profiles of the WGSR only. This highlights the importance of performing macroscopic simulations, using either microkinetic models or kMC with the latter providing many additional details of the overall process.

Surface coverage effects were also analysed indicating that, for the WGSR on the Cu(3 2 1) surface, OH is the dominant adsorbed species and H the less important. Nevertheless, H_2O and H were the main adsorbed species at low temperatures, and both OH and H for higher temperatures for Cu(1 1 1).

Regarding the reaction mechanism, the associative COOH route is the dominant pathway in all the studied conditions like in the flat Cu(1 1 1) surface, but the surface redox route becomes also important at high temperatures, contributing around a 12% of the overall TOF. This effect was not observed in Cu(1 1 1) surface.

The determination of RDSs using the Campbell's degree of rate control in kMC simulations, as in microkinetic modelling, seems to be accurate enough and coincident with the analysis of the frequencies of the surface processes.

The RDS at both temperatures appears to be the formation of CO_2 through the associative COOH route. This finding is not altered when reactant mixture composition is modified. Contrarily, water dissociation was the rate-determining step for Cu(1 1 1) surface.

As a closing remark, it is necessary to insist in the important results on the present work highlighting that the catalytic activity of stepped surfaces, and hence of low coordinated sites, is not always higher than that corresponding to terrace sites, and even this type of sites exhibits higher adsorption energies for reactants and/or lower energy barriers for several forward processes (*e.g.*, for the possible RDSs) through the minimum energy reaction path. In fact, RDSs usually depend not only on the catalyst and P and T conditions but also on the surface coverages and on the details of the possible reverse processes. Therefore, only through kMC simulations or microkinetic modelling the RDSs can be unequivocally established.

Acknowledgments

Financial support to this research has been provided by the Spanish MINECO CTQ2014-53987-R and CTQ2015-64618-R grants and, in part, from the Generalitat de Catalunya grants 2014SGR97, 2014SGR1582 and XRQTC. This project received funding from the NOMAD Center of Excellence project from the European Union's Horizon 2020 research and innovation programme under grant agreement No 676580. PG is a Serra Húnter Fellow. HP thanks Generalitat de Catalunya for a predoctoral FI-DGR-2015 grant and FI acknowledges additional support from the 2015 ICREA Academia Award for Excellence in University Research. Computational resources provided by *Consorci de Serveis Universitaris de Catalunya* (CSUC, former CESCA) are gratefully acknowledged.

Appendix A. Supplementary material

Supplementary data associated with this article can be found, in the online version, at http://dx.doi.org/10.1016/j.jcat.2016.07.013.

References

[1] J.T. Yates, Surface-chemistry at metallic step defect sites, J. Vac. Sci. Technol. A 13 (1995) 1359–1367.
[2] B.L.M. Hendriksen, M.D. Ackerman, R. van Rijn, D. Stoltz, I. Popa, O. Balmes, A. Resta, D. Wermeille, R. Felici, S. Ferrer, J.W.M. Frenken, The role of steps in surface catalysis and reaction oscillations, Nature Chem. 2 (2010) 730–734.

[3] J. Rostrup-Nielsen, J.K. Norskov, Step sites in syngas catalysis, Topics Catal. 40 (2006) 45–48.
[4] B. Hammer, O.H. Nielsen, J.K. Norskov, Structure sensitivity in adsorption: CO interaction with stepped and reconstructed Pt surfaces, Catal. Lett. 46 (1997) 31–35.
[5] R.T. Vang, K. Honkala, S. Dahl, E.K. Vestergaard, J. Schnadt, E. Laegsgaard, B.S. Clausen, J.K. Norskov, F. Besenbacher, Controlling the catalytic bond-breaking selectivity of Ni surfaces by step blocking, Nat. Mater. 4 (2005) 160–162.
[6] K. Honkala, A. Hellman, I.N. Remediakis, A. Logadottir, A. Carlsson, S. Dahl, C.H. Christensen, J.K. Nørskov, Ammonia synthesis from first-principles calculations, Science 307 (2005) 555–563.
[7] C.H. Bartholomew, Mechanisms of catalyst deactivation, App. Catal. A: Gener. 212 (2001) 17–60.
[8] D.S. Newsome, The water-gas shift reaction, Catal. Rev.: Sci. Eng. 21 (1980) 275–318.
[9] D. Mendes, A. Mendes, L.M. Madeira, A. Iulianelli, J.M. Sousa, A. Basile, The water-gas shift reaction: from conventional catalytic systems to Pd-based membrane reactors – a review, Asia-Pac. J. Chem. Eng. 5 (2010) 111–137.
[10] D.W. Jeong, W.J. Jang, J.O. Shim, W.B. Han, H.S. Roh, U.H. Jung, W.L. Yoon, Low-temperature water-gas shift reaction over supported Cu catalysts, Renew. Energy 65 (2014) 102–107.
[11] N.A. Koryabkina, A.A. Phatak, W.F. Ruettinger, R.J. Farrauto, F.H. Ribeiro, Determination of kinetic parameters for the water-gas shift reaction on copper catalysts under realistic conditions for fuel cell applications, J. Catal. 217 (2003) 233–239.
[12] D. Falleiros, F. Ademar, M. Kaminski, P. Matar, in: V. Patel (Ed.), Petrochemicals, Intech, Rijeka, Croatia, 2012 (Chapter 4).
[13] A. Bruix, J.A. Rodriguez, P.J. Ramírez, S.D. Senanayake, J. Evans, J.B. Park, D. Stacchiola, P. Liu, J. Hrbek, F. Illas, A new type of strong metal-support interaction and the production of H_2 through the transformation of water on $Pt/CeO_2(111)$ and $Pt/CeO_x/TiO_2(110)$ catalysts, J. Am. Chem. Soc. 134 (2012) 8968–8974.
[14] J.A. Rodriguez, P.J. Ramírez, G.G. Asara, F. Viñes, J. Evans, P. Liu, J.M. Ricart, F. Illas, Charge polarization at a Au-TiC interface and the generation of highly active and selective catalysts for the low-temperature water-gas shift reaction, Angew. Chem., Int. Ed. 53 (2014) 11270–11274.
[15] A.A. Gokhale, J.A. Dumestic, M. Mavrikakis, On the mechanism of low-temperature water gas shift reaction on copper, J. Am. Chem. Soc. 130 (2008) 1402–1414.
[16] J.L.C. Fajín, M.N.D.S. Cordeiro, F. Illas, J.R.B. Gomes, Influence of step sites in the molecular mechanism of the water gas shift reaction catalysed by copper, J. Catal. 268 (2009) 131–141.
[17] H. Prats, P. Gamallo, R. Sayós, F. Illas, Unexpectedly large impact of van der Waals interactions on the description of heterogeneously catalysed reactions: the water gas shift reaction Cu(321) as a case example, Phys. Chem. Chem. Phys. 18 (2016) 2792–2801.
[18] H. Prats, L. Álvarez, F. Illas, R. Sayós, Kinetic Monte Carlo simulations of the water gas shift reaction on Cu(111) from density functional theory based calculations, J. Catal. 333 (2016) 217–226.
[19] G. Wang, L. Jiang, X. Pang, Z. Cai, Y. Pan, X. Zhao, Y. Morikawa, J. Nakamura, A theoretical study of surface-structural sensitivity of the reverse water-gas shift reaction over Cu(hkl) surfaces, Suf. Sci. 543 (2003) 118–130.
[20] G. Wang, L. Jiang, Z. Cai, Y. Pan, X. Zhao, W. Huang, K. Xie, Y. Li, Y. Sun, B. Zhong, Surface structure sensitivity of the water-gas shift reaction on Cu(hkl) surfaces: a theoretical study, J. Phys. Chem. B 107 (2003) 557–562.
[21] C.A. Callaghan Doctoral Thesis, in: Kinetics and Catalysis of the Water-Gas-Shift Reaction: A Microkinetic and Graph Theoretic Approach, Worcester Polytechnic Institute, 2006.
[22] C.T. Campbell, Micro- and macro-kinetics: their relationship in heterogeneous catalysis, Topics Catal. 1 (1994) 353–366.
[23] C.A. Callaghan, S.A. Vilekar, I. Fishtik, R. Datta, Topological analysis of catalytic reaction networks: Water gas shift reaction on Cu(111), Appl. Catal. A: Gener. 345 (2008) 213–232.
[24] J.A. Dumesic, Analyses of reaction schemes using De Donder Relations, J. Cat. 185 (1999) 496–505.
[25] A. Stegelmann, C.T. Andreasen, Campbell, Degree of rate control: how much the energies of intermediates and transition states control rates, J. Am. Chem. Soc. 131 (2009) 8077–8082.
[26] H. Meskine, S. Matera, M. Scheffler, K. Reuter, H. Metiu, Examination of the concept of degree of rate control by first-principles kinetic Monte Carlo Simulations, Surf. Sci. 603 (2009) 1724–1730.
[27] G. Kresse, J. Hafner, Ab initio olecular dynamics for liquid metals, Phys. Rev. B: Condens. Matter Mater. Phys. 47 (1993) 558–561.
[28] G. Kresse, J. Furthmüller, Efficiency of ab-initio total energy calculations for metals and semiconductors using a plane-wave basis set, Condens. Comput. Mater. Sci. 6 (1996) 15–50.
[29] G. Kresse, J. Furthmüller, Efficient iterative schemes for ab initio total-energy calculations using a plane-wave basis set, J. Phys. Rev. B: Condens. Matter Mater. Phys. 54 (1996) 11169–11186.
[30] D.R. Lide, in: D.R. Lide (Ed.), CRC Handbook of Chemistry and Physics, 88th ed., CRC Press, Boca Raton, USA, 2008.
[31] J.P. Perdew, K. Burke, M. Ernzerhof, Generalized gradient approximation made simple, Phys. Rev. Lett. 77 (1996) 3865–3868.
[32] S. Grimme, Semiempirical GGA-type density functional constructed with a long-range dispersion correction, J. Comput. Chem. 27 (2006) 1787–1799.
[33] P.E. Blöchl, Projector augmented-wave method, Phys. Rev. B: Condens. Matter Mater. Phys. 50 (1994) 17953–17979.
[34] G. Kresse, D. Joubert, From ultrasoft pseudopotentials to the projector augmented-wave method, Phys. Rev. B: Condens. Matter Mater. Phys. 59 (1999) 1758–1775.
[35] H.J. Monkhorst, J.D. Pack, Special points for Brillouin-zone integrations, Phys. Rev. B: Condens. Matter Mater. Phys. 13 (1976) 5188–5192.
[36] M. Stamatakis, Kinetic modelling of heterogeneous catalytic systems, J. Phys. Condens. Matter. 27 (2015) 1–28. 013001.
[37] M. Stamatakis, D.G. Vlachos, A graph-theoretical kinetic Monte Carlo framework for on-lattice chemical kinetics, J. Chem. Phys. 134 (2011) 1–13. 214115.
[38] J. Nielsen, M. d'Avezac, J. Hetherington, M. Stamatakis, Parallel kinetic monte Carlo simulation framework incorporating accurate models of adsorbate lateral interactions, J. Chem. Phys. 139 (2013) 1–13. 224706.
[39] M. Stamatakis, D.G. Vlachos, Unravelling the complexity of catalytic reactions via kinetic Monte Carlo simulation: current status and frontiers, ACS Catal. 2 (2012) 2648–2663.
[40] A.P.J. Jansen, An introduction to kinetic Monte Carlo simulations of surface reactions, Lecture Notes in Physics, vol. 856, Springer-Verlag, Heidelberg, Germany, 2012.
[41] M. Stamatakis, Y. Chen, D.G. Vlachos, First-principles-based kinetic Monte Carlo simulation of the structure sensitivity of the water-gas shift reaction on platinum surfaces, J. Phys. Chem. C 115 (2011) 24750–24762.
[42] K.J. Laidler, Chemical Kinetics, Harper & Row Publishers, New York, USA, 1987.
[43] D.A. McQuarrie, Statistical Mechanics, second ed., Harper & Row, New York, 2000.
[44] H. Tang, A. Van der Ven, B.L. Trout, Phae diagram of oxygen adsorbed on platinum (111) by first-principles investigation, Phys. Rev. B 70 (2004) 1–10. 045420.
[45] B.C. Han, A. Van der Ven, G. Ceder, B. Hwang, Surface segregation and ordering of alloy surfaces in the presence of adsorbates, J. Phys. Rev. B 72 (2005) 1–9. 205409.
[46] S.D. Miller, J.R. Kitchin, Uncertainty and figure selection for DFT based cluster expansions for oxygen adsorption on Au and Pt(111) surfaces, Mol. Simul. 35 (2009) 920–927.
[47] D. Lerch, O. Wieckhorst, G. Hart, R. Forcade, S. Müller, UNCLE: a code for constructing cluster expansions for arbitrary lattices with minimal user-input, Modell. Simul. Mater. Sci. Eng. 17 (2009) 1–19. 055003.
[48] C. Wu, D.J. Schmidt, C. Wolverton, W.F. Schneider, Accurate coverage-dependence incorporated into first-principles kinetic models: catalytic NO oxidation on Pt(111), J. Catal. 286 (2012) 88–94.
[49] R.B. Getman, W.F. Schneider, DFT-based coverage-dependent model of Pt-catalyzed NO oxidation, Chem. Cat. Chem. 2 (2010) 1450–1460.
[50] J.K. Nørskov, T. Bligaard, A. Logadottir, S. Bahn, L.B. Hansen, M. Bollinger, H. Bengaard, B. Hammer, Z. Sljivancanin, M. Mavrikakis, Y. Xu, S. Dahl, J.H. Jacobsen, Universality in heterogeneous catalysis, J. Catal. 209 (2002) 275–278.
[51] L.C. Grabow, A.A. Gokhale, S.T. Evans, J.A. Dumestic, M. Mavrikakis, Mechanism of the water gas shift reaction on Pt: first principles, experiments, and microkinetic modelling, J. Phys. Chem. C 112 (2008) 4608–4617.
[52] S. Piccinin, M. Stamatakis, CO oxidation on Pd(111): a first-principles-based kinetic Monte Carlo study, ACS Catal. 4 (2014) 2143–2152.
[53] I. Bönicke, W. Kirstein, S. Spinzig, F. Thieme, CO adsorption studies on a stepped Cu(111) surface, Surf. Sci. 313 (1994) 231–238.
[54] B.J. Hinch, L.H. Dubois, Water adsorption on Cu(111): evidence for Volmer-Weber film growth, Chem. Phys. Lett. 181 (1991) 10–15.
[55] L. Yang, A. Karim, J.T. Muckerman, Density functional kinetic Monte Carlo simulation of water-gas shift reaction on Cu/ZnO, J. Phys. Chem. C 117 (2013) 3414–3425.
[56] M. Stamatakis, D.G. Vlachos, Equivalence of on-lattice stochastic chemical kinetics with the well-mixed chemical master equation in the limit of fast diffusion, Comput. Chem. Eng. 35 (2012) 2602–2610.
[57] Y.C. Huang, T. Zhou, C. Ling, S. Wang, J.Y. Du, Do Ni/Cu and Cu/Ni alloys have different catalytic performances towards water-gas shift? A density functional theory investigation, ChemPhysChem 15 (2014) 2490–2496.
[58] S.-C. Huang, C.-H. Lin, J.-H. Wang, Trends of water gas shift reaction on close-packed transition metal surfaces, J. Phys. Chem. C 114 (2010) 9826–9834.

Supporting information

Comparing the catalytic activity of the water gas shift reaction on Cu(321) and Cu(111) surfaces: step sites do not always enhances reactivity

Hèctor Prats, Pablo Gamallo, Francesc Illas and Ramón Sayós*

Departament de Ciència de Materials i Química Física & Institut de Química Teòrica i Computacional (IQTCUB), Universitat de Barcelona, C/Martí i Franquès 1, 08028 Barcelona, Spain.
**Corresponding author: Ramón Sayós*
Email: r.sayos@ub.edu / Tel. +34934034760

I. Energy profiles

Energy barriers ($E_i^0(0)$ in eV) and reaction energies ($\Delta E_i(0)$ in eV) at the zero-coverage limit for the LH-type and diffusion processes included in the simulation are shown below. Zero-point energy correction is included in all the stationary states.

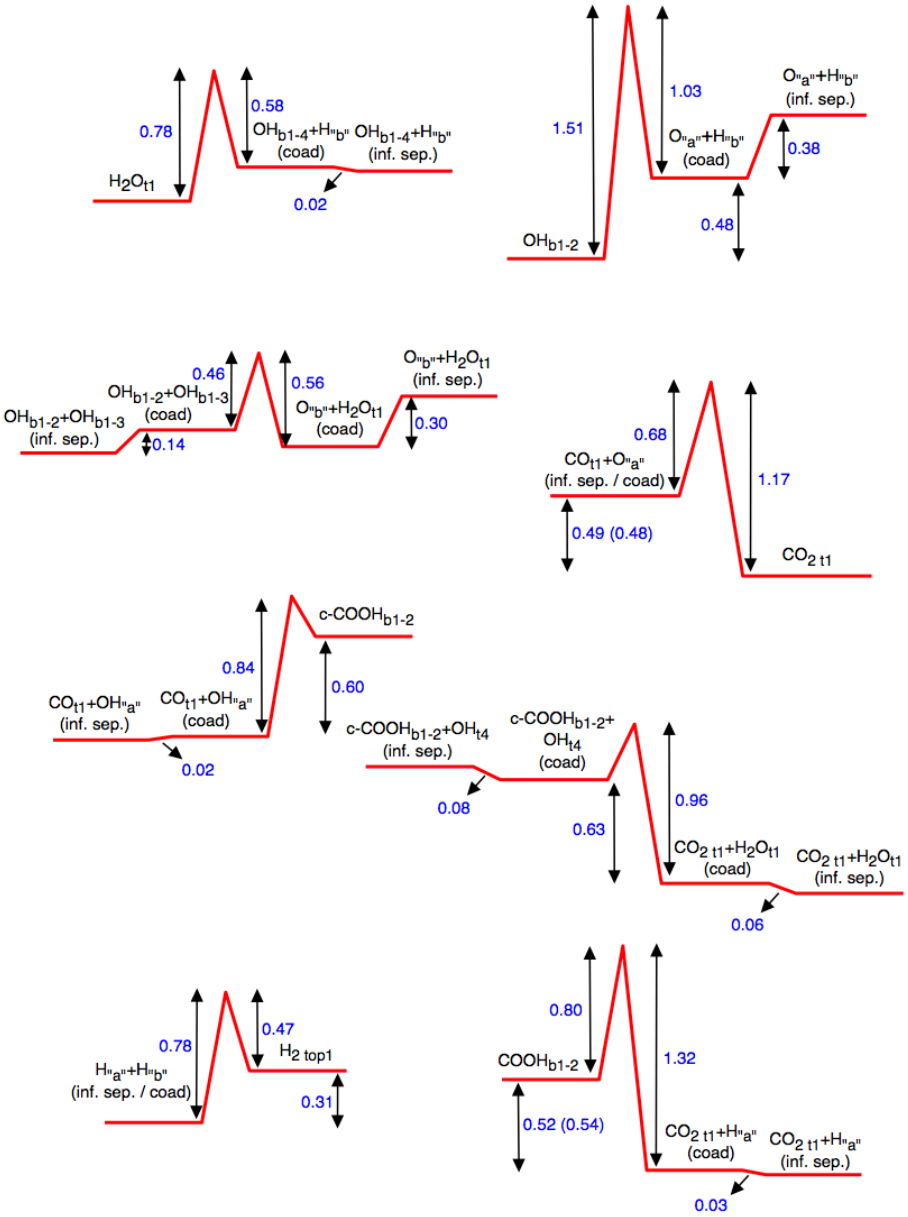

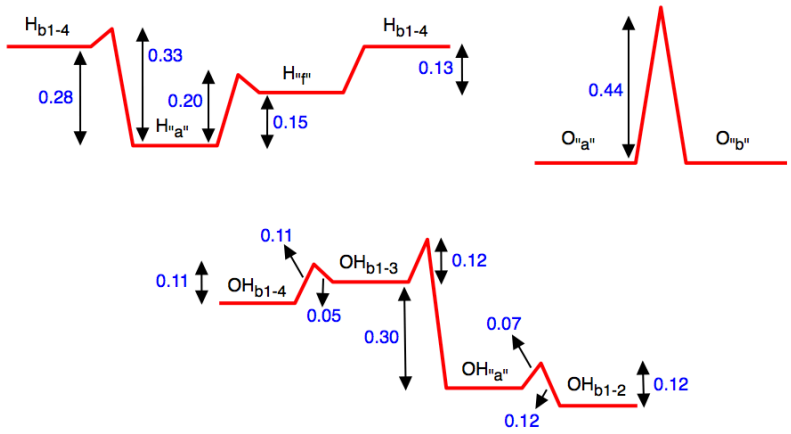

II. Equivalency between real and lattice-model occupation of OH, O and H molecule

DFT calculations have shown that OH, O and H species are found mainly in bridge and hollow sites. However, in the present lattice-model, only top sites are explicitly defined, and then equivalency relationships between the real and the lattice-model occupations are needed.

If the real occupation is a top site (*i.e.*, H_2O, CO, H_2 and CO_2) there is no problem. For molecules adsorbed on bridge sites the equivalence is straightforward: COOH is found at $b_{1\text{-}2}$, and thus in the lattice model this molecule is like occupying two neighbouring *top* 1 and *top* 2 sites. Finally, for molecules adsorbed in hollow sites, the first approximation would be to consider the occupation of the three surrounding top sites in the lattice-model. However, this is a very bad choice, because it would prevent many reactions to occur. For example, a H atom adsorbed in hollow "a" would prevent another hydrogen to be adsorbed on the neighbouring hollow "f" (*i.e.*, the middle *top* 3 site would be doubly occupied and this is not allowed) and therefore H_2 formation would never be possible. Additionally, H or O species adsorbed on hollow "a" or hollow "b" sites (*i.e.*, occupying the surrounding *top* 1, *top* 2 and *top* 3 sites in the lattice model) are small enough to allow adsorption of other molecules like CO or H_2O in the neighbouring *top* 1 - step site.

The equivalencies between the real (left) and lattice-model occupation (right) for OH, O and H species used in the present work are shown below. They have been chosen in order to correctly reproduce the correct surface kinetics, allowing the reactions to take place with the proper relative arrangement between coadsorbed reactant pairs.

Oxygen

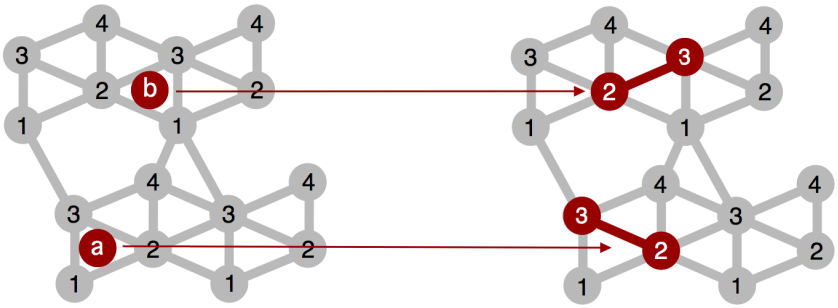

Hydrogen

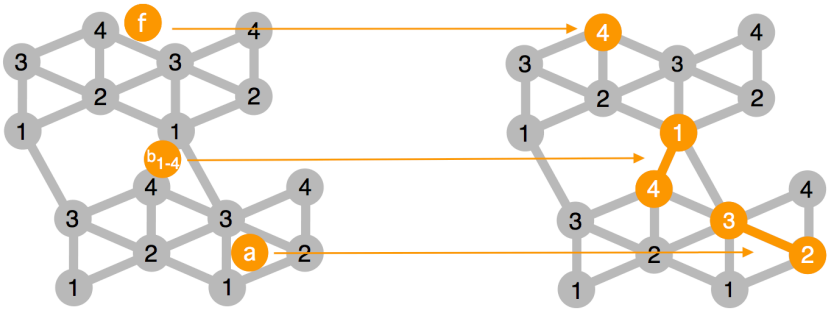

Hydroxyl

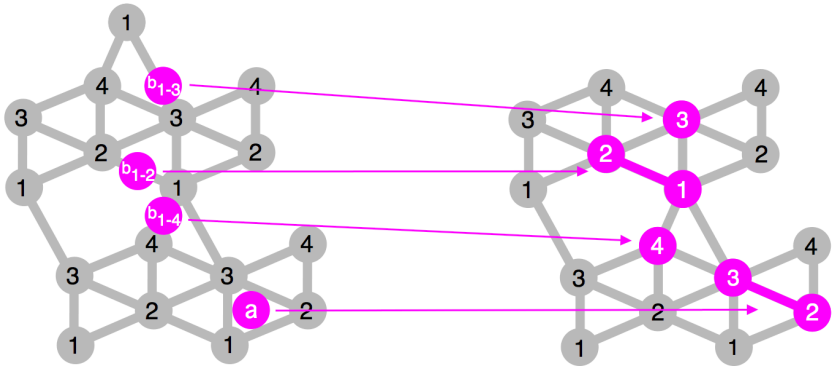

III. Elementary step representation

Graph patterns representing the elementary steps considered in the reaction mechanism of the WGSR over the Cu(321) surface, along with the reaction rate parameters at T = 625K, P_{CO} = 26 Torr and P_{H2O} = 10 Torr, are described below, along with the formula used for calculating the TST pre-exponential factor A_i. Diffusion processes are not included here. Forward and reverse processes are defined using the same criteria as in Table 1.

$$A_i = \frac{k_B T}{h} \frac{Q_i^{\neq}}{Q_R}$$

1. CO adsorption

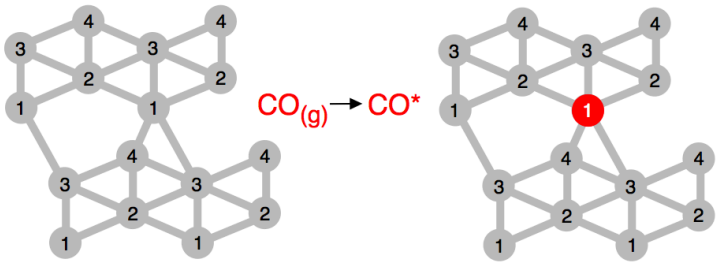

A_{fwd} = 1.16x10^{8} s^{-1}

A_{fwd}/A_{rev} = 1.20x10^{-6}

$E_{fwd}(0)$ = 0.00 eV

2. H_2 desorption

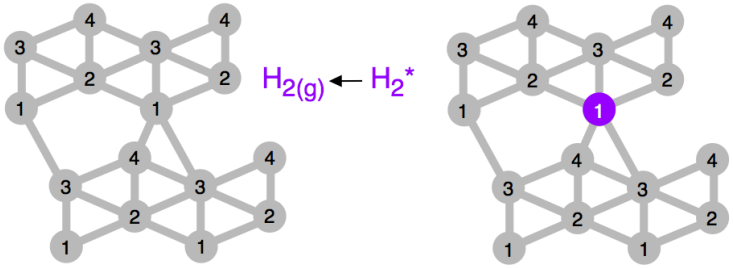

A_{rev} = 1.70x10^{11} s^{-1}

A_{fwd}/A_{rev} = -

$E_{rev}(0)$ = 0.12 eV

3. H_2O adsorption

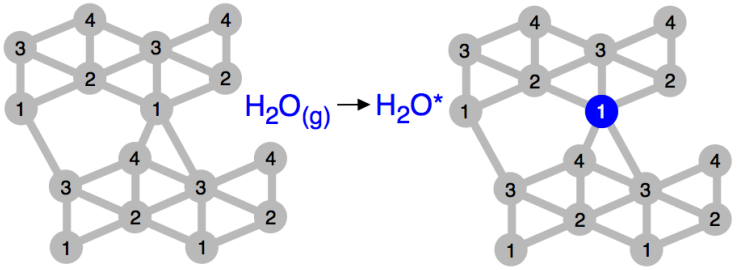

A_{fwd} = 1.44x10^{8} s^{-1}

A_{fwd}/A_{rev} = 4.36x10^{-3}

$E_{fwd}(0)$ = 0.00 eV

4. CO_2 desorption

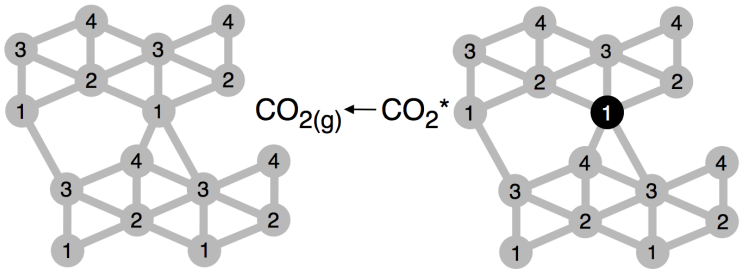

$A_{rev} = 3.25 \times 10^{9}\ s^{-1}$

$A_{fwd}/A_{rev} = -$

$E_{rev}(0) = 0.28$ eV

5. Water dissociation

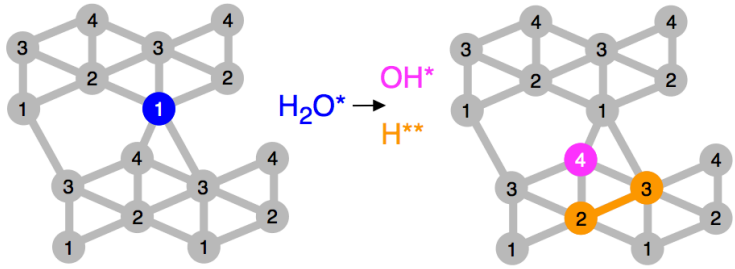

$A_{fwd} = 2.94 \times 10^{12}\ s^{-1}$

$A_{fwd}/A_{rev} = 1.67 \times 10^{-1}$

$E_{fwd}(0) = 0.78$ eV

6. OH dissociation

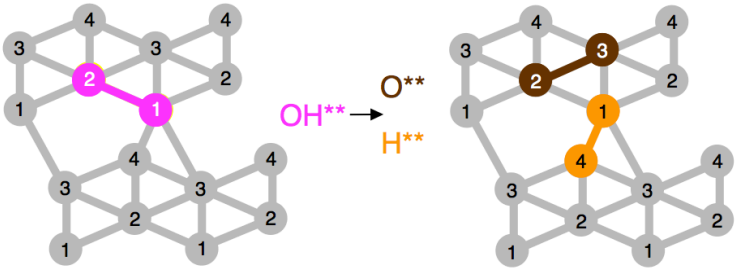

$A_{fwd} = 3.77 \times 10^{12}\ s^{-1}$

$A_{fwd}/A_{rev} = 2.83 \times 10^{-1}$

$E_{fwd}(0) = 1.51$ eV

7. OH disproportionation

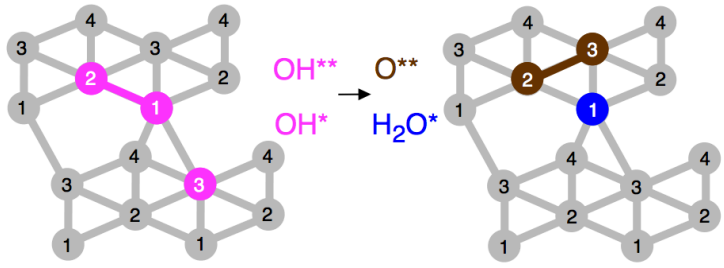

$A_{fwd} = 4.66 \times 10^{12}\ s^{-1}$

$A_{fwd}/A_{rev} = 5.74 \times 10^{-1}$

$E_{fwd}(0) = 0.46$ eV

8. CO oxidation by atomic oxygen

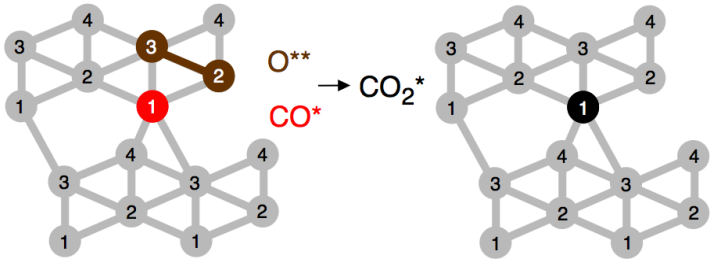

$A_{fwd} = 2.24x10^{12}\ s^{-1}$

$A_{fwd}/A_{rev} = 3.06x10^{-1}$

$E_{fwd}(0) = 0.68$ eV

9. CO oxidation by OH: carboxyl formation

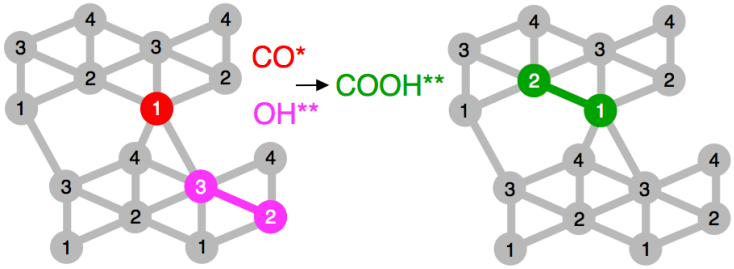

$A_{fwd} = 2.78x10^{13}\ s^{-1}$

$A_{fwd}/A_{rev} = 2.74x10^{0}$

$E_{fwd}(0) = 0.84$ eV

10. Carboxyl dehydrogenation

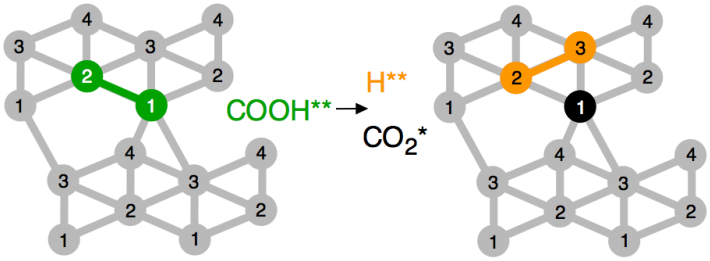

$A_{fwd} = 3.31x10^{13}\ s^{-1}$

$A_{fwd}/A_{rev} = 4.61x10^{0}$

$E_{fwd}(0) = 0.80$ eV

11. Carboxyl disproportionation by hydroxyl

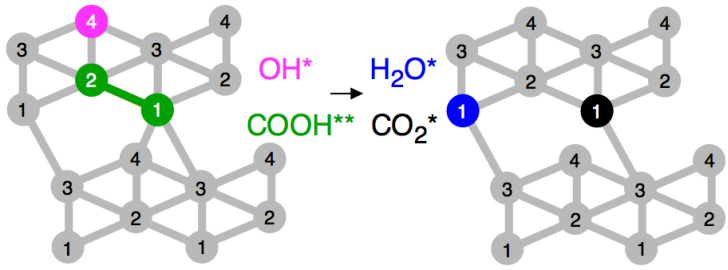

$A_{fwd} = 1.23x10^{12}\ s^{-1}$

$A_{fwd}/A_{rev} = 5.50x10^{2}$

$E_{fwd}(0) = 0.33$ eV

12. H recombination

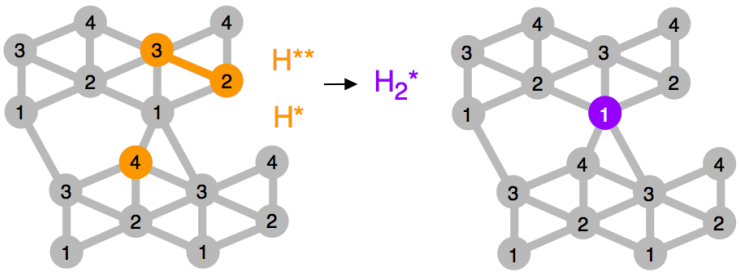

$A_{fwd} = 3.03 \times 10^{13}\ s^{-1}$

$A_{fwd}/A_{rev} = 1.46 \times 10^{1}$

$E_{fwd}(0) = 0.78$ eV

IV. Cluster expansion

Graph patterns for each figure included in the CE Hamiltonian (Eq. 2) to model the lattice energy are shown below, along with the corresponding cluster energy. Labels *point* and *pair* are used for figures involving one and two adsorbates, respectively, and numbers 1-4 are related with the top sites that the adsorbates of each figure are occupying in the present lattice model.

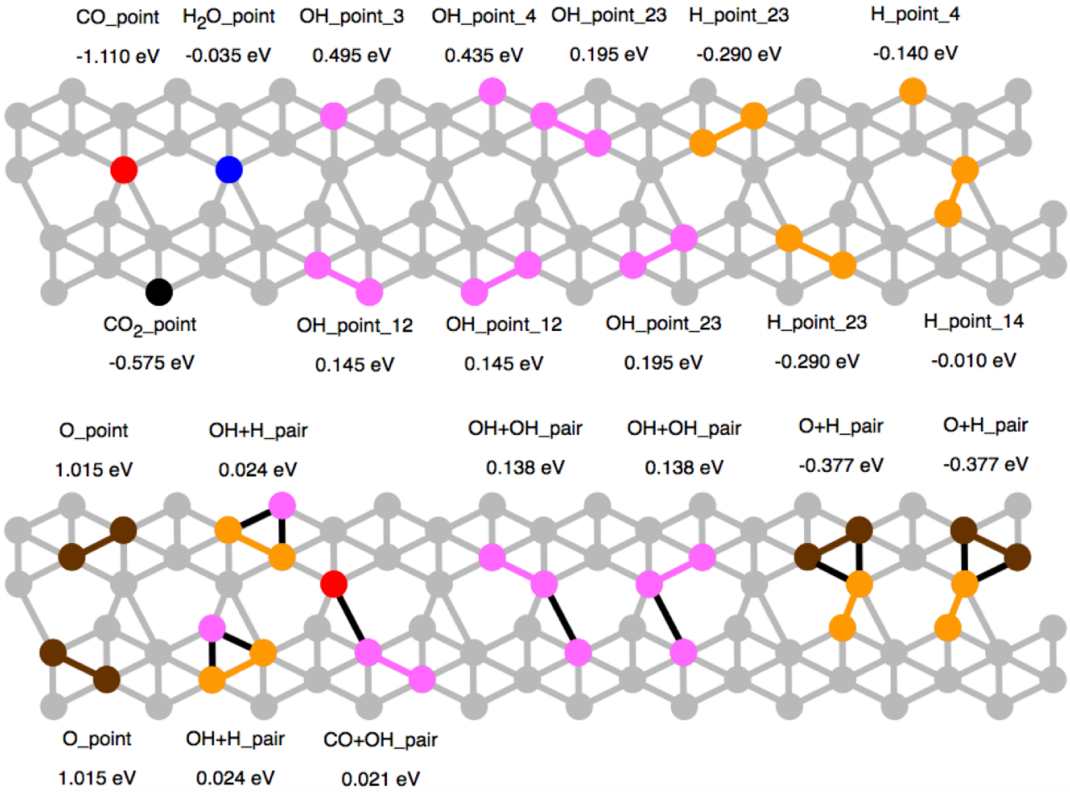

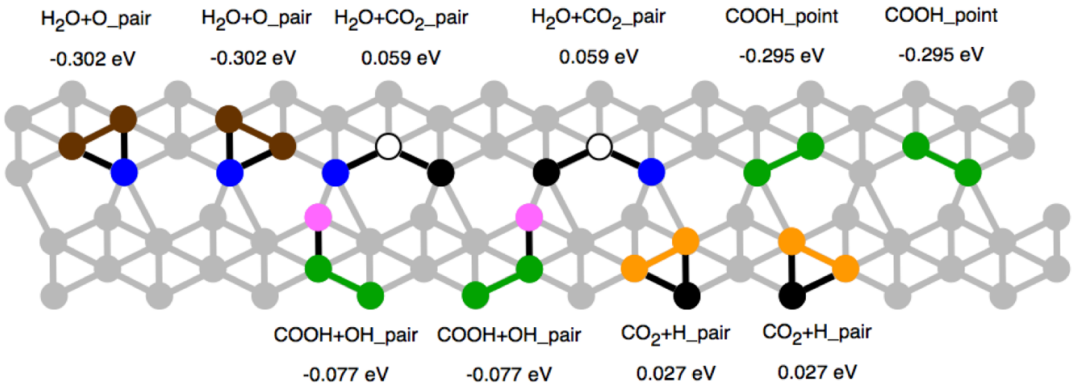

Gas energies (in eV) used in ZACROS for the calculation of $\Delta E_i(\sigma)$ are shown in the following table:

gas molecule	CO	H_20	CO_2	H_2
$\boldsymbol{E_i^{gas}}$	0.000	0.625	-0.295	0.000

Finally, CE lattice energy as a function of time for the simulation performed at T = 625 K, P_{CO} = 26 Torr and P_{H2O} = 10 Torr is plotted below. The steady-state is reached around a simulation time of 4 ms, which corresponds to 300 million kMC steps.

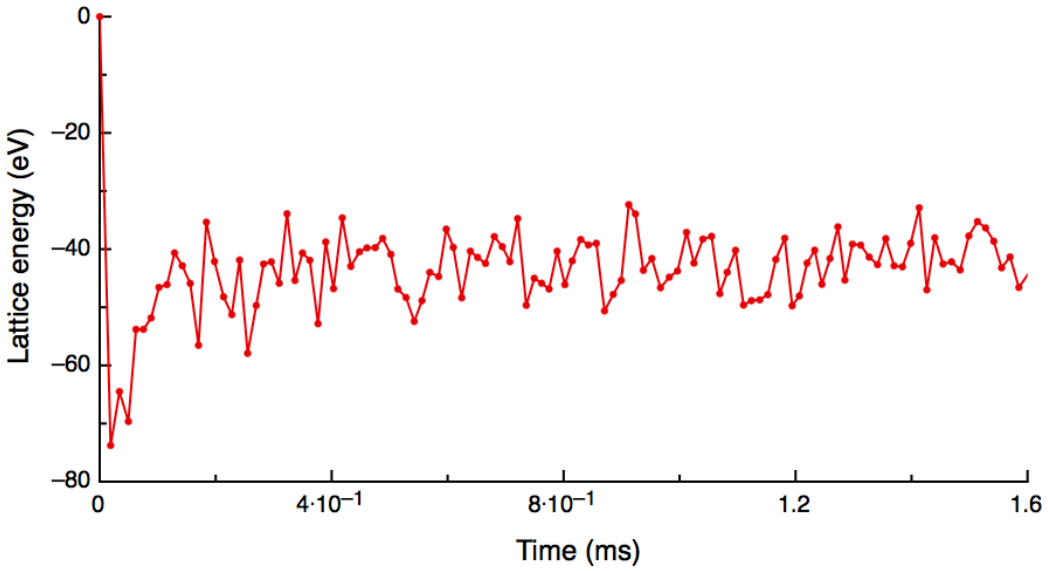

6.3. Summary and conclusions

The effect of step sites in the WGSR catalyzed by copper has been studied by means of kMC simulations on the stepped Cu(321) surface, including a total of 36 elementary steps such as adsorption/desorption, diffusion and other elementary surface chemical reactions. The recently developed graph-theoretical kMC approach[13] is used and coupled with cluster expansion Hamiltonians to model the lateral interactions between adsorbates. Due to the presence of the steps, the Cu(321) surface presents a high heterogeneity of adsorption sites. Hence, the lattice model used for the present system includes 4 different sites (i.e., unlike in the flat Cu(111) surface where all sites in the lattice model were considered equivalent).

A first comparison between both surfaces shows that, within the 463-625 K temperature range studied, the TOF for the WGSR on the stepped Cu(321) surface is between two (at 625 K) and four (at 463 K) orders of magnitude lower than that on the flat Cu(111) surface. This fact constitutes an unexpected conclusion, which possibly cannot be anticipated by inspection of the energy profiles only. For P_{CO} = 26 Torr and P_{H2O} = 10 Torr, OH is the most dominant species at the surface in all the temperature range, followed by CO, H_2O and finally atomic H (see Figure 4 from Publication 5). On the contrary, H coverage presents the largest value at the Cu(111) surface, excepting at the highest temperature where OH also becomes dominant (see Figure 4 from Publication 3). As in the flat surface, an Arrhenius behavior is found in two temperature intervals, with apparent activation energies of 1.2 eV (550-625 K) and 1.6 eV (463-550K). Noticeably, these values are larger than those corresponding to the Cu(111) surface (i.e., 0.5 and 0.8 eV).

Regarding the reaction mechanism, the associative route (i.e., formation of CO_2 from COOH intermediate, processes 9-11 from Table 1 in Publication 5) is the dominant pathway in all the studied conditions, even when we change the ratio of partial pressures for both reactants. The same result was observed on the flat Cu(111) surface. However, notice that the surface redox route (i.e., formation of CO_2 from CO oxidation, processes 6-8 from Table 1 in Publication 5), which does not play any role in the flat surface, becomes important on the Cu(321) surface at high temperatures, contributing around a 12% of the overall TOF. On Cu(111) this mechanism is severely hindered, because when atomic O is formed by OH recombination it rapidly goes backwards forming OH again (i.e., the reverse reaction rate is very high). Another difference comes from the direct

COOH dehydrogenation to form CO_2 and H species. This process is not observed in the Cu(111) surface due to a high energy barrier of 1.18 eV. However, it is one of the main router for CO_2 production on the Cu(321) surface, where the energy barrier at zero-coverage limit is 0.80 eV only.

Finally, the RDSs were investigated by using the Campbell's degree of rate control[11]. This analysis show that COOH dehydrogenation and COOH disproportionation by OH (i.e., steps 10 and 11 in Table 1 from Publication 5) are clearly the RDSs at all studied conditions of P and T, with water dissociation being also a RDS at low P_{CO}/P_{H2O} ratios and H_2 formation being also a RDS at high P_{CO}/P_{H2O} ratios (see Table 2 from Publication 5). This is in agreement with the results derived from the analysis of the TOFs of the steps.

At this point, one may wonder why the computed TOFs for the stepped surface, where three different routes for CO_2 formation are participating, are lower than for the flat Cu(111) surface, where direct COOH dehydrogenation and CO oxidation do not occur. The reason is very simple. On the one hand, COOH formation is endoergic by 0.62 eV in the Cu(321) surface, whereas on the Cu(111) surface becomes endoergic by only 0.15 eV. This change implies that the energy barrier in the reverse direction is much lower in the stepped surface (i.e., 0.24 eV) than in the Cu(111) surface (i.e., 0.55 eV). The same happens with water dissociation: whereas in the flat surface this process is exoergic and has an energy barrier of 1.15 eV for the reverse direction, in the stepped surface it is endoergic, with a reverse energy barrier of 0.60 eV (i.e., leading to an equilibrium constant at 625 K of only $5.9 \cdot 10^{-3}$). On the other hand, the poisoning of step sites by CO and, to a lesser extent, by water, prevents some elementary reactions to occur. Therefore, establishing a ranking of the most efficient crystal surfaces for catalyzing a complex reaction (e.g., WGSR) based only on the energy barriers of forward processes is not always correct, although this is often the only data taken into account[9,14,15].

6.4. References

1 J. T. Yates, Surface chemistry at metallic step defect sites, J. Vac. Sci. & Tech. A, **1995**, 13, 1359–1367.

2 B. L. M. Hendriksen, M. D. Ackermann, R. van Rijn, D. Stoltz, I. Popa, O. Balmes, A. Resta, D. Wermeille, R. Felici, S. Ferrer and J. W. M. Frenken, The

role of steps in surface catalysis and reaction oscillations, *Nat. Chem*., **2010**, 2, 730–734.

3 J. Rostrup-Nielsen and J. K. Nørskov, Step sites in syngas catalysis, *Top. Catal.*, **2006**, 40, 45–48.

4 B. Hammer, O. H. Nielsen and J. K. Nørskov, Structure sensitivity in adsorption: CO interaction with stepped and reconstructed Pt surfaces, *Catal. Letters*, **1997**, 46, 31–35.

5 R. T. Vang, K. Honkala, S. Dahl, E. K. Vestergaard, J. Schnadt, E. Lægsgaard, B. S. Clausen, J. K. Nørskov and F. Besenbacher, Controlling the catalytic bond-breaking selectivity of Ni surfaces by step blocking, *Nat. Mat*., **2005**, 4, 160–162.

6 K. Honkala, A. Hellman, I. N. Remediakis, A. Logadottir, A. Carlsson, S. Dahl, C. H. Christensen and J. K. Nørskov, Ammonia synthesis from first-principles calculations, *Science*, **2005**, 307, 555–558.

7 C. H. Bartholomew, Mechanisms of catalyst deactivation, *App. Catal. A: General*, **2001**, 212, 17–60.

8 G.-C. Wang, L. Jiang, X.-Y. Pang, Z.-S. Cai, Y.-M. Pan, X.-Z. Zhao, Y. Morikawa and J. Nakamura, A theoretical study of surface-structural sensitivity of the reverse water-gas shift reaction over Cu(hkl) surfaces, *Surf. Sci*., **2003**, 543, 118–130.

9 Wang, L. Jiang, Cai, Pan, Zhao, W. Huang, Xie, Li, Sun and B. Zhong, Surface structure sensitivity of the water−gas shift reaction on Cu(hkl) surfaces: a theoretical study, *J. Phys. Chem. B*, **2003**, 107, 557–562.

10 H. Prats, F. Illas and R. Sayós, General concepts, assumptions, drawbacks, and misuses in Kinetic Monte Carlo and microkinetic modeling simulations applied to computational heterogeneous catalysis, *Int. J. Quantum Chem*., **2017**, e25518.

11 C. T. Campbell, Future directions and industrial perspectives micro- and macro-kinetics: their relationship in heterogeneous catalysis, *Top. Catal.*, **1994**, 1, 353–366.

12 A. A. Gokhale, J. A. Dumesic and M. Mavrikakis, On the mechanism of low-temperature water gas shift reaction on copper, *J. Am. Chem. Soc*., **2008**, 130, 1402–1414.

13 M. Stamatakis and D. G. Vlachos, A graph-theoretical kinetic Monte Carlo framework for on-lattice chemical kinetics, *J. Chem. Phys*., **2011**, 134, 214115.

14 Y. C. Huang, T. Zhou, H. Liu, C. Ling, S. Wang and J. Y. Du, Do Ni/Cu and Cu/Ni alloys have different catalytic performances towards water-gas shift? A density functional theory investigation, *ChemPhysChem*, **2014**, 15, 2490–2496.

15 S.-C. Huang, C.-H. Lin and J.-H. Wang, Trends of water gas shift reaction on close-packed transition metal surfaces, *J. Phys. Chem. C*, **2010**, 114, 9826–9834.

CHAPTER SEVEN

General concepts, assumptions, drawbacks, and misuses in kMC

7.1. Introduction

The last chapter of results of the present thesis aims to take advantage of all the knowledge gained in Chapter 4 and Chapter 6 regarding kMC simulations, and to delve into some general aspects that may serve as a guide for future kinetic studies. To that end, we discuss typical assumptions, advantages and drawbacks of the kMC method, and the differences between kMC and the most common approach to study the kinetics of heterogeneous catalytic reactions: microkinetic modeling. Concretely, the WGSR over Cu(111) and Cu(321) surfaces is chosen to discuss several issues as for instance potential and free energy diagrams, diffusion processes, lateral interactions or the accuracy of the reaction rates.

7.2. Publication 6

General concepts, assumptions, drawbacks, and misuses in Kinetic Monte Carlo and microkinetic modeling simulations applied to computational heterogeneous catalysis

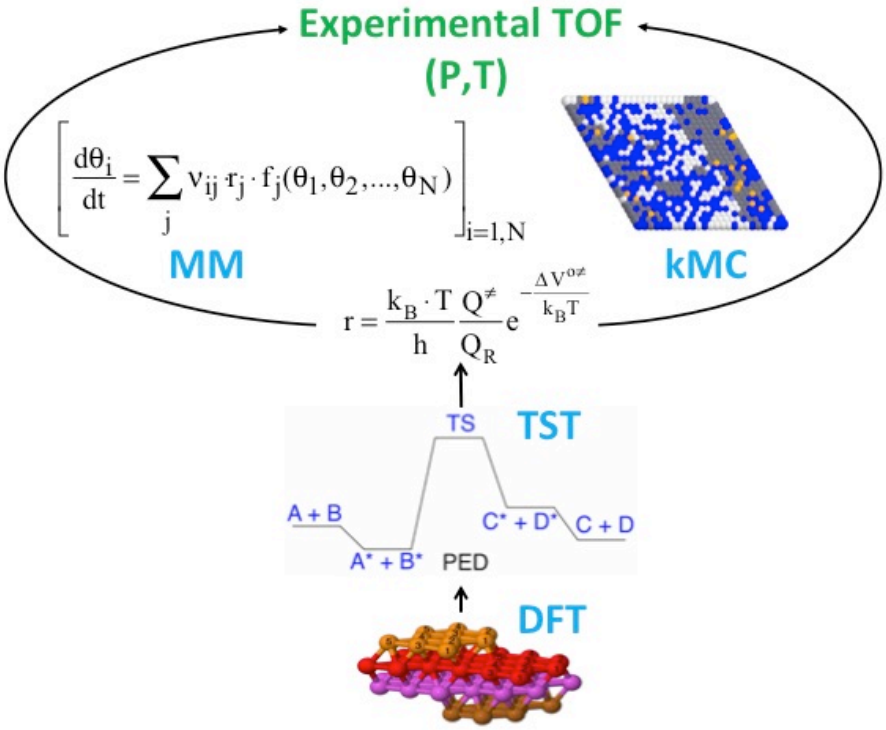

Received: 20 August 2017 | Revised: 29 September 2017 | Accepted: 3 October 2017

DOI: 10.1002/qua.25518

TUTORIAL REVIEWS

WILEY

General concepts, assumptions, drawbacks, and misuses in Kinetic Monte Carlo and microkinetic modeling simulations applied to computational heterogeneous catalysis

Hèctor Prats | **Francesc Illas** | **Ramón Sayós**

Departament de Ciència de Materials i Química Física & Institut de Química Teòrica i Computacional (IQTCUB), Universitat de Barcelona, C. Martí i Franquès 1, 08028 Barcelona, Spain

Correspondence
Francesc Illas, Departament de Ciència de Materials i Química Física & Institut de Química Teòrica i Computacional (IQTCUB), Universitat de Barcelona, C. Martí i Franquès 1, 08028 Barcelona, Spain.
Email: francesc.illas@ub.edu and Ramón Sayós, Departament de Ciència de Materials i Química Física & Institut de Química Teòrica i Computacional (IQTCUB), Universitat de Barcelona, C. Martí i Franquès 1, 08028 Barcelona, Spain.
Email: r.sayos@ub.edu

Funding information
Ministerio de Economía y Competitividad, Grant/Award Number: CTQ2014-53987-R and CTQ2015-64618-R; Generalitat de Catalunya, Grant/Award Number: 2014SGR97, 2014SGR1582, XRQTC; Generalitat de Catalunya for a predoctoral, Grant/Award Number: FI-DGR-2015; 2015 ICREA Academia Award for Excellence in University Research

Abstract

In the present article, we survey two common approaches widely used to study the kinetics of heterogeneous catalytic reactions. These are kinetic Monte Carlo simulations and microkinetic modeling. We discuss typical assumptions, advantages, drawbacks, and differences of these two methodologies. We also illustrate some wrong concepts and inaccurate procedures used too often in this kind of kinetics studies. Thus, several issues as for instance minimum energy diagrams, diffusion processes, lateral interactions, or the accuracy of the reaction rates are discussed. Some own examples mainly based on water gas shift reaction over Cu(111) and Cu(321) surfaces are chosen to explain the different developed topics on the kinetics of heterogeneous catalytic reactions.

KEYWORDS

computational heterogeneous catalysis, energy and free energy diagrams, kinetic Monte Carlo and microkinetic modeling, reaction rates

1 | INTRODUCTION

Heterogeneous catalysis employing solid surfaces as catalysts for gas reactions has huge impact and many applications in metallurgical and chemical industries. More than 90% of the chemical and energy industries utilize this type of catalysts. In the past two decades, the study of the molecular mechanism of heterogeneous catalysis has led to significant advances and established a systematic approach to obtain total and free energy profiles as well as quite accurate reaction rates derived from transition state theory.[1,2] The understanding of the kinetics of heterogeneous catalytic reactions experienced similar progress but the available approaches are far from being generally applicable. Clearly, a better understanding of kinetic aspects can help to improve the design of reactors operating in steady-state regime, proposing more suitable initial conditions (i.e., T, P, and initial gas composition) or improved catalysts (e.g., with high conversion at low temperatures). Normally, catalytic reactors use porous pellets with nm-sized catalyst particles at the available (external or internal) surfaces of pores. Nowadays, surface science allows one to study the reaction kinetics on catalyst models working on controlled conditions. Similar experiments can be carried out involving surfaces of porous catalysts, pellets, and/or the whole reactor, therefore, implying different size and time scales.[3] The present work focuses on those cases, where experimentally single- or poly-crystal samples can be used as catalytic models under ultrahigh vacuum conditions.

Heterogeneous catalytic reactions are complex reactions, which involve frequently a large list of several elementary surface processes, where one or several mechanisms can be competing in both main and side reactions. Usually five consecutive stages are involved: (1) diffusion of reactant

species from gas-phase to the surfaces, (2) adsorption of the gases on the surfaces, (3) reaction and diffusion processes at the surfaces, (4) desorption of the products, and (5) diffusion of the desorbed products into the gas-phase.[2] In general, the diffusion processes are faster than the chemical reactions at the surface and the global reaction is not diffusion-limited. The main types of surface processes can be classified as: (a) molecular or dissociative adsorptions, (b) molecular desorptions, (c) unimolecular processes (e.g., molecular dissociation), and (d) bimolecular reactions, involving two adsorbed species (i.e., Langmuir-Hinshelwood (LH) step) or involving one gas species and one adsorbed species (i.e., Eley-Rideal (ER) step) although the later dominates in a limited number of cases. LH and ER reactions can give rise to gas and/or adsorbed products. Moreover, even for pristine well defined single crystal surfaces, several types of sites (e.g., top, bridge, fcc-hollow, hcp-hollow, etc.) where the same reactants can present different reaction rates (sometimes originating also different products), thus, enlarging the already long list of existing elementary surface processes.

Density functional theory (DFT) calculations represent a good first-principles approach for a proper description of these individual surface processes, although adsorbate–adsorbate lateral interactions should be included too to account for the significant coverage effects in the reaction kinetics. These DFT data can be used later to study the global catalytic heterogeneous reaction using mean-field microkinetic modeling (MM)[2] or kinetic Monte Carlo (kMC)[4] simulations. Here, a caveat is necessary: energy profiles, and hence energy barriers and transition state theory derived reaction rates, are sensitive to the choice of the exchange-correlation method and also to the inclusion of dispersion terms, which were neglected in many articles in the past, but they are often crucial.

In this article, we describe in detail how to use both MM and kMC methods to study a heterogeneous (i.e., gas-surface) catalytic reaction, highlighting the main advantages and limitations of these techniques. Moreover, we review and discuss some concepts and inaccurate procedures, used very regularly in this kind of kinetics studies. These inaccuracies could be possibly originated from the very multidisciplinary character of this research field, involving scientists from different backgrounds (e.g., chemists, physicists, chemical engineers, etc.), which is also visible through the wide spectrum of important journals where these studies are frequently published.

2 | SYSTEM MODEL AND KINETIC METHODS

A consistent MM or kMC kinetics study on a complex heterogeneously (gas-surface) catalysed reaction should define clearly the model system (i.e., reactor) aimed at closely simulating an experimental kinetic study. This model system involves the choice of a gas model, a lattice model and a reaction model. The gas model normally implies a gas mixture of reactants (sometimes including also inert or product species) at a fixed temperature, total pressure and initial gas composition (i.e., partial pressures). The surface of a real solid catalyst (i.e., exposed surface) can be sometimes modeled by choosing a given well defined single crystal surface represented by a slab model described by a periodic 2D unit cell (i.e., lattice), and exhibiting one or several types of sites. Finally, the reaction model should include all possible elementary surface processes that are likely to occur in all accessible reaction mechanisms at the selected experimental conditions. Moreover, some extra points should be taken into account if a correct comparison between experiment and simulations is intended. For instance, in a closed reactor the composition of the reactants mixture would change through the reaction. In the case of a plug flow reactor, the total flow rate should also be included into the simulation. Moreover, depending on the type of reactor, the reverse reaction of elementary surface processes producing the final products of the whole reaction should be taken into account, as these product species could react backward (even more if they appear in the initial reactant mixture). Usually, many MM or kMC studies assume an ideal experimental set-up with a fresh reactants mixture continuously impinging on an empty (or gas precovered) thermalized catalyst surface, where the heterogeneous complex reaction takes place and, afterwards, the final gas products desorb and leave the surface region implying a process not in a thermodynamic equilibrium but rather in a steady-state).

2.1 | Kinetic Monte Carlo simulations

As surface processes are rare events, direct molecular dynamics simulations would require very long run times and are thus computationally prohibitive. This is further complicated by difficulty in defining accurate force fields describing together all surface processes. In principle, one could use ab initio molecular dynamics (AIMD) but, again, the long runs needed make the overall approach unaffordable even by relying on the time-saving steps methods as in the Carr–Parrinello molecular dynamics (CPMD). Another complication comes from the enormous accumulated errors that would appear in the numerical integration of the trajectories. Thus, an alternative approach is needed where the problem can be solved by making use of stochastic techniques based on Monte Carlo like algorithms. This is the idea behind the so called kinetic Monte Carlo (kMC) method[4,5] used to solve numerically the master equation (ME; Equation 1). To make use of this approach one needs to define an appropriate lattice model defining the state of a gas-surface system. This can be described by defining a surface configuration, where both free and occupied sites are assigned (i.e., adlayer configurations). Different surface processes (i.e., adsorption, diffusion, reaction, and desorption) will modify continuously the surface configurations.

The ME, which can be derived from first principles,[4] is a lost-gain equation that governs the time evolution of the probability of any α surface configuration (P_α), Equation 1

$$\frac{dP_\alpha}{dt} = \sum_\beta \left[W_{\beta\alpha}P_\beta - W_{\alpha\beta}P_\alpha\right] \quad (1)$$

Here, the sum runs over all surface configurations, P_α (P_β) denotes the probability to find the system in the surface configuration α (β) at time t and $W_{\alpha\beta}$ is the transition probability per unit time to pass from a configuration α to a different β one in such a way that only one surface process is implied. These transition probabilities (units: s^{-1}) are synonymous to reaction rates ($r_{\alpha\beta}$) of the mentioned surface processes. Sometimes they are also called rate constants ($k_{\alpha\beta}$), but they are not necessarily coincident with the same rate constants used in macroscopic rate equations,[2] which can have different units (e.g., s^{-1} for a unimolecular reaction or molecular desorption, $m^2 \cdot s^{-1}$ for a LH reaction, etc.). The ME is solved using several efficient algorithms such as variable step-size, random selection, first reaction, rejection-free,[4] which can be appropriately selected from analysis of their influence in the numerical solution of the ME and should support the principle of detailed balance for each surface process. Thus, the rejection-free algorithm is widely used to solve the ME in kMC simulations and goes as follows.[4,5]

1. Generate an initial α surface configuration ($t = 0$), make the list of all possible surface processes ($N_{p(\alpha)}$) and define the sites involved for such processes ($N_{s(\alpha)}$).
2. Determine the $r_{\alpha\beta}$ reaction rates of all $N_{p(\alpha)}$ surface processes from this α surface configuration (i.e., all $\alpha \rightarrow \beta$ processes) and the total reaction rate $r_{tot(\alpha)}$:

$$r_{tot(\alpha)} = \sum_\beta^{N_{p(\alpha)}} r_{\alpha\beta} \quad (2)$$

3. Then, select the surface process $\alpha \rightarrow \alpha'$ that fulfils the following condition,

$$\sum_{\beta<\alpha'-1} r_{\alpha\beta} < \rho_1 \cdot r_{tot(\alpha)} \leq \sum_{\beta<\alpha'} r_{\alpha\beta} \quad (3)$$

where ρ_1 is a random number generated from a uniform distribution on the unit interval ($\rho_1 \in [0,1]$) and both summations represent the cumulative distribution functions of the reaction rates ($r_{\alpha\beta}$ is the discrete random variable), being their values for surface processes $\alpha \rightarrow \alpha'-1$ ($R_{\alpha,\alpha'-1}$) and $\alpha \rightarrow \alpha'$ ($R_{\alpha,\alpha'}$), respectively.

4. Advance the time, using a second random number

$$t \rightarrow t - \frac{\ln(\rho_2)}{r_{tot(\alpha)}} \quad (4)$$

5. Update the system to the new surface configuration α′ (i.e., adding, moving or removing adsorbed species on the lattice), make the new list of all possible surface processes ($N_{p(\alpha')}$) and repeat again the cycle from step 2).

Typically, every kMC simulation will involve a huge number of steps (i.e., 10^8–10^{11}) until the system achieves a steady-state [i.e., temporal convergence of coverages (θ) and turnover frequencies (TOF), sometimes also called turnover rates (TOR)]. Temporal acceleration of kMC simulations to overcome the problem of the large differences in the time scales of surface processes can be carried out using more refined algorithms.[6–8]] Additional simple techniques can also be considered to reduce the kMC computational cost, as for instance, the use of scaling factors in reaction rates for the very fast processes (e.g., diffusion rates[9,10]) or beginning the kMC simulation from a lattice with an initial coverage obtained from a MM solution.

The reaction rates of the different surface processes ($r_{\alpha\beta}$), which are defined as the number of times a process occurs per site and time unit, can be computed by means of collision theory (CT) and/or the transition state theory (TST).[2,4] For LH reactive processes, desorption processes and atomic or molecular diffusion processes the reaction rates can be calculated using the canonical TST formula

$$r = \frac{k_B \cdot T}{h} \frac{Q^{\neq}}{Q^R} e^{-\frac{\Delta V^{0\neq}}{k_B \cdot T}} \quad (5)$$

where h denotes Planck's constant, k_B the Boltzmann's constant, and $Q^{\neq}$ and Q^R are the partition functions (dimensionless) of the transition state (TS) and the reactants, respectively, which are calculated from standard statistical mechanical expressions.[11] $\Delta V^{0\neq}$ represents the energy barrier of the surface process, including the zero-point energy (ZPE) correction. In some works, the term of activation energy (E_a) is inadequately used for labeling $\Delta V^{\neq}$or $\Delta V^{0\neq}$ values. This term should be kept for one of the parameters derived from the empirical Arrhenius equation (the other is the pre-exponential factor, A), which explain the temperature dependence of many reaction rates.[2]

The rate of adsorption (nondissociative) processes can be estimated using the Hertz–Knudsen equation, Equation 6

$$r_{ad} = S_0(T) \cdot A_{site} \cdot \frac{P}{\sqrt{2\pi\ m\ k_B T}} \quad (6)$$

where S_0 is the initial sticking coefficient, A_{site} corresponds to the area of a single site, P is the gas partial pressure, and m is the molecular mass of the gas species.

The rate of desorption processes, where $\Delta V^{0\neq} = \Delta V_R^0$ (the reaction endothermicity or adsorption energy) can be determined from TST, assuming an early 2D gas-like TS, Equations 7 and 8,

$$r_{des} = \frac{k_B \cdot T}{h} \frac{Q_{vib}^{gas} \cdot Q_{rot}^{gas} \cdot Q_{trans,2D}^{gas}}{Q_{vib}^{R}} e^{-\frac{\Delta V^{0\neq}}{k_B \cdot T}} \tag{7}$$

$$Q_{trans,2D}^{gas} = A_{site} \cdot \frac{2\pi\ mk_B T}{h^2} \tag{8}$$

where Q_i^{gas} are the different contributions to the partition function of the gas species, Q_{vib}^{R} represents the partition function (i.e., vibrational term) of the adsorbed species and A_{site} corresponds to the area of a single site.

The energy barriers and the vibrational frequencies of minima and transition states are normally calculated from first-principles using DFT calculations[1,12] although the choice of the DFT method requires some caution and, whenever possible, calibration by comparison to available accurate experimental data. Moreover, additional DFT calculations are necessary to introduce also the adsorbate–adsorbate lateral interactions for all reactant and product pairs (*vide infra*), which may affect the values of the energy barriers of the surface processes (i.e., coverage-dependent energy barriers) and hence, their reaction rates, becoming especially important for high coverage situations.

Note also that kMC method applied to the study of heterogeneously catalysed gas-phase reactions is not limited only to flat crystal surfaces; it can also be used for simulating complex systems such as surface reactions on supported nanoparticles exhibiting different facets.[13]

2.2 | Microkinetic modeling

Kinetic models can be used for the study of many complex reactions (e.g., gas-phase, solution-phase or gas-surface processes), including also the transport phenomena when they are relevant (i.e., diffusivity, viscosity, and heat conduction). These models afford treating several kinds of experimental reactor models.[14] When dealing with the reaction kinetics on pore or crystalline solid surfaces, simpler microkinetic models can be used in a similar way as it was explained before for kMC simulations.[15,16] In this case, macroscopic rate equations (Equation 9) are applied to describe all surface processes involved in the proposed reaction model, usually within the mean-field approximation, in which it is assumed that the adsorbates are uncorrelated,

$$\left(\frac{d\theta_i}{dt} = \sum_j \nu_{ij}\ r_j f_j(\theta_1, \ldots, \theta_N)\right)_{i=1,N} \tag{9}$$

where θ_i is the surface coverage of *i* species at time *t* (among the all *N* possible adsorbates), ν_{ij} is the stoichiometric number for *i* species in *j* surface process (positive or negative for species formation or removal, respectively), r_j the reaction rate, and f_j is a function of several coverages involved in the *j* surface process; the summation covers all possible surface processes where the i species is involved. Frequently, these equations are expressed using rate constants (k_j), which are easily related with reaction rates (r_j). DFT data along with TST and CT can be applied to determine the reaction rates from first-principles as already explained for kMC simulations. However, sometimes they can be used as fitting parameters together with some available values of experimental rate constants aiming to reproduce the observed experimental global reaction kinetics data, assuming a reasonable reaction mechanism. Clearly, such empirical fitting hinders a validation of the proposed mechanism.

The set of coupled differential equations are numerically integrated until steady-state values of coverages and TOFs are achieved. Apparent activation energies (E_a^{ap}) and partial reaction orders (α_i) can also be derived from the values of total reaction rates using either the net overall reaction rate r_{net} (the forward minus the reverse reaction rate) or the forward reaction rate r_f,

$$E_a^{ap} = k_b T^2 \cdot \left(\frac{\partial \ln (r_f)}{\partial T}\right)_P \tag{10}$$

$$\alpha_i = \left(\frac{\partial \ln (r_f)}{\partial \ln [i]}\right)_P \tag{11}$$

that also can be calculated in kMC simulations in a similar way, and compared later with experimental values.

2.3 | kMC vs. MM studies

The simplest possible comparison between kMC and MM methods for a given complex gas-surface reaction involves assuming the same gas model, lattice model and reaction model (i.e., the same number of surface processes including also diffusion). kMC gives a stochastic solution of the ME whereas MM provides a deterministic solution of the differential rate equations (Equation 9). However, a first difference arises from the assumption of uniform coverages in mean-field MM, while kMC simulations reveal the existence of structures or ordered adlayers even at high temperatures. Moreover, kMC and MM predicted TOFs and final average coverages are usually different.[4] For instance, compared to similar kMC simulations, mean-field models can overestimate the catalytic activity by several orders of magnitude as shown in the case of CO methanation on stepped transition metal surfaces.[6] This is the case even when lateral interactions are neglected in both methods.

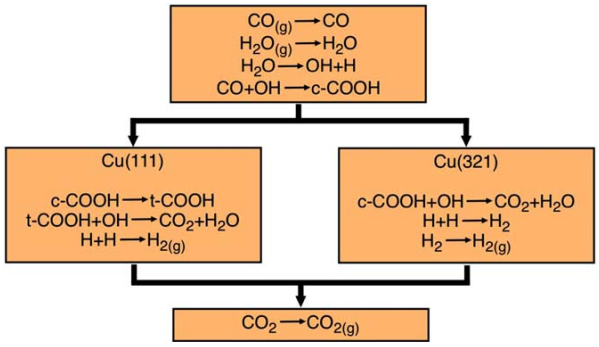

FIGURE 1 Simplified reaction model of the WGSR with an associative mechanism on Cu(111) and Cu(321) surfaces. Note that forward and backward reactions have to be taken into account. Cis- and trans-COOH species are shown

In general, a considerable number of early published mean-field MM studies disregards lateral interactions,[17–20] which are very important for the overall reaction as kMC studies show. However, MM beyond the mean-field approximation have been successfully applied for methane oxidation over PdO(101), subdividing the relevant adsorbates into "paired" and "unpaired" species,[16] obtaining a good agreement with a range of experimental findings. To include these lateral interactions, the coverage dependence of the energy barriers of the surface processes is also included in some recent MM studies as in the case of ethylene hydrogenation over transition metal surfaces.[21]

From a practical point of view, kMC simulations have a larger computational cost than for corresponding MM simulations applied to the study of catalytic heterogeneous reactions based on first-principles DFT data. However, this is a fraction of the computational cost required to obtain the CT and TST rates and, on the other hand, kMC method allows an easier and deeper introduction of complex lattice models including for instance explicit or grouped kinds of sites, monodentate or bidentate-adsorbed species, diffusion processes and lateral interactions than using MM methods.

Finally, a direct comparison of kMC and MM simulations about the time evolution of the surface reactions is not appropriate. In spite of using the same reaction rates which in fact represent thermally averaged values, the stochastic kMC time evolution of the rejection-free algorithm is governed by Equation 4. Hence, the step-time to advance the clock is independent of the process which is chosen.[5] For instance, for a selected surface process $\alpha \rightarrow \alpha'$ compare $1/r_{tot(\alpha)}$ and $1/r_{\alpha\alpha'}$ which are different from the deterministic time propagation followed in MM simulations (Equation 9). Finally, it is worth pointing out that neither kMC nor MM match the real-time evolution of the experimental surface reactions, being the experimental and theoretical comparisons made mainly through the final steady-state properties such as TOFs, coverages, degrees of rate control, among others.

3 | DISCUSSION OF SOME TOPICS RELATED WITH KMC AND MM STUDIES

3.1 | Water gas shift reaction as an example

In order to illustrate and discuss several topics that appear in both kMC and MM kinetic studies of complex gas-surface reactions, we have selected as an example the water gas shift reaction (WGSR) on the flat Cu(111)[10] and on the stepped Cu(321)[22] surfaces, that have recently studied by means of kMC simulations.

Two general reaction mechanisms have been proposed for the WGSR on metal-based catalysts, both starting with water dissociation. Next, in the so called redox mechanism, carbon dioxide is formed by direct reaction between adsorbed CO and O, whereas the so called associative mechanism is based on the formation of a carboxyl intermediate (see Figure 1). The associative mechanism has been found to be the most important in both surfaces[10,22–24] and has been selected in the present study for the construction of several minimum energy diagrams and to better explain the issues discussed below. Nevertheless, all kMC simulations were performed including both mechanisms in the reaction model. A complete list of all surfaces processes can be found in previous works.[10,22] In the case of the Cu(111) surface, all terrace sites were considered equivalent, and only pairwise additive lateral interactions between neighboring CO adsorbates were included. Moreover, diffusion processes for the most mobile species (essentially CO, H_2O, OH and O) were added into the reaction model. On the other hand, in the study of the Cu(321) surface, different types of sites were distinguished, and pairwise interactions for all possible reactant and product pairs were included using a cluster expansion model.[25,26] Additionally, diffusion processes for H_2O, OH, and O species were included as in the case of the Cu(111) surface. All kMC calculations have been carried out by means of ZACROS code,[25,27] although some of them used also an in-house developed C^{++} code.

3.2 | Construction and use of several kinds minimum energy diagrams

DFT-based calculations carried out on suitable periodic surfaces, complemented by statistical thermodynamics, is currently the main tool to investigate heterogeneously catalysed reactions at the molecular level.[1,12] These constitute a necessary previous stage to kMC or MM studies. This

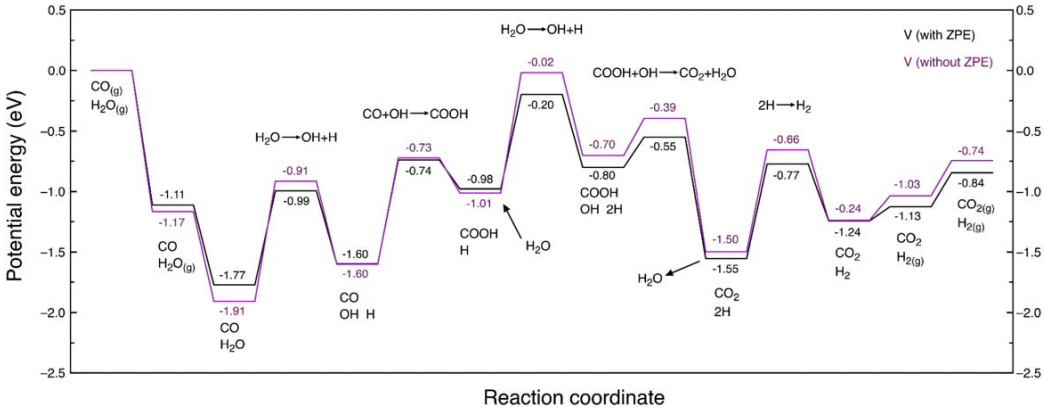

FIGURE 2 Simplified PEDs for the associative mechanism of the WGSR on Cu(321) with (black) and without (violet) the ZPE correction. The energy barriers are calculated for reactant species at infinite separation

computational framework allowed us to calculate accurate minimum energy diagrams for many complex processes involving several elementary steps with detailed information about transition states and stable intermediate species. From the minimum energy profiles the equivalent pictures for Gibbs free energies can be obtained, which summarize the proposed reaction model or the main reaction mechanisms observed in kMC or MM studies. Nevertheless, the construction, the use and the interpretation of these energy diagrams needs to be handled with caution.

Minimum energy diagrams based on DFT calculated total energies lead to potential energy diagram (PED). These, should include the ZPE correction and provide a first view of a given reaction mechanism. ZPE can be calculated for a harmonic oscillator model as a sum of contribution from all vibrational modes. Low frequencies ($< 500\ cm^{-1}$) do not contribute to ZPE, while high frequencies can contribute with several tenths of eV.[1] This trend is opposite to that of the frequency contribution to the entropy, as discussed later. ZPE correction is especially important in surface reactions involving H atoms, like water dissociation or hydrogenation reactions, because the atom-H stretching frequencies are typically between 3000 and 4000 cm^{-1}. Figure 2 shows the effect of the inclusion of the ZPE correction on the PED for the WGSR on Cu(321) (associative mechanism). Small differences of up to 0.22 eV can be observed in some energy barriers (i.e., water dissociation), which have large effects on the corresponding reaction rates. For instance, the reaction rate corresponding to the water dissociation at 625 K including ZPE is $1.5{\cdot}10^6\ s^{-1}$, whereas the value without ZPE is only $2.5{\cdot}10^4\ s^{-1}$, 60 times smaller! Therefore, ZPE should always be included in all energy barriers (i.e., $\Delta V^{0\neq}$) used for reaction rate calculations (e.g., in Equations 5 and 7).

The commonly generalized gradient approximation (GGA) functionals widely used in past years neglect dispersion terms, which may play an important role in chemical and physical processes. Dispersion interactions largely affect the adsorption properties of molecules at surfaces,[28] and can be the dominant term as in the case of aromatic molecules interacting with the basal plane of MoS_2,[29] graphene on metallic surfaces[30] or hydrocarbons interacting with zeolites.[31] Even if the process being studied involves small size species such as, CO or CO_2 only, the contribution of dispersion interactions to the overall energy may be important and should not be ignored. In a previous study on the effect of vdW interactions in the WGSR on Cu(321) using the PBE-D2 approach,[32] it has been shown that the dispersion contribution is different for reactants, intermediates, and products, with a clear net effect and with no compensation of errors. These terms affect adsorption structures and adsorption energies but also the overall PED, producing tremendous changes in the predicted reaction rates. For instance, the calculated binding energy of CO_2 on Cu(321) surface is increased from 0.06 to 0.28 eV when vdW corrections are included (i.e., at PBE-D2 DFT level), resulting in a desorption reaction rate 60 times smaller (at $T = 625$ K). Another example is the energy barrier associated to the carboxyl disproportionation by hydroxyl (i.e., $COOH + OH \rightarrow CO_2 + H_2O$) for the same system, which decreases from 0.55 to 0.33 eV when dispersion forces are included, resulting in an increase of a factor of also 60 in the reaction rate (at $T = 625$ K). Consequently, dispersion terms should be always included when aiming at obtaining reliable information to be used in MM or kMC approaches. Fortunately, most of the often-used codes include the contribution of dispersion terms even the choice of the appropriate methods is still a matter of debate.[33] Here, is important that recent experiments for energies of formation reactions measured from accurate microcalorimetry techniques constitute an invaluable dataset to benchmark the different available methods.[34]

PEDs are good tools to have an overview of the different elementary reaction steps in a complex surface reaction such as the WGSR. However, for processes involving large shifts in entropy (e.g., adsorption and desorption), they often fail to make even qualitative predictions. Gibbs free energy diagrams are more useful for making such predictions (e.g., the most favorable mechanisms, accurate reaction rates), because they take into account the effects of pressure and temperature. Figure 3 shows the Gibbs free energy diagram for the associative mechanism of the WGSR on Cu (321). The process is even exothermic at temperatures as high as 625 K but becomes about thermoneutral at 1000 K and endothermic at even higher temperatures. The PED and the Gibbs free energy diagrams are very different, mainly regarding the adsorption and desorption processes. This is because in for molecules in the gas phase, the largest fraction of the standard entropy contribution arises from the translation degrees of

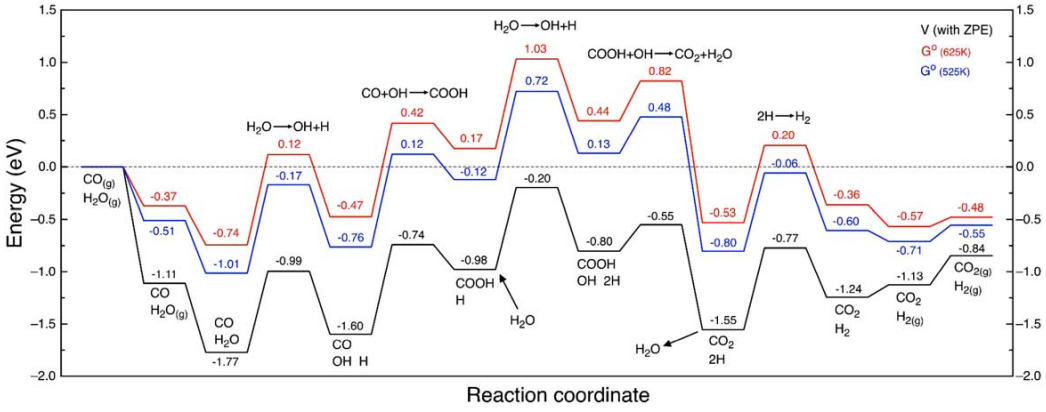

FIGURE 3 Comparison between PED with ZPE (black) and two Gibbs free energy diagrams ($P = 1$ bar, $T = 525$ K, blue and $T = 625$ K, red) for the associative mechanism of the WGSR on Cu(321) surface (adsorbates at infinite separation)

freedom, while the vibrational and rotational parts constitute a minor contribution. For adsorbed species, the translational and rotational degrees of freedom become constrained and turn into vibrational degrees of freedom (i.e., frustrated translational and rotational modes). The Gibbs free energy of adsorption is commonly estimated by an approximate procedure proposed by Nørskov et al.[1] where, in absence of mechanical work, the enthalpy of adsorption is approximated by the corresponding change in the potential energy, the entropy of gas-phase is computed by taking into account all contributions to the partition function with the assumption of rigid rotor and harmonic frequencies, and finally the entropy of adsorbed species can be neglected or computed from the vibrational modes.

However, as in kMC and MM studies the reaction rates need to be calculated for all surface processes, their values can also be used to determine the standard free energies of activation for each surface process ($\Delta G^{0\neq}$), using the thermodynamic formulation of TST expression (Equation 12),

$$r(T) = \frac{k_B \cdot T}{h} e^{-\frac{\Delta G^{0\neq}(T)}{k_B \cdot T}} \tag{12}$$

The standard free energies of reaction for each surface process (ΔG^0) can be obtained using the rates of forward and reverse processes and the detailed balance principle,[35] Equation 13,

$$\frac{r_{\text{forward}}(T)}{r_{\text{reverse}}(T)} = e^{-\frac{\Delta G^{0}(T)}{k_B \cdot T}} \tag{13}$$

From Equations 5 and 12 one can derive a simple relationship between $\Delta G^{0\neq}$ and $\Delta V^{0\neq}$, Equation 14,

$$\Delta G^{0\neq} = \Delta V^{0\neq} - k_B \; T \; \ln\left(\frac{Q^{\neq}}{Q_R}\right) \tag{14}$$

The contribution to the partition functions (i.e., $Q^{\neq}$ and Q^R) for a given vibrational mode (q_i) is large for low vibrational frequencies, and vice-versa, contrary to what happened with the ZPE correction to the energy barrier. Vibrational frequencies larger than 1000 cm^{-1} have a negligible contribution to the total partition function (i.e., $q_i \approx 1$), while frequencies below 50 cm^{-1} give significant contributions to Q (i.e., $q_i > 10$). In the free energy diagrams shown in many published works, it is commonly assumed that the entropy contributions of adsorbed species are zero,[36] which means that for a given surface process $Q^{\neq}/Q_R \approx 1$ and hence $\Delta V^{0\neq} \approx \Delta G^{0\neq}$ as derived from Equation 4. However, this usual assumption may not be valid in surface processes involving more than four atoms (with a large number of low vibrational modes) or at high temperatures. In the WGSR example at $T = 625$ K, most of the elementary steps satisfy that $|\Delta V^{0\neq} - \Delta G^{0\neq}| < 0.10$ eV, but for certain processes $|\Delta V^{0\neq} - \Delta G^{0\neq}|$ is very large (e.g., for $CO_2 + H_2O \rightarrow COOH + OH$, being ≈ 0.35 eV), as shown in Table 1, and it can no longer be assumed that $\Delta V^0 \approx \Delta G^0$. This also holds for adsorption and desorption processes.

Another feature observed when looking in detail at minimum energy diagrams is that sometimes the ΔG^0 or ΔV (with ZPE) values reported for the overall reaction are different from the DFT values computed directly from gas-phase species (i.e., using only reactants and products). For instance, in the PED of Figure 3 one can see that for WGSR on Cu(321) the value of ΔV is -0.84 eV whereas a value of -0.80 eV is obtained from DFT gas-phase calculations. The differences in ΔG^0 are even larger (e.g., at 525 K, compare -0.55 eV (Figure 3) against -0.48 eV (Table 2) at PBE level). For other systems, these differences can reach up to several tenths of eV. Clearly, this comparison between gas phase and through the surface calculated thermodynamic values has to be investigated and for large discrepancies further studies are require finding out their origin and to minimize them. A possible reason for this disagreement is that adsorbed species may react from several adsorption sites (i.e., top, bridge, hollow, etc.), and the binding energy at each site is really

TABLE 1 Values of $|\Delta V^{0\neq} - \Delta G^{0\neq}|$ (eV) and $Q^{\neq}/Q_R$ for different elementary surface processes of the WGSR on Cu(321) at 625 K

	$\lvert\Delta V^{0\neq} - \Delta G^{0\neq}\rvert$ (eV)		$Q^{\neq}/Q_R$	
Surface process	Forward	Reverse	Forward	Reverse
$H_2O \rightarrow OH+H$	0.08	0.01	0.22	1.26
$2OH \rightarrow H_2O+H$	0.06	0.09	0.34	0.18
$CO+O \rightarrow CO_2$	0.09	0.28	0.17	< 0.01
$CO+OH \rightarrow COOH$	0.04	0.01	0.51	0.87
$COOH+OH \rightarrow CO_2+H_2O$	0.13	0.35	0.09	< 0.01
$H+H \rightarrow H_2$	0.05	0.10	2.33	0.16

different. Diffusion processes are often not included in minimum energy diagrams, leading to an inaccurate value of ΔV for the overall reaction. Another reason is that occasionally these energy diagrams are constructed from energy barriers for coadsorbed reactants and products, instead of using the energy barriers at infinite separation on the slab. Finally, in DFT calculations only the slab and the reactant species for a given step are included, while spectator species are missing. This implies a lack of consistency in the energy calculations simply because the unit cells are different. In the case of using a plane wave basis set this implies a different number of plane waves for the same kinetic energy cut-off whereas in the case of using atomic like basis sets such as Gaussian type orbitals or numerical orbitals one faces the problem of basis set superposition error. Ideally, a much more accurate calculation including all possible reaction intermediates is possible but this would require the use of very large supercells, with a concomitant unaffordable increase in the computationally cost.

Finally, it is worth pointing out that a comparison between theoretical and available experimental ΔG^0 values, especially for the overall reaction, can and should be done to check even more the quality of the DFT data, which may slightly affect the PED but largely affect the final kMC or MM results. Most often, commonly used GGA type functionals are accurate enough to provide physically meaningful results. Table 2 compares the experimental values of the equilibrium constants (K_{eq}) and ΔG°[37] for the WGSR at two temperatures (525 and 625 K) with some calculations carried out by means of GAUSSIAN code,[38] using different quantum chemistry methods. Despite being the most used functionals for metallic systems, both PW91 and PBE poorly describe the thermochemistry of WGSR, although the agreement with experiment is better at higher temperature. Even the broadly used B3LYP functional,[39,40] which was designed precisely to improve the thermochemistry of gas-phase molecules[41]; reports an equilibrium constant which is around 45 times larger than the experimental value at 625 K. Only the golden standard Coupled Cluster CCSD(T) method exhibits a pretty good agreement, though not perfect, with experiment.

At this point, one may argue that results obtained from DFT calculations of reactions taking place at metallic surfaces are doubtful. However, this claim is incorrect because, unlike for gas-phase chemistry, when a reaction takes place above a metallic surface the electrons in the reacting species are largely screened by the electrons in the conduction band and, in addition, constitute a fraction of the total number of electrons. This is an important remark since it is well-established that both PBE and PW91 GGA type functionals provide a very good description of the metal properties,[42–44] while hybrid functionals, describing better the thermochemistry in gas-phase, fail[45,46] because of the failure to attain the exact homogeneous electron gas limit.[47] The large body of literature showing good agreement between DFT calculations at the GGA level with experimental values for adsorption and reaction energies[21,22] supports this view, and it is reinforced by the evidence that the transition states for reactions catalysed by non-magnetic metals do not evidence any spin polarization.[48] Moreover, note that most of the available kMC studies correspond to open systems in a nonequilibrium state. Thus, even if the calculated results for reaction rates and related properties are by no means exact, it is very likely that the overall physical description is correct.

TABLE 2 Comparison between experimental data and calculated values of the equilibrium constant (K_{eq}) and ΔG° of the overall WGSR, using an aug-cc-pVTZ basis set with different DFT functionals and the post-HF CCSD(T) method

T (K)	ΔG° 525 K	ΔG° 625 K	K_{eq} 525 K	K_{eq} 625 K
PBE	−0.48	−0.41	41 627	1905
PW91	−0.48	−0.41	43 079	2046
B3LYP	−0.40	−0.36	7561	877
CCSD(T)	−0.12	−0.07	13	4
exp.[37]	−0.20	−0.16	80	20

TABLE 3 Calculated turnover frequency and coverages of several adsorbates for the WGSR on Cu(111) with and without including diffusion processes

		coverage			
	TOF (molec.·s^{-1}·$site^{-1}$)	CO	H_2O	OH	H
Diffusion	7826	$2.7{\cdot}10^{-4}$	$1.2{\cdot}10^{-2}$	$1.8{\cdot}10^{-1}$	$1.3{\cdot}10^{-1}$
No diffusion	6391	$2.3{\cdot}10^{-4}$	$1.1{\cdot}10^{-2}$	$2.7{\cdot}10^{-1}$	$1.6{\cdot}10^{-1}$

kMC simulation conditions: $T = 625$ K, $P_{CO} = 26$ Torr, and $P_{H2O} = 10$ Torr.

3.3 | Modeling fast processes

A diffusion (usually fast) process can be represented as a hopping of an adsorbate from one site to a neighboring one on the lattice model. Although sometimes ignored,[49] it is important to include diffusion steps of the mobile species into the reaction model since diffusion controlled processes cannot be discarded beforehand. When various site types are distinguished in the lattice model, ignoring diffusion processes can have as a consequence that important intermediate species are not formed during the simulation. For instance, in the kMC model of the WGSR on the stepped Cu (321) surface, OH species are produced from water dissociation on bridge sites, but they must migrate to hollow sites to react with CO species in order to produce the COOH species. On the other hand, in the kMC study of the WGSR on the flat Cu(111) surface, all adsorption sites were considered equivalent (i.e., all sites are labeled as terrace sites). However, in spite of product molecules can be formed without including diffusion in the reaction model for this simple lattice model, calculated values of TOFs and coverages (Table 3) are different enough from the values obtained when including diffusion processes.

The vast majority of complex heterogeneous reactions contain processes with very dissimilar reaction rates. The slowest surface processes are commonly chemical reaction processes with high energy barriers of up to 2 eV. On the other hand, the fastest ones are usually diffusion processes with energy barriers of only a few hundredths of eV and quite often adsorption/desorption processes can be also very fast. At a temperature of 625 K a slow surface process with an energy barrier of 1.6 eV will have a reaction rate of around 1 s^{-1}, while the reaction rate for a fast diffusion process with an energy barrier of only 0.05 eV will be around 10^{12} s^{-1}, implying that along the kMC simulation the diffusion will dominate and extremely long simulation are required to observe some evolution of the overall chemical process. Some solutions to improve the performance of kMC simulations were mentioned in section 2.1. For instance, a reduction by some constant factor of the reaction rates of these fast processes has been successfully applied in many kMC studies,[9,10,22,50] but not all fast processes can be correctly scaled. Another alternative but equivalent solution is to increase all the energy barriers of these processes by the same amount.[20]

Chatterjee and Voter developed a temporal acceleration scheme by automatically modifying the reaction rates of fast processes without the need for the user to specify these processes in advance. In this method, called Accelerated Superbasin Kinetic Monte Carlo (AS-KMC), the algorithm keeps track of how often configurations are revisited. When this occurs too often one has an indication of the system being stuck in a set of configurations connected by fast processes (i.e., the superbasin). The reaction rates of these processes are then decreased. This procedure may be repeated until the fast processes are slowed down enough so as escape from the superbasin finally occurs. However, the fact that AS-KMC identifies processes based on the configuration of the entire system is likely to make it not efficient enough for complex reaction models such as, WGSR or Fischer–Tropsch synthesis where an enormous number of possible configurations needs to be considered. This latter problem was addressed in the recently developed algorithm by Dybeck et al.,[8] where the acceleration is accomplished by reducing the reaction rates of the fast-quasi-equilibrated processes to enable more frequent execution of the slower reactive surface processes. The main improvement is that the partitioning and the scaling is applied to all of the processes in a given reaction channel rather than to the individual processes as done in the Voter scheme. This method has been successfully applied to model the Fischer–Tropsch synthesis reaction over ruthenium. However, the procedure may not be optimum since Andersen et al. used this algorithm to model the CO methanation on stepped transition metal surfaces finding poor accuracy in certain situations.[6]

3.4 | Coadsorption and lateral interactions

A physically meaningful representation of the description of the kinetics of complex surface reactions requires a quantitative account of the lateral interactions between coadsorbed species. Figure 4 shows the PED for a bimolecular surface reaction $A + B \rightarrow C + D$ at zero-coverage limit, this is in a situation where only reactants or products and no spectator species are present at the surface. These interactions can be attractive or repulsive for either reactants or products as shown in Figure 4. At low temperature, these interactions can lead to any correlation in the occupation of neighboring sites or even result in island formation or ordered adlayers. Only at very high temperatures they will become negligible, which is where mean field approximation is valid and MM simulations meaningful.

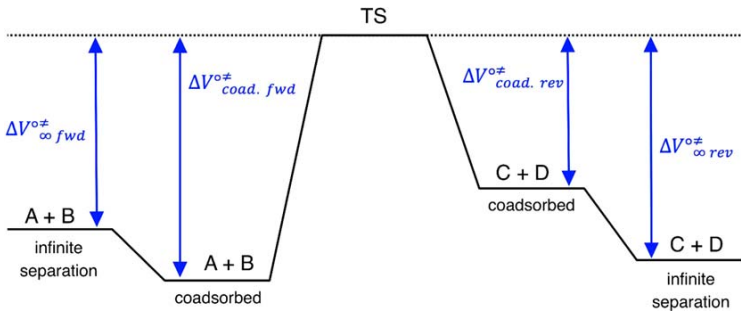

FIGURE 4 Potential energy profile for a bimolecular surface reaction A + B → C + D at zero-coverage limit

Lateral interactions in small systems are commonly described with a cluster expansion model.[25,26,51] This expansion can be made so as to reproduce both the energy profile for reactants at infinite separation and for coadsorbed states (Figure 4) for all the elementary steps. Moreover, energy barriers at a given coverage can be parameterized relying on Brønsted–Evans–Polanyi (BEP) relationships.[52,53] As an example, consider the COOH → CO + OH step of the WGSR on Cu(321).[22] The energy barrier value used for the calculation of the reaction rate is 0.24 eV, without any neighboring adsorbates (i.e., zero-coverage limit). However, the presence of other adsorbed molecules can increase the value of the energy barrier of this step up to 0.30 eV, depending on the new lateral interactions that could appear if this process was executed in kMC simulations. Table 4 shows the significant effect of the lateral interactions between coadsorbed species in the kMC calculations for the WGSR on Cu(321)[22] even at low pressures and high temperature, where these effects should be lesser.

Due to the high number of species and site types present in complex reaction mechanisms (e.g., in WGSR), it is impossible to obtain a complete data set of DFT energies for all possible lateral interactions, which could appear through the reaction (i.e., at high coverages). Thus, kMC models for such complex systems typically employ simpler models for the adlayer energetics. One possibility is then to truncate the cluster expansion to one-body terms and pairwise interactions only for all possible reactant and product pairs, as done in Ref. [22]. Fortunately, many lateral interactions are small enough and a cheaper although less accurate choice is to use the energy barriers at infinite separation and to include only the most important lateral interactions between nearest neighbors, assuming that those lateral interactions are pairwise additive; this was the choice in Refs. [9].

3.5 | Quality of reaction rates

The accuracy of the reaction rates used in MM and kMC calculations completely determines the quality of the final results of these simulations. Usually rates are obtained from canonical TST and CT. Most likely, variational TST (VTST)[2] would be more appropriate, as shown for gas-phase reactions when comparing calculated to experimental data.[54] However, VTST requires a significantly large set of DFT data including many configurations along the minimum energy path between the transition state (TS) and reactants and products. Hence, it has seldom used in this kind of studies. Additionally, for surface processes involving light atom/molecule transfers, a one-dimensional tunnelling correction factor in the reaction rates can be introduced, for instance assuming an Eckart barrier.[10]

As mentioned above, the use of TST implies obtaining the necessary DFT data of the adsorbed reactants and products and TSs which implies not only structural data but energy barrier and vibrational frequencies as well which are needed to apply Equation 5.

The calculation of TST reaction rates (Equation 5) needs DFT data (i.e., geometry, energy and vibrational frequencies) for reactants and TSs. Unfortunately, most of the published works describing the main elementary surface processes of a given complex reaction at a DFT level report only the largest vibrational frequencies of the stationary points (i.e., minima and TS).[23,52,55,56] Neglecting the lowest frequencies has almost no effect on the PED of the reaction, but it can lead to large errors in the Gibbs free energy diagrams and in the calculation of the reaction rates, as discussed above. Figure 5 shows the effect of neglecting the frequencies below 500 cm^{-1} on the Gibbs free energy diagram for the WGSR on Cu (321). The most drastic changes are found in the adsorption and desorption processes, due to the underestimated value of Q_R, resulting in an erroneously high value of r_{des}.

TABLE 4 Calculated turnover frequencies and coverages of several adsorbates for the WGSR on Cu(321) with and without including lateral interactions in kMC simulations for $T = 625$ K, $P_{CO} = 26$ Torr, and $P_{H2O} = 10$ Torr

		Coverage			
	TOF (molec.·s^{-1}·$site^{-1}$)	CO	H_2O	OH	H
Lateral int.	199	$1.3{\cdot}10^{-1}$	$7.3{\cdot}10^{-2}$	$2.1{\cdot}10^{-1}$	$3.6{\cdot}10^{-2}$
No lateral int.	130	$1.6{\cdot}10^{-1}$	$5.1{\cdot}10^{-2}$	$2.8{\cdot}10^{-1}$	$4.9{\cdot}10^{-2}$

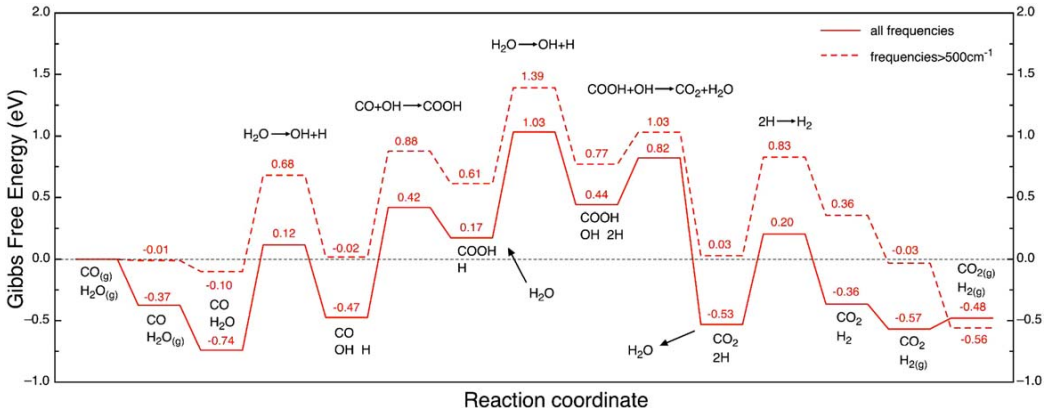

FIGURE 5 Gibbs free energy diagrams for the associative mechanism of the WGSR on Cu(321) ($P = 1$ bar, $T = 625$ K). The correct profile computed using all the vibrational frequencies is plotted in solid line, whereas the same profile neglecting the frequencies below 500 cm^{-1} is plotted in dashed line

3.6 | Proposal of plausible mechanisms and catalysts

Compared to PED profiles, Gibbs free energy diagrams provide a more detailed picture of the overall surface reaction network. Both diagrams should be used to unravel the underlying molecular mechanism although with the necessary caution when aiming to make predictions regarding the performance of a given catalyst for a given complex gas-surface reaction. Establishing a ranking of plausible reaction mechanisms and the most efficient catalysts based only on the values of energy barriers of some forward processes [e.g., the rate-determining steps (RDSs)] is not always fully justified although this is often the choice in many studies.[57–59] Very low energy barriers for reverse processes can greatly hinder reactivity, even if the forward energy barrier is affordable. Moreover, the RDSs may change from one catalyst to another, or even simply by changing the temperature or the reactants partial pressures, and these steps may not coincide with the processes having the highest energy barriers in the energy diagrams.[22] For instance, consider again the WGSR on Cu-based catalysts. It is commonly accepted that the initial water dissociation is the RDS on pure metal surfaces.[57] The forward energy barrier for this process on the stepped Cu(321) surface is 0.78 eV,[22] lower than the 1.01 eV energy barrier for the flat Cu(111) surface.[10] Thus, one may assume that the stepped surface is more efficient than the flat surface. However, the values for the energy barrier of its reverse process are 0.60 eV and 1.15 eV for the stepped and the flat surface, respectively, making the Cu(111) surface more suitable for WGSR, as found by computing the H_2 TOF. Moreover, inspection of the RDSs using a combination of kMC simulations and Campbell's degree of rate control[60,61] shows that CO_2 formation by carboxyl intermediate is really more limiting than water dissociation in all temperature and pressure range studied for the WGSR on Cu(321).[22]

Therefore, to draw any reliable conclusion on the overall complex reaction, apart from the construction and the previous examination of the mentioned minimum energy diagrams, it is also necessary including the contribution of all reverse processes together with the concentrations of all adsorbed species (or their coverages). Thus, kMC or MM methods along with reliable determination of RDSs are the appropriate methods to obtain a detailed information of the time evolution of complex heterogeneously catalysed reactions catalysis.

4 | CONCLUDING REMARKS

In the present work, kinetic Monte Carlo and microkinetic modeling methods applied to the study of the heterogeneous catalysis using first-principles data based mainly on density functional theory are critically reviewed yet details on both methods are given, which also could serve as a short tutorial for beginners in this area. Several important issues that need to be taken into account appear usually in kMC and MM kinetic studies of complex gas-surface reactions are highlighted. To illustrate the discussions, we rely on recent work on the water gas shift reaction on the flat Cu (111) surface and on the stepped Cu(321) surface. Several additional kMC calculations were also carried out to better support our conclusions.

The effect in kMC and MM studies of the inclusion of dispersion energies in the DFT calculations, of the inclusion of diffusion processes into the reaction model or of the addition of adsorbate-adsorbate lateral interactions has been analysed in detail. Moreover, the accuracy of calculated reaction rates, with a noteworthy effect in the final results, is also examined.

A throughout description regarding the construction, use and interpretation of minimum potential energy and minimum Gibs free energy diagrams is presented. The results of kMC simulations show that extracting reliable conclusions on the overall complex reaction based on these diagrams, specially using PEDs, only may lead to misleading conclusions. A meaningful simulation requires also including the contribution of all reverse processes together with the concentrations of all adsorbed species. Hence, kMC or MM methods should be applied to correctly treat complex reactions with heterogeneous catalysis.

From the overall discussion, it appears that kMC method offers a more detailed picture of the overall process than that arising from MM. In fact, kMC facilitates an easier and deeper introduction of several important features: refined lattice models, diffusion processes, and lateral interactions. However, kMC involves higher computational cost and the need to construct appropriate lattice models, which is far from being automatic. Moreover, more efficient kMC algorithms are needed to better account for surfaces processes with very dissimilar reaction rates.

ACKNOWLEDGMENTS

Financial support to this research has been provided by the Spanish MINECO CTQ2014-53987-R and CTQ2015-64618-R grants and, in part, from the Generalitat de Catalunya grants 2014SGR97, 2014SGR1582 and XRQTC. HPG thanks Generalitat de Catalunya for a predoctoral FI-DGR-2015 grant and FI acknowledges additional support from the 2015 ICREA Academia Award for Excellence in University Research.

ORCID

Francesc Illas http://orcid.org/0000-0003-2104-6123

REFERENCES

[1] J. K. Nørskov, F. Studt, F. Abild-Pedersen, T. Bligaard, *Fundamental Concepts in Heterogeneous Catalysis*, Wiley, Hoboken, New Jersey **2014**.

[2] K. J. Laidler, *Chemical Kinetics*, Harper & Row Publishers, New York **1987**.

[3] V. P. Zhdanov, *Surf. Sci.* **2002**, *500*, 966.

[4] A. P. J. Jansen, *An Introduction to Kinetic Monte Carlo Simulations of Surface Reactions*, *Lecture Notes in Physics*, Vol. *856*, Springer-Verlag, Heidelberg **2012**.

[5] K. Reuter, in *Modeling and Simulation of Heterogeneous Catalytic Reactions* (Ed: O. Deutschmann), Wiley-VCH Verlag GmbH and Co. KGaA, Weinheim, Germany, **2011**, pp. 71–111.

[6] M. Andersen, C. P. Plaisance, K. Reuter, *J. Chem. Phys.* **2017**, *147*, 152705.

[7] A. Chatterjee, A. F. Voter, *J. Chem. Phys.* **2010**, *132*, 194101.

[8] E. C. Dybeck, C. P. Plaisance, M. Neurock, *J. Chem. Theory Comput.* **2017**, *13*, 1525.

[9] L. Yang, A. Karim, J. T. Muckerman, *J. Phys. Chem. C* **2013**, *117*, 3414.

[10] H. Prats, L. Álvarez, F. Illas, R. Sayós, *J. Catal.* **2016**, *333*, 217.

[11] D. A. McQuarrie, *Statistical Mechanics*, Harper & Row, New York **2000**.

[12] L. Grabow, W. Schneider, M. J. Janik, T. Manz, A. van Duin, S. Sinnott, D. Scholl, *Computational Catalysis*, Royal Society of Chemistry Books, Burlington House; London **2013**.

[13] L. Kunz, F. M. Kuhn, O. Deutschmann, *J. Chem. Phys.* **2015**, *143*, 044108.

[14] R. van de Vijver, N. M. Vandewiele, P. L. Bhoorasingh, B. L. Slakman, F. Seyedzadeh Khanshan, H. H. Carstensen, M. F. Reyniers, G. B. Marin, R. H. West, K. M. van Geem, *Int. J. Chem. Kinet.* **2015**, *47*, 199.

[15] V. Morón, P. Gamallo, R. Sayós, *Theor. Chem. Acc.* **2011**, *128*, 683.

[16] M. Van den Bossche, H. Grönbeck, *J. Am. Chem. Soc.* **2015**, *137*, 12035.

[17] C. Callaghan, I. Fishtik, R. Datta, M. Carpenter, M. Chmielewski, A. Lugo, *Surf. Sci.* **2003**, *541*, 21.

[18] N. A. Koryabkina, A. A. Phatak, W. F. Ruettinger, R. J. Farrauto, F. H. Ribeiro, *J. Catal.* **2003**, *217*, 233.

[19] C. V. Ovesen, B. S. Clausen, B. S. Hammershøi, G. Steffensen, T. Askgaard, I. Chorkendorff, J. K. Nørskov, P. B. Rasmussen, P. Stoltze, P. Taylor, *J. Catal.* **1996**, *158*, 170.

[20] M. J. Hoffmann, K. Reuter, *Top. Catal.* **2014**, *57*, 159.

[21] C. J. Heard, C. Hu, M. Skoglundh, D. Creaser, H. Grönbeck, *ACS Catal.* **2016**, *6*, 3277.

[22] H. Prats, P. Gamallo, F. Illas, R. Sayós, *J. Catal.* **2016**, *342*, 75.

[23] A. A. Gokhale, J. A. Dumestic, M. Mavrikakis, *J. Am. Chem. Soc.* **2008**, *130*, 1402.

[24] Q. Tang, Z. Chen, X. He, A theoretical study of the water-gas shift reaction mechanism on Cu(111) model system, *Surf. Sci.* **2009**, *603*, 2138.

[25] J. Nielsen, M. d'Avezac, J. Hetherington, M. Stamatakis, *J. Chem. Phys.* **2013**, *139*, 224706.

[26] M. Stamatakis, D. G. Vlachos, *ACS Catal.* **2012**, *2*, 2648.

[27] M. Stamatakis, D. G. Vlachos, *J. Chem. Phys.* **2011**, *134*, 214115.

[28] J. P. Prates Ramalho, J. R. B. Gomes, F. Illas, *RSC Adv.* **2013**, *3*, 13085.

[29] P. G. Moses, J. J. Mortensen, B. I. Lundqvist, J. K. Nørskov, *J. Chem. Phys.* **2009**, *130*, 104709.

[30] P. Janthon, F. Viñes, S. M. Kozlov, J. Limtrakul, F. Illas, *J. Chem. Phys.* **2013**, *138*, 244701.

[31] B. A. De Moor, M. F. Reyniers, M. Sierka, J. Sauer, G. B. Marin, *J. Phys. Chem. C* **2008**, *112*, 11796.

[32] H. Prats, P. Gamallo, R. Sayós, F. Illas, *Phys. Chem. Chem. Phys.* **2016**, *18*, 2792.

[33] J. Hermann, R. A. DiStasio Jr, A. Tkatchenko, *Chem. Rev.* **2017**, *117*, 4714.

[34] T. L. Silbaugh, C. T. Campbell, *J. Phys. Chem. C* **2016**, *120*, 25161.

[35] K. Reuter, M. Scheffler, *Phys. Rev. B* **2006**, *73*, 045433.

[36] S. Chakrabarty, T. Das, P. Banerjee, R. Thapa, G. P. Das, *Appl. Surf. Sci.* **2017**, *418*, 92.

[37] D. Mendes, A. Mendes, L. M. Madeira, A. Iulianelli, J. M. Sousa, A. Basile, *Asia-Pac. J. Chem. Eng.* **2010**, *5*, 111.

[38] M. J. Frisch, G. W. Trucks, H. B. Schlegel, G. E. Scuseria, M. A. Robb, J. R. Cheeseman, G. Scalmani, V. Barone, B. Mennucci, G. A. Petersson, H. Nakatsuji, M. Caricato, X. Li, H. P. Hratchian, A. F. Izmaylov, J. Bloino, G. Zheng, J. L. Sonnenberg, M. Hada, M. Ehara, K. Toyota, R. Fukuda, J. Hasegawa, M. Ishida, T. Nakajima, Y. Honda, O. Kitao, H. Nakai, T. Vreven, J. A. Montgomery Jr, J. E. Peralta, F. Ogliaro, M. Bearpark, J. J. Heyd, E. Brothers, K. N. Kudin, V. N. Staroverov, R. Kobayashi, J. Normand, K. Raghavachari, A. Rendell, J. C. Burant, S. S. Iyengar, J. Tomasi, M. Cossi, N. Rega, J. M. Millam, M. Klene, J. E. Knox, J. B. Cross, V. Bakken, C. Adamo, J. Jaramillo, R. Gomperts, R. E. Stratmann, O. Yazyev, A. J. Austin, R. Cammi, C. Pomelli, J. W. Ochterski, R. L. Martin, K. Morokuma, V. G. Zakrzewski, G. A. Voth, P. Salvador, J. J. Dannenberg, S. Dapprich, A. D. Daniels, Ö. Farkas, J. B. Foresman, J. V. Ortiz, J. Cioslowski, D. J. Fox, *Gaussian 09*, *Revision D.01*, Gaussian Inc, Wallingford, CT **2013**.

[39] A. D. Becke, *J. Chem. Phys.* **1993**, *98*, 5648.

[40] C Lee, W. Yang, R. G. Parr, *Phys. Rev. B* **1988**, *37*, 785.

[41] S. F. Sousa, P. A. Fernandes, M. J. Ramos, *J. Phys. Chem. A* **2007**, *111*, 10439.

[42] P. Janthon, S. Luo, S. M. Kozlov, F. Viñes, J. Limtrakul, D. G. Truhlar, F. Illas, *J. Chem. Theory Comput.* **2014**, *10*, 3832.

[43] P. Janthon, S. M. Kozlov, F. Viñes, J. Limtrakul, F. Illas, *J. Chem. Theory Comput.* **2013**, *9*, 1631.

[44] A. Notario-Estévez, S. M. Kozlov, F. Viñes, F. Illas, *Chem. Commun.* **2015**, *51*, 5602.

[45] Y. Zhao, D. G. Truhlar, *J. Chem. Phys.* **2006**, *124*, 224105.

[46] N. E. Schultz, Y. Zhao, D. G. Truhlar, *J. Phys. Chem. A* **2005**, *109*, 11127.

[47] J. Paier, M. Marsman, G. Kresse, *J. Chem. Phys.* **2007**, *127*, 024103.

[48] J. L. C. Fajín, M. N. D. S. Cordeiro, J. R. B. Gomes, F. Illas, *J. Chem. Theory Comput.* **2012**, *8*, 1737.

[49] L. Thian, C. Huo, D. Cao, Y. Yang, J. Xu, B. Wu, H. Xiang, Y. Xu, Y. Li, *J. Mol. Struct. THEOCHEM* **2010**, *941*, 30.

[50] S. Piccinin, M. Stamatakis, *ACS Catal.* **2014**, *4*, 2143.

[51] E. Vignola, S. N. Steinmann, B. D. Vandegehuchte, D. Curulla, M. Stamatakis, P. Sautet, *J. Chem. Phys.* **2017**, *147*, 054106.

[52] R. B. Getman, W. F. Schneider, *ChemCatChem.* **2010**, *2*, 1450.

[53] J. K. Nørskov, T. Bligaard, A. Logadottir, S. Bahn, L. B. Hansen, M. Bollinger, H. Bengaard, B. Hammer, Z. Sljivancanin, M. Mavrikakis, Y. Xu, S. Dahl, J. H. Jacobsen, *J. Catal.* **2002**, *209*, 275.

[54] P. Gamallo, M. González, R. Sayós, *J. Chem. Phys.* **2003**, *119*, 2545.

[55] J. L. C. Fajín, M. N. D. S. Codeiro, F. Illas, J. R. B. Gomes, *J. Catal.* **2009**, *268*, 131.

[56] L. C. Grabow, A. A. Gokhale, S. T. Evans, J. A. Dumesic, M. Mavrikakis, *J. Phys. Chem. C.* **2008**, *112*, 4608.

[57] G. Wang, L. Jiang, Z. Cai, Y. Pan, X. Zhao, W. Huang, K. Xie, Y. Li, Y. Sun, B. Zhong, *J. Phys. Chem. B* **2003**, *107*, 557.

[58] Y. C. Huang, T. Zhou, C. Ling, S. Wang, J. Y. Du, *ChemPhysChem* **2014**, *15*, 2490.

[59] S.-C. Huang, C.-H. Lin, J.-H. Wang, *J. Phys. Chem. C* **2010**, *114*, 9826.

[60] C. T. Campbell, *Top. Catal.* **1994**, *1*, 353.

[61] C. T. Campbell, *ACS Catal.* **2017**, *7*, 2770.

AUTHOR BIOGRAPHIES

Hèctor Prats was born in Barcelona (1992) and received his B.S. degree in Chemistry (2013) from the University of Barcelona (UB). During 2013–2015, he completed a two-year European interuniversity master's degree in theoretical chemistry and computational modeling. He is currently a PhD student at the UB with a FI scholarship, under the supervision of Prof. Ramón Sayós and Prof. Francesc Illas.

Francesc Illas is Full Professor of Physical Chemistry at the University of Barcelona. He published over 560 papers cited ~16000 times (h-index = 60) and received several research awards: Distinguished Professor Mention for the Research Promotion awarded by the Generalitat de Catalunya (2001), Bruker Physical Chemistry Research Award of the Spanish Royal Society of Chemistry (2004), ICREA Academia Award (2009 and 2015) and was elected Fellow of the European Academy of Sciences (2012).

RAMÓN SAYÓS is Full Professor at Materials Science and Physical Chemistry Department of the University of Barcelona. He is head of the Applied Computational Chemistry and Molecular Modeling Group and has mainly developed his research activities in the theoretical and computational chemistry area, with a special attention in the last research projects for its application to several industrial processes. He is an active member of the European Division of Computational and Theoretical Chemistry of EuCheMS.

How to cite this article: Prats H, Illas F, Sayós R. General concepts, assumptions, drawbacks, and misuses in Kinetic Monte Carlo and microkinetic modeling simulations applied to computational heterogeneous catalysis. *Int J Quantum Chem*. 2017;e25518. https://doi.org/10.1002/qua.25518

7.3. Summary and conclusions

In the present chapter, several important issues regarding the theoretical description of the kinetics of surface reactions have been highlighted and discussed in detail, relying on our previous works on the WGSR on copper surfaces. Several additional kMC simulations have been also carried out to better support our conclusions.

DFT-based calculations carried out on suitable periodic surfaces, complemented by statistical thermodynamics, is currently the main tool to investigate heterogeneously catalyzed reactions at the molecular level, and constitutes a necessary previous stage to kinetic modeling studies. Minimum energy diagrams based on DFT calculated total energies lead to potential energy diagrams (PED), which provide a first view of a given reaction mechanism. The PED should include the ZPE correction, which can be calculated using the harmonic oscillator model as a sum of contribution from all vibrational modes. Low frequencies (i.e., < 500 cm^{-1}) contribute very little to the ZPE, while high frequencies can contribute with several tenths of eV. However, note that this trend is opposite to that of the frequency contribution to the entropy, as discussed later. Figure 2 from Publication 6 shows that neglecting the ZPE correction leads to differences of up to 0.22 eV in some energy barriers, which have large effects on the corresponding reaction rates. For instance, the reaction rate corresponding to water dissociation at 625 K including ZPE is $1.5 \cdot 10^{6}$ s^{-1}, whereas the value without ZPE is only $2.5 \cdot 10^{4}$ s^{-1}, 60 times smaller. Apart from the ZPE correction, all PEDs should also include the contribution from dispersion terms, as discussed in Chapter 5.

PED often fail to make even qualitative predictions for processes involving large shifts in entropy (e.g., adsorption and desorption). Hence, they should be replaced by Gibbs free energy diagrams, which take into account the effects of pressure and temperature. Several authors only consider the entropic changes in adsorption and desorption processes, and assume that the entropy contributions of adsorbed species are zero, which means that for a given surface process the free energy barrier can be taken equal to the potential energy barrier. Section 3.2 in Publication 6 shows that this assumption may not be valid for surface processes involving more than four atoms (i.e., because a large number of low vibrational modes will be present) or at high temperatures.

Although free energy diagrams can provide crucial understanding of the reaction mechanisms that underpin a chemical process[1–3], it may be difficult to make statements about their performance under operating conditions, especially in the presence of

competing pathways with similar barriers. Reaction rate theory calculations and kinetic modeling are required to close the gap between calculations and surface science experiments. To this end, mean-field MM[4–6] or more sophisticated kMC simulations[7–10] can be employed. Among them, kMC avoids the mean-field approximation by making use of a spatially resolved lattice model, and allows for the inclusion of lateral interactions between the adsorbates, using either site-blocking rules[11] or cluster expansion models.[10] The downside is that kMC simulations are much costly and time-consuming, especially when the surface is heterogeneous and the number of processes is high.

During the last fifteen years, most kMC studies have focused on simple chemical processes, such as O_2 adsorption/desorption[12], CO oxidation[13,14], water formation[15] or hydrogen diffusion[16]. It is only since the last five years that the number of kMC studies involving complex reactions with dozens of surface processes (e.g., CO methanation[17], methanol partial oxidation[18], WGSR[19] …) has started to grow. However, the vast majority of them neglect lateral interactions between adsorbates. These interactions can affect both the coverage of surface species as well as the energy barriers for the different elementary processes and the final TOF. Table 4 from Publication 6 shows the quantitative effect of lateral interactions in the final surface coverage and TOF for the WGSR on Cu(321), where differences up to $\pm$50% in the calculated values are found. Apart from lateral interactions, a good theoretical description of surface kinetics should include a quantitative description of the diffusion processes, which are also neglected in the free energy profiles. In the case of WGSR on Cu(111), neglecting diffusion processes imply a 25% reduction in the TOF and differences up to 50% on the surface coverage (see Table 3 from Publication 6). In cases where the lattice model includes different type of adsorption sites, neglecting diffusion processes may inhibit the formation of the reaction products. In those cases where diffusion processes are very fast (i.e., implying that along the kMC simulation the diffusion will dominate and extremely long simulations will be required to observe some evolution of the overall chemical process) a reduction by some factor of the diffusion reaction rates should be done. This reduction can be done manually or using a temporal acceleration scheme[20].

7.4. References

1 J. Greeley, T. F. Jaramillo, J. Bonde, I. Chorkendorff and J. K. Nørskov, Computational high-throughput screening of electrocatalytic materials for hydrogen evolution, *Nat. Mater.*, **2006**, 5, 909–913.

2 J. Greeley and M. Mavrikakis, Alloy catalysts designed from first principles, *Nat. Mater.*, **2004**, 3, 810–815.

3 D. A. Hansgen, D. G. Vlachos and J. G. Chen, Using first principles to predict bimetallic catalysts for the ammonia decomposition reaction, *Nat. Chem.*, **2010**, 2, 484–489.

4 C. Callaghan, I. Fishtik, R. Datta, M. Carpenter, M. Chmielewski and A. Lugo, An improved microkinetic model for the water gas shift reaction on copper, *Surf. Sci.*, **2003**, 541, 21–30.

5 L. C. Grabow, A. A. Gokhale, S. T. Evans, J. A. Dumesic and M. Mavrikakis, Mechanism of the water gas shift reaction on Pt: first principles, experiments, and microkinetic modeling, *J. Phys. Chem. C*, **2008**, 112, 4608–4617.

6 A. B. Mhadeshwar and D. G. Vlachos, Microkinetic modeling for water-promoted CO oxidation, water−gas shift, and preferential oxidation of CO on Pt, *J. Phys. Chem. B*, **2004**, 108, 15246–15258.

7 M. Stamatakis, Kinetic modelling of heterogeneous catalytic systems, *J. Phys. Cond. Matter*, **2015**, 27, 013001.

8 M. Stamatakis and D. G. Vlachos, Unraveling the complexity of catalytic reactions via kinetic Monte Carlo simulation: current status and frontiers, *ACS Catal.*, **2012**, 2, 2648–2663.

9 K. Reuter and M. Scheffler, First-principles kinetic Monte Carlo simulations for heterogeneous catalysis: Application to the CO oxidation at RuO_2(110), *Phys. Rev. B*, **2006**, 73, 045433.

10 H. Prats, P. Gamallo, F. Illas and R. Sayós, Comparing the catalytic activity of the water gas shift reaction on Cu(321) and Cu(111) surfaces: step sites do not always enhance the overall reactivity, J. Catal., **2016**, 342, 75–83.

11 J. M. Lorenzi, S. Matera and K. Reuter, Synergistic inhibition of oxide formation in oxidation catalysis: a first-principles kinetic Monte Carlo study of NO+CO oxidation at Pd(100), *ACS Catal.*, **2016**, 6, 5191–5197.

12 S. Pogodin and N. López, A more accurate kinetic Monte Carlo ppproach to a monodimensional surface reaction: the interaction of oxygen with the $RuO_2(110)$ surface, *ACS Catal*., **2014**, 4, 2328–2332.

13 S. Piccinin and M. Stamatakis, CO Oxidation on Pd(111): A first-principles-based kinetic Monte Carlo study, *ACS Catal.*, **2014**, 4, 2143–2152.

14 M. J. Hoffmann and K. Reuter, CO Oxidation on Pd(100) Versus PdO(101)-$(\sqrt{5}\times\sqrt{5})$R27º: first-principles kinetic phase diagrams and bistability conditions, *Top. Catal*., **2014**, 57, 159–170.

15 R. Hu, S. Huang, Z. Liu and W. Wang, Water formation on Pt(111) surfaces at high temperatures studied by kinetic Monte Carlo simulations, *App. Surf. Sci*., **2005**, 242, 353–361.

16 X. Yang and W. O. Oyeniyi, Kinetic Monte Carlo simulation of hydrogen diffusion in tungsten, *Fus. Eng. Des.*, **2017**, 114, 113–117.

17 M. Andersen, C. P. Plaisance and K. Reuter, Assessment of mean-field microkinetic models for CO methanation on stepped metal surfaces using accelerated kinetic Monte Carlo, *J. Chem. Phys*., **2017**, 147, 152705.

18 T. B. Rawal, S. R. Acharya, S. Hong, D. Le, Y. Tang, F. F. Tao and T. S. Rahman, High catalytic activity of Pd1/ZnO(1010) toward methanol partial oxidation: a DFT+KMC study, *ACS Catal*., **2018**, 8, 5553–5569.

19 L. Yang, A. Karim and J. T. Muckerman, Density functional kinetic Monte Carlo simulation of water–gas shift reaction on Cu/ZnO, *J. Phys. Chem. C*, **2013**, 117, 3414–3425.

20 E. C. Dybeck, C. P. Plaisance and M. Neurock, Generalized temporal acceleration scheme for kinetic Monte Carlo simulations of surface catalytic processes by scaling the rates of fast reactions, *J. Chem. Theory Comput*., **2017**, 13, 1525–1538.

CHAPTER EIGHT

Conclusions

The results of this thesis are contained in Chapters 3 to 7, each of them containing a Summary and Conclusions section drawing the main ideas to be extracted from it. The aim of this chapter is therefore to present all the conclusions of the thesis in an ordered an summarized manner, in order to provide with a general view of the work.

On the post-combustion gas separation

- GCMC simulations combined with an accurate force-field represents a good methodology to screen over different adsorbent materials to study their performance towards gas separation at different temperature and pressure conditions.

- FAU-type zeolites are great candidates as adsorbent materials for post-combustion gas separation thanks to the possibility of modifying their properties by changing the Al content (i.e., the Si/Al ratio).

- CO_2 purity values at outlet higher than 90% are obtained for faujasite structures containing more than 48 Al atoms per unit cell and using a TSA unit.

- There is no FAU structure that works well for all three PSA, VSA and TSA units. Depending on the selected process and the temperature and pressure conditions one or another FAU structure should be chosen in order to minimize the energetic cost per ton of CO_2 captured. While high Al content structures are the best choice for a TSA unit, intermediate and low Al content faujasites perform better at VSA and PSA units, respectively.

On the WGSR on Cu surfaces

- In spite of the small size of the species involved in the molecular mechanism of the WGSR on copper, the contribution of dispersion to the overall picture is important, with a clear net effect and with no compensation of errors on several reaction steps, and therefore should not be ignored.

- Non-stoichiometric mixtures containing higher CO proportion enhance the production of H_2 in the WGSR on both Cu(111) and Cu(321) surfaces.

- At low temperatures, H_2O-H islands are observed on the flat Cu(111) surface. This correlation in the occupation of neighboring sites is not observed at higher temperatures.

- The associative mechanism involving the COOH intermediate is the dominant pathway on both Cu(111) and Cu(321) surfaces. However, the redox mechanism becomes also important on the Cu(321) surface at high temperatures, contributing around a 12% of the overall TOF.

- The stepped Cu(321) surface is less active than the flat Cu(111) surface. This fact constitutes a new and unexpected conclusion, which possibly cannot be anticipated by inspection of the energy profiles only. The reason is that some reverse processes present very high reaction rates on the Cu(321) surface. Moreover, the poisoning of step sites by CO and, to a lesser extent, by water, prevents some elementary reactions to occur.

On the kMC method

- Although free energy diagrams can provide crucial understanding of the reaction mechanism that underpin a complex chemical reaction, it may be difficult to make statements about their performance under operating conditions, especially in the presence of competing pathways with similar energy barriers.

- The kMC method allows to obtain more reliable results than mean-field MM method because it avoids the mean-field approximation by making use of a spatially resolved lattice model, and allows for the inclusion of lateral interactions between adsorbates, which may lead to correlation in the occupation of neighboring sites.

- For a correct description of the kinetics of a surface reaction using the kMC method, one should always include diffusion processes of the most mobile species as well as lateral interactions between adsorbates.

- The RDSs for a complex chemical reaction should never be predicted only by inspection to the potential or free energy diagrams. Instead, one should combine kMC simulations with a sensitivity analysis (e.g., by using the Campbell's degree of rate control), and keep in mind that the RDSs can change with temperature or reactants partial pressure.

CHAPTER NINE

Contribution to publications

The results of this thesis are presented as a compendium of publications which are coauthored by more than just the author of this thesis. This chapter describes the contribution of the author of this thesis to each of the publications.

- **Prats, H**.; Bahamon, D.; Alonso, G.; Giménez, X.; Gamallo, P.; Sayós, R. Optimal Faujasite Structures for Post Combustion CO_2 Capture and Separation in Different Swing Adsorption Processes. *Journal of CO2 Utilization* **2017**, *19*, 100–111
    - Contribution: carrying out all GCMC simulations, preparing data for analysis, contributing to scientific discussions, and writing a first draft of the manuscript.

- **Prats, H**.; Bahamon, D.; Giménez, X.; Gamallo, P.; Sayós, R. Computational Simulation Study of the Influence of Faujasite Si/Al Ratio on CO_2 Capture by Temperature Swing Adsorption. *Journal of CO2 Utilization* **2017**, *21*, 261–269
    - Contribution: carrying out all GCMC simulations, preparing data for analysis, contributing to scientific discussions, and writing a first draft of the manuscript.

- **Prats, H**.; Álvarez, L.; Illas, F.; Sayós, R. Kinetic Monte Carlo Simulations of the Water Gas Shift Reaction on Cu(111) from Density Functional Theory Based Calculations. *Journal of Catalysis* **2016**, *333*, 217–226
    - Contribution: carrying out all kMC simulations, preparing data for analysis, contributing to scientific discussions, and writing a first draft of the manuscript.

- **Prats, H**.; Gamallo, P.; Sayós, R.; Illas, F. Unexpectedly Large Impact of van Der Waals Interactions on the Description of Heterogeneously Catalyzed Reactions: The Water Gas Shift Reaction on Cu(321) as a Case Example. *Physical Chemistry Chemical Physics* **2016**, *18*, 2792–2801
    - Contribution: carrying out all DFT calculations, preparing data for analysis, contributing to scientific discussions, and writing a first draft of the manuscript.

- **Prats, H**.; Gamallo, P.; Illas, F.; Sayós, R. Comparing the Catalytic Activity of the Water Gas Shift Reaction on Cu(3 2 1) and Cu(1 1 1) Surfaces: Step Sites Do Not Always Enhance the Overall Reactivity. *Journal of Catalysis* **2016**, *342*, 75–83
    - Contribution: carrying out all DFT calculations and KMC simulations, preparing data for analysis, contributing to scientific discussions, and writing a first draft of the manuscript.

- **Prats, H**.; Illas, F.; Sayós, R. General Concepts, Assumptions, Drawbacks, and Misuses in Kinetic Monte Carlo and Microkinetic Modeling Simulations Applied to Computational Heterogeneous Catalysis. *International Journal of Quantum Chemistry* **2017**, 118, e25518
    - Contribution: carrying out all KMC simulations, preparing data for analysis, contributing to scientific discussions, and writing a first draft of the manuscript.

CHAPTER TEN

Resum en català
Summary in Catalan

En aquesta memòria s'han aplegat els resultats corresponents a la tesi doctoral titulada "Mètodes Monte Carlo aplicats a catàlisis heterogènia i separació de gasos", durant el transcurs de la qual s'han estudiat els dos grans temes esmentats en el títol. Tot i que els sistemes estudiats en ambdós temes són força diferents, tenen dos semblances fonamentals: els dos sistemes tenen un elevat interès industrial i s'han estudiat mitjançant mètodes estocàstics. Concretament, la primera part de la tesis es centra en l'avaluació de deu zeolites diferents (totes elles de la família de les faujasites) per a ser usades en la captura i separació de CO_2 en mescles de post-combustió. Per altra banda, la segona part tracta de l'estudi de la reacció *water-gas shift* catalitzada per coure, tant des de un punt de vista termodinàmic com cinètic.

10.1. Captura de CO_2 mitjançant faujasites

10.1.1. Introducció

El creixement econòmic i el desenvolupament industrial han provocat un augment de la crema de combustibles fòssils, com ara petroli, carbó o gas natural. En l'actualitat, les centrals elèctriques de combustibles fòssils representen el 80% de la producció total d'energia a tot el món i continuaran sent una font important d'energia en el futur pròxim. No obstant això, la producció d'electricitat a partir de combustibles fòssils haurà d'afrontar les preocupacions creixents per les emissions antropogèniques de gasos d'efecte hivernacle, com ara el CO_2, que contribueixen al canvi climàtic global. Aquestes emissions es poden veure reduïdes per diverses mesures, com ara el desenvolupament d'energies renovables (per exemple, energia eòlica i solar). Tanmateix, la transició necessària cap a una producció energètica sostenible és poc probable que es produeixi a un ritme prou ràpid. Per tant, s'han dedicat molts esforços al desenvolupament de tecnologies eficients per a la separació i captura de diòxid de carboni.

Actualment, el mètode a gran escala més utilitzat per evitar les emissions de CO_2 i d'altres gasos àcids a l'atmosfera és l'absorció d'aquests en una solució d'amines[1,2]. Aquest procés es duu a terme mitjançant la reacció del CO_2 amb les amines per donar bicarbonat. No obstant, l'absorció en amines té alguns desavantatges, com ara uns elevats requeriments energètics per a la regeneració dels absorbents, la pèrdua d'absorbent per evaporació i la seva tendència a produir corrosió. Per aquests motius, hi ha un gran interès

a trobar mètodes alternatius per a la separació eficient del CO_2 d'un corrent de gas a gran escala. Així, destaquen els mètodes cíclics de fisisorció/desorció, com ara el PSA, el VSA o el TSA, els quals han despertat grans expectatives en els darrers anys. En aquests mètodes, una vegada produïda l'adsorció del CO_2 o d'un altre compost, es disminueix la pressió (PSA i VSA) o s'incrementa la temperatura (TSA) per tal de regenerar-lo. Òbviament, s'ha d'arribar a un compromís entre les temperatures o pressions d'adsorció i les de regeneració per tal de fer el procés més econòmic. En aquest sentit, interessa per exemple modificar adequadament aquests materials adsorbents per tal d'augmentar-ne la selectivitat envers un component determinat.

Fig. 10.1. Imatges de quatre zeolites naturals. Chabazita[3] (dalt esquerra), estilbita[4] (dalt dreta), mordenita[5] (baix esquerra) i faujasita[6] (baix dreta).

Com a possibles materials adsorbents, es troben les zeolites[7] i els MOFs[8], que presenten una sèrie d'avantatges respecte de l'absorció en amines. Així, en tractar-se

d'estructures sòlides, són més fàcils de manipular que els líquids en l'àmbit industrial. A més, des del punt de vista econòmic, representen un estalvi tant en el procés de síntesi de l'adsorbent com en el procés de captura i regeneració. Concretament, les zeolites són materials microporosos que es poden trobar a la natura. El terme zeolita neix el 1756, quan el mineralogista Axel Fredrik Cronstedt va descobrir que, en escalfar el mineral actualment conegut com a estilbita, deixava anar una gran quantitat de vapor. El producte resultant, el va anomenar zeolita, que prové del grec, on ζεω (zeo) significa 'bullir' i λιθος (lithos) significa 'pedra'.

Les zeolites són aluminosilicats de fórmula molecular $M_{x/n}\left[(AlO_2)_x(SiO_2)_y\right] \cdot wH_2O$ on M és un catió de valència n (sovint Na o Ca), x i y són el nombre d'àtoms de Al i Si per cel·la unitat, i w el nombre de molècules d'aigua per cel·la unitat. Les propietats de zeolites depenen fortament de la relació Si/Al (és a dir, y/x a la fórmula molecular). A mesura que la relació Si/Al augmenta, el contingut de cations disminueix, l'estabilitat tèrmica és més alta, la superfície es torna més hidròfoba i la zeolita perd les seves propietats catalítiques. Així, les zeolites riques en alúmina poden capturar molècules polars com l'aigua, mentre que les zeolites riques en sílice funcionen millor amb molècules no polars. Les zeolites s'utilitzen amb freqüència en processos de PSA i VSA per eliminar el CO_2 de l'aire com una impuresa a causa de la seva elevada selectivitat[9]. A més, ofereixen una estabilitat tèrmica i mecànica molt millor que altres materials adsorbents descrits recentment a la literatura, com els MOF[10].

Com s'ha dit anteriorment, les centrals elèctriques de combustibles fòssils constitueixen la font estacionària més gran d'emissions de CO_2. Pel que fa a les plantes de carbó, els principals components de gasos de combustió són N_2 (75-80%), CO_2 (15-16%) i O_2 (4-5%), amb pressions totals properes a 100 kPa i temperatures entre 313 i 333 K[11]. Tot i la gran quantitat d'estudis sobre materials adsorbents que s'han publicat en el context de la captura de CO_2, la gran majoria d'ells s'ha basat exclusivament en les isotermes d'adsorció de CO_2 i N_2 purs. Els resultats de les mescles es prediuen habitualment amb la IAST presentada per Myers i Prausnitz[12]. Aquesta teoria, però, no considera els fenòmens com coadsorció i/o la competència pels llocs d'adsorció (en anglès *sites*). A més, les mesures experimentals d'adsorció de mescles de gasos sovint requereixen molt de temps, equips personalitzats dissenyats acuradament i una anàlisi de dades força complexa[13]. Com a conseqüència, hi ha una manca important de dades d'adsorció a la literatura de mescles amb més de dos components, tot i que moltes

separacions de gasos industrials impliquen mescles multi-components. En lloc d'haver de confiar en la IAST, en aquest treball es calculen directament les isotermes d'adsorció de mescla corresponents a la següent mescla ternària: CO_2 (15%), N_2 (80%) i O_2 (5%).

L'objectiu principal d'aquesta part, per tant, és avaluar les diferents estructures de faujasita en el procés de captura de CO_2 de mescles de post-combustió per tal de trobar les estructures òptimes per a unes determinades condicions de P i T i per a un procés d'adsorció concret (PSA, VSA o TSA). La Publicació 1 (Capítol 3) es centra en els processos de PSA, VSA i també el procés híbrid VPSA. D'altra banda, la Publicació 2 (Capítol 3) se centra en el procés de TSA i estableix una comparació exhaustiva entre les diferents estructures de faujasita i els processos d'adsorció en termes d'energia (o sigui, de cost econòmic).

10.1.2. Metodologia

Per a determinar si una estructura de zeolita en concret és una bona candidata a ser usada en tècniques de captura de CO_2, primer cal saber quina és la quantitat i composició de gasos que adsorbeix de la mescla de post-combustió a uns valors de temperatura i pressió determinats. Aquesta informació es troba en les isotermes d'adsorció, i es poden calcular teòricament mitjançant el mètode GCMC. A diferència de les simulacions MC convencionals, on es mesuren mitjanes temporals en el col·lectiu canònic (NVT constant), el mètode GCMC treballa en el col·lectiu grand-canònic (μVT constant, on μ es el potencial químic del sistema). En aquest col·lectiu el nombre de partícules del sistema pot anar variant fins que el potencial químic del sistema s'iguala al d'un reservori amb el gas en qüestió a una temperatura i pressió determinades.

En les simulacions GCMC, primer de tot s'escull aleatòriament entre un pas de desplaçament MC de prova (translació o rotació) o un pas de intercanvi GCMC de prova (inserció o eliminació). Si s'escull una translació, una de les partícules del sistema (en el nostre cas, una de les molècules de CO_2, N_2 o O_2) és seleccionada aleatòriament i es desplaça una distància aleatòria d en una direcció també aleatòria, on $d \in [0, d_{max}]$. Si s'escull una rotació, la partícula seleccionada es rota un angle aleatori al voltant d'un eix aleatori. Si s'escull una inserció, es col·loca una partícula dins del sistema en una posició aleatòria. Finalment, si s'escull una eliminació, una de les partícules del sistema és seleccionada aleatòriament i s'elimina. Com s'ha dit inicialment, aquests moviments són tots de prova. Que s'acceptin o no dependrà de les energies respectives de la configuració

inicial i final. A grans trets, el moviment de prova serà sempre acceptat quan l'energia de la configuració final sigui més baixa que la inicial. En cas contrari, hi ha una probabilitat de que el moviment de prova no s'accepti. Aquesta probabilitat serà més gran a mesura que augmenti la diferència d'energia entre els dos estats[14]. Totes les simulacions GCMC s'han realitzat amb el paquet de càlcul LAMMPS[15].

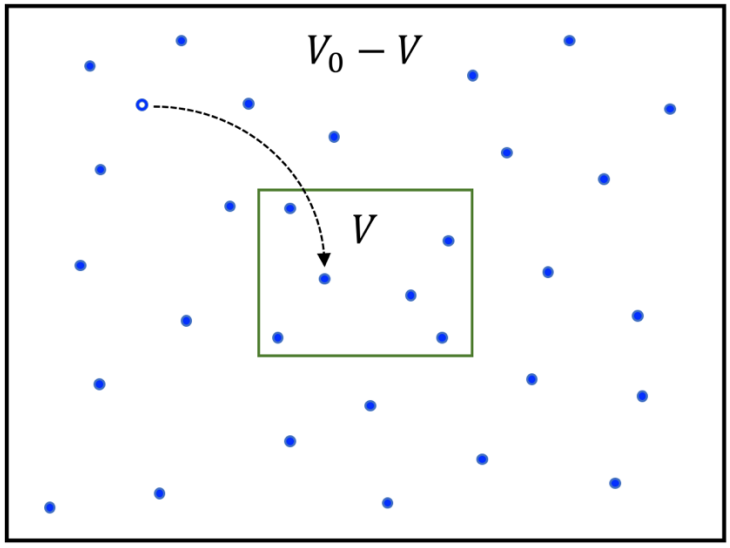

Fig. 10.2. Sistema de N partícules de volum V envoltades d'un reservori de volum V_0-V

10.1.3. Resultats i conclusions

Les isotermes d'adsorció de gasos purs obtingudes a partir de les simulacions GCMC mostren que les molècules de CO_2 interactuen fortament amb els cations de Na^+. Atès que la quantitat de cations de Na^+ i el nombre d'àtoms de Al són sempre iguals, podem afirmar que les faujasites que tenen un alt contingut d'Al són les que adsorbeixen una quantitat major de CO_2 (veure la Figura 10.3). Per tant, l'estructura 96-FAU (és a dir, l'estructura amb el màxim contingut Al possible) és la que mostra saturació a una pressió més baixa, mentre que la 0-FAU no se satura fins a pressions molt elevades. No obstant això, el volum ocupat pels cations de Na^+ no és insignificant, i provoca que el volum disponible per a l'adsorció de CO_2 disminueixi a mesura que augmenta el contingut d'Al. Per tant, a pressions elevades (20-50 bar) trobem que la màxima absorció correspon a les faujasites que tenen un contingut intermedi d'Al. A partir de les isotermes d'adsorció de gasos purs s'observa que l'adsorció de CO_2 és significativament superior a la de N_2 o O_2 (en les mateixes condicions de P i T), el que indica una bona selectivitat cap al CO_2. A

causa de la forta interacció entre les molècules de CO_2 i els cations de Na^+, el calor isostèric augmenta de 13 a 42 $kJ \cdot mol^{-1}$ quan passem de l'estructura 0-FAU a la 96-FAU.

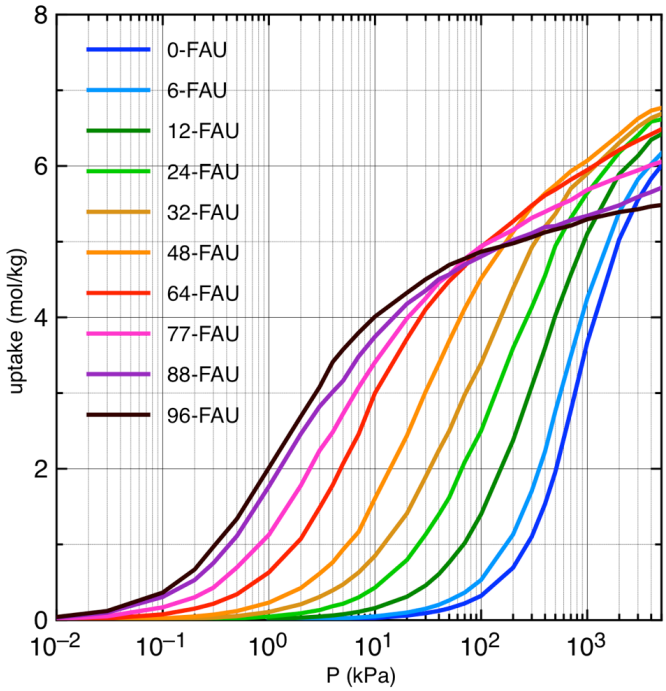

Fig. 10.3. Isotermes d'adsorció pures de CO_2 corresponents a les deu estructures de faujasita estudiades a 313 K. Cada isoterma s'ha obtingut a partir de 29 punts equidistants en escala logarítmica.

Les simulacions de mescles ternàries mostren que l'estructura de 96-FAU és realment la que presenta la màxima selectivitat cap al CO_2 (vegeu la Figura 4 de la Publicació 1), especialment a baixes pressions, superant altres materials adsorbents molt populars com ara la zeolita Ca-A, el MOF Mg-74 i el MOF Cu-BTC. La selectivitat disminueix quan es redueix el contingut d'Al, i per tant l'estructura 0-FAU és la que presenta els valors més baixos.

En aquest punt, es podria pensar que les estructures amb més contingut d'Al són les millors faujasites per a la captura de CO_2, a causa de la seva alta adsorció i selectivitat. Però aquesta informació és suficient per a afirmar que això és cert? En aquest context, és crucial estimar l'energia necessària per separar una determinada quantitat de CO_2, expressada normalment en GJ per tona de CO_2. Aquesta energia depèn de molts factors, com ara la quantitat de CO_2 extret per cicle, el cost operatiu d'un cicle d'adsorció/desorció (que al seu torn depèn del tipus de procés triat i de les condicions de treball), així com els costos capitals d'equips i materials adsorbents, els costos de des-humidificació prèvia de la mescla de post-combustió i els costos de compressió i transport finals. Suposant que la majoria d'aquests costos són independents del procés triat i de l'estructura de faujasita

seleccionada, podem centrar-nos en dos factors principals: 1) la quantitat de CO_2 extret per cicle, també coneguda com la capacitat de treball (en anglès *working capacity*), i 2) la quantitat d'energia necessària per cicle d'adsorció/desorció. La relació entre el primer i el segon terme determinarà el rendiment d'una estructura de faujasita determinada a unes condicions operatives determinades.

Comencem centrant la nostra atenció en la capacitat de treball. Aquesta quantitat es pot calcular a partir de la diferència entre la quantitat de CO_2 adsorbida en les condicions d'adsorció i desorció (o regeneració). El resultat és que no hi ha cap estructura millor. En canvi, depenent del procés seleccionat i de les condicions de funcionament (P_{ads}, P_{regen}, T_{ads} and T_{regen}), la faujasita que s'ha de triar per maximitzar la capacitat de treball és una o una altra. Tot i que les estructures d'alt contingut en Al presenten les capacitats de treball més altes per al procés TSA, les estructures de contingut intermedi i baix d'Al són millors candidates per als processos VSA i PSA, respectivament (vegeu la Figura 6c a la Publicació 2).

Què passa doncs amb els requisits energètics? La quantitat d'energia (potència) requerida per cicle d'adsorció en una unitat PSA o VSA es pot calcular com al treball adiabàtic de compressió o expansió, respectivament, que depèn principalment de les pressions d'adsorció i regeneració, i de la capacitat de treball (vegeu les equacions (7) i (8) a la Publicació 1). Aquestes quantitats es poden comparar amb l'energia de regeneració tèrmica requerida per cicle d'adsorció en una unitat TSA. Aquest últim valor depèn de la capacitat calorífica del material adsorbent, el calor isostèric i la capacitat de treball (vegeu l'equació (6) a la Publicació 2). Per descomptat, si reduïm la pressió d'adsorció en una unitat PSA, o bé reduïm la temperatura de regeneració en una unitat TSA, o bé augmentem la pressió de regeneració en una unitat VSA, l'energia requerida per cicle d'adsorció/desorció serà menor. Tanmateix, també disminuirà la capacitat de treball, de manera que s'haurà de triar un bon compromís entre ambdós valors.

El present estudi mostra que, en general, el procés TSA emprant faujasites com a material adsorbent és més car que el PSA o VSA, excepte per a les estructures de contingut alt d'Al (vegeu la Figura 6d en la Publicació 2). Cal tenir en compte que, per a una veritable comparació entre l'energia tèrmica (barata) i el treball adiabàtic (costós), s'hauria de considerar un coeficient de conversió, que reduiria els requisits energètics del procés TSA. Finalment, els nostres resultats mostren que el menor cost energètic per tona de CO_2 capturat es pot aconseguir treballant amb una unitat VSA i utilitzant les estructures de faujasita amb un contingut intermedi d'Al.

10.2. La reacció WGSR catalitzada per Cu

10.2.1. Introducció

L'hidrogen, que és necessari per a operar el procés Haber-Bosch, també juga un paper central en moltes altres indústries, des de la química fins a la metal·lúrgica i l'electrònica[16]. L'ús d'hidrogen es basa principalment en la seva reactivitat més que en les seves propietats físiques, i es pot dividir àmpliament en les següents categories: 1) com a reactiu en els processos d'hidrogenació - per saturar compostos o bé per eliminar determinats àtoms (com ara S o N), 2) per eliminar traces d'O_2 i, per tant, evitar l'oxidació i la corrosió, 3) com a combustible en els motors dels coets i 4) com a refrigerant en els generadors elèctrics.

Actualment, la tecnologia dominant per a la producció directa d'hidrogen és la coneguda com a *steam reforming*, a partir de combustibles com el metà o el gas natural. Aquest procés consisteix a escalfar el gas natural en presència de vapor d'aigua (al voltant de 700 ºC) i un catalitzador de níquel[17]. La reacció endotèrmica resultant trenca les molècules de metà i forma monòxid de carboni i hidrogen:

$$CH_4 + H_2O \rightleftarrows CO + 3H_2 \quad (\Delta_r G^o_{298.15K} = 1.47 \text{ eV}) \qquad (10.1)$$

Es pot aconseguir hidrogen addicional en una segona etapa a través de la reacció WGSR[18]:

$$CO + H_2O \rightleftarrows CO_2 + H_2 \quad (\Delta_r G^o_{298.15K} = -0.30 \text{ eV}) \qquad (10.2)$$

El CO_2 produït es pot separar de l'H_2 a través d'una unitat PSA[19] o bé mitjançant membranes[20].

Originalment, la reacció WGSR va ser descoberta pel físic italià Felice Fontana al 1780. No obstant això, no va ser fins al desenvolupament de nous processos industrials que requerien hidrogen (com ara la síntesi d'amoníac a partir del procés Haber-Bosch) quan es va tenir consciència del gran valor industrial d'aquesta reacció. A més, la reacció WGSR és una de les més importants per a equilibrar la relació H_2/CO en el procés Fischer-Tropsch[21]. Avui en dia, l'interès de la reacció WGSR s'ha renovat a causa dels estrictes requisits d'hidrogen d'alta puresa que es necessiten en les piles de combustible[22], on es necessita una concentració de CO per sota del 0,5% per evitar l'enverinament de

l'ànode de platí, un component clau d'aquests dispositius. Cal destacar també que la conversió de CO a partir d'aquesta reacció s'afavoreix a baixes temperatures a causa de la seva exotermicitat. A mesura que augmenta la temperatura, la constant d'equilibri i la conversió final disminueixen. Per tant, aquest procés es realitza normalment en dues etapes: una primera a una temperatura força elevada (300-450 ºC) que afavoreix el consum ràpid de CO, i una segona etapa a una temperatura més baixa (200-300 ºC) per aconseguir conversions més elevades[23]. Per a aquesta segona fase s'utilitzen catalitzadors basats en òxids[24] ($Fe_2O_3/Cr_2O_3/MgO$), mentre que els catalitzadors utilitzats en la primera fase sovint es basen en coure i òxids de Zn, Cr i Al[25,26], encara que també s'han proposat altres metalls i suports[27,28].

No obstant, malgrat el progrés en la recerca de catalitzadors més eficients per a la reacció WGSR, el coure continua sent l'ingredient principal dels catalitzadors utilitzats industrialment. No és sorprenent que s'hagi dedicat un gran esforç a comprendre el mecanisme de la reacció en coure a nivell microscòpic. Atès que en aquests catalitzadors hi ha grans partícules de coure, que presenten predominantment cares (111), la superfície de Cu(111) s'ha pres generalment com a sistema de referència per als estudis de la reacció WGSR. En el Capítol 4 d'aquesta tesis es presenta un estudi cinètic d'aquesta reacció en la superfície de Cu(111) emprant càlculs DFT i el mètode kMC, que s'explicaran breument en el següent apartat.

Per altra banda, les interaccions de vdW (també conegudes com a forces de dispersió) tenen un paper important en els processos químics i físics[29]. S'ha demostrat que les forces de dispersió són molt importants en el cas de les interaccions de molècules aromàtiques amb el pla basal de MoS_2[30], d'hidrocarburs que interactuen amb zeolites[31] o del grafè amb superfícies metàl·liques[32], entre múltiples exemple més. Malgrat la gran quantitat d'articles dedicats a estudiar la importància de les forces de dispersió en la interacció entre espècie adsorbida i superfície, gairebé no hi ha informació sobre el seu efecte en el perfil energètic de les reaccions catalitzades heterogèniament, especialment per a aquelles que presenten mecanismes de reacció complexos amb molts passos elementals. L'objectiu del Capítol 5, per tant, és estudiar l'impacte de les interaccions de van der Waals en la reacció WGSR.

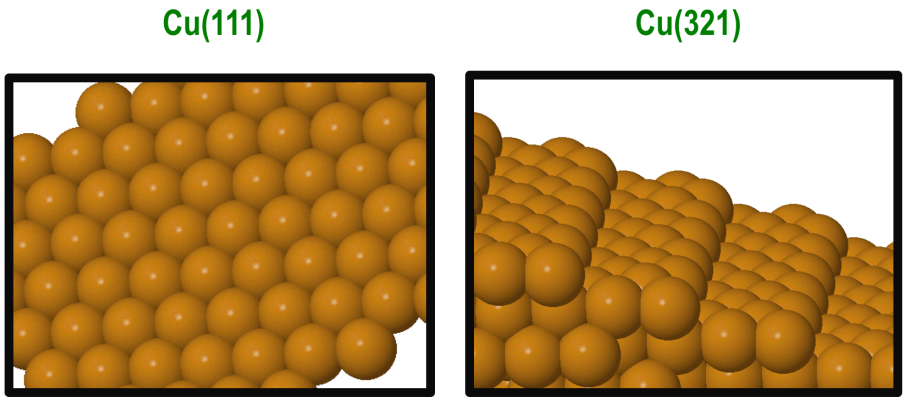

Fig. 10.4. Representació gràfica de la superfície plana Cu(111) (esquerra) i la superfície esglaonada Cu(321) (dreta).

Després d'estudiar el mecanisme de la reacció WGSR en la superfície plana Cu(111) al Capítol 4, i també quantificar l'efecte de les interaccions vdW al Capítol 5, falta estudiar l'efecte les superfícies esglaonades en l'activitat de la reacció. Les zones amb defectes o irregularitats dels catalitzadors tenen un paper important en la catàlisi heterogènia[33–35], degut a que presenten llocs d'adsorció amb baixa coordinació (veure Figura 10.4). En el cas d'esglaons, que és el que tractarem aquí, els llocs d'adsorció s'anomenen *step sites*. Aquests *sites*, per exemple, permeten noves maneres diferents d'unió a la superfície del catalitzador,[36] i faciliten el trencament d'enllaços dels reactius.[37] En general, es creu que la presència de *step sites* millora l'activitat catalítica de les reaccions complexes augmentant les energies d'adsorció dels reactius i disminuint les barreres energètiques[38]. Tanmateix, aquesta hipòtesi no sempre és correcta. Encara que les barreres energètiques dels RDSs en els *step sites* són sovint més baixes que en els llocs d'adsorció de superfícies planes, no es pot concloure rotundament que la presència de *step sites* sigui sempre beneficiosa sense haver estudiat la reacció amb més detall. Per exemple, els *step sites* poden tenir com a conseqüència la reducció de les barreres energètiques dels RDS també en la direcció inversa, augmentant la velocitat de la reacció inversa sobre les posteriors, provocant una disminució de l'activitat catalítica. A més, una forta quimisorció de reactius, productes o impureses als *step sites* pot causar l'enverinament del catalitzador[39].

Estudis previs de la reacció WGSR inversa[40] i de la reacció WGSR sobre superfícies de coure Cu(hkl)[41] conclouen que l'activitat catalítica segueix l'ordre Cu(110) > Cu(100) > Cu(111). Tanmateix, aquestes afirmacions es basen només en comparar barreres energètiques d'alguns RDS assumits. Clarament, un enfocament més rigorós

implicaria introduir efectes de temperatura, pressió, inclusió dels processos inversos i els efectes del recobriment superficial. Això es pot fer utilitzant models microcinètics o simulacions amb el mètode kMC. Normalment, els RDSs per a una reacció complexa, com ara la reacció WGSR, depenen del catalitzador emprat i també de les condicions de T i P[42].

En el Capítol 5 trobem el perfil energètic de la reacció WGSR a la superfície esglaonada Cu(321) mitjançant càlculs DFT, i aquest el comparem amb el de la superfície plana Cu(111)[43]. Tanmateix, la resposta a la pregunta de quina de les dues superfícies serà més reactiva de cara a la reacció WGSR no està gens clara (com veurem a la Secció 10.2.3). L'objectiu principal del Capítol 6 és per tant estudiar l'efecte dels *step sites* en la reacció WGSR catalitzada per coure.

Finalment, l'últim capítol de resultats de la present tesi pretén aprofitar tots els coneixements obtinguts en els Capítols 4 i 6 sobre simulacions amb el mètode kMC i aprofundir en alguns aspectes generals que poden servir com a guia per a futurs estudis cinètics. Per això, es discuteixen les aproximacions, els avantatges i els inconvenients més típics del mètode kMC i les diferències entre kMC i els models microcinètics. Concretament, s'escull la reacció WGSR catalitzada sobre Cu(111) i Cu(321) com a exemple pràctic per a discutir diversos aspectes, com ara els diagrames d'energia potencial i d'energia lliure, la importància d'incloure els processos de difusió i les interaccions laterals, o el càlcul de les velocitats de reacció.

10.2.2. Metodologia

Els resultats presentats en aquesta segona part de la tesi s'han obtingut mitjançant càlculs DFT i simulacions amb el mètode kMC. A continuació s'explicaran els aspectes més bàsics de cada mètode.

L'origen de la Teoria del Funcional de la Densitat es remunta als anys vint, quan Thomas i Fermi van desenvolupar el model del gas d'electrons[44], que expressava les propietats de l'estat fonamental d'un sistema constituït per electrons distribuïts uniformement sota la influència d'un camp nuclear en funció de la densitat electrònica $\rho(r)$. Aquest model va ser millorat posteriorment per Dirac[45,46] i Bloch[47] incloent un terme de canvi que donava lloc al model Thomas-Fermi-Dirac. No obstant això, els model resultant era menys acurat que els mètodes convencionals basats en la funció d'ona i no es van començar a aplicar als sistemes químics fins a l'aparició de la teoria desenvolupada

per Hohenberg i Kohn[48] el 1964, on es van introduir dos teoremes que van establir les bases per a la DFT moderna:

- Primer teorema: *"El potencial extern $V_{ext}(r)$ d'un estat electrònic no degenerat, i per tant l'energia total, es un únic funcional de $\rho(r)$"*
- Segon teorema: *"L'energia de l'estat fonamental es pot obtenir variacionalment: la densitat que minimitza l'energia total és la densitat exacta de l'estat fonamental"*

El primer teorema estableix una relació directa entre la densitat electrònica i la funció d'ona a partir del potencial extern. Per a un determinat $V_{ext}(r)$, el funcional de l'energia total és

$$E[\rho] = \int \rho(r)\, V_{ext}(r) dr + F_{HK}[\rho] \qquad (10.3)$$

on $F_{HK}[\rho]$ és un funcional universal de ρ(r) (també conegut com a funcional de Hohenberg-Kohn). Coneixent aquest funcional, es pot usar el segon teorema per obtenir la densitat exacta de l'estat fonamental i l'energia total. No obstant, aquests teoremes no proveeixen una ruta per construir aquests funcionals o un mètode per calcular la densitat electrònica de l'estat fonamental.

Més endavant, Kohn i Sham[49] van presentar una aproximació que permet substituir el intractable sistema de N cossos (electrons) interaccionant per un sistema de referència auxiliar d'electrons que no interaccionen entre ells movent-se en un potencial efectiu extern. Aquest potencial efectiu inclou el potencial extern i els efectes de les interaccions de Coulomb entre els electrons (les anomenades interaccions de bescanvi i correlació). La dificultat resideix en modelar correctament aquestes dues últimes interaccions, que estan incloses en l'anomenat funcional de bescanvi-correlació $E_{XC}[\rho]$. Els diferents mètodes basats en la DFT varien en l'expressió amb la que es calcula $E_{XC}[\rho]$, la qual pot dependre de la densitat[49] (aproximació de la densitat local, LDA), de la densitat i del seu gradient[50] (aproximació del gradient generalitzat, GGA), o bé de la densitat, el seu gradient i la seva laplaciana (funcionals meta-GGA). En aquesta tesi s'han utilitzat funcionals basats en l'aproximació GGA, com ara PBE[51] o PW91[52]. Tots els càlculs s'han realitzat amb el paquet VASP[53], el qual utilitza models periòdics i funcions de base basades en ones planes.

Per altra banda, el mètode kMC s'utilitza per seguir l'evolució cinètica d'una reacció en superfície a nivell microscòpic. La idea bàsica d'aquest mètode és ignorar totes les vibracions, rotacions, i moviments en general del sistema al voltant d'un mínim local

de la superfície d'energia potencial que es simulen, per exemple, en dinàmica molecular, i centrar-se únicament en els moviments que passen d'un mínim local de la PES a un altre. Aquests moviments s'anomenen esdeveniments estranys (*rare events*, en anglès), i poden correspondre a adsorcions, desorcions, difusions o bé reaccions químiques. Els esdeveniments estranys ocorren en una escala de temps molt diferent de l'escala temporal de les vibracions/rotacions. Per tant, es pot suposar que cadascun d'aquests esdeveniments ocorre independentment de tots els moviments que han ocorregut anteriorment, igual que en una cadena de Markov. Les transicions d'una configuració del sistema a una altra a partir de l'ocurrència d'esdeveniments estranys estan descrites per una equació mestra Markoviana

$$\frac{d\rho_u(t)}{dt} = \sum_v [\omega_{v\to u}\rho_v - \omega_{u\to v}\rho_u] \qquad (10.4)$$

on $\rho_u(t)$ és la probabilitat de que el sistema estigui en la configuració u a l'instant de temps t, i $\omega_{u\to v}$ és la velocitat de transició (també anomenada *reaction rate*, en anglès) per passar de la configuració u a la configuració v. Per exemple, en el cas d'una reacció en superfície el pas d'una configuració a una altra pot correspondre a la difusió d'un CO adsorbit d'un lloc d'adsorció a un altre de veí. Aquests llocs d'adsorció equivalen als mínims de la PES, i en el mètode kMC es descriuen amb un model de xarxa, on cada punt de la xarxa representa un lloc d'adsorció. La idea rere l'algoritme del kMC és resoldre numèricament l'equació (10.4) i poder proporcionar informació sobre la velocitat de formació dels productes de la reacció així com del recobriment de la superfície. Un dels algoritmes més populars del mètode kMC és el següent[54]:

1. Inicialització

Començar a partir d'una configuració inicial u

Definir $t = 0$

Crear una llista de tots els processos possibles i calcular les seves velocitats de transició

Calcular la suma de les velocitats de transició de tots els processos de la llista, $W_{tot,u}$.

Escollir les condicions de finalització de la simulació

2. Increment de temps

Generar dos nombre aleatoris $r_1, r_2 \in [0,1]$

Calcular l'interval de temps Δt de que no ocorri cap procés: $\Delta t = -\ln(r_1)/W_{tot}$

Incrementar el temps: $t \rightarrow t + \Delta t$

3. Selecció d'un procés

Emprant el segon nombre aleatori, seleccionar un dels processos de la llista i executar-lo. La selecció es fa ponderada, de manera que els processos amb una velocitat de transició més alta tenen una probabilitat més elevada de ser escollits

4. Actualització

Actualitzar la llista de processos afegint nous processos possibles i eliminant aquells processos que ja no són possibles

5. Continuació

Si es compleixen les condicions de finalització, s'atura la simulació. En cas contrari, es torna al pas numero 2

Les velocitats de transició dels diferents processos es poden calcular a partir de la teoria de col·lisions (per a processos d'adsorció) o bé a partir de la teoria de l'estat de transició, per a la resta de processos. A més, a diferència dels MM, el mètode kMC permet incloure interaccions laterals atractives o repulsives entre les diferents espècies adsorbides[55].

10.2.3. Resultats i conclusions

En el Capítol 4 de la tesis s'ha estudiat el mecanisme de la reacció WGSR sobre la superfície plana Cu(111) mitjançant simulacions kMC. Les velocitats de reacció s'han calculat a partir de dades DFT ja publicades[43,56], encara que s'han realitzat alguns càlculs addicionals emprant mateix nivell de càlcul per a obtenir alguns paràmetres que faltaven.

Un dels principals reptes de simulacions kMC és tractar conjuntament processos amb velocitats de reacció molt diferents. En el nostre cas, els processos de difusió de les espècies CO, OH i H tenen barreres energètiques força inferiors que la resta (vegeu la Taula 1 de la Publicació 3). Això implica que s'han de fer simulacions kMC extremadament llargues per tal d'observar una certa evolució del procés químic global. Per accelerar les simulacions, hem comprovat que podem reduir les velocitats dels processos de difusió en dos ordres de magnitud sense que el resultat final variï. No obstant això, si les seves velocitats es redueixen en quatre o més ordres de magnitud, el sistema entra en un règim de difusió lenta on els resultats de la simulació es veuen afectats.

Després de trobar el factor d'escalat adequat per als processos de difusió, hem investigat tant els efectes de la temperatura com de les pressions parcials dels reactius. L'efecte de la temperatura s'ha estudiat en el rang 463-625 K, mostrant un comportament d'Arrhenius en dos intervals de temperatura, i trobant un bon acord entre l'energia aparent d'activació calculada i l'experimental. El canvi de pendent es pot explicar a causa d'un canvi en RDS (vegeu més avall). Pel que fa a l'efecte de la composició de la barreja de reactius, hem observat que la producció d'H_2 es veu incrementada en mescles riques en CO (P_{CO}:P_{H2O} = 60:40, P_{TOT} = 100 Torr). La raó és que la velocitat de desorció del CO és al voltant de dos ordres de magnitud major que la de H_2O; per tant, s'ha d'utilitzar una pressió parcial més alta de CO per compensar.

Els RDSs s'han investigat analitzant les freqüències de tots els passos elementals (és a dir, la quantitat de vegades que s'executa un procés determinat per unitat de temps, vegeu la Figura 3 a la Publicació 3). Aquí, assumim que els RDSs seran aquells amb una baixa freqüència en la direcció cap endavant i gairebé nul·la en la direcció inversa (és a dir, no equilibrats). Aquesta anàlisi mostra que l'isomerització del COOH i la formació de CO_2 per la reacció entre COOH i OH són els RDSs a altes temperatures (625 K), mentre que la dissociació d'aigua és el RDS a baixes temperatures (463 K). El fet que hi hagi un canvi de RDS quan es redueix la temperatura és probablement el motiu pel qual hi ha dues pendents diferents en la gràfica d'Arrhenius. Finalment, veiem que el mecanisme associatiu (és a dir, el que implica l'intermedi COOH) proporciona la ruta de reacció dominant en totes les condicions de reacció estudiades, mentre que el mecanisme redox (és a dir, la formació de CO_2 per reacció entre CO i O) i el mecanisme de format (és a dir, el que implica l'intermedi HCOO), no tenen un paper important.

En el Capítol 5 de la tesi s'ha estudiat amb detall l'efecte de les interaccions vdW sobre les energies d'adsorció, les barreres energètiques i les velocitats de reacció dels diferents processos elementals que pertanyen a la reacció WGSR en Cu(321). Tal i com es mostra a la Taula 1 de la Publicació 4, la introducció de forces de dispersió té un efecte gairebé insignificant sobre les energies d'adsorció de la majoria d'espècies, excepte en el cas especial de CO_2, on el valor calculat de -0.28 eV és molt superior al valor de -0.06 eV sense dispersió. Per tal de validar aquest resultat, s'han emprat dues correccions de vdW més sofisticades que la D2 (la que hem utilitzat), que són la D3[57] i la de Tkatchencko *et. al*.[58]. mostrant resultats molt similars a la correcció D2. Clarament, l'adsorció d'una molècula tan estable com és la de CO_2 només es pot descriure correctament quan

s'inclouen les interaccions de vdW. Aquest efecte també s'observa per a la molècula CO, encara que en menor mesura: de -0.95 a -1.11 eV.

Tanmateix, l'efecte de les interaccions de vdW no només es limita a estabilitzar algunes molècules, sinó que també pot modificar les barreres energètiques dels processos en superfície. Per exemple, si considerem la formació del carboxil (és a dir, CO+OH → COOH), en absència de forces de dispersió, la barrera energètica només és de 0.46 eV, però si incloem aquestes forces, la parella CO+OH s'estabilitza gairebé 0.4 eV (vegeu la Taula 2 de la Publicació 4) i la barrera energètica augmenta a 0.84 eV. A banda de la formació de carboxil, altres processos superficials com ara la recombinació d'OH (OH+OH → H_2O+O) i la dissociació de COOH (COOH → CO_2+H) també experimenten una modificació important de la seva barrera energètica. Pel que fa a la resta de processos en superfície, l'efecte de les interaccions de vdW en les energies totals de reactius, de l'estat de transició i de productes són similars, donant lloc a un efecte net molt petit al calcular les barreres energètiques com a diferències d'energies totals.

Malgrat la mida reduïda de les espècies implicades en la reacció WGSR, els resultats mostren que la contribució de les forces de dispersió és important en termes generals, amb un efecte net i sense compensació d'errors en els diversos passos (processos) de la reacció, i que per tant, no s'hauria d'ignorar. Cal tenir en compte que si es vol estudiar la cinètica de la reacció en condicions realistes, incorporant els efectes de pressió i temperatura (per exemple, a través d'un MM o simulacions kMC), ignorar les interaccions de vdW pot produir canvis immensos en les velocitats de reacció calculades, amb diferències de fins a 4 ordres de magnitud (vegeu la Taula 3 a la Publicació 5). Aquests errors en les velocitats de reacció poden fer que obtinguem valors erronis de TOFs i de recobriments superficials.

Finalment, una comparació ràpida entre els perfils energètics de la superfície plana Cu(111) i la superfície esglaonada Cu(321) mostra que els àtoms de Cu de baixa coordinació (els que formen l'esglaó) impliquen una forta adsorció de les espècies reactives. L'efecte d'aquests *step sites* és especialment rellevant en el cas dels reactius, donant lloc a energies d'adsorció dos i tres vegades més grans per a CO i H_2O, respectivament. Pel que fa a l'efecte dels *sites* de baixa coordinació sobre les barreres energètiques, no hi ha una tendència clara. Alguns disminueixen (com ara la dissociació de l'aigua i la dissociació del carboxil), però altres augmenten (com ara la recombinació de carboxil i OH). Per tant, no és possible fer cap predicció fiable sobre l'efecte dels *step sites* en la cinètica de la reacció WGSR en coure: cal realitzar simulacions kMC.

L'efecte dels *step sites* en la reacció WGSR s'ha estudiat en el Capítol 6 de la tesis mitjançant el simulacions kMC, i introduint un total de 36 processos elementals. Les interaccions laterals entre adsorbats s'han introduït mitjançant el model d'expansions de clústers[59,60]. A causa de la presència d'esglaons, la superfície Cu(321) presenta una alta heterogeneïtat dels *sites* d'adsorció. Per tant, el model de xarxa utilitzat per al sistema actual inclou 4 tipus de *sites* diferents (a diferència del model de xarxa emprat per descriure la superfície plana Cu(111), on tots els *sites* es consideren equivalents).

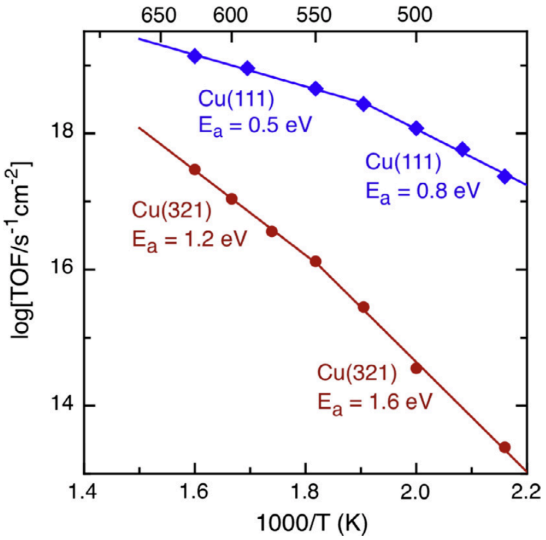

Fig. 10.5. Gràfic d'Arrhenius de la reacció WGSR en Cu(321) (cercles vermells) i en Cu(111) (quadrats blaus), en el rang de temperatures 463-625 K. Les pressions parcials de CO i H_2O són 26 Torr i 10 Torr, respectivament.

Una primera comparació entre ambdues superfícies mostra que, dins del rang de temperatura de 463-625 K estudiat, el TOF de la reacció WGSR en la superfície Cu(321) és entre dos (625 K) i quatre (a 463 K) ordres de magnitud inferior a la superfície Cu(111) (veure Figura 10.5). Aquest fet constitueix un clar exemple de que les superfícies amb *step sites* no sempre afavoreixen la catàlisi. Per a les pressions parcials P_{CO} = 26 Torr i P_{H2O} = 10 Torr, les espècies més dominants a la superfície en tot el rang de temperatures estudiat són els grups OH, seguit del CO, l'H_2O i finalment l'H atòmic (vegeu la Figura 4 de la Publicació 5). En canvi, en el cas de la superfície plana Cu(111) l'espècie predominant és l'H, excepte a la temperatura més alta (625 K) on els grups OH també esdevenen dominants (vegeu la Figura 4 de la Publicació 3). Ambdues superfícies tenen en comú un comportament Arrhenià en dos intervals de temperatura, amb energies d'activació aparent en el cas de la superfície Cu(321) d'1.2 eV (550-625 K) i 1.6 eV (463-

550K). Aquests valors són més grans que els corresponents a la superfície Cu(111) (0.5 i 0.8 eV, respectivament).

Pel que fa al mecanisme de reacció, la ruta associativa (és a dir, la formació de CO_2 a partir de l'intermedi COOH intermedi, que correspon als processos 9-11 de la Taula 1 a la Publicació 5) és la via dominant en totes les condicions estudiades, fins i tot quan canviem la proporció de pressions parcials de reactius. El mateix resultat es va observar en el cas de la superfície plana Cu(111). No obstant això, cal destacar que la ruta redox (és a dir, la formació de CO_2 a partir de l'oxidació de CO, que correspon als processos 6-8 de la Taula 1 de la Publicació 5), esdevé important en la superfície Cu(321) a altes temperatures, contribuint al voltant d'un 12% del TOF total. En la superfície Cu(111) aquesta ruta no és activa, ja que quan l'O atòmic es forma per la recombinació d'OH, la reacció torna cap enrere (la velocitat de reacció en el sentit invers és molt alta). Una altra diferència entre ambdues superfícies apareix si ens fixem en la deshidrogenació directa de COOH per formar CO_2 i H. Malgrat que aquest procés no s'observa en la superfície Cu(111) a causa d'una barrera energètica força elevada (1.18 eV), és una de les principals vies per a la producció de CO_2 a la superfície Cu(321), on la barrera energètica és de 0.80 eV.

Finalment, els RDSs s'han determinat emprant el criteri proposat per Campbell basat en el grau de control de velocitat[61]. Aquesta anàlisi mostra que la deshidrogenació de COOH i la reacció entre COOH i OH (és a dir, els processos 10 i 11 de la Taula 1 de la Publicació 5) són clarament els RDSs en totes les condicions estudiades de P i T. A més a més, la dissociació d'aigua és també un RDS quan la relació P_{CO}/P_{H2O} és baixa, i finalment la formació de H_2 també és un RDS a alts valors de P_{CO}/P_{H2O} (vegeu la taula 2 de la Publicació 5).

En aquest punt, hom es pot preguntar-se per què el TOF corresponent a la superfície esglaonada, on participen tres rutes diferents per a la formació de CO_2, és inferior al TOF de la superfície plana Cu(111), on no es produeixen ni la deshidrogenació directa de COOH i ni la oxidació de CO. La raó és molt senzilla. Per una banda, la formació de COOH és 0.62 eV endoèrgica en la superfície Cu(321), mentre que en la superfície Cu(111) es només 0.15 eV endoèrgica. Aquest canvi implica que la barrera d'energia en sentit invers és molt més baixa a la superfície esglaonada (0.24 eV) que a la superfície Cu(111) (0.55 eV). El mateix passa amb la dissociació de l'aigua: mentre que a la superfície plana aquest procés és exoèrgic i té una barrera energètica de 1.15 eV en el sentit invers, en la superfície esglaonada és endoèrgica, amb una barrera energètica

inversa de 0.60 eV (que correspon a una constant d'equilibri a 625 K de només $5.9 \cdot 10^{-3}$). D'altra banda, l'enverinament dels *step sites* per CO i, en menor mesura, per l'aigua, evita que es produeixin algunes reaccions elementals. Per tant, establir un rànquing de les superfícies més actives per catalitzar una reacció complexa com ara la WGSR basat únicament en les barreres energètiques dels processos directes (i no inversos) no sempre és correcte, tot i que sovint es fa[41,62,63].

En l'últim capítol de resultats de la tesi, el Capítol 7, s'han ressaltat i discutit diversos aspectes importants relacionats amb la descripció teòrica de l'estudi cinètic de reaccions químiques en superfície, emprant la reacció WGSR sobre superfícies de coure com a exemple pràctic. També s'han realitzat diverses simulacions kMC addicionals per donar suport a les nostres conclusions.

Els càlculs DFT sobre models adequats constitueixen una etapa prèvia necessària per als estudis cinètics de reaccions en superfície. A partir dels diagrames mínims d'energia basats en les energies DFT totals s'obtenen els PED, que proporcionen una primera visió d'un mecanisme de reacció determinat. El PED ha d'incloure la correcció ZPE, que es pot calcular utilitzant el model d'oscil·lador harmònic. Les freqüències baixes (<500 cm^{-1}) contribueixen molt poc a la ZPE, mentre que les altes poden contribuir en diverses desenes d'eV. No obstant això, s'ha de tenir en compte que aquesta tendència és inversa a la de la contribució de les freqüències vibracionals en l'entropia, tal com es comentarà més endavant. La Figura 2 de la Publicació 6 mostra que ometre la correcció ZPE comporta diferències de fins a 0.22 eV en algunes barreres energètiques, provocant grans canvis en les velocitats de reacció corresponents. Per exemple, la velocitat de reacció corresponent a la dissociació d'aigua a 625 K, incloent-hi ZPE, és d'$1.5 \cdot 10^{6}$ s^{-1}, mentre que el valor sense ZPE és només $2.5 \cdot 10^{4}$ s^{-1}, 60 vegades més petit. A més de la correcció ZPE, tots els PED també haurien d'incloure la contribució dels termes de dispersió, tal com s'ha discutit anteriorment.

Sovint, els PEDs fallen a l'hora de fer prediccions fins i tot qualitatives sobre els processos que impliquen grans canvis en l'entropia (com ara les adsorcions i desorcions). Per a tenir una visió més realista, cal substituir els PEDs pels diagrames d'energia lliure de Gibbs, que sí que tenen en compte els efectes de pressió i temperatura (veure Figura 10.6). Diversos autors només consideren els canvis entròpics en els processos d'adsorció i desorció, i assumeixen que les contribucions a l'entropia de les espècies adsorbides són zero, el que significa que, per a un determinat procés en superfície, la barrera d'energia lliure es pot considerar igual a la barrera energètica potencial. La secció 3.2 de la

Publicació 6 mostra que aquesta hipòtesi pot no ser vàlida per a processos de superfície que impliquin més de quatre àtoms, ja que en aquests casos hi haurà una gran quantitat de modes vibracionals baixos que tindran una gran contribució a l'entropia, o a altes temperatures.

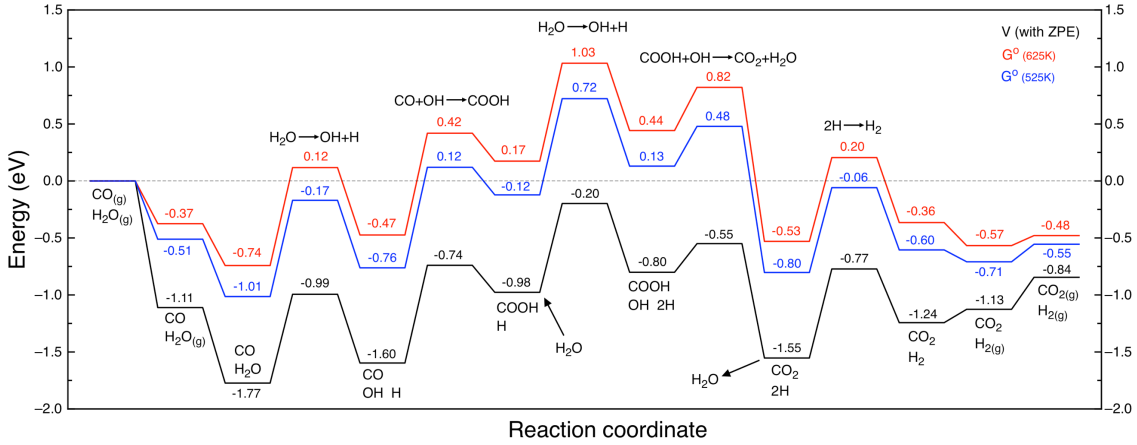

Fig. 10.6. Comparació entre el diagrama d'energia potencial amb ZPE (línia negra) i dos diagrames d'energia lliure de Gibbs (P = 1 bar, T = 525 K, blau i T = 625 K, vermell), corresponents al mecanisme associatiu de la reacció WGSR en Cu(321).

Encara que els diagrames d'energia lliure poden proporcionar una bona comprensió sobre els mecanismes de reacció que dominen una reacció química determinada[64–66], pot ser difícil fer estimacions sobre l'activitat d'un mecanisme o un altre en condicions realistes, especialment quan varis mecanismes amb barreres energètiques similars competeixen entre ells. Les simulacions cinètiques són necessàries per tancar la bretxa entre càlculs i els experiments. D'aquesta manera, podem utilitzar el models microcinètics[67,68] o les simulacions kMC més sofisticades. Entre els dos mètodes, el kMC evita l'aproximació del camp mitjà, i permet la introducció d'interaccions laterals entre els adsorbats, utilitzant les regles de bloqueig[69] o models d'expansió del clúster[70]. El desavantatge és que les simulacions kMC són més costoses, especialment quan la superfície és heterogènia i la quantitat de processos que intervenen és elevada.

Durant els últims quinze anys, la majoria dels estudis kMC s'han centrat en processos químics simples, com ara l'adsorció/desorció de O_2[71], l'oxidació de CO[72,73], la formació d'aigua[74] o la difusió d'hidrogen[75]. És només a partir dels últims cinc anys que s'han començat a publicar estudis kMC que impliquen reaccions complexes amb dotzenes de processos superficials (com ara metanació de CO[76], oxidació parcial del metanol[77], WGSR[56] ...). No obstant això, la gran majoria d'ells no incorporen interaccions laterals entre els adsorbats. Aquestes interaccions poden afectar tant al recobriment superficial

com a les barreres energètiques per als diferents processos elementals i al TOF final. La Taula 4 de la Publicació 6 mostra l'efecte quantitatiu de les interaccions laterals en el recobriment superficial i el TOF per a la reacció WGSR en Cu(321), on es troben diferències de fins a un 50%. A banda de les interaccions laterals, una bona descripció teòrica de la cinètica d'una reacció en superfície hauria d'incloure una descripció quantitativa dels processos de difusió, que s'ignoren en els perfils d'energia lliure. En el cas de la reacció WGSR en Cu(111), no incloure les difusions provoca una reducció d'un 25% en el TOF i diferències de fins a un 50% en el recobriment superficial d'algunes espècies (vegeu la Taula 3 de la Publicació 6). En els cas que el model de xarxa del kMC inclogui diferents tipus de llocs d'adsorció, el fet de no introduir els processos de difusió pot produir que directament no s'observi la formació de productes.

10.3. Bibliografia

1 A. Hartono, E. F. da Silva and H. F. Svendsen, Kinetics of carbon dioxide absorption in aqueous solution of diethylenetriamine (DETA), *Chem. Eng. Sci*., **2009**, 64, 3205–3213.

2 M.-O. Schach, R. Schneider, H. Schramm and J.-U. Repke, Techno-economic analysis of postcombustion processes for the capture of carbon dioxide from power plant flue gas, *Ind. Eng. Chem. Res*., **2010**, 49, 2363–2370.

3 Salmon-pink chabazite upon pearlescent heulandite crystals. Attribution: Rob Lavinsky, iRocks.com - CC-BY-SA-3.0.

4 A large, cauliflowerlike cluster of ivory colored stilbite. Attribution: Rob Lavinsky, iRocks.com - CC-BY-SA-3.0.

5 Spherical mordenite on a field of stilbite crystals. Attribution: Rob Lavinsky, iRocks.com - CC-BY-SA-3.0.

6 Faujasite with a beautiful "crackled glaze" surface. Attribution: Modris Baum - Public domain.

7 T.-H. Bae, M. R. Hudson, J. A. Mason, W. L. Queen, J. J. Dutton, K. Sumida, K. J. Micklash, S. S. Kaye, C. M. Brown and J. R. Long, Evaluation of cation-exchanged zeolite adsorbents for post-combustion carbon dioxide capture, *Energy Environ. Sci*., **2013**, 6, 128–138.

8 S. Chaemchuen, N. A. Kabir, K. Zhou and F. Verpoort, Metal–organic frameworks for upgrading biogas via CO_2 adsorption to biogas green energy, *Chem. Soc. Rev*., **2013**, 42, 9304–9332.

9 M. Palomino, A. Corma, F. Rey and S. Valencia, New insights on CO_2 −methane separation using LTA zeolites with different Si/Al ratios and a first comparison with MOFs, *Langmuir*, **2010**, 26, 1910–1917.

10 Y.-S. Bae and R. Q. Snurr, Development and evaluation of porous materials for carbon dioxide separation and capture, *Angew. Chem. Int. Ed*., **2011**, 50, 11586–11596.

11 E. J. Granite and H. W. Pennline, Photochemical removal of mercury from flue gas*, Ind. Eng. Chem. Res*., **2002**, 41, 5470–5476.

12 A. L. Myers and J. M. Prausnitz, Thermodynamics of mixed-gas adsorption, *AIChE Journal*, **1965**, 11, 121–127.

13 O. Talu, Measurement and Analysis of Mixture Adsorption Equilibrium in Porous Solids, *Chem. Ing. Tech*., **2011**, 83, 67–82.

14 D. Frenkel, B. Smit, Understanding Molecular Simulation, Academic Press, London, **2002**.

15 S. Plimpton, Fast parallel algorithms for short-range molecular dynamics, *J. Comp. Phys*., **1995**, 117, 1–19.

16 R. Ramachandran and R. K. Menon, An overview of industrial uses of hydrogen, *Int. J. Hydrog. Energy*, **1998**, 23, 593–598.

17 S. Rakass, H. Oudghiri-Hassani, P. Rowntree and N. Abatzoglou, Steam reforming of methane over unsupported nickel catalysts, *J. Power Sources*, **2006**, 158, 485–496.

18 H. Prats, L. Álvarez, F. Illas and R. Sayós, Kinetic Monte Carlo simulations of the water gas shift reaction on Cu(111) from density functional theory based calculations, *J. Catal*., **2016**, 333, 217–226.

19 L. Riboldi and O. Bolland, Overview on pressure swing adsorption (PSA) as CO_2 capture technology: state-of-the-art, limits and potentials, *Energy Procedia*, **2017**, 114, 2390–2400.

20 S. H. Lee, J. N. Kim, W. H. Eom, Y. D. Ko, S. U. Hong and I. H. Back, Development of water gas shift/membrane hybrid system for precombustion CO_2 capture in a coal gasification process, *Energy Procedia*, **2011**, 4, 1139–1146.

21 D. B. Bukur, B. Todic and N. Elbashir, Role of water-gas-shift reaction in Fischer–Tropsch synthesis on iron catalysts: a review, *Catal. Today*, **2016**, 275, 66–75.

22 J.R. Ladebeck, J.P. Wagner, in: W. Vielstich, A. Lamm, A.H. Gasteiger (Eds.), Handbook of fuel cells: fundamentals, technology and applications, vol. 3, John Wiley and Sons, Chichester, UK, **2003**.

23 D. Mendes, A. Mendes, L. M. Madeira, A. Iulianelli, J. M. Sousa and A. Basile, The water-gas shift reaction: from conventional catalytic systems to Pd-based membrane reactors - a review, *Asia-Pac. J. Chem. Eng*., **2010**, 5, 111–137.

25 D.-W. Jeong, W.-J. Jang, J.-O. Shim, W.-B. Han, H.-S. Roh, U. H. Jung and W. L. Yoon, Low-temperature water–gas shift reaction over supported Cu catalysts, *Renew. Energy*, **2014**, 65, 102–107.

26 N. A. Koryabkina, A. A. Phatak, W. F. Ruettinger, R. J. Farrauto and F. H. Ribeiro, Determination of kinetic parameters for the water–gas shift reaction on copper catalysts under realistic conditions for fuel cell applications, *J. Catal*., **2003**, 217, 233–239

27 A. Bruix, J. A. Rodriguez, P. J. Ramírez, S. D. Senanayake, J. Evans, J. B. Park, D. Stacchiola, P. Liu, J. Hrbek and F. Illas, A new type of strong metal–support interaction and the production of H_2 through the transformation of water on $Pt/CeO_2(111)$ and $Pt/CeO_x/TiO_2(110)$ catalysts, *J. Am. Chem. Soc*., **2012**, 134, 8968–8974.

28 J. A. Rodriguez, P. J. Ramírez, G. G. Asara, F. Viñes, J. Evans, P. Liu, J. M. Ricart and F. Illas, Charge polarization at a Au-TiC interface and the generation of highly active and selective catalysts for the low-temperature water-gas shift reaction, *Angew. Chem. Int. Ed*., **2014**, 53, 11270–11274.

29 S. Grimme, Density functional theory with London dispersion corrections, *Wiley Interd. Rev.: Comp. Mol. Sci*., **2011**, 1, 211–228.

30 P. G. Moses, J. J. Mortensen, B. I. Lundqvist and J. K. Norskov, Density functional study of the adsorption and van der Waals binding of aromatic and conjugated compounds on the basal plane of MoS_2, *J. Chem. Phys*., **2009**, 130, 104709.

31 B. A. De Moor, M.-F. Reyniers, M. Sierka, J. Sauer and G. B. Marin, Physisorption and chemisorption of hydrocarbons in H-FAU using QM-Pot(MP2//B3LYP) calculations, *J. Phys. Chem. C*, **2008**, 112, 11796–11812.

32 P. Janthon, F. Viñes, S. M. Kozlov, J. Limtrakul and F. Illas, Theoretical assessment of graphene-metal contacts, *J. Chem. Phys*., **2013**, 138, 244701.

33 J. T. Yates, Surface chemistry at metallic step defect sites, *J. Vac. Sci. Tech. A*, **1995**, 13, 1359–1367.

34 B. L. M. Hendriksen, M. D. Ackermann, R. van Rijn, D. Stoltz, I. Popa, O. Balmes, A. Resta, D. Wermeille, R. Felici, S. Ferrer and J. W. M. Frenken, The role of steps in surface catalysis and reaction oscillations, *Nat. Chem*., **2010**, 2, 730–734.

35 J. Rostrup-Nielsen and J. K. Nørskov, Step sites in syngas catalysis, *Top. Catal*., **2006**, 40, 45–48.

36 B. Hammer, O. H. Nielsen and J. K. Nørskov, Structure sensitivity in adsorption: CO interaction with stepped and reconstructed Pt surfaces, *Catal. Letters*, **1997**, 46, 31–35.

37 R. T. Vang, K. Honkala, S. Dahl, E. K. Vestergaard, J. Schnadt, E. Lægsgaard, B. S. Clausen, J. K. Nørskov and F. Besenbacher, Controlling the catalytic bond-breaking selectivity of Ni surfaces by step blocking, *Nat. Mater*., **2005**, 4, 160–162.

38 K. Honkala, A. Hellman, I. N. Remediakis, A. Logadottir, A. Carlsson, S. Dahl, C. H. Christensen and J. K. Nørskov, Ammonia synthesis from first-principles calculations, *Science*, **2005**, 307, 555–558.

39 C. H. Bartholomew, Mechanisms of catalyst deactivation, *Appl. Catal. A: General*, **2001**, 212, 17–60.

40 G.-C. Wang, L. Jiang, X.-Y. Pang, Z.-S. Cai, Y.-M. Pan, X.-Z. Zhao, Y. Morikawa and J. Nakamura, A theoretical study of surface-structural sensitivity of the reverse water-gas shift reaction over Cu(hkl) surfaces, *Surf. Sci*., **2003**, 543, 118–130.

41 Wang, L. Jiang, Cai, Pan, Zhao, W. Huang, Xie, Li, Sun and B. Zhong, Surface structure sensitivity of the water−gas shift reaction on Cu(hkl) surfaces: a theoretical study, *J. Phys. Chem. B*, **2003**, 107, 557–562.

42 H. Prats, F. Illas and R. Sayós, General concepts, assumptions, drawbacks, and misuses in Kinetic Monte Carlo and microkinetic modeling simulations applied to computational heterogeneous catalysis, *Int. J. Quantum Chem*., **2017**, 118, e25518.

43 A. A. Gokhale, J. A. Dumesic and M. Mavrikakis, On the mechanism of low-temperature water gas shift reaction on copper*, J. Am. Chem. Soc*., **2008**, 130, 1402–1414.

44 L. H. Thomas, The calculation of atomic fields, *Math. Proc. Cambridge*, **1927**, 23, 542–548.

45 P. a. M. Dirac, The quantum theory of the electron, *Proc. R. Soc. Lond. A*, **1928**, 117, 610–624.

46 P. a. M. Dirac, Note on exchange phenomena in the Thomas atom, *Math. Proc. Cambridge*, **1930**, 26, 376–385.

47 F. Bloch, Bemerkung zur elektronentheorie des ferromagnetismus und der elektrischen leitfähigkeit, *Z. Physik*, **1929**, 57, 545–555.

48 P. Hohenberg and W. Kohn, Inhomogeneous electron gas, *Phys. Rev*., **1964**, 136, B864–B871.

49 W. Kohn and L. J. Sham, Self-consistent equations including exchange and correlation effects, *Phys. Rev*., **1965**, 140, A1133–A1138.

50 X. Hua, X. Chen and W. A. Goddard, Generalized gradient approximation: an improved density-functional theory for accurate orbital eigenvalues, *Phys. Rev. B*, **1997**, 55, 16103–16109.

51 J. P. Perdew, K. Burke and M. Ernzerhof, Generalized gradient approximation made simple, *Phys. Rev. Lett*., **1996**, 77, 3865–3868.

52 J. P. Perdew and Y. Wang, Accurate and simple analytic representation of the electron-gas correlation energy, *Phys. Rev. B*, **1992**, 45, 13244–13249.

53 G. Kresse and J. Furthmüller, Efficient iterative schemes for ab initio total-energy calculations using a plane-wave basis set, *Phys. Rev. B,* **1996**, 54, 11169–11186.

54 A. P. J. Jansen, An introduction to kinetic Monte Carlo simulations of surface reactions, Springer, Heidelberg, **2012**.

55 J. Nielsen, M. d'Avezac, J. Hetherington and M. Stamatakis, Parallel kinetic Monte Carlo simulation framework incorporating accurate models of adsorbate lateral interactions, *J. Chem. Phys*., **2013**, 139, 224706.

56 L. Yang, A. Karim and J. T. Muckerman, Density functional kinetic Monte Carlo simulation of water–gas shift reaction on Cu/ZnO, *J. Phys. Chem. C*, **2013**, 117, 3414–3425.

57 S. Grimme, J. Antony, S. Ehrlich and H. Krieg, A consistent and accurate ab initio parametrization of density functional dispersion correction (DFT-D) for the 94 elements H-Pu, *J. Chem. Phys*., **2010**, 132, 154104.

58 A. Tkatchenko, R. A. DiStasio, R. Car and M. Scheffler, Accurate and efficient method for many-body van der Waals interactions, *Phys. Rev. Lett*., **2012**, 108, 236402.

59 E. Vignola, S. N. Steinmann, B. D. Vandegehuchte, D. Curulla, M. Stamatakis and P. Sautet, A machine learning approach to graph-theoretical cluster expansions of the energy of adsorbate layers, *J. Chem. Phys*., **2017**, 147, 054106.

60 M. Stamatakis and D. G. Vlachos, A graph-theoretical kinetic Monte Carlo framework for on-lattice chemical kinetics, *J. Chem. Phys*., **2011**, 134, 214115.

61 C. T. Campbell, Future directions and industrial perspectives micro- and macro-kinetics: their relationship in heterogeneous catalysis, *Top. Catal*., **1994**, 1, 353–366.

62 Y. C. Huang, T. Zhou, H. Liu, C. Ling, S. Wang and J. Y. Du, Do Ni/Cu and Cu/Ni alloys have different catalytic performances towards water-gas shift? A density functional theory investigation, *ChemPhysChem*, **2014**, 15, 2490–2496.

63 S.-C. Huang, C.-H. Lin and J.-H. Wang, Trends of water gas shift reaction on close-packed transition metal surfaces, *J. Phys. Chem. C*, **2010**, 114, 9826–9834.

64 J. Greeley, T. F. Jaramillo, J. Bonde, I. Chorkendorff and J. K. Nørskov, Computational high-throughput screening of electrocatalytic materials for hydrogen evolution, *Nat. Mater*., **2006**, 5, 909–913.

65 J. Greeley and M. Mavrikakis, Alloy catalysts designed from first principles, *Nat. Mater*., **2004**, 3, 810–815.

66 D. A. Hansgen, D. G. Vlachos and J. G. Chen, Using first principles to predict bimetallic catalysts for the ammonia decomposition reaction, *Nat. Chem*., **2010**, 2, 484–489.

67 C. Callaghan, I. Fishtik, R. Datta, M. Carpenter, M. Chmielewski and A. Lugo, An improved microkinetic model for the water gas shift reaction on copper, *Surf. Sci*., **2003**, 541, 21–30.

68 L. C. Grabow, A. A. Gokhale, S. T. Evans, J. A. Dumesic and M. Mavrikakis, Mechanism of the water gas shift reaction on Pt: first principles, experiments, and microkinetic modeling, *J. Phys. Chem. C*, **2008**, 112, 4608–4617.

69 J. M. Lorenzi, S. Matera and K. Reuter, Synergistic inhibition of oxide formation in oxidation catalysis: a first-principles kinetic Monte Carlo study of NO+CO oxidation at Pd(100), *ACS Catal*., **2016**, 6, 5191–5197.

70 H. Prats, P. Gamallo, F. Illas and R. Sayós, Comparing the catalytic activity of the water gas shift reaction on Cu(321) and Cu(111) surfaces: step sites do not always enhance the overall reactivity, *J. Catal*., **2016**, 342, 75–83.

71 S. Pogodin and N. López, A more accurate kinetic Monte Carlo approach to a monodimensional surface reaction: the interaction of oxygen with the RuO_2(110) Surface, *ACS Catal*., **2014**, 4, 2328–2332.

72 S. Piccinin and M. Stamatakis, CO oxidation on Pd(111): a first-principles-based kinetic Monte Carlo study, *ACS Catal.*, **2014**, 4, 2143–2152.

73 M. J. Hoffmann and K. Reuter, CO oxidation on Pd(100) Versus PdO(101)-($\sqrt{5}\times\sqrt{5}$)R27^{o}: first-principles kinetic phase diagrams and bistability conditions, *Top. Catal*., **2014**, 57, 159–170.

74 R. Hu, S. Huang, Z. Liu and W. Wang, Water formation on Pt(111) surfaces at high temperatures studied by kinetic Monte Carlo simulations, *Appl. Surf. Sci*., **2005**, 242, 353–361.

75 X. Yang and W. O. Oyeniyi, Kinetic Monte Carlo simulation of hydrogen diffusion in tungsten, *Fusion Eng. Des*., **2017**, 114, 113–117.

76 M. Andersen, C. P. Plaisance and K. Reuter, Assessment of mean-field microkinetic models for CO methanation on stepped metal surfaces using accelerated kinetic Monte Carlo, *J. Chem. Phys*., **2017**, 147, 152705.

77 T. B. Rawal, S. R. Acharya, S. Hong, D. Le, Y. Tang, F. F. Tao and T. S. Rahman, High catalytic activity of Pd1/ZnO(1010) toward methanol partial oxidation: a DFT+KMC study, *ACS Catal*., **2018**, 8, 5553–5569.